On Algorithmical Methods Facilitating Clinical Translation of Magnetic Particle Imaging

Vom Promotionsausschuss der
Technischen Universität Hamburg

zur Erlangung des akademischen Grades

Doktor-Ingenieur (Dr.-Ing.)

genehmigte kumulative Dissertation

von
Konrad Scheffler

aus Dresden

2025

Author's ORCID: https://orcid.org/0000-0002-6842-9204

1. Gutachter: Prof. Dr.-Ing Tobias Knopp
2. Gutachterin: Prof. Dr. rer. nat. Christina Brandt

Tag der mündlichen Prüfung: 13.10.2025

Abstract

Magnetic Particle Imaging (MPI) is an emerging tomographic imaging modality that has demonstrated significant potential in pre-clinical applications. As MPI moves towards clinical translation, the field faces a variety of interdisciplinary challenges that must be addressed through advancements in hardware, algorithmic methodologies, and application-driven refinements. This dissertation explores algorithmic methods that facilitate the transition of MPI from a research-oriented technology to a clinically viable imaging tool.

The work presented in this dissertation highlights the crucial interplay between applicational demands, hardware design and limitations, and methodological development. Hardware innovations define the fundamental capabilities of MPI, such as sensitivity, resolution, and acquisition speed. However, these capabilities alone are insufficient to meet the stringent requirements of clinical imaging. Algorithmic research plays a pivotal role in bridging this gap by optimizing imaging performance, improving reconstruction accuracy, and addressing practical constraints in system usability. From accelerating system calibration to refining signal processing techniques and optimizing field encoding strategies, computational advancements serve as a critical link between hardware constraints and the needs of real-world medical applications. By focusing on the synergies between these three domains, this dissertation demonstrates how methodological improvements can drive the clinical adoption of MPI.

Building on this foundation, the dissertation presents key methodological contributions that address specific challenges in MPI. The research contributions of the author are embedded within this broader framework, showcasing innovations that improve the efficiency and feasibility of MPI for clinical use. The core of the dissertation is composed of three peer-reviewed research articles, each addressing a distinct methodological challenge in MPI.

The first contribution introduces a novel approach to system calibration by leveraging extrapolation techniques for system matrices. Traditional MPI calibration is time-intensive and requires extensive measurements, limiting the scalability of the method for clinical applications. By employing an extrapolation-based methodology, this work significantly reduces the calibration burden while maintaining reconstruction accuracy, thereby improving efficiency and reducing experimental effort.

The second contribution focuses on regularization techniques in MPI reconstruction, presenting a method with automatically tuned parameters. Image reconstruction in MPI requires balancing noise suppression with the preservation of fine structural details, which is particularly crucial for medical imaging applications. This research introduces an adaptive regularization framework that dynamically adjusts parameters based on image characteristics,

enhancing robustness, improving reconstruction quality, and reducing the need for manual parameter selection.

The third contribution explores the use of ellipsoidal harmonic expansions to efficiently represent magnetic fields, addressing a fundamental challenge in MPI system modeling. Accurate field representations are essential for precise spatial encoding and the development of tailored field-cameras for MPI scanners. Compared to spherical harmonic representations, ellipsoidal harmonics provide greater geometric flexibility, enabling optimized field encoding strategies that are better suited for specific scanner designs. This study develops a mathematically rigorous yet efficient method for representing complex field distributions, offering improvements in encoding efficiency and adaptability to application-specific requirements.

Additional research contributions contextualize these advancements within collaborative efforts involving multiple research institutions. These collaborations have furthered the development of MPI modeling techniques, investigated the MPI performance of the clinically approved tracer Resotran, and contributed to studies on the development of novel MPI tracers. The findings presented in this dissertation have been disseminated through various peer-reviewed journal articles and conference proceedings, reinforcing the significance of algorithmic research in driving the clinical translation of MPI.

In conclusion, this dissertation demonstrates that algorithmic innovations are fundamental to bridging the gap between pre-clinical research and clinical implementation in MPI. By enhancing calibration processes, improving reconstruction methodologies, and optimizing field representations, these advancements facilitate the practical deployment of MPI in medical imaging. The final chapter provides a summary of the key findings and an outlook on future algorithmic research directions that will further support the integration of MPI into clinical workflows.

Kurzfassung

Die Magnetpartikelbildgebung (MPI) ist eine aufstrebende tomographische Bildgebungsmethode, die bereits großes Potenzial in präklinischen Anwendungen gezeigt hat. Mit der zunehmenden klinischen Translation von MPI steht das Forschungsfeld vor einer Vielzahl interdisziplinärer Herausforderungen, die durch Fortschritte in der Hardwareentwicklung, algorithmischen Methoden und anwendungsgetriebenen Optimierungen bewältigt werden müssen. Diese Dissertation untersucht algorithmische Methoden, die den Übergang von MPI von einer forschungsorientierten Technologie zu einem klinisch einsetzbaren Bildgebungsverfahren erleichtern.

Die in dieser Arbeit vorgestellten Untersuchungen betonen das entscheidende Zusammenspiel zwischen anwendungsspezifischen Anforderungen, Hardwaredesign und -beschränkungen sowie algorithmischer und methodischer Entwicklung. Hardware-Innovationen definieren die grundlegenden Leistungsmerkmale von MPI, wie Sensibilität, Auflösung und Bildaufnahmerate. Diese Eigenschaften allein reichen jedoch nicht aus, um die hohen Anforderungen der klinischen Bildgebung zu erfüllen. Algorithmische Forschung spielt eine Schlüsselrolle bei der Überbrückung dieser Lücke, indem sie die Bildgebungsleistung optimiert, die Rekonstruktionsgenauigkeit verbessert und praktische Einschränkungen in der Systemanwendbarkeit adressiert. Von der Beschleunigung der Systemkalibrierung über die Verfeinerung der Signalverarbeitung bis hin zur Optimierung der Feldkodierung stellen algorithmische Entwicklungen eine essenzielle Verbindung zwischen Hardwaregrenzen und den Anforderungen realer medizinischer Anwendungen dar. Durch die Fokussierung auf die Synergien zwischen diesen drei Bereichen zeigt diese Dissertation, wie methodische Verbesserungen die klinische Etablierung von MPI vorantreiben können.

Aufbauend auf dieser Grundlage präsentiert die Dissertation wesentliche methodische Beiträge, die spezifische Herausforderungen in der MPI-Technologie adressieren. Die Forschungsarbeiten des Autors sind in dieses übergeordnete Rahmenwerk eingebettet und demonstrieren Innovationen, die die Effizienz und Realisierbarkeit von MPI für den klinischen Einsatz verbessern. Der Kern dieser Dissertation besteht aus drei begutachteten Forschungsartikeln, die jeweils eine spezifische methodische Fragestellung in MPI behandeln.

Der erste Beitrag stellt einen neuartigen Ansatz zur Systemkalibrierung vor, der auf Extrapolationstechniken für Systemmatrizen basiert. Die herkömmliche Kalibrierung von MPI ist zeitaufwendig und erfordert umfangreiche Messungen, was die Skalierbarkeit der Methode für klinische Anwendungen einschränkt. Durch die Verwendung eines extrapolationsbasierten Verfahrens reduziert diese Arbeit die Kalibrierungsanforderungen erheblich, während die Rekonstruktionsgenauigkeit erhalten bleibt. Die steigert die Effizienz und senkt den experimentellen Aufwand.

Der zweite Beitrag konzentriert sich auf Regularisierungstechniken in der MPI-Rekonstruktion und stellt eine Methode mit automatisch gewählten Parametern vor. Die Bildrekonstruktion in MPI erfordert eine sorgfältige Balance zwischen Rauschunterdrückung und der Erhaltung feiner struktureller Details, was insbesondere für medizinische Anwendungen von entscheidender Bedeutung ist. Diese Arbeit entwickelt ein adaptives Regularisierungsverfahren, das Parameter dynamisch an die Bildcharakteristika anpasst, wodurch die Robustheit erhöht, die Rekonstruktionsqualität verbessert und der Bedarf an manueller Parameterauswahl reduziert wird.

Der dritte Beitrag untersucht den Einsatz von ellipsoidischen Harmonischen zur effizienten Darstellung magnetischer Felder, um eine zentrale Herausforderung in der MPI-Systemmodellierung zu bewältigen. Eine präzise Feldbeschreibung ist essenziell für die räumliche Kodierung und die Entwicklung maßgeschneiderter Feldkameras für MPI-Scanner. Im Vergleich zu sphärischen harmonischen Darstellungen bieten ellipsoidische Harmonische eine größere geometrische Flexibilität, die optimierte Feldkodierungsstrategien ermöglicht und spezifische Scannerdesigns besser unterstützt. Diese Studie entwickelt eine mathematisch fundierte und effiziente Methode zur Darstellung komplexer Feldverteilungen, die Verbesserungen in der Kodierungseffizienz und der Anpassungsfähigkeit an anwendungsspezifische Anforderungen bietet.

Weitere Forschungsarbeiten betten diese Entwicklungen in den Kontext gemeinschaftlicher Projekte mit verschiedenen Forschungseinrichtungen ein. Diese Kooperationen umfassten neben der Entwicklung von Modellierungstechniken für MPI auch Studien zur Leistungsfähigkeit des klinisch zugelassenen Tracers Resotran sowie Untersuchungen zur Entwicklung neuer MPI-Tracer. Die in dieser Dissertation vorgestellten Ergebnisse wurden durch verschiedene begutachtete Fachartikel und Konferenzbeiträge verbreitet und unterstreichen die Bedeutung der algorithmischen Forschung für die klinische Translation von MPI.

Zusammenfassend zeigt diese Dissertation, dass algorithmische Innovationen entscheidend sind, um die Lücke zwischen präklinischer Forschung und klinischer Anwendung in MPI zu schließen. Durch die Verbesserung der Kalibrierungsprozesse, die Optimierung von Rekonstruktionsmethoden und die Weiterentwicklung von Feldrepräsentationen erleichtern diese Fortschritte die praktische Implementierung von MPI in der medizinischen Bildgebung. Das abschließende Kapitel der Arbeit bietet eine Zusammenfassung der zentralen Erkenntnisse sowie einen Ausblick auf zukünftige algorithmische Forschungsrichtungen, welche die Integration von MPI in klinische Arbeitsabläufe weiter vorantreiben werden.

Contents

Acronyms

ADC analog-to-digital converter.

ADMM alternating direction method of multipliers.

AI artificial intelligence.

CS compressed sensing.

CT computed tomography.

DF-FOV drive-field field of view.

DSPs digital signal processors.

FFL field-free line.

FFP field-free point.

FFT fast Fourier transform.

FNOs Fourier neural operators.

FOV field of view.

FPGAs field-programmable gate arrays.

GUI graphic user interface.

LFR low-field region.

MPI magnetic particle imaging.

MRI magnetic resonance imaging.

OR overscan region.

PDF probability density function.

PEG polyethylene glycol.

PET positron emission tomography.

PNS peripheral nerve stimulation.

RF radio frequency.

SAR specific absorption rate.

SDE Stochastic Differential Equation.

SNR signal-to-noise ratio.

SPIONs superparamagnetic iron oxide nanoparticles.

1

Introduction

1.1 Medical Imaging

Medical imaging is a cornerstone of modern healthcare, offering non-invasive techniques to visualize the internal structures and functions of the human body. Historically, this field began as a diagnostic tool, starting with Wilhelm Conrad Röntgen's discovery of X-rays in 1895, which allowed physicians for the first time to examine the skeletal system without surgery. This discovery laid the foundation for the entire field of radiology and soon became essential for diagnosing fractures, infections, and later, lung diseases. Over the last century, medical imaging has rapidly evolved, integrating principles from physics, biology, engineering, mathematics, and computer science, leading to the development of a variety of imaging modalities, each with its own strengths and limitations.

These modalities can be classified into projection imaging methods, such as classical radiography [205], which produces static two-dimensional images, and tomographic methods, such as computed tomography (CT) [184] and magnetic resonance imaging (MRI) [292], which produce detailed cross-sectional views. Techniques such as ultrasound, which emerged in the mid-20th century, and MRI in the 1980s revolutionized soft tissue imaging, allowing precise visualisation of organs and structures such as the brain, muscles and joints [23].

Beyond diagnostics, the role of medical imaging has expanded significantly into the realm of intervention and therapy. The shift began with the advent of interventional radiology in the 1960s, pioneered by advances such as the Seldinger technique for vascular access [250] and the development of angiography. In the 1970s and 1980s, techniques such as percutaneous transluminal angioplasty and image-guided biopsies began to replace more invasive surgical procedures, reducing patient recovery times and improving outcomes. This marked the beginning of the use of imaging not only for diagnosis but also to guide therapeutic interventions, a trend that has continued with technologies such as real-time ultrasound and CT for minimally invasive procedures [23, 228, 20, 224].

Indirect imaging methods, which are dependent on the use of tracers, have further broadened the scope of medical imaging. Techniques such as positron emission tomography (PET) [289] and potentially magnetic particle imaging (MPI) [87] allow clinicians to assess metabolic and molecular processes, providing critical insights into diseases like cancer, where functional information is as important as anatomical detail [42, 213].

Methodological research and development are essential for advancing tomographic imaging, as they enable the full potential of hardware innovations and optimize imaging performance

for specific clinical and research applications. The scope of methodological development is illustrated by the following two examples. The incorporation of prior knowledge into the solution is evident in the case of compressed sensing (CS) in CT and MRI, where methodological advances in signal processing and reconstruction algorithms have led to significant improvements in image acquisition efficiency. CS exploits the sparsity of medical images in a suitable transform domain, allowing for high-fidelity reconstruction from undersampled data, thereby reducing radiation exposure in CT without compromising diagnostic quality [157]. In MRI, CS accelerates acquisition by undersampling k-space data and applying nonlinear reconstruction algorithms, effectively reducing scan times [84]. Another example – showing the improvement of models through algorithmic approaches – is the optimization of MRI shimming, a critical technique for counteracting magnetic field inhomogeneities that can degrade image quality, particularly in high-field and ultra-high-field MRI. Recent developments have introduced higher-order spherical harmonics for dynamic shimming, improving field uniformity in complex anatomical regions [120]. Moreover, more advanced ellipsoidal harmonics have been proposed as an orthogonal basis for designing shim coils, offering precise field corrections tailored to specific anatomical geometries [49, 24]. These refinements in shimming methods enable improved spectral and functional imaging, reduce susceptibility artifacts, and enhance quantitative imaging accuracy. By continuously refining acquisition strategies, reconstruction algorithms, and signal processing techniques, methodological research directly influences the practical utility and clinical translation of tomographic imaging technologies. As a result, different imaging modalities have evolved to address specific clinical needs, each with distinct strengths and limitations that define their applications and complementary roles in medical diagnostics. Examples of their use on the human body are shown in the representative Figure 1.1. A brief introduction to the basic principles and applications of the aforementioned methods is given below.

X-ray Radiography

In projection radiography, ionizing X-rays are emitted from a source and traverse the body before reaching a detector. The attenuation coefficients of different tissues vary, resulting in differing levels of X-ray absorption. The detector records these variations in intensity, thereby creating a two-dimensional projection image. Dense structures, such as bones, absorb more radiation, resulting in a white appearance. Conversely, softer tissues absorb less radiation, appearing in shades of gray or black. This modality is fundamental for the diagnosis of fractures, lung infections, dental issues and breast abnormalities (mammography) [178].

The fundamental principle is the Beer-Lambert law, which describes how X-ray intensity decreases as it passes through tissues of varying thickness and density. Modern advancements, such as digital radiography, facilitate the acquisition of higher-quality images while reducing radiation exposure [205]. Despite its benefits, X-ray radiography offers limited soft tissue contrast and involves exposure to ionizing radiation, necessitating dose optimization for patient safety. Nevertheless, the speed, cost-effectiveness and versatility of this technique make it a cornerstone of diagnostic imaging.

Computed Tomography

Computed tomography produces detailed cross-sectional and three-dimensional images by combining multiple X-ray projections taken from different angles around the body. This method is of great value for the visualization of complex structures and the differentiation of tissues with subtle density variations [178]. Computed tomography is a widely utilized diagnostic modality for a multitude of conditions, including brain injury, stroke, cancer,

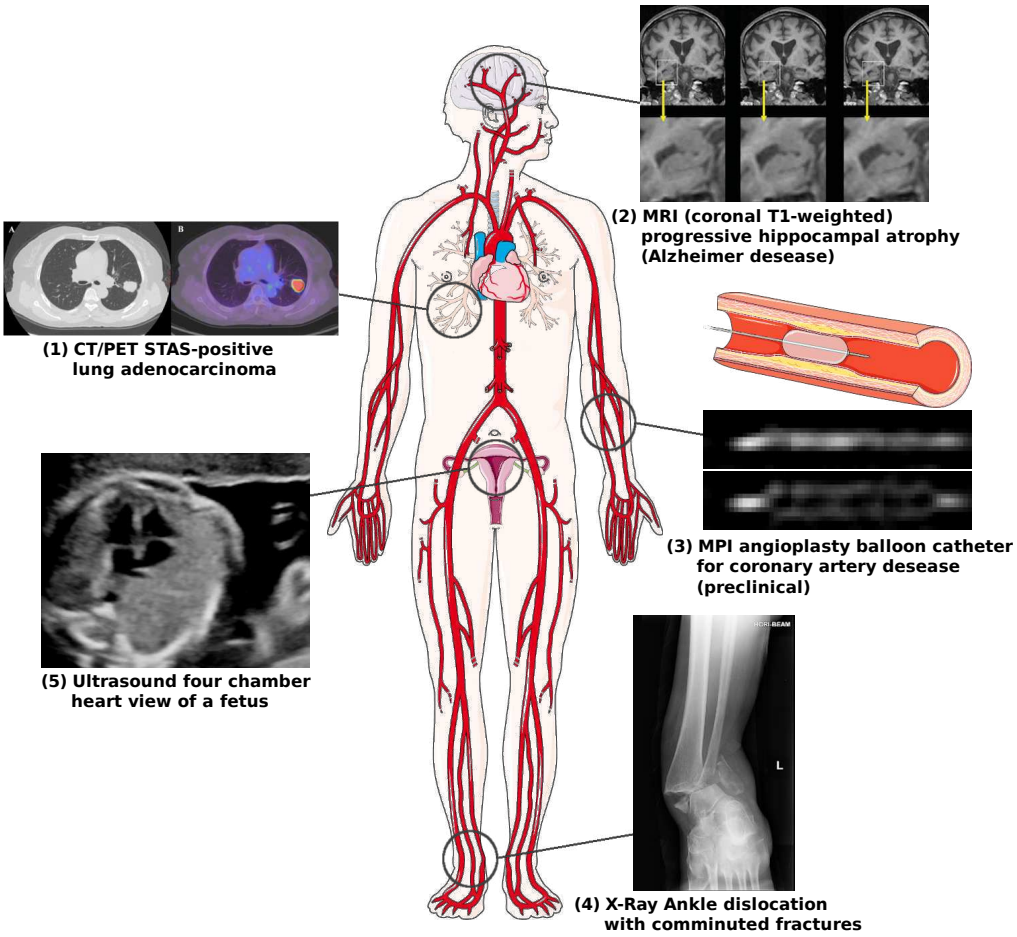

Figure 1.1: Important medical imaging modalities and examples of their use on the human body. (1) CT (left) and PET/CT (right) images show a STAS-positive lung adenocarcinoma [163]. (2) A series of three coronal T1-weighted MRI scans taken one year apart shows a progressive hippocampal atrophy consistent with Alzheimer's disease [126]. (3) Preclinical MPI scans of a dedicated balloon catheter for the treatment of coronary artery disease [270]. (4) A classic projection radiography of an ankle dislocation with comminuted fractures [139]. (5) Ultrasound image of the four chamber heart view of a fetus in the second trimester [231].

vascular disease, and internal bleeding. Furthermore, it is a vital instrument in the field of emergency medicine and surgical planning [311].

The reconstruction of CT images is dependent upon the Radon transform, which converts projections into spatial representations. The process is typically achieved through filtered back projection, a mathematical algorithm that inverts the Radon Transform in order to generate high-resolution cross-sectional images [311]. Modern CT scanners utilize iterative reconstruction algorithms with the objective of reducing image noise, enhancing detail and lowering radiation exposure [184].

The technology of CT has advanced significantly, with innovations like high-speed spiral (helical) CT enabling entire body scans in seconds [184]. Dual-energy CT, which employs two distinct X-ray energy levels, can differentiate materials more effectively, thus facilitating the characterization of tissues and the detection of pathologies. Contrast-enhanced CT scans further improve the visualization of vascular and organ structures. Despite the involvement

of ionizing radiation, CT is a fundamental tool in modern diagnostics due to its speed, accuracy, and capacity to provide comprehensive anatomical details [224].

Magnetic Resonance Imaging

Magnetic resonance imaging employs the use of strong magnetic fields and radio frequency (RF) pulses to generate detailed images of soft tissues, particularly the brain, spinal cord, muscles, and internal organs. It is a crucial diagnostic tool for neurological, musculoskeletal, and cardiovascular disorders [178, 132].

MRI exploits the magnetic properties of hydrogen atoms, which are abundant in water and fat. When exposed to a magnetic field, the spin of hydrogen nuclei align, and RF pulses temporarily disturb this alignment. As the nuclei undergo relaxation and return to their equilibrium state, the nuclei emit RF signals, which are detected by the scanner. These signals are encoded spatially with the aid of magnetic gradient fields [132].

The image reconstruction process uses the inverse Fourier transform, which converts the frequency-domain data (k-space) into a spatial image. This enables the generation of high-contrast images, particularly of soft tissues [132]. Furthermore, MRI incorporates sophisticated methodologies such as functional MRI for mapping cerebral activity and diffusion-weighted imaging to assess tissue integrity [127].

Since MRI does not involve ionizing radiation, it is a safer modality for repeated use. Its capacity to produce high-resolution images of soft tissues renders it an indispensable tool in modern medical imaging [292, 127]. However, it remains relatively expensive and complex and is primarily used in advanced healthcare settings.

Ultrasound Imaging

Ultrasound imaging, also referred to as sonography, uses high-frequency sound waves to generate real-time images of internal structures. A transducer emits sound waves that pass through tissues, with the reflected echoes being measured to generate images. The absence of ionizing radiation and the capacity for real-time imaging render sonography an indispensable and adaptable instrument across a spectrum of medical specialities [122, 302]. It is extensively used in obstetrics for monitoring fetal development, in cardiology for the evaluation of cardiac function, and in musculoskeletal imaging for the assessment of soft tissues, joints, and tendons [255]. Furthermore, it is commonly utilized in point-of-care diagnostics for the examination of organs such as the liver, kidneys, and bladder.

The fundamental mathematical technique employed in ultrasound is beamforming, in which signals emanating from multiple transducer elements are processed to create a focused image. This process involves combining the echoes from various angles, using time delays to steer the signal, ultimately constructing a coherent image. Doppler ultrasound takes advantage of the Doppler effect to measure blood flow. By analyzing frequency shifts in the echoes caused by moving blood cells, Doppler imaging allows clinicians to assess blood flow direction and speed, which is vital for diagnosing conditions like blockages, clots, or valve dysfunction [125, 38].

Positron Emission Tomography

Positron emission tomography imaging allows for the visualization of metabolic and molecular activity in the body by using radioactive tracers that emit positrons. These positrons interact with electrons in the body, annihilating and producing gamma rays. These gamma rays are detected by the PET scanner, which creates images based on the tracer distribution. PET

is particularly useful for assessing functional activity in tissues and organs, as the tracers accumulate in areas with higher metabolic activity [284].

The image reconstruction process is commonly based on iteratively solving inverse problems by incorporating the physics of positron annihilation to reconstruct accurate images. PET is invaluable in oncology for detecting cancer, in cardiology for assessing myocardial perfusion, and in neurology for evaluating conditions such as Alzheimer's disease, epilepsy, and brain tumors [249]. By tracking metabolic processes, PET provides detailed functional insights that complement structural imaging modalities like CT and MRI.

PET is often combined with CT or MRI to produce hybrid images (PET/CT or PET/MRI), improving the accuracy of anatomical information, enhancing diagnostic precision, and providing a more comprehensive understanding of disease processes [289].

Magnetic Particle Imaging

Magnetic particle imaging is an emerging modality that employs superparamagnetic iron oxide nanoparticles (SPIONs) as tracers to directly assess their response to oscillating magnetic fields. Tailored and biocompatible SPIONs must be injected prior to imaging. MPI provides quantitative, high-contrast and sensitive images of the tracer concentration with sub-millimeter resolution and without ionizing radiation, complementing imaging modalities that provide anatomical information such as MRI and CT. The MPI image reconstruction is based on the solution of a Fredholm integral of the first kind [87, 141] and can be achieved in a fast way [142].

As this work is focused on algorithmical methods in the context of the clinical translation of MPI, further details on the state of the art of MPI are provided in the following section 1.2 and section 1.3.

The field of medical imaging is undergoing a transformation driven by technological advancements, such as artificial intelligence (AI) (in particular machine learning), and hybrid imaging systems like CT/PET. These innovations are enhancing image quality, reducing radiation exposure, and facilitating more sophisticated analysis of complex data. AI is particularly influencing workflows by assisting radiologists in detecting subtle abnormalities, forecasting disease progression, and tailoring treatment strategies to individual patients [290, 321]. However, these developments also give rise to ethical concerns, including the assurance of data privacy, the safeguarding of patient confidentiality, and the addressing of biases inherent in AI systems. It is essential to establish robust frameworks for informed consent and the responsible use of imaging data in order to effectively address these challenges [130, 19, 327]. Furthermore, the integration of real-time imaging into minimally invasive surgeries and targeted drug delivery is revolutionizing patient care by enabling precision medicine [122, 142, 162, 287, 95]. Portable and bedside imaging devices, such as point-of-care ultrasound and low field MRI, are facilitating the accessibility of medical imaging in resource-limited settings. These technologies are closing gaps in healthcare access, enhancing equity, and improving global health outcomes.

1.2 Basic Principle of MPI

Magnetic particle imaging was invented by Bernhard Gleich and Jürgen Weizenecker at the Phillips Research Department in Hamburg in the early 2000s [87]. As an indirect imaging method, it relies on SPIONs injected into the body prior to imaging. SPIONs have an

iron-core size of approximately 10–50 nm, ensuring superparamagnetic behavior. In the absence of an external field these particles show a zero net magnetization because thermal fluctuations lead to constant change of the magnetic moment. However, when exposed to an external magnetic field, the magnetic moment of the particles align with the field over a characteristic relaxation time, producing a measurable net magnetization [141].

MPI uses oscillating drive fields $\boldsymbol{H}^D(t) : \mathbb{R} \to \mathbb{R}^3$ to excite the SPIONs, causing nonlinear magnetization changes. These changes induce voltage signals in receive coils, which are often processed in the frequency domain using a fast Fourier transform (FFT). The relative amplitudes of higher harmonics in the signal provide quantitative information about SPION concentration [141].

To achieve spatial encoding, a static magnetic gradient field is superimposed. This gradient creates a field-free line (FFL) or field-free point field-free point (FFP) – locations where the magnetic field strength is exactly zero. In the following we will focus on FFP based MPI. The gradient or selection field can be described mathematically as $\boldsymbol{H}^S : \mathbb{R}^3 \to \mathbb{R}^3$. Ideally $\boldsymbol{H}^S$ is assumed to be linear and can thus be represented by the gradient matrix $\boldsymbol{G} \in \mathbb{R}^{3\times3}$ with $\boldsymbol{H}^S(\boldsymbol{r}) = \boldsymbol{G}\boldsymbol{r}$. Surrounding the FFP is the low-field region (LFR), a small area where the field is weak enough that SPIONs remain unsaturated and respond dynamically to the drive fields. Outside the LFR, SPIONs are saturated and have only a negligible contribution to the signal. By systematically shifting the FFP along a predefined trajectory using controlled changes in the superposition of gradient and drive fields $\boldsymbol{H}(\boldsymbol{r}, t) = \boldsymbol{H}^S(\boldsymbol{r}) + \boldsymbol{H}^D(t)$, the system scans the region of interest and collects spatially resolved data on the SPION distribution. This process enables high-resolution 3D imaging of tracer concentration [141]. The two most widely used movement trajectories are discussed in subsection 2.2.1. For a three-dimensional Lissajous excitation, the drive field $\boldsymbol{H}^D(t) : \mathbb{R} \to \mathbb{R}^3$ can be represented as

$$\boldsymbol{H}^D(t) = \begin{pmatrix} A_x \sin(\omega_x t + \varphi_x) \\ A_y \sin(\omega_y t + \varphi_y) \\ A_z \sin(\omega_z t + \varphi_z) \end{pmatrix},$$

with amplitudes $A_i \in \mathbb{R}$, angle frequencies $\omega_i = 2\pi f_i$ and phase-shifts $\varphi_i \in [0, 2\pi)$ for $i \in \{x, y, z\}$. The excitation frequencies f_i can be defined through $f_x = \frac{f_B}{N_B}, f_y = \frac{f_B}{N_B - 1}, f_z = \frac{f_B}{N_B + 1}$ for a frequency divider $N_B \in \mathbb{N}$ and the scanners base frequency f_B [220].

The linear dependence between the time-dependent voltage signal $u(t)$ with $t \in \mathbb{R}_+$ and the particle concentration $c(\boldsymbol{r})$ with $\boldsymbol{r} \in \Omega \subset \mathbb{R}^3$ can be described via the following Fredholm integral of first kind [146, 135]

$$u_l(t) = \int_\Omega s_l(\boldsymbol{r}, t) c(\boldsymbol{r}) \, \mathrm{d}\boldsymbol{r}, \tag{1.1}$$

where $l \in \{1, ..., L\}$, $L \in \mathbb{N}$ denotes the receive coil index and the so-called system function $s_l : \mathbb{R}^3 \times \mathbb{R}_+ \to \mathbb{C}$ includes various parameters like the receive coil sensitivity profiles, the predefined trajectory of the FFP and the temporal derivative of the particle magnetization. This magnetization response is governed by the dynamic behavior of the tracer particles under the influence of the spatio-temporally varying magnetic field. A visual representation of the MPI signal Equation (1.1) in the time domain and it's terms is given in Figure 1.2.

With the knowledge of the time-dependent position of the LFR at hand, and assuming a simplified analytical model of an instatanous particle relaxation, the particle concentration can be directly mapped and deconvolved [92–94, 48]. This so-called X-space reconstruction

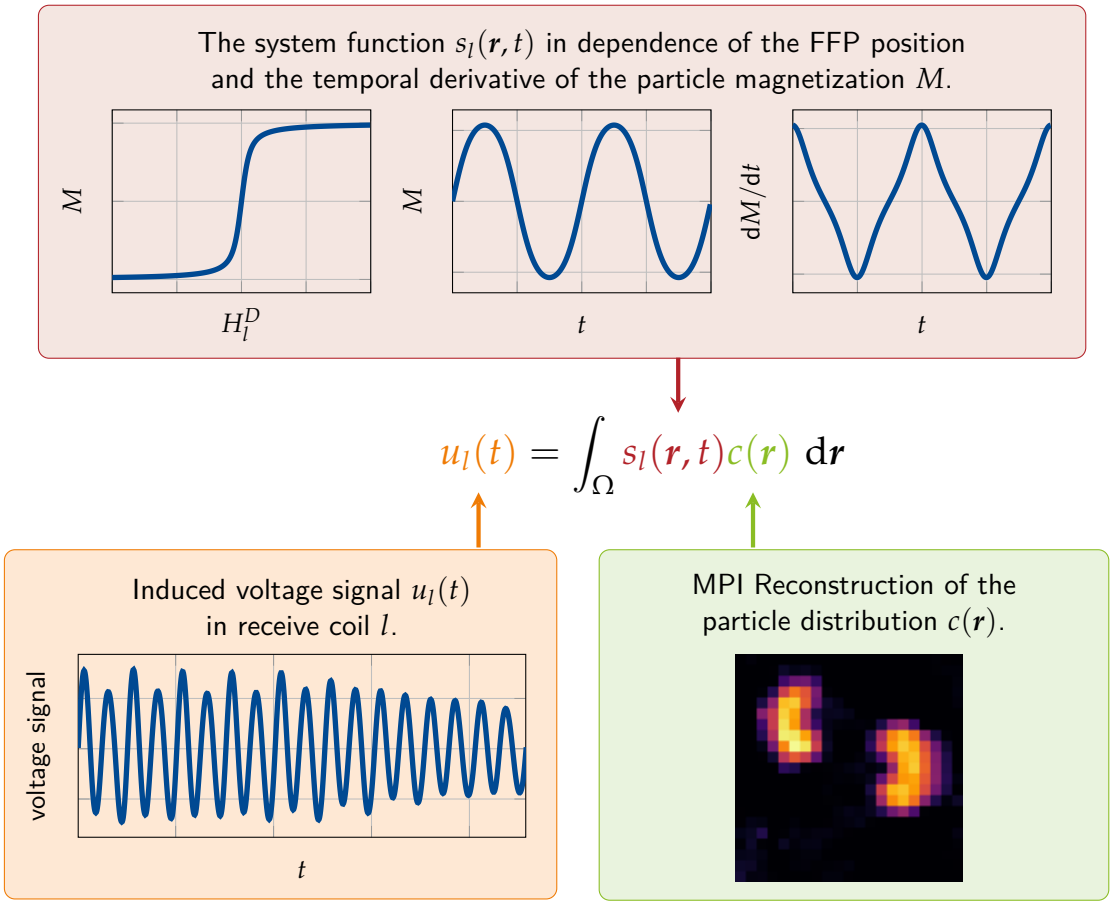

Figure 1.2: The MPI signal equation in time domain for receive coil l and one dimensional excitation field H_l^D. Top: The system function describes the relation between measured voltage signal and particle concentration in dependence of the temporal derivative of the particle magnetization M for each point r and time t. Left: The induced voltage signal in one receive coil l. Right: The reconstructed particle concentration after solving the integral equation.

is a fast and straightforward method but the assumptions introduce several inaccuracies and challenges: the reconstructed signal may appear blurred, and spatial resolution is biased. The signal does not perfectly map the instantaneous position of the LFR [220, 92, 48]. Another approach is to formulate the reconstruction of the particle concentration c from the measured voltage signal u as a linear inverse problem in the frequency domain. A Fourier series expansion of Equation (1.1) gives the Fourier coefficients

$$\hat{u}_{l,k} = \int_\Omega \hat{s}_{l,k}(\boldsymbol{r}) c(\boldsymbol{r}) \, \mathrm{d}\boldsymbol{r}, \tag{1.2}$$

with $K \in \mathbb{N}$ frequency components and $k \in \{1, ..., K\}$. With a spatial discretization of the field of view (FOV) Ω at $N \in \mathbb{N}$ nodes $\boldsymbol{r}_n, n \in I_N = \{1, ..., N\}$, the integral in Equation (1.2) can be approximated as a finite sum and the MPI reconstruction problem can be stated in matrix-vector form as

$$\boldsymbol{u}_{\text{meas}} = \boldsymbol{S}\boldsymbol{c}. \tag{1.3}$$

Here $\boldsymbol{S} = (w_n s_k(\boldsymbol{r}_n))_{k\in I_{L,K}, n\in I_N}$ denotes the system matrix with quadrature weights w_n and $I_{L,K} = \{1, ..., L \cdot K\}$ and $\boldsymbol{c} = (c(\boldsymbol{r}_n))_{n\in I_N}$ is the particle concentration vector. $\boldsymbol{u}_{\text{meas}} = (u_k)_{k\in I_{l,K}} + \boldsymbol{\eta}$ with $\boldsymbol{\eta} \in \mathbb{C}^{L\cdot K}$ is the measured voltage vector with additive background noise. The system matrix $\boldsymbol{S}$ can be obtained through various approaches. The most common method in practice involves measurement-based calibration, where a single delta sample of the tracer is used to characterize the scanner's response [141]. This approach fully captures the physical behavior of the system but ties the calibration and subsequent image resolution to a predefined grid. For a fully measured system matrix, a delta probe – mounted on a robot – is moved systematically across the grid to sample the entire FOV. This process is labor-intensive and time-consuming, particularly for three-dimensional and large high-resolution grids [17, 268]. A faster alternative is the hybrid system matrix approach, in which the delta sample is measured only in the central voxel [300]. This single measurement can be performed using an MPI scanner, but also with a magnetic particle spectrometer with three-dimensional excitation. Spatial encoding is achieved by using a magnetic offset field that represents the magnetic gradient field at an infinitesimal area. However, this approach is limited because the drive field range restricts the achievable displacement [300, 301]. Alternatively, the system matrix can be constructed using model-based methods, which rely on physical models incorporating assumptions about magnetic particle dynamics and magnetic fields [146]. These models vary in accuracy and computational cost [135]. The main advantage of the model-based approach is that it minimizes scanner calibration and provides flexibility in resolution, making it particularly suitable for scenarios requiring rapid setup.

With the system matrix at hand, solving the linear system (1.3) for the particle concentration boils down to a discrete linear inverse problem, which is typically solved using a least squares approach. However, the MPI system is highly ill-posed, it is overdetermined and the measurements have additive background noise [65, 137]. Therefore, a Tikhonov regularized least squares approach is usually considered [141]:

$$\boldsymbol{c}_\lambda \;=\; \underset{\boldsymbol{c}\in\mathbb{R}_+^N}{\operatorname{argmin}} \; \|\boldsymbol{S}\boldsymbol{c} - \boldsymbol{u}_{\text{meas}}\|_2^2 \;+\; \lambda \, \|\boldsymbol{c}\|_2^2 \,. \tag{1.4}$$

The parameter $\lambda \in \mathbb{R}_+$ controls the influence of the regularization term and real and non-negativity constraints are typically applied [141, 306]. There are many well-known algorithms for solving optimization problems of this type. Due to the size and high memory demands of the MPI system matrix, iterative solvers – in particular the regularized Kaczmarz method – have proven to be the most suitable. The Kaczmarz method [128] operates on a row-by-row basis, iteratively improving the solution by projecting it onto hyperplanes defined by the rows of the system matrix. This approach is both memory- and computationally efficient, as it avoids storing or manipulating the full matrix, and it is robust to small fluctuations arising from the ill-posed nature of the reconstruction problem. Moreover, the Kaczmarz method achieves relatively fast convergence, especially when the matrix rows are processed in optimized order [143, 110]. Regardless of the specific solver used, the strength and formulation of regularization have a profound impact on the quality of the reconstruction. In addition to the regularization parameter λ, several other factors – for example the choice of the regularization term and the number of iterations – contribute to a high-dimensional and interdependent parameter space. This complexity makes parameter selection a challenging and active area of research in MPI reconstruction [26, 242].

The linear relationship between MPI signal strength and iron mass allows absolute quantification of nanoparticle concentration in a given volume. This is particularly useful for

applications such as drug delivery monitoring, where knowing the exact tracer concentration allows precise evaluation of the dosage at the target site to ensure therapeutic efficacy while minimizing side effects.

1.3 State of the art in MPI

Since its introduction, MPI has attracted significant research interest as a novel imaging modality [141]. This section highlights key advancements and the current state of MPI research.

Hardware advancements have played a critical role in MPI's evolution since its first demonstration in 2005. Initial efforts focused on scaling scanner bores for preclinical rodent imaging [89] and later adapting the technology for human-sized systems [180, 219, 99, 294, 280, 183], facilitated by the introduction of focus-field coils. Innovations like higher magnetic field gradients [155] and optimized receiver coils [97] have significantly enhanced sensitivity and spatial resolution, achieving sub-millimeter accuracy and enabling detection of SPIONs in minute concentrations. Moreover, novel hardware designs, such as combined MRI/MPI systems [295, 79], MRI/CT systems [296], single-sided MPI [234, 186], flexible receive coils [294], and handheld MPI systems [181, 123, 320], have expanded MPI's potential clinical applications.

With classical sinusoidal excitation fields and spatial encoding using a gradient field, the size of the FOV is determined by the ratio of the excitation amplitude to the gradient strength. Consequently, increasing the gradient strength to achieve higher spatial resolution reduces the FOV. Conversely, increasing the excitation amplitude can expand the FOV, but at typical excitation frequencies of 10 kHz to 100 kHz, higher amplitudes risk inducing peripheral nerve stimulation (PNS) in the patient [280, 206, 101]. Multi-patch sequencing overcomes these limitations by dividing the imaging volume into smaller patches, acquired sequentially and combined into a complete image. Patch displacement is achieved using a low-frequency focus field, enabling efficient imaging of larger regions without exceeding PNS or FOV constraints [268, 89, 144].

The first commercially available preclinical MPI scanner for three dimensional imaging was introduced by Bruker BioSpin GmbH in 2014 [90]. Magnetic Insight Inc. developed the first commercially available FFL MPI system in 2017 [177]. Both companies have since iterated on their designs and are actively developing next generation scanners.

Since the introduction of MPI, significant efforts have been made to accurately model the MPI system equation, as model-based reconstruction allows for arbitrary resolution and rapid system calibration. While the modeling of the signal acquisition chain has advanced to a stage where minimal calibration is required [281], the development of an adequate particle magnetization model remains an active area of research [220, 146, 135, 150, 308]. The most accurate particle magnetization model to date is based on the Fokker-Planck equation, but its high computational requirements make it impractical for three-dimensional imaging [4]. A major breakthrough in MPI modeling was the derivation of an analytical formulation for the equilibrium model using the Langevin function [176], which provides computational efficiency but does not account for relaxation effects. Recently, this model has been extended to include anisotropy [175], allowing for better reconstruction results, and a formulation for fast reconstruction has been introduced and validated [58].

MPI's real-time imaging capabilities are supported by sequence speeds of up to 46 volumes per second using Lissajous trajectories [306, 140] and iterative reconstruction methods [142,

143]. These advancements facilitate dynamic applications, such as monitoring blood flow, cardiac perfusion, and drug delivery tracking *in vivo* [306, 97, 98].

Advances in nanoparticle development have also been instrumental for higher sensitivity and resolution. Optimizing SPION core size for MPI performance was demonstrated early [68], followed by the presentation of an high-performing tracer featuring monodisperse iron cores coated with polyethylene glycol (PEG) [67]. Micelle-based tracers [259] achieved comparable results, while studies on commercially available tracers [171, 62, 63] highlighted the significant impact of particle clustering on MPI signals. Furthermore, polyethylene glycol (PEG)-coated SPIONs with long circulation times and strong MPI performance in blood have been introduced [134]. More recently, MPI-tailored and commercially available tracers have been developed by micromod Partikeltechnologie GmbH [315, 170, 85].

Functional contrast in MPI is achieved by distinguishing between different nanoparticle types or environments that affect relaxation dynamics or spectral responses, such as variations in ambient temperature or viscosity [217, 190, 293, 56]. This capability enables applications like multi-functional imaging, environmental sensing, and enhanced diagnostics, offering both spatial and material-specific insights.

In addition to the preclinical MPI research focused on vascular medicine and cerebral hemorrhage [123, 170, 47, 15, 271, 297], there are various studies on the ability to use SPIONs not only as imaging agents but also as therapeutic tools, positioning MPI as a promising theranostic platform. Examples are hyperthermia therapy [196, 3, 272, 43, 34], targeted drug delivery [291, 158, 102, 35], tumor targeting [69, 70, 8], implantation and treatment monitoring [43, 230, 103, 276], cardiovascular interventions [113, 115, 222, 288, 189], and untethered activation of micro- and nanorobots [201, 16, 14, 36].

1.4 Publications, Research Contributions, and Dissertation Structure

The current challenges in MPI research are largely focused on bringing the technology and its various potential applications to the clinical stage. This interdisciplinary task requires a strong interplay between hardware development, methodological advancements, and application-driven requirements. While hardware innovations define the fundamental capabilities of MPI – such as sensitivity, resolution, and acquisition speed – methodological research is crucial for optimizing these capabilities and ensuring their clinical viability. Advanced algorithmic techniques not only enhance image reconstruction but also address practical limitations in system calibration, signal processing, field optimization, and artifact reduction.

For example, compressed sensing has been instrumental in reducing the time required for MPI system calibration [104, 105], making the technology more feasible for clinical use. Likewise, efficient representations of magnetic fields using spherical or ellipsoidal harmonics improve field parameterization, ultimately enhancing hardware development and reconstruction accuracy [28, 74, 243]. These examples demonstrate that, just as in CT and MRI, methodological advancements in MPI are not merely supplementary but are fundamental to overcoming hardware limitations and unlocking the full potential of the technology. By improving efficiency, reducing acquisition times, and refining imaging precision, these developments play a critical role in driving MPI toward clinical translation.

The second chapter 2 of this dissertation provides a structured overview of the clinical translation of MPI, emphasizing the interplay between hardware, algorithmic research, and application-driven constraints. It highlights key methodological advancements that facilitate

this transition, embedding and contextualizing the author's research contributions within the broader framework of MPI development.

The three peer-reviewed research articles that comprise the main part of this cumulative dissertation are presented in the ensuing chapters. Chapter 3 presents a methodology for reducing MPI calibration time and memory usage by extrapolating system matrices beyond the measured field-of-view [237]. Chapter 4 addresses the challenge of regularization in MPI reconstruction and introduces a method for automatic parameter tuning, enabling robust and user-independent image reconstruction [239]. Chapter 5 introduces the use of ellipsoidal harmonic expansions to efficiently measure and represent magnetic fields in tomographic imaging. The primary research article delves into the theoretical underpinnings and provides extensive validation of the method through simulations in MRI [243]. To contextualize this topic within the scope of this dissertation, the author has elected to follow up with two peer-reviewed proceedings articles. The first is a simulation study [241], and the second is a measurement study [240] of ellipsoidal harmonic expansions on magnetic fields present in MPI.

Other notable research publications that the author worked on during his doctoral studies are embedded in the context of this dissertation in chapter 2. They include collaborations with various research groups from the Swiss Federal Institute of Technology ETH Zürich and the Swiss Federal Laboratories for Materials Science and Technology EMPA St. Gallen [194, 260], the University of Salento and the University of Urbino [256], the Fraunhofer Research Institution for Individualized and Cell-Based Medical Engineering IMTE Lübeck, the University of Lübeck and the University of Würzburg [192], the German Research Center for Artificial Intelligence DFKI Lübeck, the University of Lübeck, and the University of Bremen [175, 58]. Furthermore, a variety of proceedings articles and abstracts have been presented at the International Workshop on Magnetic Particle Imaging (IWMPI) 2022 in Würzburg [236, 193], the IWMPI 2023 in Aachen [238, 235, 244, 5], the IWMPI 2024 in Flüeli-Ranft [110, 241, 279, 174, 136] and the IWMPI 2025 in Lübeck [240, 119, 286].

In the last chapter 6, the dissertation is concluded with a small summarizing discussion and an outlook on algorithmical research for clinical translation of MPI.

2

Clinical Translation of MPI

Since its inception, MPI has undergone significant advancements, as presented in Chapter 1. These breakthroughs have expanded the boundaries of the technology, demonstrating its immense potential across a wide range of applications. However, despite its promising capabilities, MPI has yet to transition from preclinical research to widespread clinical adoption. This critical milestone remains a distant goal, as numerous challenges still need to be addressed. Comprehensive scientific review articles on clinical translation of MPI have been presented by Chandrasekharan et al. [44] and more recently in german by Gräser et al. [100].

2.1 Pathways to Translating MPI into Clinical Practice

The journey toward clinical translation is undeniably complex, requiring progress on multiple fronts – technological, algorithmic, regulatory, and industrial. Encouragingly, many of the foundational elements for this transition are either well understood or actively being explored by research groups worldwide. The interplay of advancements in these domains holds the potential to accelerate progress. For instance, a landmark achievement such as obtaining the first human MPI image could serve as a pivotal moment, sparking heightened interest, additional research efforts, and significant industrial investments.

This chapter provides a comprehensive overview of the multifaceted pathway toward the clinical implementation of MPI. While a range of contributing factors will be discussed, the primary focus lies on algorithmic advancements, reflecting the author's specific area of expertise. The first section aims to offer a general perspective on MPI's translational journey. It begins by outlining the key domains of fundamental research that underpin MPI's potential in clinical imaging. This is followed by an overview of prospective clinical applications, highlighting how MPI could be integrated into routine practice. The section concludes with a discussion of the overarching challenges and limitations that currently hinder clinical adoption, thereby motivating the more detailed investigations that follow. These subsequent sections explore the major research domains – hardware development, methodological development, and tracer development – while also situating the author's own contributions within the broader context of MPI's clinical translation. The chapters that follow, forming the core of this cumulative dissertation, present and discuss these algorithmic contributions in detail.

2.1.1 Fundamental Research Domains

The diverse potential clinical applications of MPI each demand a unique emphasis on specific technological aspects. However, three primary research domains stand out as the essential roots for establishing MPI in clinical practice. These domains, visualized as the foundational roots of clinical translation in Figure 2.1, are deeply interconnected, with progress in one area often driving advancements in the others.

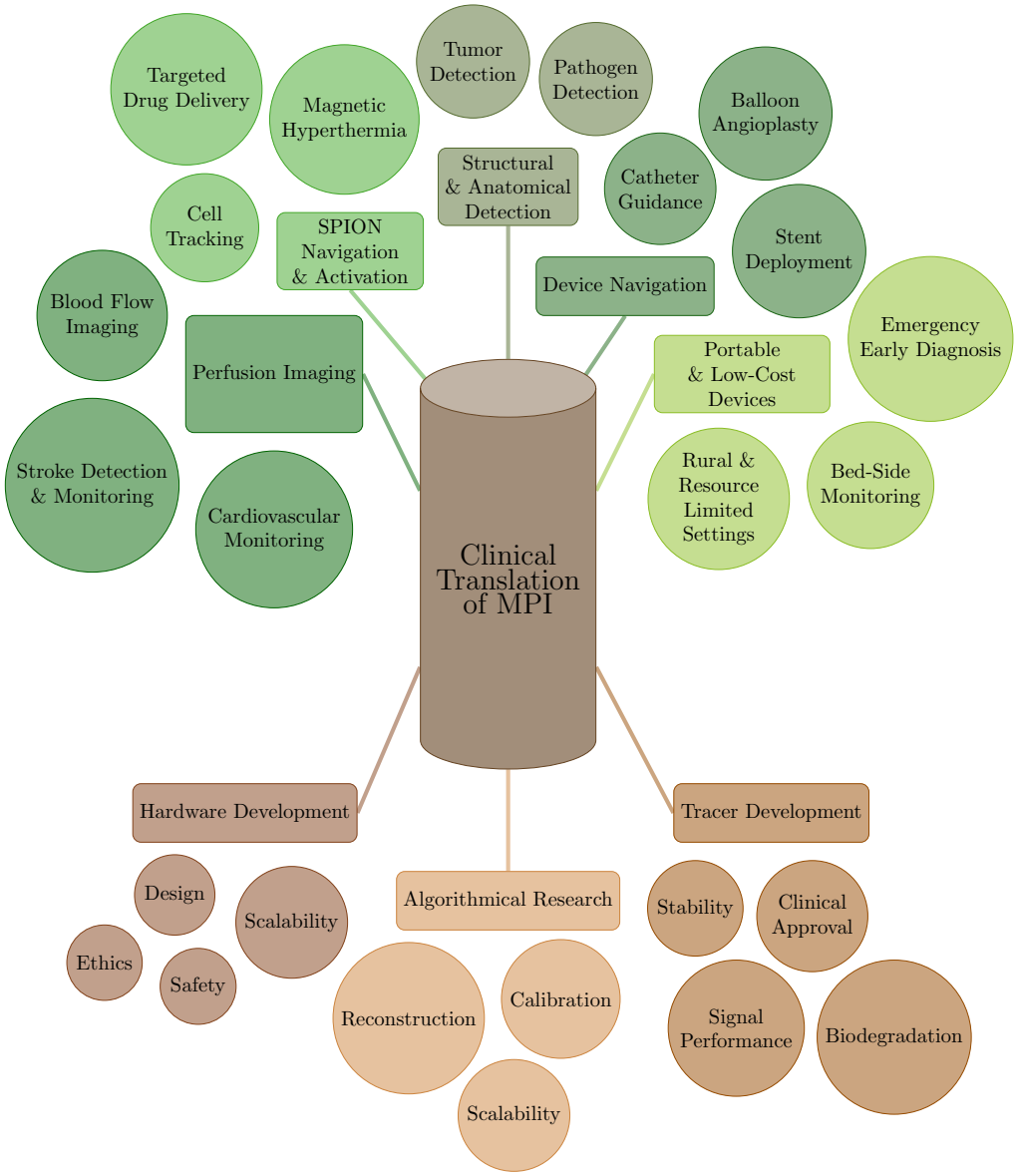

Figure 2.1: The clinical translation of MPI is illustrated in a tree-shaped mind map. The three primary research domains are represented by fundamental roots: hardware development, algorithmical research, and tracer development, which have associated sub-roots. The treetop illustrates various potential clinical applications, which are sorted into five categories from left to right: perfusion imaging, SPION navigation and activation, structural and anatomical detection, device navigation, and portable and low-cost imaging devices.

The first and most apparent root is the development of advanced hardware solutions. This encompasses intelligent and efficient design across all components of the send-and-receive chains, tailored to the requirements of specific use cases. Key challenges include scaling up hardware to accommodate full-body scanners and addressing patient safety concerns, along with ethical considerations regarding risks and benefits.

The second crucial domain is algorithmic research, which is central to extracting meaningful images from the measured signals. This involves two primary steps: calibration, which ensures accurate system interpretation, and reconstruction, which visualizes the tracer's distribution within the tissue. As MPI evolves, there is an increasing need for algorithms that enable fast and efficient image acquisition and reconstruction, with minimal calibration effort. Advancements are also vital for overcoming hardware limitations, particularly in scaling MPI to larger fields of view or higher resolutions. Ensuring rapid, high-quality imaging is key to making MPI practical for real-time clinical applications.

The third foundational area is tracer development. Since MPI relies on the magnetization behavior of SPIONs, the quality of the image is inherently tied to the signal performance of the tracer. For MPI to transition to clinical practice, SPIONs must meet stringent requirements for safety and biocompatibility. This includes ensuring that they are non-toxic, biodegradable, and stable in the bloodstream, with the ability to maintain a stable signal for a predefined duration before degradation. Additionally, these particles must be cleared from the body in a safe manner, particularly in applications involving repeated imaging, such as chronic disease monitoring, where the risk of accumulation or long-term adverse effects must be minimized.

In section 2.2, section 2.3, and section 2.4 we will delve deeper into these three roots, exploring their individual challenges, interdependencies, and contributions to the clinical translation of MPI.

2.1.2 Prospective Clinical Applications

Returning to the many potential clinical applications of MPI, as depicted in Figure 2.1, many of these are already being explored in preclinical research, with feasibility studies highlighted in chapter 1. These applications all rely on MPI's unique properties and capabilities, which often make it more suitable than traditional imaging modalities for specific scenarios [314]. However, realizing the full clinical potential of MPI depends not only on identifying these applications but also on addressing the technological challenges that underpin them.

One of MPI's strongest capabilities lies in its ability to not only detect SPIONs but also navigate and activate them, including heating for therapeutic purposes. The latter is usually accomplished by using specific inserts to stimulate particles at higher frequencies, as well as gradient fields for arbitrary localization [272]. This multifunctionality naturally distinguishes between purely diagnostic applications, such as perfusion imaging, and theranostic applications, such as magnetic hyperthermia. However, because diagnostic imaging often serves as a prerequisite for therapy planning, guidance, and monitoring, a more integrated and application-oriented categorization is required. This categorization should reflect the overlapping functional requirements and shared technical challenges of combined diagnostic-therapeutic MPI use cases.

Perfusion imaging is a major category of MPI applications, focusing on the visualization of blood flow and tissue perfusion with high temporal resolution [30]. This allows for quantitative imaging of vascular dynamics, which is critical for assessing conditions like stroke and cardiovascular health. For perfusion imaging to be effective, it requires fast image acquisition

to capture rapid changes in blood flow, high spatial resolution to detect anomalies or blockages, and low noise to ensure sharp, clear images. Additionally, the use of a suitable tracer is essential for providing consistent signal strength throughout the imaging process. MPI's high sensitivity to the SPION distribution offers significant advantages over established imaging modalities like MRI or CT, particularly in terms of temporal resolution and tracer-specific contrast, making it especially valuable for real-time monitoring and assessment of vascular conditions [169]. A number of pre-clinical studies have demonstrated the feasibility of perfusion imaging with MPI [97, 170, 189, 169, 313, 207]. Recently first angiographic studies in a human cadaveric perfusion model have been presented [297].

Structural and anatomical detection is another key area for MPI applications, leveraging its high sensitivity and contrast through the use of magnetic nanoparticles. These nanoparticles can be functionalized to bind specifically to antigens on targets such as tumors or pathogens, enabling direct imaging with exceptional clarity [69, 70, 8, 227]. Targeted imaging of specific biomarkers necessitates advancements in nanoparticle design to improve targeting efficiency and imaging specificity, which are critical for enabling early detection and precise monitoring of disease progression [273]. This capability is particularly valuable for early tumor detection and pathogen identification, where MPI's precision and sensitivity outperforms many conventional imaging modalities [227, 273]. Additionally, the dual functionality of these nanoparticles bridges diagnostic and therapeutic applications. The same particles used for imaging can be heated via magnetic hyperthermia, enabling localized treatment [272]. In this area, too, many feasibility studies have paved the way towards clinical application [314].

This seamless integration of diagnostic and therapeutic capabilities naturally leads to another categorie of applications: SPION navigation and activation. MPI's ability to provide real-time tracking and manipulation of SPIONs makes it particularly well-suited for applications like targeted drug delivery [291, 158, 102, 35] and magnetic hyperthermia [196, 3, 272, 43, 34]. By combining high-resolution imaging with functional capabilities, MPI establishes itself as a powerful theranostic platform, especially in areas such as localized cancer treatment and other specialized therapies.

Device navigation is another transformative application of MPI, combining both imaging and active navigation capabilities [113, 115, 222, 288, 201, 16, 14, 36]. The real-time imaging capabilities of MPI are crucial for the precise guidance of interventional devices, such as catheters or balloons, significantly enhancing the safety and accuracy of minimally invasive procedures [113]. MPI's ability to provide immediate, high-resolution images enables clinicians to make informed decisions during the procedure, ensuring optimal outcomes [181]. Beyond imaging, the magnetic fields intrinsic to MPI can actively navigate nano- and microrobots, as well as assist in directing catheters through complex vascular networks to specific targets [14]. This dual functionality, which combines both real-time imaging and active navigation, is an important ingredient for the clinical translation of MPI, as it facilitates advanced interventions such as delivering therapeutic agents or performing targeted procedures with high precision [102]. The ability to track and control devices in real-time is essential for minimizing risks, improving efficiency, and expanding the potential of minimally invasive treatments [142, 201].

Finally, MPI's scalability and hardware design potential make it a promising candidate for the development of portable and low-cost imaging systems [294, 234, 186, 181, 123, 320, 112]. Such devices could facilitate rapid diagnostics in resource-limited settings, such as rural areas or emergency scenarios, where access to advanced imaging modalities is often restricted [314]. Additionally, integrating MPI with existing imaging modalities like MRI or CT in

well-equipped clinical environments could provide complementary diagnostic information, combining MPI's sensitivity to tracer distribution with the anatomical detail of MRI or CT to offer more comprehensive assessments [97, 295, 79, 296].

2.1.3 Challenges and Limitations

By organizing MPI applications according to their core clinical functions, we establish a framework that clarifies how MPI can contribute to diverse medical scenarios. This perspective not only helps to align technical development with clinical priorities but also exposes key gaps where further innovation is needed to translate MPI into routine clinical use. In doing so, it becomes evident that the path to clinical translation is shaped as much by MPI's potential as by its current limitations.

A general limitation of MPI is its lack of structural information. As a tracer-based modality, its clinical utility is significantly enhanced when combined with anatomical imaging techniques such as MRI or CT. For MPI to function independently or in hybrid settings, it must demonstrate tangible benefits over established modalities like PET, especially in terms of workflow integration, operational simplicity, and clinical outcome relevance [313].

The clinical translation of MPI will depend on rigorous validation through clinical trials to confirm its safety, efficacy, and reproducibility. At the same time, compliance with regulatory standards for medical devices is essential for progressing from preclinical promise to real-world impact.

In the following sections, we provide a detailed breakdown of the challenges MPI faces in clinical adoption, focusing on key research areas related to hardware, methodology, and tracer development. These challenges will be explored in greater depth, with a focus on their potential solutions and how they contribute to the successful clinical implementation of MPI.

2.2 Hardware Developement

While MPI has demonstrated strong potential for clinical applications, it remains in the preclinical stage, with human-sized imaging systems still in development [180, 219, 99, 294, 280, 183]. Bringing MPI into clinical practice requires substantial advancements in hardware design to meet performance, safety, and regulatory requirements. This section explores the critical hardware innovations necessary for clinical translation, addressing both the challenges and opportunities associated with widespread adoption.

As a starting point, let us first outline one of the potential use cases described in subsection 2.1.2. Consider an emergency room where a stroke patient arrives exhibiting severe neurological symptoms. Traditionally, a CT scan would be used to rule out bleeding, but it lacks real-time perfusion imaging capabilities. MRI might provide better soft tissue contrast but is often too slow and unavailable in emergency settings due to high costs and maintenance demands [169]. With an MPI scanner, emergency physicians could immediately visualize cerebral perfusion in real time, accurately identifying blockages and guiding rapid intervention without exposure to ionizing radiation [314]. Furthermore, portable MPI systems could be deployed even earlier in the diagnostic chain – inside an ambulance [169]. As soon as paramedics suspect a stroke, an onboard MPI scanner could assess cerebral perfusion en route to the hospital. This early insight would allow for critical decisions regarding the choice of treatment facility: should the patient be transported to the nearest hospital for immediate stabilization, or should they be taken to a specialized stroke center equipped

with neurosurgical teams and advanced imaging modalities? By providing rapid and precise information, portable MPI could significantly optimize pre-hospital decision-making, ensuring patients receive the most appropriate and timely care, potentially improving long-term outcomes [210].

Translating such applications into clinical reality demands significant hardware innovations. We categorize the primary hardware-related challenges into three key areas that are highly interdependent: Scaling & Engineering, Efficiency & Safety, and Cost & Accessibility, as shown on the left side of Figure 2.2.

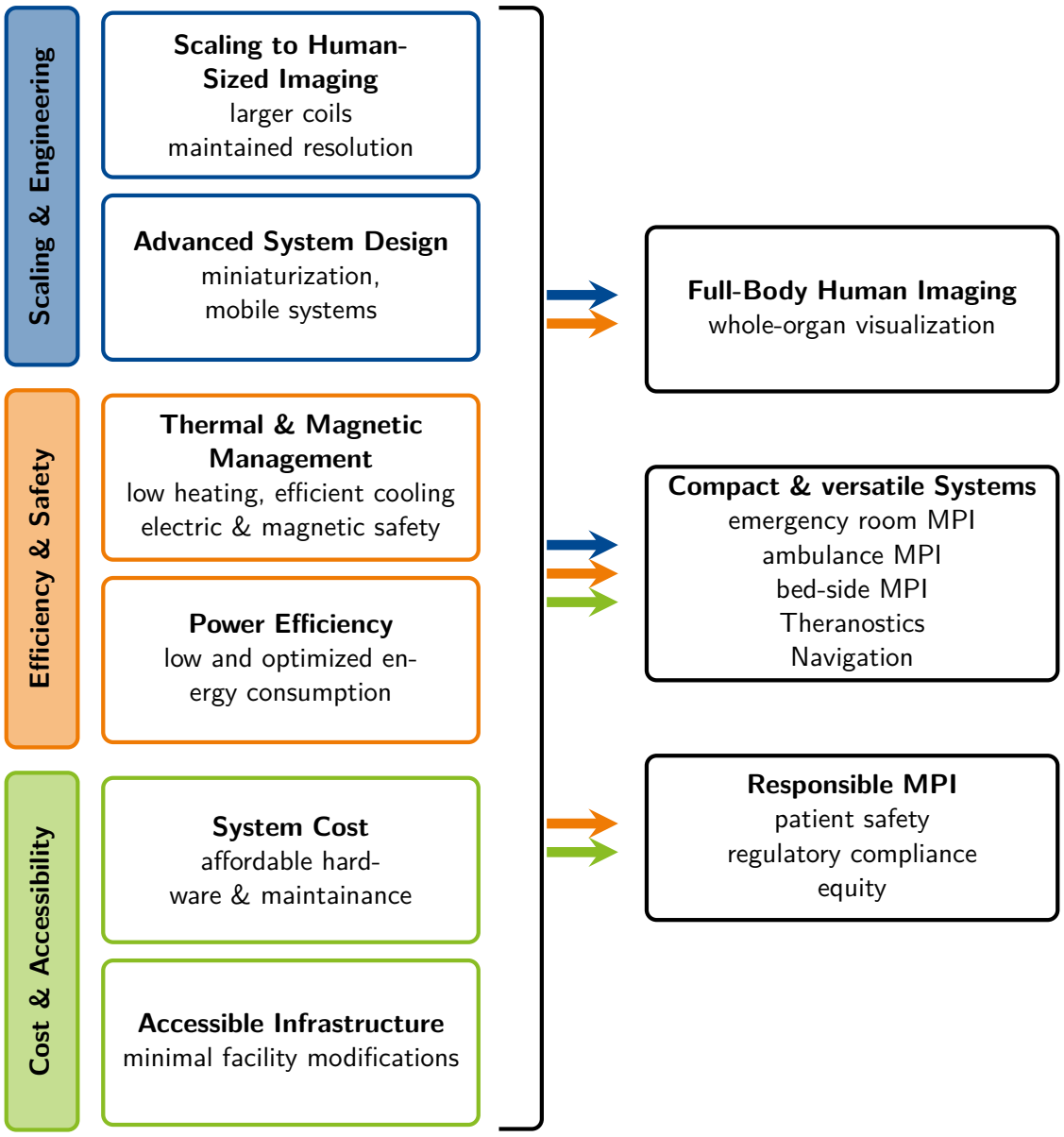

Figure 2.2: The left side presents key challenges in MPI hardware development, categorized into Scaling & Engineering, Efficiency & Safety, and Cost & Accessibility. The right side highlights essential properties for future MPI applications, along with a mapping of the hardware challenges that are critical to achieving these goals.

On the right side of Figure 2.2, these barriers are linked to critical performance requirements for clinical applications:

Scaling MPI systems to human dimensions presents several challenges, particularly in achieving high spatial resolution and a sufficiently large field of view while maintaining patient safety. This requires overcoming the inherent trade-off between gradient strength and excitation amplitude [12]. For example, stroke imaging demands a resolution of at least 5 mm [204, 39], which is difficult to achieve in a single large FOV. Splitting a large region of interest into several patches – called multi-patch MPI and described in more detail later – addresses these limitations but introduces additional complexity and may compromise image quality [144, 237, 305, 2]. Moreover, scaling MPI for human use involves engineering and regulatory challenges, such as the need for larger gradient fields, powerful drive-field generators, and advanced coil designs, all while ensuring high spatial and temporal resolution [30].

Power consumption in large-scale MPI systems significantly impacts system flexibility, particularly in real-world clinical settings [73]. This constraint is especially critical in use cases demanding compact or mobile systems, such as emergency or bedside imaging, where miniaturization must be achieved without compromising performance or requiring specialized power supplies and excessive cooling [12]. Efficient system design must balance power consumption, magnetic field strength, and heat dissipation to ensure practical clinical deployment. Additionally, patient safety remains a top priority, necessitating measures to minimize tissue heating, control magnetic field exposure, and ensure the biocompatibility and stability of SPIONs used as tracers.

Moreover, to enable widespread adoption, MPI hardware must be economically viable, with low-cost designs, reduced maintenance, and minimal infrastructure requirements. These factors are critical in determining MPI's comparative advantage over established modalities and directly impact its accessibility and healthcare equity. Additionally, patient safety is essential for the clinical translation of MPI, ensuring compliance with medical device standards and addressing concerns related to long-term nanoparticle administration and equitable access to this emerging technology [280]. While tracer development is discussed in section 2.4, the following subsection focuses on hardware development, particularly magnetic field generation and scanner design, followed by receive coil and signal acquisition. Subsequently, subsection 2.2.2 discusses the associated safety and ethical considerations.

2.2.1 Hardware Design

As the advancement of MPI technology hinges on the continuous improvement of hardware components to enhance imaging performance, this section aims to outline key considerations in hardware development. A crucial aspect of MPI hardware design is the generation of the necessary magnetic fields that facilitate imaging, as well as the engineering of scanner configurations optimized for clinical applications.

Magnetic Field Generation and Scanner Design

MPI relies on precisely controlled magnetic fields to encode spatial and temporal information, facilitating the visualization of SPIONs distributed within the body. The design of these magnetic fields plays a fundamental role in image resolution, sensitivity, and scanning speed, making hardware development a critical aspect of MPI's translation into clinical applications.

The first fundamental component of MPI hardware is the gradient $\boldsymbol{H}^S$, which offers a LFR where SPIONs remain unsaturated and thus contribute to the imaging signal. As described in section 1.2, this region can take the form of either an FFP or an FFL. The gradient

field is generated by one or multiple gradient coils that produce a static selection field with a gradient strength typically ranging from $0.3\,\mathrm{T\,m^{-1}}$ to $6\,\mathrm{T\,m^{-1}}$ [280, 53]. High gradient strengths are necessary to ensure that SPIONs outside the field free region remain magnetically saturated, preventing background signal contributions. FFP-based MPI systems offer high spatial selectivity and flexibility in sampling strategies [280], making them well-suited for high-resolution imaging. In contrast, FFL-based systems provide increased sensitivity due to the larger volume of the LFR, improving signal strength and enabling more efficient imaging of large volumes [141, 294, 183, 13]. The choice between FFP and FFL configurations influences scanning trajectories, image acquisition speed, and resolution, all of which are critical considerations in system design [91].

The generation of sufficiently strong and stable magnetic fields over an expanded FOV requires substantial power, with the majority of it being allocated to the static selection field [73]. Maintaining high gradient strengths while scaling up from small-animal (cm-range) to human-sized (dm-range) imaging volumes leads to a superlinear increase in power demand due to the growing current density. Consequently, optimizing power efficiency is essential for the feasibility of clinical MPI systems. One promising approach is the development of power-optimized field generators utilizing soft magnetic materials, which enhance magnetic flux generation while reducing energy losses [73, 1]. The optimization process involves complex nonlinear dependencies due to the iron core coils. Additional design constraints such as weight, cost, and thermal management must be carefully considered.

As marked out in the beginning of section 1.2, MPI employs drive coils in addition to the selection field, to generate time-varying magnetic fields that manipulate the position of the LFR. These drive fields typically oscillate at frequencies of $10 - 25\,\mathrm{kHz}$, with field strengths of $0.1 - 20\,\mathrm{mT}$ [53]. The high frequency of drive coils facilitates rapid scanning, making real-time imaging feasible and positioning MPI as a promising modality for the many dynamic applications discussed above.

The movement of the LFR follows specific scanning trajectories that determine the efficiency and speed of image acquisition. The two most widely used patterns are Cartesian and Lissajous trajectories. Cartesian scanning follows a structured, grid-based pattern, resulting in a high signal-to-noise ratio (SNR) and uniform sampling. This approach is advantageous for static imaging and applications requiring high spatial resolution. Lissajous scanning is based on the superposition of the frequencies of two orthogonal drive fields, producing a trajectory that covers the imaging volume more efficiently. Lissajous-based scanning allows for faster image acquisition, as it exploits frequency-dependent resonance properties to achieve high resolution with fewer excitation cycles [142, 306]. This makes it particularly beneficial for dynamic imaging applications where rapid data acquisition is essential.

The physical design of MPI scanners significantly impacts imaging depth, field of view, and clinical applicability. Several bore configurations have been developed, each presenting specific advantages and challenges. Closed-bore systems, such as the author's institute's head scanner [280], maximize coil efficiency and penetration depth, making them well-suited for whole-body and deep-tissue imaging [294]. However, their enclosed design limits accessibility and poses challenges for interventional procedures. Open-bore Systems provide greater patient accessibility and accommodate interventional applications, but they require novel hardware solutions to maintain high penetration depths [283]. Current developments focus on optimizing gradient and drive field configurations to balance FOV size and imaging performance. Single-sided MPI systems [181, 276, 208] prioritize portability and bedside imaging but currently suffer from limited penetration depths (approximately 2-4 cm). De-

spite this limitation, they hold promise for targeted applications such as superficial imaging, interventional guidance, and pre-hospital diagnostics.

A comprehensive understanding of the magnetic field properties of MPI – spatial inhomogeneities, gradient distributions, and dynamic interactions – is crucial for the design and optimization of clinically viable scanner systems. Detailed characterization of gradient strength and field uniformity directly informs the engineering of selection and drive fields, enabling more accurate spatial encoding and consistent LFR trajectories [73]. This, in turn, supports the design of coils that maximize sensitivity and resolution.

The impact of magnetic field variations on MPI image reconstruction is illustrated in Figure 2.3.

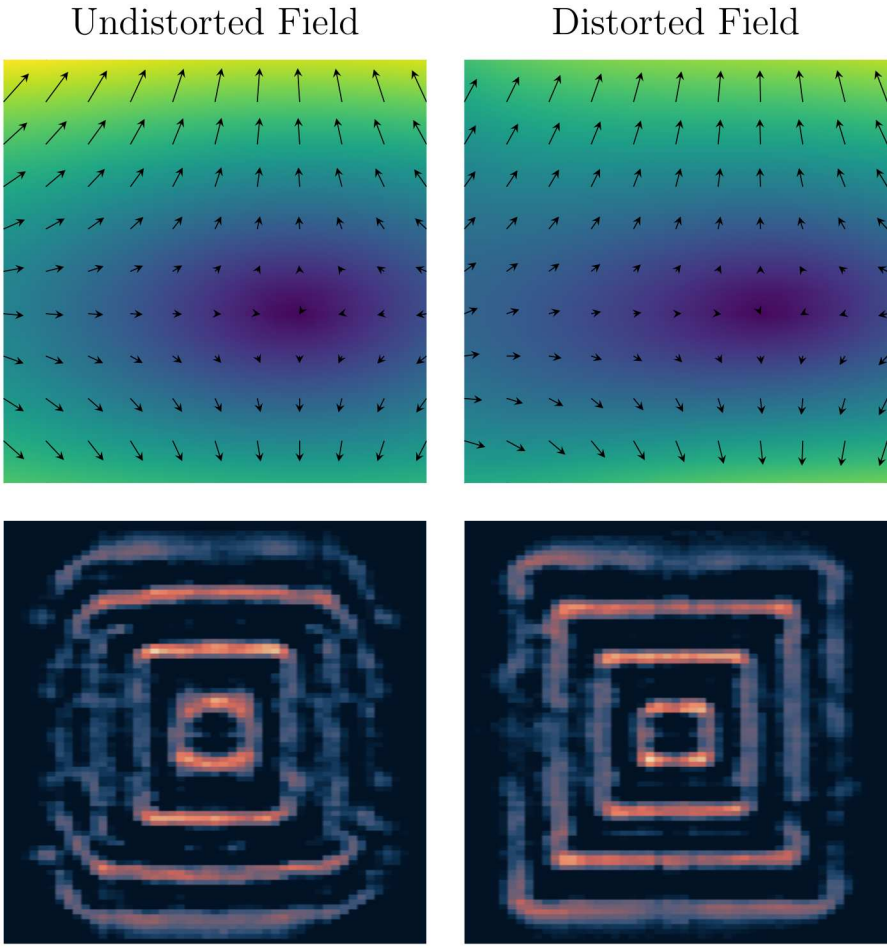

Figure 2.3: Effect of magnetic field distortion on multi-patch MPI reconstruction. Top right: Magnetic field with a shifted FOV as encountered in off-center patches. Top left: Undistorted magnetic field from the central patch. Bottom left: Reconstruction artifacts caused by assuming an undistorted field across all patches. Bottom right: Improved reconstruction result when using patch-specific system matrices that account for field distortions. Adapted from Szwargulski et al. [268].

The top right shows a magnetic field with a shifted FOV, as it may occur in an off-center patch. The adjacent image displays the undistorted field from a central patch (top left). The shift is most obvious in the lower left corner and in the color-coded absolute value. cornerUsing the undistorted field assumption for all patches in a joint multi-patch recon-

struction (see subsection 2.3.2) leads to artifacts, as demonstrated in the bottom left image [268]. In contrast, incorporating field distortions by using the corresponding system matrix significantly improves reconstruction quality, as shown in the bottom right.

Moreover, a precise understanding of magnetic field behavior allows for the implementation of advanced compensation strategies to reduce imaging artifacts and improve spatial resolution [27].

Thus, efficient methods for measuring and representing magnetic fields are crucial and part of current research [28, 33]. Spherical harmonic expansions provide a mathematical framework for reconstructing the magnetic field from a sparse set of measurement points distributed on a spherical surface. This approach enables the calculation of the field within a spherical region $\mathcal{B}_R(\boldsymbol{p})$ of arbitrary radius $R \in \mathbb{R}_+$ centered at $\boldsymbol{p} \in \mathbb{R}^3$:

$$H_i(\boldsymbol{a}) = \sum_{n=0}^{\infty} \sum_{m=-n}^{n} A_S^{n,m}(\boldsymbol{p}, R) \left(\frac{1}{R}\right)^n Z_n^m(\boldsymbol{a} - \boldsymbol{p}) \; \forall \boldsymbol{a} \in \mathcal{B}_R(\boldsymbol{p}), \; i \in \{x, y, z\}, \tag{2.1}$$

where $A_S^{n,m} \in \mathbb{R}$ are the spherical harmonic coefficients, and $Z_n^m : \mathbb{R}^3 \to \mathbb{R}$ denote the normalized real solid spherical harmonics. The coefficients are determined through measurements taken at discrete nodes on the spherical surface using a t-design quadrature. Further details on this methodology are provided in section 5.4. While the representation in Equation (2.1) neglects the temporal dependence of the magnetic field, the technique can be leveraged for high temporal and spatial resolution field measurements through the design of a field-camera, which enables single-shot magnetic field acquisition over a spherical surface [74]. Such a system has significant potential for advanced current-to-field prediction [76] and power-efficiency control [265] in nonlinear magnetic systems, including the iron-core field generation array discussed earlier [73]. Beyond MPI, the field-camera presents broad applications for developing and validating magnetic field generation hardware. However, a key limitation of this approach is its restriction to a spherical domain with a predefined radius, which often fails to fully encompass the entire region of interest. To address this limitation, an alternative approach employing ellipsoidal harmonic expansions has been proposed by the author [243]. The underlying procedure follows the same principles as the spherical harmonic method but extends the representation to an ellipsoidal coordinate system (ρ, μ, ν):

$$H_i(\rho, \mu, \nu) = \sum_{n=0}^{\infty} \sum_{m=1}^{2n+1} A_{a_1}^{n,m} \mathbb{E}_n^m(\rho, \mu, \nu), \; i \in \{x, y, z\} \tag{2.2}$$

where $\mathbb{E}_n^m(\rho, \mu, \nu) \in \mathbb{R}$ are the inner ellipsoidal harmonics, and $A_{a_1}^{n,m} \in \mathbb{R}$ are the corresponding coefficients, dependent on a reference ellipsoid with semi-axes $0 < a_3 < a_2 < a_1$. While ellipsoidal harmonic expansions offer greater geometric flexibility compared to their spherical counterparts, their implementation introduces additional computational challenges. Specifically, the calculation of $\mathbb{E}_n^m$ and $A_{a_1}^{n,m}$ is inherently more complex due to the structure of the ellipsoidal coordinate system. Chapter 6 presents a detailed discussion of ellipsoidal harmonic expansions as a tool for magnetic field measurement and representation. The method is validated through simulations of magnetic fields encountered in both MRI and MPI, as well as experimental MPI field data. The key advantage of this approach lies in its enhanced geometric adaptability, enabling dedicated field-camera configurations specifically optimized for the FOV constraints of MPI and MRI systems.

Receive Coils and Signal Acquisition

In MPI, receive coils play a crucial role in capturing the signal induced by the dynamic magnetization response of SPIONs within the LFR. As with drive coils, it is common practice

to use orthogonal receive coils for each spatial dimension being imaged; however, multiple receive channels are not necessarily required to reconstruct three-dimensional images. In this regard, single-channel systems that are optimized for SNR may offer certain advantages, as multiple channels exhibit data redundancy and require decoupling effort [280, 269]. To maximize the SNR, receive coils are typically positioned as close as possible to the FOV.

Receive coils detect signals in the form of an induced voltage, which arises due to the nonlinear magnetization response of SPIONs within the oscillating LFR. However, because receive coils are placed in close proximity to the drive coils, they are susceptible to unwanted inductive coupling from the fundamental drive frequency f_0. Since the SPION-generated signal consists of higher harmonics of f_0, effective signal separation techniques are required to extract the relevant imaging information while suppressing interference from the fundamental drive frequency. Two primary methods are employed in the receive chain to mitigate this interference. The first one is frequency-based filtering: since the unwanted drive-field signal primarily occurs at the fundamental frequency f_0, while the SPION response generates harmonics at $f = kf_0$ for a one dimensional excitation and $k \in \mathbb{N}, k \geq 2$, band-pass filtering techniques can selectively retain the higher harmonic components while attenuating the fundamental frequency. The second one is a geometric gradiometric design, where differential coil configurations exploit symmetry to cancel out the strong drive field signal while preserving the SPION signal [97, 185], illustrating that the design of the receive coils has a significant impact on system sensitivity and SNR. Both approaches are integral components of the MPI receive chain, which also introduces its own frequency-dependent scaling and phase shifts to the voltage signal. Accurate receive path calibration is essential to account for these transformations and ensure precise image reconstruction [281].

Once the signal has been filtered and amplified, it must be digitized for further processing [141, 142, 112]. An analog-to-digital converter (ADC) sampels the voltage signal at a defined sampling rate and with a specific sampling resolution. The sampling rate determines how frequently the analog signal is measured and must be sufficiently high to capture the highest significant harmonics of the SPION response. Insufficient sampling rates can lead to aliasing artifacts, distorting the reconstructed signal and reducing image quality. The sampling resolution, defined by the bit depth of the ADC, determines the precision with which signal amplitudes are digitized. A higher bit depth reduces quantization noise, improving SNR and allowing the detection of weak SPION signals. In practice, however, sampling resolution is not the primary source of weak SNR.

To handle the high data throughput of MPI systems, field-programmable gate arrays (FPGAs) and digital signal processors (DSPs) are frequently used. FPGAs enable real-time signal demodulation and filtering with low latency, while DSPs provide additional computational flexibility for adaptive noise suppression and gain correction. While high-performance ADCs are typically employed in MPI systems, low-cost data acquisition platforms such as Red Pitaya-based systems have been explored as compact and affordable alternatives. These platforms offer sufficient performance for certain applications, particularly in portable or resource-limited MPI implementations [112].

Several research groups around the world are currently working on advancing MPI hardware for human imaging. A recent review of the state of the art in human-sized MPI systems is given by Davida [53]. This is complemented by two recent papers on the current progress of the Berkeley-based head system [183] and the head system of the authors' research group in Hamburg [280].

2.2.2 Hardware Safety and Ethics

The transition of MPI from preclinical research to human imaging requires rigorous evaluation of patient safety and ethical considerations. While MPI does not expose patients to ionizing radiation like CT or PET, it involves strong, time-varying magnetic fields and contrast agents that must be carefully assessed for biological effects, long-term safety, and equitable access. Regulatory agencies such as the U.S. Food and Drug Administration (FDA) and the European Medicines Agency (EMA) require comprehensive safety evaluations and ethical justifications before any new imaging technology can be approved for human use. Even research publications based on first human MPI measurements must adhere to strict patient safety regulations and require ethical approval regarding the risks and benefits of the measurements.

One of the primary concerns in MPI hardware safety is electromagnetic exposure, which can affect the human body in multiple ways. Unlike MRI, which operates at higher frequencies, MPI employs low-frequency oscillating magnetic fields in the kilohertz range. Two key physiological effects must be addressed: PNS and specific absorption rate (SAR). Rapidly changing magnetic fields induce electric fields within biological tissue, potentially triggering involuntary nerve activation. PNS thresholds are dependent on the size of the imaged body part and stabilize for arms and legs at approximately 15 mT peak-to-peak for frequencies above 25 kHz, meaning that exceeding this limit may induce neuromuscular effects [233]. For MPI head-imaging, however, PNS limits of about 6.5 mT peak-to-peak have been found [206]. Unlike MRI, where PNS can be tolerated at higher intensities, MPI's continuous drive field operation necessitates stricter constraints. Simultaneously, power absorption from magnetic field interactions with tissue leads to heating, with SAR limits decreasing as frequency increases. While remaining above 15 mT peak-to-peak at the typical MPI frequency range of $25 - 50$ kHz [233], hardware must be carefully optimized to ensure safe operation without excessive heating.

These constraints on drive field amplitude directly affect the design of the selection field, which determines spatial resolution. High gradient strengths are required for fine spatial resolution but inherently restrict the FOV. To achieve whole-organ imaging while maintaining a resolution of ≤ 5 mm, two primary approaches are employed: mechanical translation of the scanner or subject, which extends coverage but limits temporal resolution [183], and focus fields, which enable flexible FOV shifting through additional low-frequency magnetic fields [280] as described in section 1.3. Since focus fields typically operate in the $5 - 100$ Hz range, they remain well below PNS and SAR thresholds, making them a safer alternative for large-volume imaging.

Beyond electromagnetic exposure, the strong electrical currents required for MPI scanner operation pose additional safety considerations. High-power gradient and drive coils, particularly in human-scale systems, generate intense magnetic flux and necessitate active cooling mechanisms to prevent overheating [180]. Moreover, high-voltage circuits in close proximity to the patient require stringent electrical isolation and emergency shutoff mechanisms to mitigate the risk of accidental exposure [280]. These factors must be thoroughly assessed before regulatory approval to ensure that MPI hardware balances spatial resolution, imaging speed, and patient safety within clinically acceptable limits.

Another key safety concern is the use of SPION tracers, which must be evaluated for biocompatibility, biodistribution, and clearance [192]. While some iron oxide nanoparticles are FDA-approved for therapeutic use, MPI tracers may have different properties requiring further assessment. Determining safe dosage levels is essential to ensure sufficient signal

generation without exceeding safety thresholds. A detailed overview on tracer development is given in section 2.4.

Furthermore, data security is an integral component of hardware safety and ethical compliance in human MPI imaging. The high data throughput of MPI systems requires secure acquisition, processing, and storage to protect patient information from unauthorized access. All hardware components must adhere to medical cybersecurity standards, ensuring encrypted data transmission and restricted access to prevent breaches. Ethical approval for clinical use mandates compliance with stringent data protection regulations, reinforcing the need for secure system design.

Regarding ethical approval of human imaging trials, guidelines such as the Declaration of Helsinki, the Belmont Report, and national research ethics frameworks define the standards for human subject research, ensuring that safety, patient autonomy, and fair access are prioritized. A fundamental requirement in this process is informed consent, which ensures that patients fully understand the potential risks, benefits, and alternatives before undergoing experimental imaging procedures. While MPI presents a radiation-free alternative to PET and CT, its benefit-risk assessment must be carefully compared to existing imaging modalities. MRI, for example, offers superior soft tissue contrast but is expensive and often requires superconducting magnets, while PET-CT provides functional imaging at the cost of ionizing radiation exposure and dependence on short-lived radiotracers. MPI, if proven clinically viable, could serve as a safer alternative for certain applications, as discussed before. However, any current limitations and risks must be clearly communicated.

Another important ethical consideration is equitable access. Advanced medical imaging technologies are often concentrated in high-income healthcare systems, raising concerns about their availability in lower-resource settings. While MPI does not require expensive infrastructure like traditional MRI, it still involves high power demands and advanced electronics, which may limit accessibility in remote or underfunded healthcare facilities. The cost of MPI tracers will also play a crucial role in its adoption. Although iron oxide nanoparticles are relatively inexpensive to produce compared to PET radiotracers, the regulatory approval process and large-scale manufacturing could influence affordability.

However, MPI's potential for portable, low-cost scanner designs may facilitate broader accessibility, particularly in emergency or pre-hospital settings, offering an alternative for mobile healthcare applications where traditional imaging modalities are not feasible [112]. In this context, open-hardware initiatives play a critical role in reducing development costs, fostering innovation, and enabling broader access to MPI technology. By sharing designs, hardware specifications, and software implementations openly, researchers and engineers can collaborate to create cost-effective, scalable solutions tailored for low-resource environments. Open-hardware approaches also encourage modular, adaptable designs, ensuring that MPI systems can be customized for specific clinical needs while remaining financially viable. Integrating these efforts with open-source software development can further accelerate the broader accessibility of MPI, making it a more practical option for widespread medical deployment.

As MPI moves toward clinical translation, ensuring patient safety, regulatory compliance, and ethical integrity will be critical. Strict control of electromagnetic exposure, comprehensive evaluation of contrast agent safety, and a transparent ethical framework for human trials are essential for gaining approval. Furthermore, considerations regarding cost, infrastructure requirements, and global accessibility must be addressed to ensure that MPI can be equitably integrated into diverse healthcare environments.

2.3 Methodological Development

Even with secure, cost-efficient, flexible, and low-noise hardware solutions, the clinical success of MPI hinges on easy-to-handle, fast, and reproducible measurement protocols. MPI's unique strengths – such as its ability to provide real-time, radiation-free imaging with high sensitivity to SPIONs – make it particularly promising for various clinical applications, including emergency diagnostics. However, for MPI to realize its potential in such settings, its workflows must be carefully streamlined. This includes optimizing calibration and reconstruction processes to enable efficient and accurate imaging.

To illustrate this, consider again an MPI system designed for use in an emergency room as described in the motivation of section 2.2. Such a system must be mobile, compact, and energy-efficient to accommodate the constraints of busy and resource-limited environments. The inherent speed and sensitivity of MPI make it ideal for acute conditions like stroke, where rapid diagnosis can mean the difference between full recovery and severe disability. In this scenario, a patient presenting with stroke symptoms may require immediate imaging to localize a potential clot and decide between thrombectomy or thrombolysis.

An MPI system could generate perfusion images of the brain with high temporal resolution and precision, accurately identifying ischemic regions [280]. Given the urgency and the possible absence of an experienced radiologist, the system must automatically produce high-quality images without requiring extensive parameter adjustments. Moreover, computationally efficient reconstruction algorithms are essential for delivering results quickly, even with limited hardware resources.

Operational readiness is equally critical in such environments. Emergency room systems must be available at all times, making lengthy calibration scans impractical. Calibration processes must account for potential variability in the clinical setup – such as differences in patient anatomy, tracer distribution, or system configuration – while remaining minimal, fast, and adaptable. These processes must also ensure reliability and reproducibility across different operators and systems, reducing variability in clinical outcomes.

The following sections focus on algorithmic strategies to address these challenges, with particular emphasis on the calibration and reconstruction steps – two interdependent processes that critically influence the temporal resolution, image quality, and robustness of MPI in clinical workflows. Within this framework, calibration refers to the generation or modeling of the system matrix $\boldsymbol{S}$, which defines the system's spatial encoding properties and underpins the fidelity of all subsequent reconstructions. Reconstruction, in turn, refers to the numerical inversion of the measured signal to recover the underlying particle distribution, as introduced in section 1.2. Methodological development in MPI must therefore address both steps simultaneously: minimizing the time, memory, and variability associated with calibration, while enabling fast, automated, and artifact-free reconstruction. Advancing these methods is essential for achieving the reproducibility and operational efficiency required for MPI to function effectively in time-sensitive, real-world clinical environments.

2.3.1 Calibration Step

While X-space MPI reconstruction offers computational efficiency and direct signal interpretation, its limitations in spatial resolution, noise propagation, and system-dependent distortions [92, 48] make system matrix-based reconstruction the preferred approach for high-quality imaging. Furthermore, achieving accurate X-space reconstruction would still require frequency- and space-dependent calibration, making it less straightforward than of-

ten assumed [316]. Thus, we consider the MPI reconstruction problem as it is decribed in Equation (1.3).

Despite ongoing developments in MPI modeling, which will be discussed later, the most commonly used approach remains a measured system matrix $\boldsymbol{S} \in \mathbb{C}^{K,N},\ K \in \mathbb{N}, N \in \mathbb{N}$, as it inherently captures the full physical behavior of the scanner, including field inhomogeneities and system-specific imperfections [175]. System matrix acquisition involves systematically shifting a small delta sample across a predefined grid of N grid-points within the FOV and recording the system's response at each position. While this method is conceptually simple, it introduces significant challenges related to image resolution and calibration time. In MPI, the spatial resolution refers to the smallest distinguishable distance between two separate sources of SPION signal within the reconstructed image. This resolution is influenced by several factors, including the strength of magnetic field gradients, the magnetic properties of the SPIONs, and, notably in system matrix-based reconstruction, the resolution of the calibration grid [274]. This calibration grid defines the sampling density at which the system's response is measured: a finer grid means smaller spatial intervals between calibration points, thereby providing more detailed information about the system's encoding characteristics. In principle, reducing the step size between calibration points improves the spatial resolution of the reconstruction, since the forward model more finely resolves the spatial encoding of particle positions. However, this improvement is not without cost: the number of grid points – and thus the duration and storage requirements of calibration – scales cubically with spatial resolution in 3D, leading to impractically long calibration durations. For example, acquiring a system matrix with $9 \times 9 \times 9$ voxels takes $32\,\mathrm{min}$, whereas increasing the resolution to $37 \times 37 \times 37$ extends the acquisition time to 32 h [17]. While such durations may be acceptable for a single calibration, they pose a significant challenge for clinical applications, where periodic recalibration is necessary to ensure consistent imaging performance. This challenge is further amplified in large-FOV imaging techniques that rely on focus field shifts. Each shift requires an additional system matrix acquisition (as demonstrated in Figure 2.3), resulting in total calibration times that can extend over several days [268]. Furthermore, refinement beyond a certain threshold offers diminishing returns due to physical and instrumental limitations, like finite sensitivity of receiver coils and the presence of thermal noise [274, 211]. Given these constraints, alternative calibration strategies are essential to reduce acquisition times or enhance resolution without significantly prolonging measurement duration. The following subsections will provide an insight into state-of-the-art approaches aimed at addressing these limitations.

Improvements in System Matrix Acquisition

A major avenue for reducing calibration time is minimizing the number of required measurements. The most straightforward strategy is sub-sampling the FOV – acquiring system matrix data only at a subset of spatial positions and reconstructing the full system matrix by solving the corresponding inverse problem. Various sub-sampling and sparse reconstruction techniques have been explored [105, 160, 154, 129, 124, 106]. Among these, compressed sensing has proven particularly effective due to the inherent sparsity of the system matrix when transformed into an appropriate basis domain, such as the discrete cosine transform [160].

By strategically selecting only a fraction of the N calibration points, compressed sensing enables high-fidelity reconstruction while significantly reducing acquisition time. Considering the kth row of the system matrix $\boldsymbol{S}_k$, dropping to $S < N$ non-zero coefficients in the vector $a \in \mathbb{C}^N$ can be described by $\boldsymbol{S}_k = \boldsymbol{\Xi}^T \boldsymbol{a}$, where $\boldsymbol{\Xi} \in \mathbb{C}^{\,Q \times N}$ being a left-invertible sparsifying

transform with pseudo-inverse Ξ^T and $Q \in \mathbb{N}$. Then, an estimator for $\boldsymbol{S}_k$ can be found, by solving

$$\underset{\boldsymbol{S}_k}{\operatorname{argmin}} \|\Xi \boldsymbol{S}_k\|_1 \text{ subject to } \frac{1}{2}\|\boldsymbol{W}_S \boldsymbol{S}_k - \boldsymbol{y}\|_2^2 < \epsilon^2. \tag{2.3}$$

Here, $\boldsymbol{W}_S \in \mathbb{C}^{S \times N}$ denotes the measurement matrix to extract the vector $y \in \mathbb{C}^S$ via $\boldsymbol{y} = \boldsymbol{W}_S \boldsymbol{S}_k + \boldsymbol{n}$, where $n \in \mathbb{C}^S$ is an additive Gaussian noise vector [105]. The effectiveness of this approach depends on the choice of the sampling pattern, which forms the measurement matrix $\boldsymbol{W}_S$. While conventional random sampling guarantees recovery of $\boldsymbol{S}_k$ and offers moderate sub-sampling rates, more advanced strategies leverage prior knowledge of the system matrix structure to improve accuracy at higher sub-sampling rates [105, 106]. As shown by Grosser et al. [105] the benefits of compressed sensing are most pronounced within the physical FOV defined by the ratio of the drive field amplitude to the gradient strength, known as the drive-field field of view (DF-FOV).

However, a principal limitation of compressed sensing is that it can only be applied to future calibrations, not retrospectively to already measured system matrices. This is where system matrix extrapolation provides an advantage. While compressed sensing is particularly strong on efficiently acquiring a system matrix inside the DF-FOV [105], extrapolation methods extend the system matrix beyond the measured region, particularly into the overscan region (OR). The OR is critical for multi-patch imaging since restricting calibration to the DF-FOV alone can introduce artifacts at patch boundaries. However, the signal in the OR is merely a smooth continuation of the signal in the DF-FOV. This fact is motivated and validated in section 3.2. The extrapolation method presented in Chapter 3 leverages this by using a variational method to ensure a harmonic continuation of the system matrix in the OR over all frequencies $k \in \{1, ..., K\}$:

$$\Delta \boldsymbol{S}_k\big|_{\mathrm{OR}} = 0. \tag{2.4}$$

Moreover, a promising approach is to combine compressed sensing within the DF-FOV with this diffusion-based extrapolation into the OR as represented in Figure 2.4. After measuring only on an optimized subsection of the grid inside the DF-FOV, the system matrix is fully retrieved on the whole DF-FOV using CS in a first step. In a second step, the signal is harmonically extrapolated into the OR. This approach was introduced by the author and is further detailed and verified on measured data in Chapter 3.

Both methods – compressed sensing and extrapolation – play a crucial role in joint reconstruction strategies for multi-patch MPI [268], as high sub-sampling rates enable the use of larger overscan regions for each patch, which effectively reduces patch boundary artifacts. Moreover, as sub-sampling rates scale with the number of patches, the advantages of these approaches become even more pronounced in large-scale imaging setups [104, 237, 106].

Beyond these techniques, alternative approaches have been proposed to mitigate the calibration burden in multi-patch imaging. Using a single (central) system matrix for all patches introduces inaccuracies, as system matrices are inherently position-dependent [268]. A more effective approach involves warping a centrally acquired system matrix to account for the spatial displacement of off-center patches. This can be achieved by leveraging knowledge of the underlying magnetic fields [27, 29], a task that benefits from efficient field measurement and representation techniques described in chapter 5 [28, 243].

Deep learning-based methods provide another promising direction for reducing calibration effort. Machine learning models can enhance system matrix resolution through post-processing

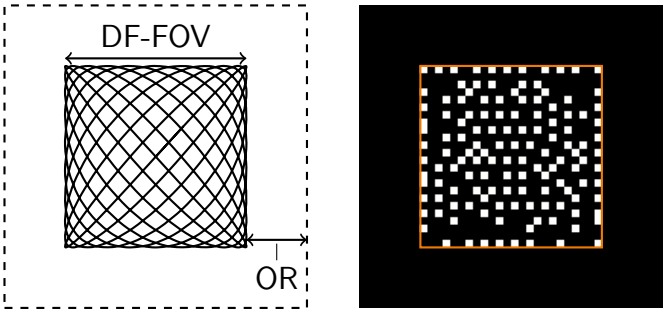

Figure 2.4: Combination of compressed sensing inside the DF-FOV and diffusion-based extrapolation in the overscan region. The optimized sparse sampling pattern within the DF-FOV (orange line) is indicated on the right. The diffusion method extrapolates the signal into the overscan region (indicated as the black area outside the orange border of the DF-FOV).

[11, 246], improve temporal resolution via denoising [286], and further refine sub-sampling strategies [17]. However, these approaches introduce their own set of challenges. Training such models requires large, high-quality datasets, which are often difficult to obtain due to the labor-intensive nature of system matrix acquisition. As a result, deep learning models are often trained on simulated datasets rather than directly on measured data. To improve generalizability, these datasets are often complemented with realistic noise distributions, helping to bridge the gap between idealized simulations and real-world MPI acquisitions. Nevertheless, results remain predominantly superior on simulated test sets, and adapting these models to measured data as in Baltruschat et al. [17] remains an active area of research. Ensuring robust performance across different scanner configurations and experimental conditions is a key challenge that must be addressed before deep learning-based calibration methods can be reliably implemented in clinical MPI systems.

Reducing system calibration time is not merely a technical challenge but a critical prerequisite for clinical translation. Long calibration durations remain a major bottleneck for integrating MPI into routine human imaging, as clinical systems require periodic recalibration to maintain consistent performance. In a clinical context, calibration procedures ideally need to be completed within minutes to an hour – comparable to quality assesment procedures for MRI or CT systems [71] – to avoid disrupting clinical workflow or causing scanner downtime. The next step is to transfer recent advances in efficient calibration strategies into preclinical MPI systems and continue refining these techniques – especially data-driven and deep learning-based approaches. Such improvements could significantly reduce scanner downtime, making MPI more practical for real-world applications. Additionally, by enabling larger FOVs and enhancing temporal resolution, these methods are essential for advancing whole-organ imaging and perfusion imaging, further strengthening MPI's potential for clinical adoption.

Model-based Imaging

In the previous section 2.3.1, we discussed strategies to address the labor-intensive acquisition of measured system matrices. Another key limitation, introduced earlier in subsection 2.3.1, is the inflexibility of measured system matrices with respect to image resolution. This constraint highlights the need for accurate and efficient modeling approaches. An ideal system matrix model would eliminate the need for exhaustive calibration while preserving high imaging fidelity and minimizing the risk of reconstruction artifacts. However, achieving this balance is inherently challenging: as model accuracy increases, so does computational

complexity. This trade-off necessitates a deep understanding of the underlying physical principles governing particle magnetization.

Particle physics: A crucial foundation for MPI modeling lies in an accurate particle model, which must capture the nonlinear magnetization and relaxation dynamics of SPIONs under periodic excitation. Understanding these mechanisms is essential for both system matrix generation and the prediction of MPI signal behavior in different imaging scenarios.

Ferromagnetic materials, when reduced to sufficiently small sizes, transition into a single magnetic domain state. At this scale, thermal fluctuations can cause spontaneous magnetization reversals, resulting in an average magnetization of zero in the absence of an external field [46]. When an external magnetic field is applied, these particles exhibit a significantly stronger response than conventional paramagnetic materials, a phenomenon known as superparamagnetism.

Superparamagnetic particles respond to external magnetic fields through two primary relaxation mechanisms: Brownian relaxation and Néel relaxation. The dominant relaxation mechanism depends on the physical state of the particle and its surrounding medium.

Brownian Relaxation: This mechanism describes the physical rotation of the entire particle within a fluid in response to an applied field. The internal magnetization remains fixed relative to the particle's crystalline structure, while the particle itself rotates. Brownian relaxation is influenced by factors such as fluid viscosity, temperature, and particle hydrodynamic size [55].

Néel Relaxation: Unlike Brownian relaxation, Néel relaxation involves internal magnetization reorientation within a stationary particle. This process depends on material-specific parameters such as the gyromagnetic ratio, saturation magnetization, and anisotropy energy [55]. Immobilized particles, such as those embedded in a solid or frozen medium, undergo Néel relaxation exclusively, as Brownian motion is suppressed.

The interplay between these two relaxation mechanisms introduces additional complexity into MPI signal modeling. At low field amplitudes, Brownian relaxation often dominates due to the relatively free rotational mobility of particles. However, at high field strengths, Néel relaxation becomes more significant due to the increasing influence of magnetic anisotropy [55]. Furthermore, particle core size strongly influences this interplay, with Brownian relaxation dominating for core sizes larger than about 25 nm [253]. These transitions highlight the intricate dependence of MPI signal behavior on both particle properties and experimental conditions, reinforcing the necessity of precise particle models for accurate system matrix generation.

Modeling the system function: Building upon the foundational understanding of particle magnetization and relaxation dynamics, the next step in MPI modeling involves constructing comprehensive mathematical representations of the system response. A fundamental assumption common to most MPI models is the neglect of particle-particle interactions, which simplifies the response to a linear dependence on tracer concentration.

As a starting point, we consider again the system Equation (1.1) describing the connection of the measured time-varying voltage signal $u_l : \mathbb{R} \to \mathbb{R}$ and the spatial SPION distribution $c : \Omega \subset \mathbb{R}^3 \to \mathbb{R}$ together with the system function $s_l : \mathbb{R}^3 \times \mathbb{R}_+ \to \mathbb{C}$. The system function can be described in general by

$$s_l(\boldsymbol{r}, t) = -\mu_0 \int_{\mathbb{R}} a_l(t-\tau) \left(\boldsymbol{p}_l(\boldsymbol{r})\right)^\top \frac{\partial}{\partial \tau} \boldsymbol{\Gamma}_{\bar{\boldsymbol{m}}}(\tau, \boldsymbol{H}(\boldsymbol{r}, \cdot)) \, \mathrm{d}\tau. \tag{2.5}$$

Here μ_0 denotes the vacuum permeability, $\boldsymbol{p}_l : \Omega \to \mathbb{R}^3$ the l-th receive coil sensitivity profile, $a_l : \mathbb{R} \to \mathbb{R}$ the analog filter and $\boldsymbol{\Gamma}_{\bar{\boldsymbol{m}}} : \mathbb{R} \times C(\mathbb{R}, \mathbb{R}^3) \to \mathbb{R}^3$ describes the mean magnetic moment of an SPION as a function of the spatio-temporally changing magnetic field $\boldsymbol{H} : \mathbb{R}^3 \times \mathbb{R} \to \mathbb{R}^3$ [175].

MPI models can be classified according to their level of abstraction in modeling $\boldsymbol{\Gamma}_{\bar{\boldsymbol{m}}}$, ranging from stochastic micro-scale simulations to analytical equilibrium models. A recent study, conducted in cooperation with the author [175], provides a structured overview of common MPI models and their hierarchical relationship, as illustrated in Figure 2.5. These models vary in complexity and accuracy, with different underlying assumptions that influence their applicability and computational feasibility. In the following we will discuss these models from top to bottom in more detail.

Stochastic Differential Equation (SDE) Models: These models directly simulate the magnetic moment of individual SPIONs using stochastic differential equations [309, 251, 96, 198]. The macroscopic magnetization required for MPI is then obtained by averaging over a sufficiently large number of simulated particles within a given volume. While this approach naturally incorporates various physical effects, such as arbitrary anisotropies [198], its major drawback is computational cost. Due to the stochastic nature of the simulation, a large number of particles must be modeled to obtain an accurate estimate of the mean magnetic moment, making this method computationally expensive and impractical. Note therefore that these models are not included in Figure 2.4. In particular, in the large particle number limit, these stochastic models become equivalent to the Fokker-Planck equation approach [175].

Fokker-Planck Models: Instead of tracking individual particles, FP models describe the probability density function (PDF) of the magnetic moment distribution within an ensemble. This formulation significantly reduces computational cost compared to SDE models while retaining high physical fidelity [4, 5, 136]. Including the Brownian and Néel magnetization dynamics requires the solution of a differential equation and $\boldsymbol{\Gamma}_{\bar{\boldsymbol{m}}}$ remains as complex as given above. A simplification neglects Brownian rotation and assumes uniacial anistropy. However, all FP models remain computationally demanding [4]. Moreover, solving for Néel relaxation dynamics necessitates detailed knowledge of material-specific parameters such as the anisotropy energy constant.

Equilibrium Models: To further reduce computational complexity, analytical equilibrium models have been introduced. These models assume that relaxation occurs instantaneously, leading to a direct relationship between the applied magnetic field and the magnetization response:

$$\boldsymbol{\Gamma}_{\bar{\boldsymbol{m}}}(t, \boldsymbol{H}(\boldsymbol{r}, \cdot)) = \bar{\boldsymbol{m}}(\boldsymbol{H}(\boldsymbol{r}, t)), \tag{2.6}$$

where $\bar{\boldsymbol{m}} : \mathbb{R}^3 \to \mathbb{R}^3$. These models are based on an analytical representation of the system function in the frequency domain for Lissajous excitation, formulated as a linear combination of products of Chebyshev polynomials convolved with a frequency-independent kernel [176]. A prominent example is the Equilibrium Model with Anisotropy (EQANIS) [175], which retains anisotropic effects. This model offers a valuable compromise between computationally intensive numerical simulations and overly simplified approximations.

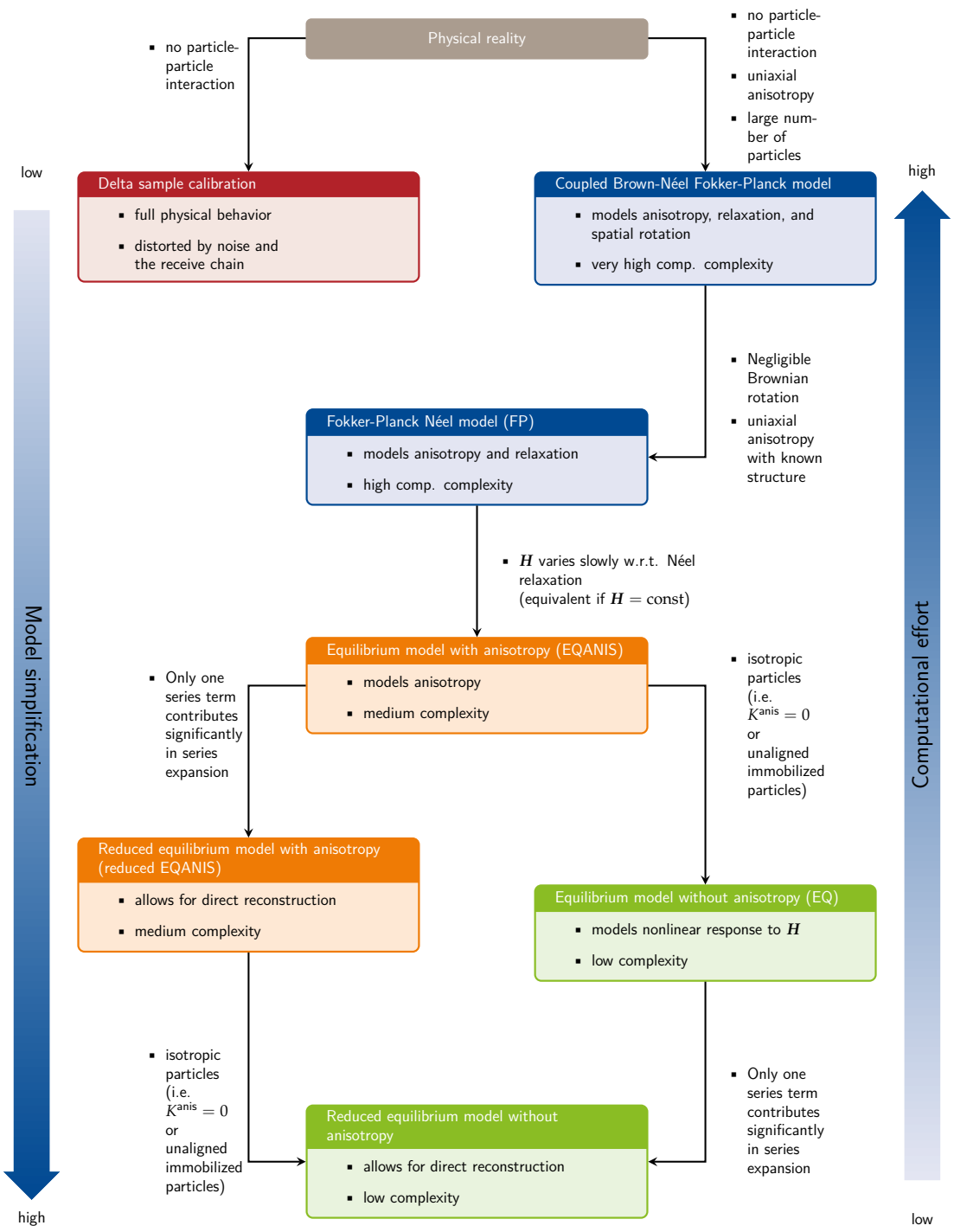

Figure 2.5: A schematic overview of various MPI particle models and their underlying assumptions. The figure starts with the measured system matrix (red), which assumes no particle interactions and a linear dependence of particle response on concentration. The Fokker-Planck model (blue) accounts for a large ensemble of particles with uniaxial anisotropy, considering both Brownian and Néel relaxation, or just Néel relaxation. The simpler equilibrium model with anisotropy (orange) assumes slow variation of the magnetic field with respect to Néel relaxation. The equilibrium model without anisotropy (green) further simplifies this by assuming isotropic particles. Finally, both the equilibrium models can be further reduced by truncating the Chebyshev series. This figure was designed by Konrad Scheffler and Marco Maass and published in 2024 [175].

Reduced Models for Computational Efficiency: The EQANIS can be simplified in two principal ways: by reducing the Chebyshev series expansion to a single coefficient, yielding the reduced EQANIS [59]; and by assuming isotropic particles, leading to the equilibrium model (EQ) [176]. These two reductions can be further combined into the reduced equilibrium model, which has been explored for direct MPI reconstruction [58, 60].

The trade-off across these models lies in balancing accuracy and computational feasibility – while high-fidelity models improve realism, their complexity often limits practical applications, especially in real-time imaging scenarios. By structuring MPI modeling in this hierarchical manner, researchers can choose an appropriate model based on the requirements of their specific imaging application, optimizing for accuracy, computational cost, and experimental feasibility.

Recent advancements in MPI modeling have significantly improved the trade-off between computational efficiency and reconstruction accuracy, marking a crucial step toward clinical feasibility. For the first time, accurate results can be achieved with computational resources suitable for clinical MPI applications. A key milestone in this progress was the comprehensive understanding and calibration of the receive path [281, 5]. When combined with the EQANIS, this represents the current pinnacle of model-based reconstruction, offering a balance between low computational complexity and accuracy comparable to measured system matrix reconstructions [175]. A major advantage of this approach is that it requires only a single calibration measurement to estimate the receive path, drastically reducing the calibration burden compared to traditional system matrix acquisition – a transformative development for medical applications. Moreover, first promising results on measured data using an efficient implementation of the reduced EQANIS have been presented [119].

Despite these advances, further research is necessary to refine model parameters such as the anisotropy constant and particle core size, ensuring optimal adaptation to different tracers and imaging conditions. A primary limitation of the EQANIS model is its inability to fully account for relaxation effects, which can become significant under specific excitation sequences, such as 1D excitations. Addressing these challenges will be essential to further improving model accuracy and expanding its applicability.

Future Directions in MPI Calibration

Beyond model development, optimizing the calibration process itself is critical for translating MPI into clinical practice. As demonstrated, accurate modeling enables the reduction of required calibration measurements without compromising image quality. This not only accelerates system calibration but also facilitates a more efficient transition from setup to imaging.

Further refinements in the calibration workflow can further increase this efficiency. Automation of calibration procedures could reduce time-consuming manual steps, minimize human error, and ensure reproducibility across imaging sessions. Standardized SPION phantoms and pre-tuned magnetic field configurations allow for streamlined setup, minimizing the need for case-specific recalibration. In addition, adaptive calibration strategies that adjust parameters in real time based on initial measurement feedback can improve system stability and reduce recalibration frequency - particularly valuable in dynamic imaging scenarios where patient motion or tracer redistribution affects signal consistency.

Looking ahead, deep learning-based approaches offer exciting opportunities to enhance MPI modeling and calibration. Neural networks trained on simulated and experimental data could refine particle response models, correct for relaxation effects, and further reduce the

dependency on extensive calibration measurements. In particular, Fourier neural operators (FNOs) have emerged as powerful tools for learning complex physical mappings in MPI. Recent studies demonstrate that FNOs can significantly accelerate the simulation of magnetization dynamics and solve system matrix estimation from limited calibration data – outperforming classical numerical solvers and compressed sensing methods in both accuracy and speed [107, 133]. These capabilities position FNOs as promising components of future model-driven calibration pipelines.

By integrating these advancements in calibration methodology with emerging AI-driven modeling techniques, MPI can move closer to becoming a practical, high-precision imaging modality suitable for routine medical use.

2.3.2 Reconstruction Step

Beyond rapid calibration, the emergency scenario introduced earlier highlights the critical need for fast, reliable, and accessible reconstruction frameworks. In clinical applications, particularly in time-sensitive settings, image reconstruction must balance efficiency, accuracy, and ease of use. Conventional reconstruction techniques often require expert knowledge for selecting regularization strategies, fine-tuning parameters, and configuring solver algorithms, making them impractical in urgent medical contexts. However, in real-world scenarios where rapid decision-making is crucial, reconstruction methods must be highly automated, intuitive, and robust, minimizing technical complexity while ensuring consistently high-quality results.

To meet these demands, recent MPI reconstruction research has advanced along several dimensions. Each of the reconstruction challenges discussed in this section originates from fundamental limitations imposed either by hardware design or clinical requirements. The difficulty of regularization parameter selection motivates the development of automated and adaptive reconstruction frameworks. FOV limitations necessitate multi-patch imaging techniques, which in turn increase the need for dynamic and time-dependent reconstruction methods. Real-time applications, such as interventional imaging, call for highly accelerated or even instantaneous reconstruction solutions. Furthermore, the growing adoption of data-driven and deep learning-based methods offers promising avenues to enhance reconstruction fidelity and speed. Lastly, we emphasize the role of software engineering and open-source initiatives.

While the following sections explore these research areas in detail, Figure 2.6 provides a structured overview that serves as a conceptual entry point. The figure outlines the progression from signal acquisition – highlighting the critical role of high-SNR voltage signal measurements – to clinical and research applications that rely on good MPI reconstruction pipelines. Central to this progression are two thematic pillars. The first, reconstruction efficiency, encompasses algorithmic innovations ranging from traditional iterative solvers to real-time reconstruction strategies and deep learning integration. The second, reconstruction handling, focuses on methodological advances and software development aimed at improving usability, automation, and clinical readiness. Particular attention is given to the challenge of regularization parameter selection, a practical bottleneck and a central focus of the author's research.

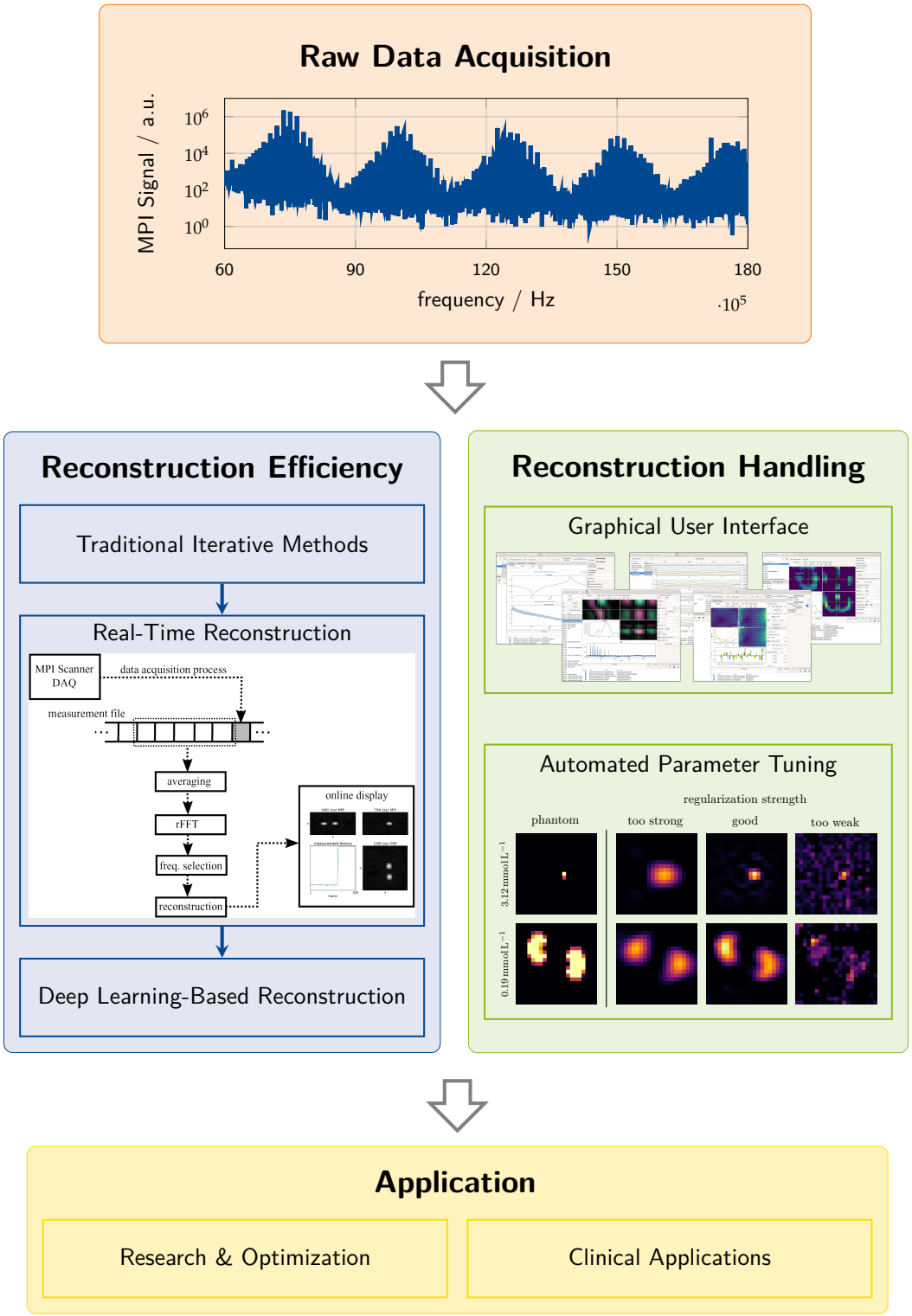

Figure 2.6: Overview of the MPI reconstruction pipeline, illustrating the stages from signal acquisition to clinical and research applications. It highlights two key aspects: reconstruction efficiency, which includes algorithmic innovations like real-time reconstruction and deep learning, and reconstruction handling, focusing on methodological and software development to improve usability and automation. The schematic description of real-time reconstruction on the left was designed and published by Knopp et al. [142].

Towards Automated Reconstruction

Recalling the discrete linear inverse problem described in section 1.2, the selection of regularization strategies presents a significant challenge. For the Tikhonov-regularized least squares problem given in Equation (1.4), the primary regularization parameter is $\lambda \in \mathbb{R}_+$. However, in practical applications involving measured system matrices, regularization is further influenced by the frequency selection, defined as

$$I_{K_\Theta} = \{k \in I_K | k \geq k_{\text{min}} \wedge \text{SNR}_k > \Theta\}\,,$$

where k_{min} denotes the minimum frequency and $\Theta \in \mathbb{R}_+$ is the SNR threshold. Additionally, in iterative reconstruction algorithms, the number of iterations $\iota \in \mathbb{N}$ acts as an implicit regularization parameter, since early termination yields stronger regularization effects [72]. The complexity of parameter tuning increases further with the inclusion of additional penalty terms, such as l_1-norm regularization or total variation constraints. Even when confined to standard l_2-norm regularization, the resulting optimization spans a highly interdependent three-dimensional parameter space. Moreover, the appropriate level of regularization is heavily dependent on measurement-specific factors, including tracer concentration and noise characteristics.

To illustrate this, we consider the example of a mouse kidney phantom shown in Figure 2.7. In each row, one of the three parameters controlling the regularization – the regularization pre-factor λ, the SNR threshold Θ, and the number of iterations ι – is varied while keeping the others fixed. Depending on the parameter setting, the reconstruction exhibits either appropriate, insufficient, or excessive regularization. These changes have a fundamental impact on the reconstructed image, affecting both the level of visible detail and the amount of noise and artifacts. While this example isolates the effect of each parameter, the real-world scenario is even more complex, as the parameters influence each other and must be jointly optimized.

Moreover, the reconstruction results in Figure 2.7 illustrate the problem of selecting regularization parameters on a single phantom. However, each individual measurement may require a different amount of regularization strength. Consequently, optimal parameter selection often necessitates expert knowledge in MPI reconstruction – expertise that cannot be expected from medical personnel in routine clinical settings. To address this barrier, an essential requirement for clinical deployment is the integration of Plug-and-Play reconstruction strategies that minimize manual parameter tuning. These approaches aim to automate the reconstruction process, offering robust default configurations and adaptive regularization schemes that dynamically adjust based on input data characteristics. By enabling immediate, high-quality image generation with minimal user intervention, such strategies are key to bridging the gap between technical reconstruction frameworks and clinical usability.

The method developed by the author and discussed in detail in Chapter 4 unifies all regularization parameters under a single control variable: the number of iterations ι. In this approach, earlier termination of the iterative reconstruction results in stronger regularization, while high-SNR data permits more iterations, progressively incorporating higher-frequency components and reducing regularization strength. A central challenge remains the determination of the optimal stopping criterion. While the author proposes a heuristic stopping rule that generalizes well across multiple datasets, leveraging a data-driven deep learning approach may offer further improvements in adaptivity and performance.

Automated regularization strategies significantly enhance consistency across varying imaging conditions and improve reproducibility in clinical applications. This is particularly advanta-

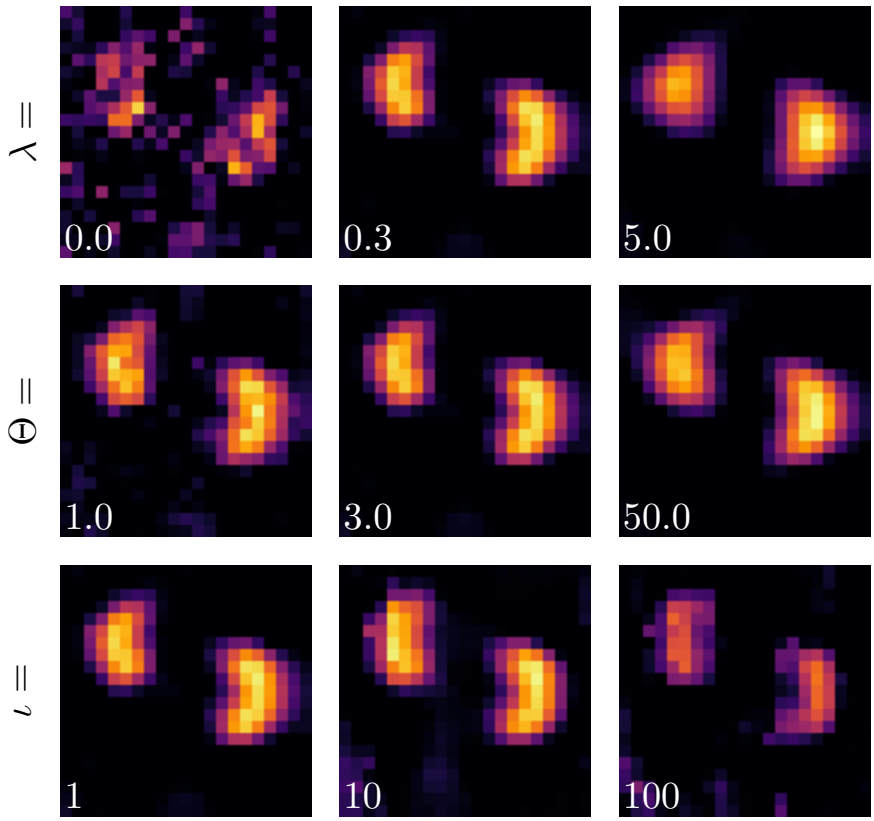

Figure 2.7: Influence of regularization parameters on the reconstruction quality of a mouse kidney phantom. Each row shows the effect of varying one regularization parameter – the pre-factor λ, the SNR threshold Θ, or the number of iterations ι – while keeping the others fixed. The examples demonstrate how insufficient or excessive regularization alters the balance between image detail, noise, and artifacts.

geous in time-sensitive scenarios, where rapid image reconstruction is critical for informed decision-making. Moreover, automated adaptation of regularization is especially beneficial in dynamic applications such as perfusion imaging, where tracer distribution evolves over time, necessitating continuous adjustment of regularization parameters to ensure high-quality image reconstruction. This concept is further explored and demonstrated with experimental data in Chapter 4.

Multi-Patch and Dynamic Reconstruction

As explained in section 2.2, MPI is constrained by a limited FOV, requiring multi-patch reconstruction to extend coverage. Signal outside the FOV of each single patch might lead to artifacts on the patch boundaries. Early approaches used overlapping patches and post-processing to mitigate these artifacts, but at the cost of increased acquisition time. More recent joint reconstruction algorithms enable artifact-free reconstruction of non-overlapping patches, significantly improving efficiency [144]. Zdun et al. [319] proposed using the stochastic primal-dual hybrid gradient method to solve the multi-patch reconstruction task, demonstrating superior reconstruction quality over Tikhonov regularization and Kaczmarz-based methods while reducing computational costs.

However, sequential scanning in multi-patch MPI reduces temporal resolution, leading to motion artifacts – particularly from cardiac and respiratory motion – necessitating advanced reconstruction strategies. A promising approach synchronizes raw data to specific motion phases, effectively "freezing" movement at different states without requiring additional navigator signals [83]. Additionally, incorporating motion priors derived from flow-parameter-dependent partial differential equations into the reconstruction process has shown significant improvements in suppressing motion artifacts. Brandt et al. [31] developed a reconstruction framework that models dynamic MPI as a time-dependent inverse problem. Their approach was validated using simulated data, rotational phantom experiments, and in-vivo mouse measurements, demonstrating enhanced image quality in dynamic MPI reconstructions.

Artifact-free dynamic multi-patch reconstruction is essential for numerous MPI applications, particularly in perfusion imaging, where high temporal fidelity is required to capture rapid tracer dynamics.

Accelerated and Real-Time Reconstruction

Reconstruction speed is a critical factor for the clinical application of MPI, as the time required for image reconstruction depends on the specific application. For routine diagnostic imaging (e.g., tumor detection), longer reconstruction durations are acceptable in exchange for higher resolution. In contrast, urgent diagnostic imaging (e.g., stroke monitoring) requires reconstruction within minutes, while real-time or near-real-time reconstruction with latencies below one second is essential for intraoperative guidance and emergency diagnostics.

To meet these diverse time constraints, several strategies are employed.

Leveraging hardware: High data rates in MPI necessitate accelerated reconstruction methods. Parallel processing and GPU acceleration are pivotal, enabling significant reduction in reconstruction times from minutes to seconds. The massively parallel architecture of modern GPUs allows real-time or near-real-time image reconstruction [216].

Sparse reconstruction: Another important strategy for acceleration involves sparse reconstruction techniques, which exploit the inherent sparsity of MPI images in specific transform domains. By incorporating compressed sensing approaches, the size of the underlying system to be solved is significantly reduced, leading to substantial computational savings while preserving image fidelity [164, 263].

Iterative solvers: Further improvements in MPI reconstruction stem from advancements in iterative solvers, with the Kaczmarz method [128] being the most widely used approach to date. Its efficiency arises from the sequential projection onto hyperplanes defined by the measured data, ensuring rapid convergence even for large-scale problems. This method is particularly well-suited for MPI, where the system matrix is typically ill-conditioned, as hyperplane projections inherently promote numerical stability [143, 110]. Additionally, preconditioned conjugate gradient methods and other optimization strategies have been explored to enhance convergence rates while reducing computational overhead, enabling high-accuracy reconstruction even in complex imaging scenarios [156, 261].

Online reconstruction: The shift from offline to online reconstruction introduces a balance between image quality and reconstruction speed. Offline reconstruction prioritizes optimal image quality with more iterations, adaptive regularization, and post-processing. In contrast, online reconstruction shifts the focus towards minimizing latency to provide continuous visualization of acquired data. This necessitates an efficient computational pipeline that balances speed and quality [142]. To achieve low-latency reconstruction, system matrices must be preloaded into memory, eliminating costly disk access delays. The reconstruction process

itself relies on the Kaczmarz method with a minimal number of iterations, significantly reducing computational effort per frame. Additionally, all required memory is preallocated and reused for successive frames, further streamlining performance. However, even with an optimized pipeline, data acquisition can still outpace reconstruction. In such cases, the system prioritizes displaying the latest available frame rather than processing every individual data set, ensuring real-time feedback at the cost of potential data loss. While frame skipping would be unacceptable in offline reconstruction, it is a practical compromise in real-time imaging. Alternatively, averaging consecutive frames can help maintain temporal coherence without excessive computational overhead. Furthermore, unlike offline reconstruction workflows, where results are stored for later analysis, real-time systems bypass disk writing entirely, directly displaying reconstructed images to ensure immediate visualization.

Direct reconstruction: An alternative approach is direct reconstruction, which bypasses iterative solvers by utilizing modeled system functions [59]. Although this method enables near-instantaneous image formation, it relies on a simplified equilibrium model that omits anisotropy effects, limiting its reconstruction accuracy. Recently, a fast implementation of direct reconstruction incorporating anisotropy has been presented in cooperation with the author [58]. However, these methods still require further integration and validation in preclinical MPI systems to assess their potential as a robust alternative for clinical applications.

These optimizations enable real-time MPI reconstruction to meet the stringent demands of interventional procedures, providing clinicians with rapid and continuous imaging feedback necessary for precision treatments.

Deep Learning-based Reconstruction

Deep learning is emerging as a transformative tool in MPI reconstruction, offering advantages in speed, accuracy, and adaptability over traditional model-based methods [200, 148, 264, 45, 323]. Conventional approaches rely on explicitly defined system models and handcrafted regularization, which can be computationally expensive and suboptimal in complex imaging scenarios. In contrast, deep learning can learn the mapping between raw MPI signals and reconstructed images, bypassing computationally intensive steps and enabling more efficient processing.

Deep learning-based approaches in MPI have shown promising potential for improving reconstruction quality, particularly in challenging scenarios with low signal-to-noise ratios [199]. Trained neural networks may learn to suppress artifacts and noise by capturing complex signal characteristics present in diverse datasets, which could lead to improved image fidelity. Additionally, data-driven super-resolution techniques offer a possible means to enhance spatial and temporal resolution by inferring fine structural details from undersampled or noisy data [17, 246, 247]. In contrast to conventional methods that rely on fixed regularization schemes, deep learning models may offer increased adaptability and robustness by adjusting dynamically to varying imaging conditions.

A particularly promising approach is deep learning-based plug-and-play reconstruction, which integrates learned priors into iterative solvers. Recent work has incorporated pre-trained priors into alternating direction method of multipliers (ADMM) frameworks, significantly improving reconstruction robustness [10, 81]. A similar method was presented for the Kaczmarz algorithm [285]. Traditional handcrafted priors struggle to capture the complex spatial and temporal patterns inherent in MPI data, while purely data-driven methods can be computationally demanding or limited in generalization. To address these issues, Güngör et al. introduced DEQ-MPI, a deep equilibrium model embedding learned data consistency into

reconstruction [109]. This approach ensures convergence while achieving high image quality and competitive inference times.

As deep learning continues to influence MPI reconstruction, it is anticipated to significantly shape algorithmic research in the coming years. Neural networks have the potential to generalize across various imaging setups, improving reconstruction processes and minimizing the need for extensive manual tuning. However, several challenges persist, including the requirement for large, high-quality training datasets, the need for improved model interpretability, and ensuring robust generalization across diverse hardware configurations.

Hybrid approaches that integrate physics-based models with deep learning frameworks offer a promising direction for real-time MPI reconstruction. By combining model-driven and data-driven methods, these techniques may refine reconstructions efficiently, reducing computational burden while preserving structural details. This synergy holds great potential for accelerating MPI reconstruction and advancing the field toward real-time, high-fidelity imaging suitable for clinical applications.

Software Development

For MPI to become a clinically viable imaging modality, reconstruction frameworks must not only be efficient and accurate but also accessible and adaptable. Open-source software platforms play a critical role in achieving these goals by ensuring standardization, reproducibility, and continuous innovation. By providing well-documented and validated reconstruction methods, these platforms enable researchers to consistently apply algorithms across different MPI systems, promoting comparability and scientific rigor.

A key factor in making these reconstruction frameworks user-friendly is the development of an intuitive graphic user interface (GUI). A well-designed GUI simplifies complex workflows, lowering the barrier to entry for clinicians and non-experts. By guiding users through intricate reconstruction processes, such interfaces shift the focus away from technical algorithmic details and towards the clinical interpretation of the images. In the open-source MPI software framework developed in Julia by the authors' research group, in collaboration with leading MPI experts worldwide, a GUI is being continuously refined to meet these usability objectives and ensure an effective user experience [111].

Moreover, the open-source approach fosters a culture of collaborative development, creating a global network where scientists and engineers can collectively refine and enhance reconstruction techniques. This exchange accelerates innovation, facilitates cross-institutional cooperation, and ensures that MPI methodologies remain at the forefront of technological advancements.

Beyond fostering innovation, open-source software also plays a crucial role in data security and regulatory compliance. Transparent and well-audited reconstruction frameworks help ensure adherence to medical standards and regulations. By making source codes openly accessible, researchers and regulatory bodies can assess and verify the implementation of safety measures, data handling protocols, and quality assurance procedures. Moreover, open-source development facilitates compliance with privacy frameworks (e.g. the Health Insurance Portability and Accountability Act in the United States and the General Data Protection Regulation in the European Union), ensuring that patient data is securely managed and anonymized when integrated into clinical workflows. This level of transparency and adaptability is vital for MPI's transition from research to clinical practice, where strict validation and regulatory oversight are required.

Recent open-source initiatives in MPI have highlighted the potential of community-driven development, enabling the rapid integration of advancements such as GPU acceleration, sparse reconstruction, and deep learning-based methods. Notably, the authors' research group has been a key contributor to these efforts, providing open-data initiatives and a comprehensive MPI open-software framework written in Julia https://www.tuhh.de/ibi/research/software/magnetic-particle-imaging [110, 111, 152, 149, 151]. In addition, numerous research groups worldwide actively contribute to open-source software development, fostering collaboration and innovation within the field https://os-mpi.github.io/ [182, 254], https://www.opensourceimaging.org/project/mfs-magnetic-field-simulator/ [131].

As research advances toward real-time, high-quality imaging, the next steps will focus on refining these approaches for robust clinical use. In particular, hybrid strategies that integrate model-based techniques with deep learning hold significant promise for achieving both speed and accuracy, ultimately enhancing MPI's utility in medical applications such as cardiovascular diagnostics, tumor tracking, and interventional guidance. By maintaining an open and collaborative approach, the field can continue evolving toward clinically viable, high-performance MPI reconstruction.

2.4 Tracer Development

The availability of suitable magnetic nanoparticle tracers with medical approval is a key factor in translating MPI to clinical applications. MPI's signal generation and spatial encoding fundamentally rely on the nonlinear magnetization response of magnetic nanoparticles. However, clinical adoption is hindered by a trade-off between MPI-optimized tracers, which exhibit strong signal responses, and SPION formulations already approved for MRI, which often lack the necessary magnetic properties for MPI. This section examines the challenges associated with MPI tracer development, focusing on clinical approval pathways, signal strength optimization, and tracer stability.

2.4.1 Clinical Approval

MPI tracers must undergo stringent regulatory approval processes governed by agencies such as the U.S. Food and Drug Administration (FDA) and the European Medicines Agency (EMA). The approval process requires extensive preclinical and clinical studies to establish safety, efficacy, and biocompatibility. Historically, SPION formulations such as ferucarbotran (Resovist®) have received medical approval for liver MRI applications, and more recently, Resotran®(b.e.imaging GmbH, Germany) has been approved for MRI in Germany and Sweden [192, 244]. Additionally, a phase III clinical trial is currently evaluating ferumoxtran (Ferrotran®), an ultra-small SPION formulation, for MRI applications. While these SPION formulations are not explicitly designed nor approved for MPI, they represent the closest available options for clinical MPI imaging.

A major challenge in tracer approval is ensuring biocompatibility and long-term safety. SPIONs are primarily cleared by the mononuclear phagocyte system, with liver and spleen uptake being the dominant clearance pathways [225, 114, 168]. Dextran-coated SPIONs, such as Resovist, exhibit rapid hepatic clearance with a half-life of approximately 10 min, whereas PEG-coated SPIONs can achieve circulation half-lives of up to 7 h in mice [168]. While these clearance mechanisms ensure iron homeostasis, iron dose limitations and potential long-term toxicity remain concerns [262, 25]. Safe iron dose ranges for human applications vary from

2.24 mgFe/kg (for Resovist) to 8.5 mgFe/kg (for Feraheme) [258], providing a reference for MPI tracer safety considerations.

The regulatory approval process is costly and time-intensive, requiring a strong business case for investment. Since tailored MPI tracers have yet to receive approval, the field faces a chicken-and-egg problem: without approved MPI-specific tracers, the clinical potential of MPI remains unproven, while the lack of clinical MPI systems discourages commercial interest in tracer development.

2.4.2 Signal Strength and Optimization

The effectiveness of MPI tracers is largely determined by their magnetic properties, particularly their ability to generate a strong signal under MPI excitation. The optimal SPION size range is dictated by a balance between Néel and Brownian relaxation mechanisms [274, 55]. Particles that are too small exhibit nearly linear magnetization behavior due to dominant thermal energy effects, making them unsuitable for MPI. In contrast, excessively large particles lose their superparamagnetism and transition to a ferromagnetic state, resulting in strong magnetic anisotropies. As a result, Néel relaxation is suppressed, and their ability to respond at MPI excitation frequencies of $10 - 150\,\mathrm{kHz}$ is significantly reduced. Additionally, system-specific optimization has been explored, such as particle chain formation, which enhances the nonlinear response for one-dimensional MPI excitations [275].

Among MRI-approved SPIONs, ferucarbotran (Resovist, Resotran) has shown the most favorable MPI properties, yet its broad size distribution results in only 3 % of its total iron mass contributing to an effective MPI signal [318]. To address these limitations, several MPI-specific tracers have been developed, a selection is listed in Table 2.1.

Table 2.1: Overview of different MPI tracers and their properties.

Tracer	Manufacturer	Description
Ferucarbotran (Resovist, Resotran)	Bayer Schering Pharma, Germany	MRI-approved, but only 3 % effective MPI signal [318]
Perimag	micromod, Germany	∼19 nm core, optimized for Brownian and Néel relaxation [63, 172]
Synomag	micromod, Germany	Improved MPI performance over ferucarbotran [315, 170]
VivoTrax+	Magnetic Insight, USA	Relabeled version of Ferucarbotran for distribution in the USA [315, 85]
PrecisionMRX	Imagion Biosystems, Australia	Monodisperse iron core SPIONs [67]
LS-008	LodeSpin Labs, USA	Designed specifically for MPI applications [67]
Magnetosomes	Biogenic sources	Biogenic SPIONs with high MPI signal potential [63, 170, 278]

Moreover, in Figure 2.8 MPI system matrices and SNR characteristics are shown for the MPI-tailored tracer Perimag and the approved MRI tracers Resotran, Resovist and Ferrotran. It is clearly visible that Perimag shows the best results – both in SNR characteristics and on the system matrix level, where clear structures can be seen even at the sideband frequency of

108.76 kHz. However, due to it's approval for MRI the ferucarbotran-based tracer Resotran is a promising candidate for first human MPI experiments.

Despite promising results, none of these MPI-specific tracers have progressed to clinical approval due to the high regulatory costs and lack of a defined commercial market. The author contributed to this research area during the course of his dissertation through multiple collaborative projects [194, 260, 256, 192].

2.4.3 Stability and Pharmacokinetics

For clinical applications, the stability of MPI tracers in the bloodstream is critical to ensuring reproducible imaging performance. Several key factors influence tracer stability, including circulation half-life, aggregation tendencies, protein interactions, and hemocompatibility.

The circulation half-life of an MPI tracer determines its suitability for different imaging applications. Long-circulating tracers are advantageous for continuous imaging, providing sustained signal availability, whereas short-circulating tracers are preferred for perfusion imaging, where repeated bolus injections are required to capture rapid physiological changes [191]. Certain strategies, such as red blood cell labeling, have been proposed to extend circulation times, with approximately 30 % of the MPI signal persisting after 24 hours [256, 6, 7]. However, prolonged circulation can increase the risk of off-target accumulation, necessitating careful optimization of tracer clearance properties.

A major challenge in MPI tracer design is the prevention of nanoparticle aggregation in biological fluids. SPIONs have a natural tendency to aggregate, which can compromise imaging efficacy and, in extreme cases, lead to embolism. Surface modifications with biocompatible coatings, such as polyethylene glycol or dextran, improve colloidal stability and reduce aggregation risk, thereby enhancing the safety and reliability of MPI contrast agents [63].

Another critical aspect of tracer stability is its interaction with serum proteins, leading to the formation of a protein corona. This corona can significantly influence the biodistribution, clearance, and overall biological behavior of the tracer [168]. Strategies to mitigate these effects include the use of anti-fouling coatings such as PEGylation, which helps minimize unwanted protein adsorption and ensures a more predictable pharmacokinetic profile.

Furthermore, MPI tracers must demonstrate excellent hemocompatibility, meaning they should not induce hemolysis, thrombosis, or immune activation. While ferucarbotran has been associated with a relatively low adverse event rate of approximately 7.1 % [303], further studies are necessary to evaluate the long-term hemocompatibility of MPI-specific tracers, particularly those optimized for high signal strength and prolonged circulation.

Ultimately, the ideal MPI tracer must balance high imaging performance with long-term stability and biocompatibility while meeting stringent regulatory requirements for clinical translation. Advancements in SPION formulation, surface engineering, and biocompatibility research will be essential in addressing these challenges, paving the way for the safe and widespread adoption of MPI in clinical practice.

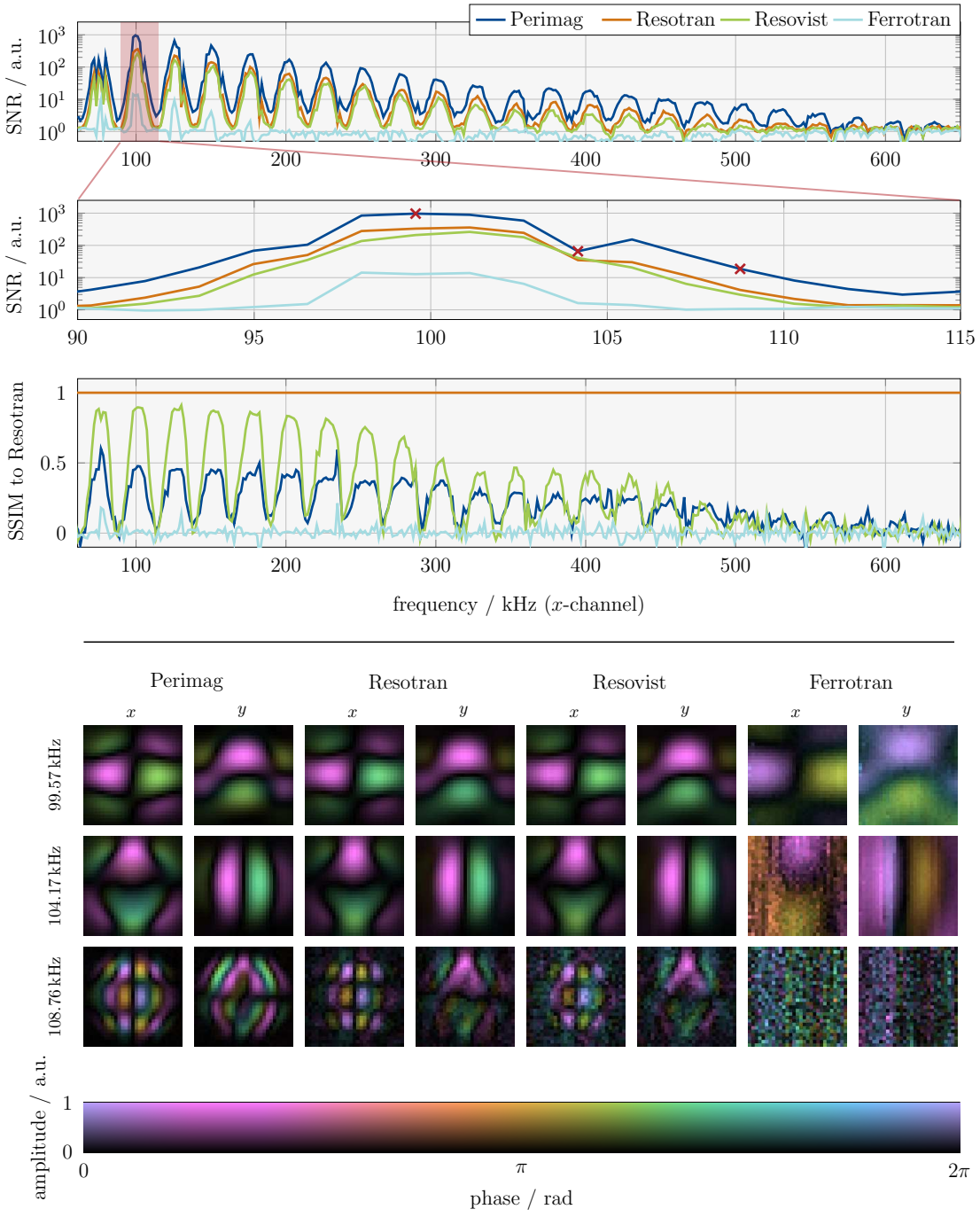

Figure 2.8: SNR characteristics and system matrices measured on the preclinical system Bruker MPI 20/25 FF for the tailored tracer Perimag, as well as the currently approved MPI tracers Resotran, Resovist, and Ferrotran. The figure provides insights into the SNR of the x-channel for all tracers, measured with xy-excitation. A zoom on the fourth harmonic ($90 - 115\,\mathrm{kHz}$) with its sidebands is shown, along with the SSIM values of Perimag, Resovist, and Ferrotran relative to Resotran for the full spectrum. Additionally, the figure includes color-coded system matrix patterns for three key frequencies (marked by red crosses), illustrating the variations across tracers. The figure was designed by the author and published in Mohn et al. [192].

3

Extrapolation of System Matrices

K. Scheffler, M. Boberg, and T. Knopp, "Extrapolation of System Matrices in Magnetic Particle Imaging", IEEE Transactions on Medical Imaging, Vol. 42, No. 4, April 2023.

Parts of this chapter have been presented at

International Workshop on Magnetic Particle Imaging 2022, Würzburg, Germany.
International Workshop on Magnetic Particle Imaging 2023, Aachen, Germany.

Abstract

Magnetic particle imaging exploits the non-linear magnetization of superparamagnetic iron-oxide particles to generate a tomographic image in a defined field-of-view. For reconstruction of the particle distribution, a time-consuming calibration step is required, in which system matrices get measured using a robot. To achieve artifact-free images, system matrices need to cover not only the field-of-view but also a larger area around it. Especially for large measurements – inevitable for future clinical application – this leads to long calibration time and high consumption of persistent memory. In this work, we analyze the signal in the outer part of the system matrix and motivate the usage of extrapolation methods to computationally expand the system matrix after restricting the calibration to the field-of-view. We propose a suitable extrapolation method and show its applicability on measured 2D and 3D data. In doing so, we achieve a considerable reduction of calibration time and consumption of persistent memory while preserving an artifact-free result.

3.1 Introduction

As a preclinical non-invasive tomographic method without ionizing radiation, magnetic particle imaging (MPI) has huge potential for biomedical imaging applications [87, 141]. The non-linear magnetization of superparamagnetic iron-oxide particles is exploited to determine their concentration by using sinusoidal excitation fields (drive fields). To obtain spatial resolution, a field-free point (FFP) is generated by applying an additional static gradient field. The FFP is moved by the drive field in the region of interest along a trajectory. The size of the area covered by this trajectory, called field-of-view (FOV), is determined by the ratio of

the drive fields amplitudes and the gradient strength of the static field. Since the drive-field amplitude is limited due to physiological constraints, the maximal possible size of the FOV is too small for human applications [141]. This limitation is commonly resolved by adding a homogeneous focus field with low frequency onto the gradient field and shifting the FOV in space [87]. In this way, the full region of interest is divided into multiple patches. Within a static multi-patch measurement, the full FOV is assembled by measuring a volume via the drive field and then moving the FFP to the next position acquiring the next patch [218]. For the reconstruction of the particle distribution, system matrices (SMs) are received in an additional calibration step by measuring a point sample on a grid covering each patch. Although in principle system matrices can be reused for multiple patches [29], this leads to a reduction in image quality due to field imperfections, which cannot be tolerated in many applications.

As shown in experiments on measured data [144, 305], particles located outside the FOV of a patch are still excited and contribute to the measurement signal. This poses a problem especially in multi-patch MPI by generating artifacts at patch boundaries. Such artifacts on a simple two-patch configuration can be seen in Fig. 3.1.

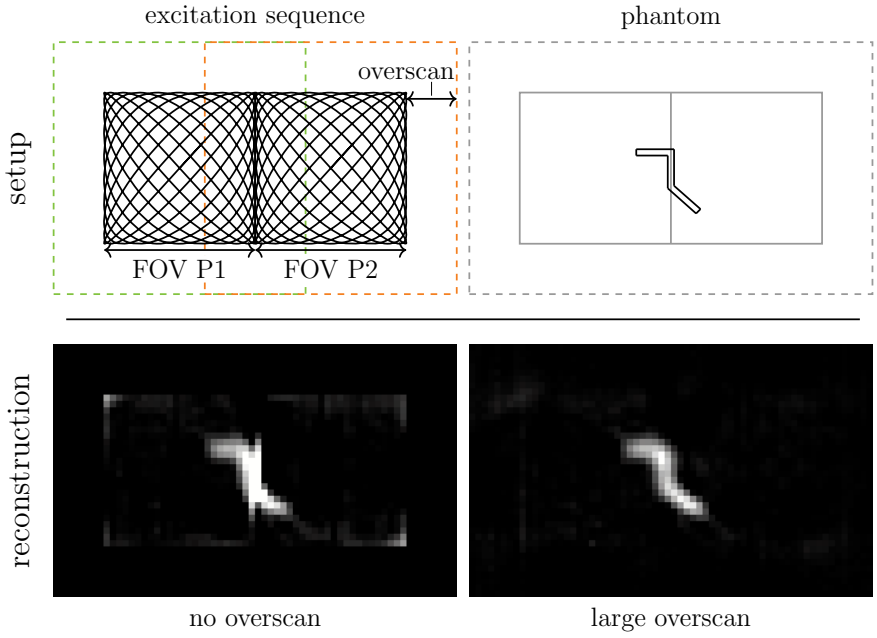

Figure 3.1: 2D MPI results on two horizontally aligned patches. Top left: schematic configuration of the two patches. Top right: visualization of the phantom. Bottom left: multi-patch reconstruction without any overscan leads to artifacts on the patch boundary. Bottom right: artifact-free reconstruction using a large overscan (long calibration time and large consumption of persistent memory).

For future use of MPI in medical applications e.g. for the diagnosis of vascular diseases like arteriosclerosis, multi-patch MPI will be important to maintain a high spatial resolution when imaging large FOVs as for instance required for heart imaging. To avoid reconstruction artifacts at patch boundaries, a joint reconstruction algorithm for non-overlapping patches was proposed in [144, 2]. While the approach can handle non-overlapping patches, it requires the patch-wise SM acquisition to not only cover the FOV, but also a bigger surrounding area, called overscan (as displayed in Fig. 3.1) [144]. This is very time and memory consuming,

especially for large 3D SMs. In practice, such system matrices are commonly measured with a small overscan to avoid execive calibration times. In turn, boundary artifacts are still present. For example in Szwargulski et al. [268], 15 SMs of size $25 \times 21 \times 27$ were used, each covering a FOV of $16 \times 16 \times 16$ voxels. The calibration took $\sim$8.67 h for each of the SMs, leading to a total net calibration time of $\sim$5.4 d. The reconstruction results still contained visible artifacts. By adding another two voxels of overscan in each direction for a better result, the net calibration time would have exceeded $\sim$8.5 d. Calibration scans have to be repeated at least after each scanner maintenance, which is needed roughly once a year.

The challenge of long calibration times has been tackled in various research articles originating to [154], which proposed to use compressed sensing (CS) in order to subsample the SM at random positions, achieving subsampling rates of about 5-10 in 2D and about 30 in 3D [106]. The method has been gradually improved by new sparsity transformations [106, 173], improved sampling strategies [105, 124] and recently, by replacing classical CS by modern learning-based algorithms [17, 108]. Another direction of research is to use model-based approaches [146, 150, 118], which have been greatly improved by the use of sophisticated particle models [4, 138]. Model-based methods usually require only a fraction of calibration data, but on the other hand, have still not reached the accuracy provided by classical delta-sample based measurement of the system matrix.

The focus of the present work lies on the overscan region (OR) and the development of methods that are capable of restoring the information in this region either without, or with only few calibration points. We examine the signal propagation in the OR from an analytical as well as from a numerical point of view. Starting from this motivation, we propose a method where the system matrices are only acquired within the FOV or a small OR. In a post-acquisition step, the SMs get computationally extrapolated into a large OR, directly before the reconstruction. To this end, we use two variations of a diffusion-ansatz with different constraints and homogeneous Dirichlet boundary conditions. On the one hand this extrapolation step can be used to reduce time and consumption of persistent memory of new calibration measurements. On the other hand, it can also be applied to already measured system matrices to enlarge the OR and enhance the reconstruction results. We show and discuss the feasibility of the proposed method on 2D and 3D experimental MPI data. We compare our method to the aforementioned system matrix retrieval methods based on sparse sampling of the system matrix and show that our method can be combined with them providing even higher subsampling rates. This paper is the full and extended version of our conference abstract [236].

3.2 Methods

3.2.1 Analytical Motivation

As a first step, we want to examine the signal in the overscan region from a model-based, analytical point of view. Considering the equilibrium model for MPI, where the particle magnetization is described with the help of the Langevin function, the reconstruction problem in MPI can be modeled as

$$\boldsymbol{u}(t) = \int_{\Omega} \boldsymbol{s}(\boldsymbol{r}, t) c(\boldsymbol{r}) \, \mathrm{d}\boldsymbol{r}, \tag{3.1}$$

where $\Omega = \Omega_{\mathrm{FOV}} \cup \Omega_{\mathrm{OS}}$, with $\Omega_{\mathrm{FOV}} \subset \mathbb{R}^3$ denoting the FOV and $\Omega_{\mathrm{OS}} \subset \mathbb{R}^3$ denoting the OR. Furthermore, $\boldsymbol{u} : \mathbb{R}_+ \to \mathbb{R}^3$ is (up to a time-constant factor consisting of

the homogeneous coil sensitivity profile, the vacuum permeability and the magnetic moment of a nanoparticle) the voltage signal, $c : \Omega \to \mathbb{R}$ is the particle distribution and $\boldsymbol{s} : \Omega \times \mathbb{R}_+ \to \mathbb{R}^3$ is the system function given as

$$\boldsymbol{s}(\boldsymbol{r}, t) = \frac{\partial}{\partial t} \mathscr{L}(\beta \boldsymbol{G}(\boldsymbol{r}_{\mathrm{FFP}}(t) - \boldsymbol{r})).$$

Here $\mathscr{L} : \mathbb{R}^3 \to \mathbb{R}^3$ is the vectorial Langevin function, $\boldsymbol{G} \in \mathbb{R}^{3\times 3}$ are the gradients of the selection field, $\boldsymbol{r}_{\mathrm{FFP}}(t) \in \mathbb{R}^3$ is the time dependent position of the FFP and $\beta \in \mathbb{R}$ are the remaining physical constants [135, 176]. Equation (3.1) is typically considered in the frequency domain after evaluating the Fourier series. In the common case of a Lissajous-trajectory of the FFP, the frequency component of the system function $\boldsymbol{s}_k : \Omega \to \mathbb{C}^3$, $k \in I_K = \{1, ..., K\} \subset \mathbb{N}$ can be described as a component-wise convolution

$$\boldsymbol{s}_k = \boldsymbol{\Psi} * \boldsymbol{\sigma}_k, \tag{3.2}$$

where $\boldsymbol{\sigma}_k : \Omega \to \mathbb{C}^3$ is a linear combination of tensor products of Chebyshev polynomials of 2nd kind (CP2s) in each component and $\boldsymbol{\Psi} : \Omega \to \mathbb{R}^3$ is a frequency-independent kernel [176]. For a 2D excitation, the kernel is defined over entries of the Hessian of the vectorial Langevin function:

$$\boldsymbol{\Psi}_{2D} = \frac{\partial^2}{\partial x_1 \partial x_2} \mathscr{L}\left(\beta \boldsymbol{G} \begin{pmatrix} x_1 \\ x_2 \\ c_3 \end{pmatrix}\right),$$

where $c_3 \in \mathbb{R}$. This convolution using $\boldsymbol{\Psi}_{2D}$ in one receive channel is examplarily shown for one frequency component in the lower part of Fig. 3.2. Recently it was proposed by Droigk et al. in [60] to interpret $\boldsymbol{\Psi}_{2D}$ as an approximate derivative in y-direction for the first component and in x-direction for the second component and respectively a smoothing filter in the other direction. With further investigation one can see, that the kernel is similar to a convolution of a central difference in one direction and a wide blurring kernel. With the central difference working only in one direction, the blurring kernel leads also to a smoothing in the other one. In other words, we can decompose $\boldsymbol{\Psi}_{2D}$ into

$$\boldsymbol{\Psi}_{2D} = \mathcal{B} * \delta,$$

where δ is the first order central difference and $\mathcal{B}$ is a wide blurring kernel, as seen in the upper part of Fig. 3.2.

It is visible in Fig. 3.2, that the convolution with the central difference δ leads to a shift shaping on the linear combination of CP2s (as derived in [176], the first derivative of CP2s are Chebyshev polynomials of 1st kind (CP1s) with some prefactors). The additional convolution with the wide blurring kernel $\mathcal{B}$ leads to a transport of information outside of the FOV (since the sharp support of the CPs gets blurred). This indicates, that the signal in the OR is – from an analytical point of view – a continuation of the blurred signal in the outer parts of the FOV. Therefore, especially frequency components with high signal amplitudes on the border of the FOV will have much signal in the OR. Because of the repeating pattern of the SM structure over higher harmonics, we assume that such components also occur in a repeating pattern, where the repetition is dependent on the frequency divider of the Lissajous-curve. Despite the fact that the analytical convolution kernel does not have a finite support leading to a theoretically infinite OR, we can see in Fig. 3.2, that the part of the kernel, which is displayed and used, already leads to a strong decay of signal in the OR. This is because the kernel tends to zero in all directions. Thus, when transferring to discrete measured system

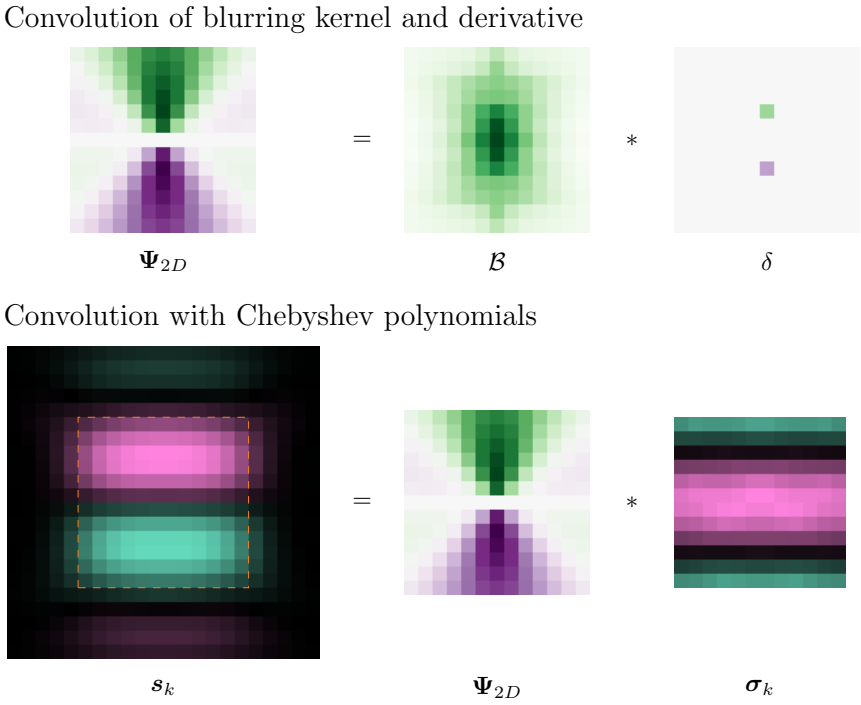

Figure 3.2: Top: frequency independent Ψ_{2D} derived from a convolution of a blurring kernel $\mathcal{B}$ and the central difference δ (note, that Ψ_{2D} is restricted in size after the convolution). Bottom: convolution of the linear combination of tensor products of CP2s σ_k with Ψ_{2D} gives the system function s_k for an exemplary frequency component $k \in I_K$. Ω_{FOV} is denoted by the dashed line.

matrices, it is meaningful to make use of homogeneous Dirichlet boundary conditions when expanding data into a finite OR. The placement of this boundary condition should be at a distance to the FOV, where the signal for the vast majority of frequencies is close to zero. This is the case for an OR of approximately one third of the size of the FOV.

The analytical representation of s_k in equation (3.2) was also derived for three dimensions [176]. In this case the linear combination of tensor products of CP2s gets convolved with a kernel derived from third order partial derivatives of the Langevin function. This kernel can be decomposed accordingly as the second order central difference convolved with a wide 3D blurring kernel and we end up with the same considerations as in the 2D case. We therefore leave out further discussions on 3D excitations.

3.2.2 Numerical Motivation

In the following we consider the system functions s_k, measured on a discrete grid of $L \in \mathbb{N}$ voxels as the system matrix $\boldsymbol{S} \in \mathbb{C}^{K \times L}$. The analytical considerations have shown that the signal in the OR is just a continuation of the signal inside the FOV, which promises good results for extrapolation methods. To verify this assumption on experimental data, we study spatial lines of voxels from the border of the FOV into the OR on measured data, as examplarily shown in Fig. 3.3.

Each voxel of these lines corresponds to a certain column $\boldsymbol{S}_l$ of the system matrix $\boldsymbol{S} \in \mathbb{C}^{K \times L}$ for $l \in I_{\tilde{L}} \subset I_L = \{1, ..., L\}$. We collect the frequency vectors along the considered spatial lines into a matrix $\boldsymbol{S}_{\tilde{L}} = (\boldsymbol{S}_{l_1} \boldsymbol{S}_{l_2} ...)$, where $\{l_1, l_2, ...\} = I_{\tilde{L}}$.

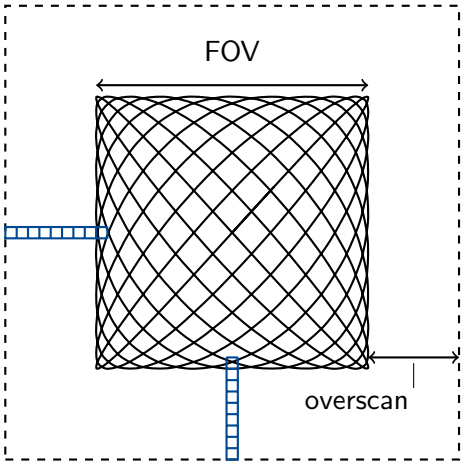

Figure 3.3: Investigation of the numerical independence of frequency vectors along straight lines in the OR.

We investigate the effective linear dependency of these frequency vectors along the spatial lines by considering the effective rank $\operatorname{erank}(S_{\tilde{L}})$ of this matrix [229]. By using the Shannon entropy, the effective rank embeds the singular value distribution of a complex valued matrix $S_{\tilde{L}}$ into a setting similar to the normal rank, such that $1 \leq \operatorname{erank}(S_{\tilde{L}}) \leq \operatorname{rank}(S_{\tilde{L}})$. An effective rank near to the amount of considered voxels implies a strong linear independence along the spatial line, whereas an effective rank of one implies a complete linear dependence. For the continuation of signal from the FOV into the OR, we therefore expect a small effective rank on measured SMs. If this expectation holds true, a continuation of signal along these lines using a harmonic extrapolation method is feasible.

Moreover, from the analytical motivation we assume, that especially frequency components with high signal amplitudes on the border of the FOV have much signal in the OR. To detect and examine such frequency components, we consider the proportion of the energy of the signal in the overscan region in relation to the total energy of the system-matrix rows, denoted by E_k^{os}. Let the index set $I_{\Omega_{\text{os}}} \subset I_L$ contain all voxels in Ω_{OS}. Then E_k^{os} is defined as

$$E_k^{\text{os}} = \frac{\sum_{l \in I_{\Omega_{\text{OS}}}} |S_{k,l}|^2}{\sum_{l \in I_L} |S_{k,l}|^2}.$$

Following the analytical considerations, we expect a majority of frequency components with low values of E_k^{os} and a repeating pattern of frequency components with higher values of E_k^{os}. Depending on the impact of such components on the reconstruction, further methods and improvements for artifact reduction are thinkable. For this reason, a comparison with the associated mixing factors [221] and the signal-to-noise ratio (SNR) [79] is meaningful. By considering the frequency-divider $N^p \in \mathbb{N}$ of the Lissajous excitation, the mixing factors $m_x, m_y, m_z \in \mathbb{Z}$ are connected to the frequency component k for a 3D excitation via

$$k = (N^p - 1)m_x + N^p m_y + (N^p + 1)m_z.$$

3.2.3 Reduced Frequency Selection

A simple method to avoid boundary artifacts is to alter the frequency selection used for reconstruction. Following the aforementioned considerations, the idea is that frequency

components with E_k^{os} higher than a certain threshold $\tau \in [0,1]$ (i.e. the frequencies with a lot of signal in the OR) are not taken into account during reconstruction. For all remaining frequency components with $E_k^{\text{os}} \leq \tau$, the system matrices restricted to the FOV are used. The threshold τ must be chosen such that the frequencies with peaks in E_k^{os} are not used for reconstruction (to suppress boundary artifacts effectively), while the vast majority of the frequencies should remain, to achieve good spatial resolution. In the following we denote this method TRUNCATED$^+$.

3.2.4 Minimization Problem

To simplify the definition of the extrapolation method, let $\Omega \subset \mathbb{R}^d$, $d \in \{2,3\}$ be of the same size in each direction. To analyze boundary artifacts on different sizes of overscan, we consider finite sequences of system matrix rows $\boldsymbol{S}_k^i$ for $i \in \{M, M-1, ..., 0\}$, $M \in \mathbb{N}$, with frequency component $k \in I_K$. The outermost voxel line in each dimension gets truncated in each step, down to a truncation to the FOV. Let $P_i \subset \Omega$ be the area to which the system matrix gets truncated in step i, such that in each step i equals the amount of lines of voxels in the overscan. I.e. for $i = M$ we obtain the original full system matrix on $P_M = \Omega$ and for $i = 0$ we get the system matrix truncated to $P_0 = \Omega_{\text{FOV}}$. The truncation sequence is shown on an exemplary grid on the left side of Fig. 3.4.

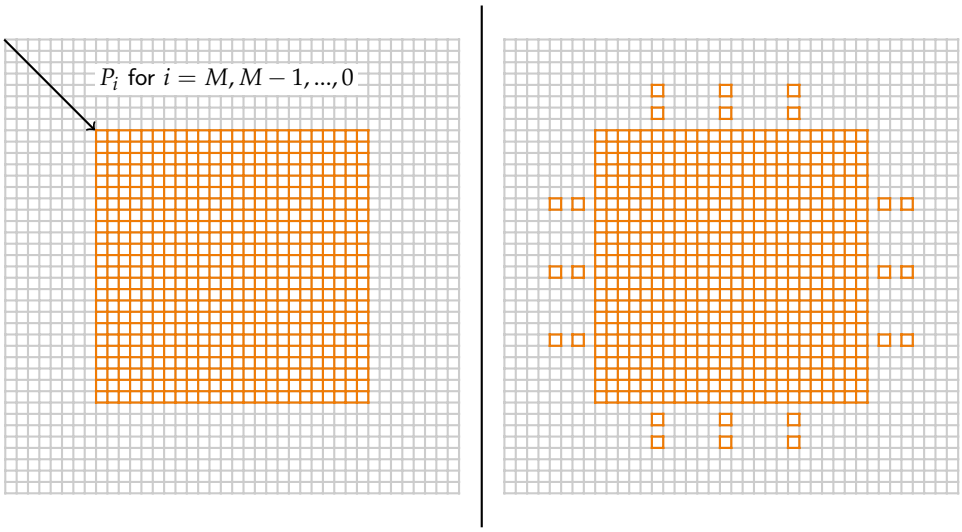

Figure 3.4: Left: sequence of system matrix truncation on grid P_i for $i \in \{M, M-1, ..., 0\}$, where $P_M = \Omega$ (gray) and $P_0 = \Omega_{\text{FOV}}$ (orange). Right: fully truncated grid with few kept voxels in the OR (VARIANT II) (all kept voxels are visualized in orange).

In order to achieve an extrapolation of the SMs, which follows the wave patterns harmonically into the overscan, we define the cost functional

$$J(\boldsymbol{v}_k) := \|\nabla \boldsymbol{v}_k\|_2^2. \tag{3.3}$$

J has to be minimized over $\boldsymbol{v}_k \in \mathcal{C}^2(\Omega, \mathbb{C}^3)$, $\forall k \in I_K$ using homogeneous Dirichlet boundary conditions [32]. After discretization of $\boldsymbol{v}_k$ on the system matrices grid to $\boldsymbol{V}_k \in \mathbb{C}^L$, we get the following minimization problem for each truncation step i:

$$\left\| \nabla \boldsymbol{V}_k^i \right\|_2^2 \overset{\boldsymbol{V}_k^i}{\to} \min, \tag{3.4}$$

under the constraints

$$\boldsymbol{V}_k^i|_{P_i} = \boldsymbol{S}_k^i \quad \text{and} \quad \boldsymbol{V}_k^i|_{\partial\Omega} = 0.$$

For a minimizer $\tilde{\boldsymbol{V}}_k^i$ to the minimization problem (3.4) it follows that

$$\Delta\tilde{\boldsymbol{V}}_k^i|_{\Omega\setminus P_i} = 0, \tag{3.5}$$

i.e. the minimization leads to a harmonic extrapolation of the system matrix. The discrete minimization problem is solved by setting up the Laplacian matrix of a discrete Laplace operator and using a least squares approach. In the following, this method is denoted as VARIANT I for the full truncation to $P_0 = \Omega_{\text{FOV}}$. Moreover, emanating from VARIANT I, we propose a second variant of the minimization problem (3.4), where few single voxels in the OR are left as additional constraints to improve the extrapolation accuracy while still truncating the vast majority of voxels in the overscan region (denoted as VARIANT II). A possible choice for additional kept voxels is shown on the right side of Fig. 3.4.

In addition, we also consider a fourth method, where the same extrapolation as in VARIANT II is used only on the frequencies with high signal in the overscan. It is therefore a combination of the methods VARIANT II and TRUNCATED$^+$ and will be denoted as VARIANT II$^+$ in the following. The advantage to VARIANT II is the reduction of the computation time, especially for 3D data.

In summary we study four methods to reduce boundary artifacts: TRUNCATED$^+$ is using a reduced frequency selection to avoid frequencies with high energy in the OR, VARIANT I is using the plain harmonic extrapolation in the OR, VARIANT II is using few voxels in the OR as additional constraints to the extrapolation and VARIANT II$^+$ is a combination where only frequencies with high energy in the OR get extrapolated to the OR. A graphical summary of the four methods is given in Fig. 3.5.

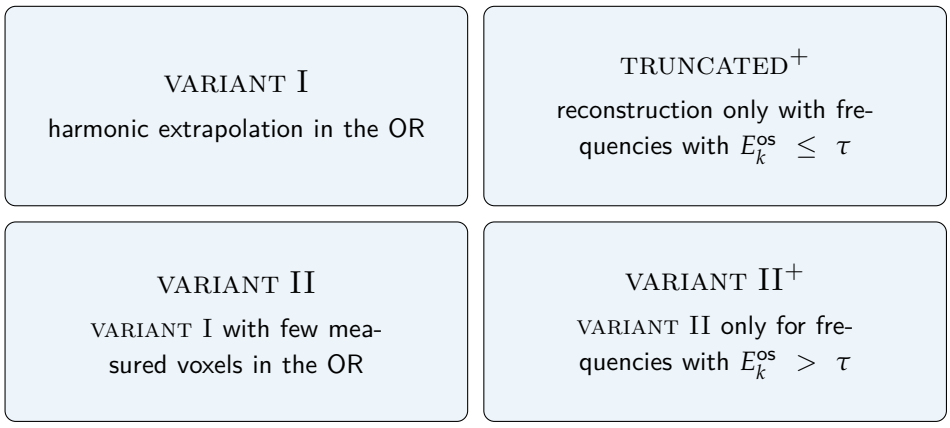

Figure 3.5: Summary of the four considered methods to reduce boundary artifacts.

3.3 Study Design

To analyze and verify the proposed methods on measured MPI data, we use a small 2D multi-patch configuration. We also show results on 3D data, by expanding the 2D setup in the third dimension. We use an artificial capillary-like phantom placed over the patch boundary in both cases.

3.3.1 Experimental 2D Setup

Consider two in the area of the FOV non-overlapping horizontally aligned patches as shown in Fig. 3.1. Both patches have a large overscan for a clear and artifact-free reconstruction as ground truth. The measurement was performed on the preclinical MPI system 25/20FF (Bruker Corporation, Ettlingen, Germany) with base frequency $f_B = 2.5\,\text{MHz}$ and measurement parameters given in Table 3.1.

Table 3.1: Measurement Parameters for 2D configuration.

excitation frequencies	$(f_B/102, f_B/96)$
gradient strength	$(-1, -1)\,\text{T m}^{-1}$
drive-field amplitude	$(12, 12)\,\text{mT}$
FOV	24x24 mm^2
composed FOV	24x48 mm^2
delta sample size	1x1 mm^2
grid	40×40 per patch
overscan	8 mm in each direction
acquisition time	~ 20 minutes per patch

For later reconstruction, we used a frequency selection $\Upsilon \subset I_K$ with a minimum cut-off frequency of 60 kHz and an SNR threshold of 5. The measured system matrices were truncated to the FOV and extrapolated by VARIANT I and VARIANT II. For the discrete 2D Laplace operator the classical 5-point stencil was used. The truncation to the FOV leads to an acquisition point reduction of 64 %. For VARIANT II, a total of 24 measured values in the OR were kept per patch: three lines with two data points placed equidistantly along each direction (as shown on the right side in Fig. 3.4). This results in an acquisition point reduction of 63 % for VARIANT II.

For evaluation of the methods on reconstructed images, we measured a phantom consisting of a seahorse-shaped capillary of 18 mm line length, 1 mm width and 5 mm height, filled with perimag (micromod Partikeltechnologie GmbH, Rostock, Germany) with an iron concentration of 10 mg/ml, placed over the patch intersection. The reconstruction problem was solved by a joint multi-patch approach [268] with 8 outer Kaczmarz iterations and a relative regularization parameter of $\lambda = 0.01$ using `MPIReco.jl` [152].

To show that a combination of CS and the described extrapolation methods is feasible, a DCT-based SM retrieval was performed on the FOV using optimal sparse sampling [105] on the FOV. In a second step the extrapolation to the OR was performed using VARIANT I and VARIANT II. Note that for VARIANT II 24 extra voxels in the OR are used. To achieve a fair comparison, the used sampling pattern was reduced by 24 voxels for this case.

3.3.2 Experimental 3D-Setup

To show the applicability of the proposed methods in three dimensions, we consider the 2D configuration in the xy-plane and expand it in z-direction. To reduce the calibration time of the full SMs, we cut the resolution in half. The measurement parameters are given in Table 3.2.

We used a frequency selection with a minimum cut-off frequency of 60 kHz and an SNR threshold of 10. For the discrete 3D Laplace operator a 7-point stencil was used. The

Table 3.2: Measurement Parameters for 3D configuration.

excitation frequencies	$(f_B/102, f_B/96, f_B/99)$
gradient strength	$(-1, -1, 2)\,\mathrm{T\,m^{-1}}$
drive-field amplitude	$(12, 12, 12)\,\mathrm{mT}$
FOV	24x24x12 mm^3
composed FOV	24x48x12 mm^3
delta sample size	2x2x2 mm^3
grid	$20 \times 20 \times 10$ per patch
overscan	$(8, 8, 4)\,\mathrm{mm}$
acquisition time	~ 2.25 hours per patch

truncation to the FOV in this 3D setup leads to an acquisition point reduction of 78 %. For VARIANT II, a total of 24 measured values in the OR were kept per patch: nine lines with two data points placed equidistantly along each direction. This equals an acquisition point reduction of 77 % for VARIANT II.

For analysis of reconstructed data, a straight capillary phantom of 20 mm length, 1 mm width and 5 mm height was used. The phantom was filled with perimag (iron concentration 10 mg/ml) and placed in the xy-plane, diagonally over the patch boundary. The reconstruction problem was solved by a joint multi-patch approach with 10 outer Kaczmarz iterations and a relative regularization parameter of $\lambda = 0.01$ using `MPIReco.jl` [152].

3.3.3 Computation

The extrapolation was performed in serial calculation on an AMD Ryzen PRO 7, using the iterative LSMR-solver based on the Golub-Kahan bidiagonalization [77]. The extrapolation for the 2D SMs fully truncated to the FOV takes less than 2 ms in serial calculation. For the fully truncated 3D SMs it takes about 30 s.

3.3.4 Error Measures

For a quantitative analysis of the results on system matrix level on the 2D data, we use the root mean squared error (RMSE) of the analyzed SMs (denoted as $\boldsymbol{S}_k^j \in \mathbb{C}^L$) compared to the original SMs (denoted as $\boldsymbol{S}_{\mathrm{OR},k}^j \in \mathbb{C}^L$) over all used frequency components $k \in \mathrm{Y}$ and both patches $j = 1, 2$:

$$\mathrm{RMSE} = \sum_{k \in \mathrm{Y}} \sum_{j=1}^{2} \frac{\left\| \boldsymbol{S}_k^j - \boldsymbol{S}_{\mathrm{OR},k}^j \right\|_2}{2|\mathrm{Y}|\sqrt{|\Omega_j|}}.$$

To quantify the reconstruction results, we consider the normalized root mean squared error (NRMSE) between the ground-truth reconstruction using the original SMs $\boldsymbol{c}_{\mathrm{OR}} \in \mathbb{R}_+^L$ and the reconstruction using the analyzed SMs $\boldsymbol{c} \in \mathbb{R}_+^L$:

$$\mathrm{NRMSE} = \frac{\|\boldsymbol{c} - \boldsymbol{c}_{\mathrm{OR}}\|_2}{\sqrt{L}(\max \boldsymbol{c}_{\mathrm{OR}} - \min \boldsymbol{c}_{\mathrm{OR}})}.$$

Since we are looking for artifact reduction, another important measure for quantitative analysis is the normalized maximum absolute error (NMaxAE), defined as

$$\text{NMaxAE} = \frac{\|\boldsymbol{c} - \boldsymbol{c}_{\text{OR}}\|_\infty}{\|\boldsymbol{c}_{\text{OR}}\|_\infty}.$$

3.4 Results

We use the data from the 2D experiments to examine the considerations from the methods section and show the proof of principle of the proposed methods. Results from the methods on the 3D data are used to show the usability in three dimensions.

3.4.1 2D

At first, let us investigate the continuation of signal from the FOV into the OR on the measured data. By considering spatial lines of 9 voxels from the border of the FOV into the OR in x- and y-direction for both patches (see Fig. 3.3) we collect the corresponding frequency vectors into eight matrices $\boldsymbol{S}^j_{\pm\xi}$ for $j \in \{1,2\}$ and $\xi \in \{x,y\}$. A part of the frequency vectors of every second voxel in $\boldsymbol{S}^1_{+x}$ (patch 1, positive x-direction) is exemplarily shown in Fig. 3.6. The real values of the frequency vectors in the overscan show a similar course, which mainly differs by a scaling factor. This indicates a strong linear dependence. Between the real values of the frequency vectors in the FOV more sign-changes are visible signifying a greater linear independence.

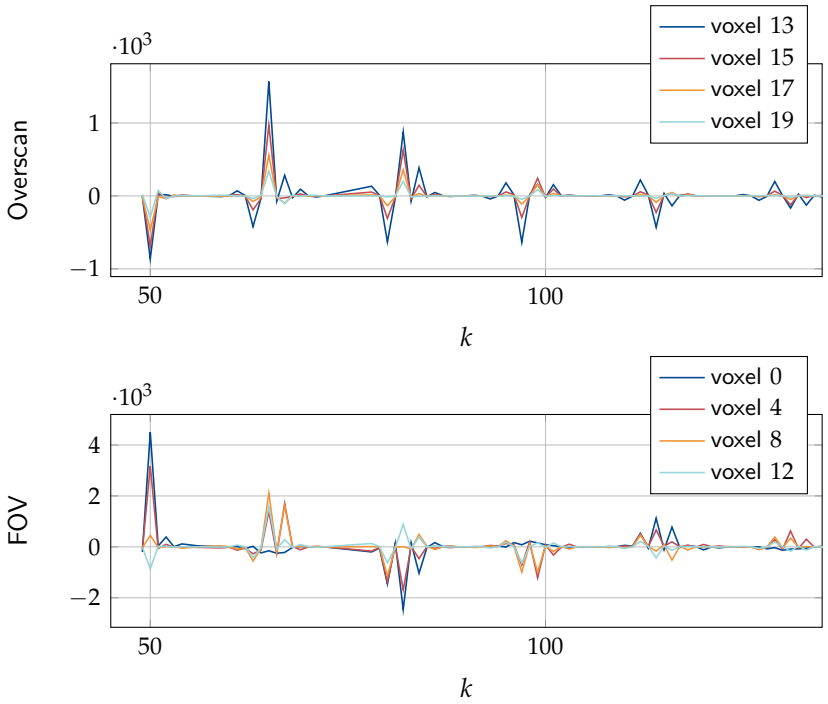

Figure 3.6: Real value of SM columns along the positive x-axis in the x-receive channel for the first eighty frequency components $k \in \Upsilon$ of the used frequency selection. Top: four equidistantly placed voxels in the overscan. Bottom: four equidistantly placed voxels in the FOV. Voxel 0 indicates the central voxel in the FOV, the other ones correspond to the respective positions along positive x-direction.

This can be verified by the calculation of the effective ranks and comparison to the full ranks of 9. The results are given in Table 3.3.

This can be verified by the calculation of the effective ranks and comparison to the full ranks of 9. The results are given in Table 3.3.

Table 3.3: Effective ranks of the matrices $S^{1/2}_{\pm\xi}$.

$j \backslash \xi$	-x	+x	-y	+y
1	2.93	2.92	2.63	2.69
2	3.15	2.78	2.79	2.79

For all eight matrices $\operatorname{erank}\left(S^j_{\pm\xi}\right) \ll \operatorname{rank}\left(S^j_{\pm\xi}\right) = 9$ is fulfilled. This shows, that there is high linear dependency between the frequency vectors along the considered lines of voxels. Therefore, it is meaningful to emulate the propagation of signal along those lines with harmonic extrapolation.

For the evaluation of the relative energy of the signal in the overscan, we calculate E^{os}_k for each frequency component $k \in \Upsilon$ and take the mean value of the values from both patches. As it can be seen in Fig. 3.7, frequencies with high E^{os}_k show up in a repeating pattern for both receive-channels.

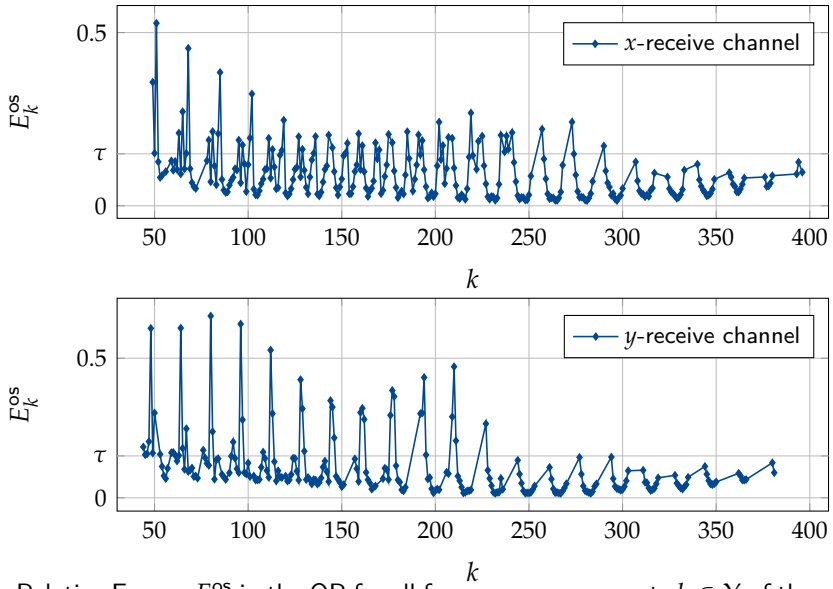

Figure 3.7: Relative Energy E^{os}_k in the OR for all frequency components $k \in \Upsilon$ of the used frequency selection.

Considering the frequency-components generating the first 5 peaks in Fig. 3.7, we find $k \in \{51, 68, 85, 102, 119\}$ in the x-receive channel and $k \in \{48, 64, 80, 96, 112\}$ in the y-receive channel. By considering the scanners frequency-ratio for a xy-excitation of $\frac{f_x}{f_y} = \frac{N^p-1}{N^p} = \frac{16}{17}$, we get the corresponding mixing factors $m_x = 0$ and $m_y \in \{3, 4, 5, 6, 7\}$ in the x-receive channel and $m_y = 0$ and $m_x \in \{3, 4, 5, 6, 7\}$ in the y-receive channel. Because one mixing factor is always zero, these frequencies have a high overall energy and a high SNR [221]. Therefore, leaving these frequencies out of the reconstruction (as done for the method TRUNCATED$^+$) may lead to less boundary artifacts, but also to a worse overall reconstruction result and must be handled with care. For the 2D reconstructions with the

reduced frequency selection TRUNCATED$^+$, as well as for method VARIANT II$^+$, we choose the threshold value $\tau = 0.15 \approx 0.25 \max_k E_k^{\text{os}}$.

For an exemplary qualitative analysis of the extrapolated SMs, we consider the frequency component $k = 68$ from the x-receive channel. As mentioned before, this is a frequency component with high E_k^{os} and therefore an appropriate extrapolation is important for a good reconstruction and more demanding in comparison to other frequency components with low E_k^{os}. In Fig. 3.8 it can be seen, that VARIANT I and VARIANT II are both able to continue the wave pattern correctly into the overscan.

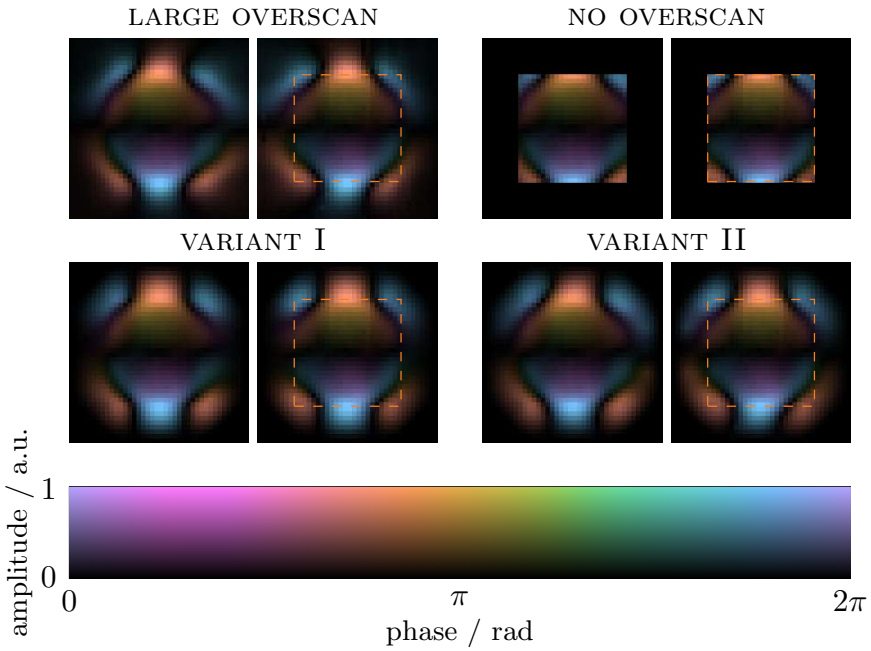

Figure 3.8: 2D system matrices of both patches for the 68th frequency component. The first row displays the original SMs (left) and the SMs truncated to the FOV (right). In the second row, the extrapolated SMs by VARIANT I (left) and VARIANT II (right) are shown. The orange dashed line exemplarily denotes the FOV in the right patch. The complex phase is color coded, the absolute value is given by the intensity, normalized to the maximum absolute value of the original SMs.

Considering the RMSE of the system matrices, we obtain

$$\text{RMSE}_{\text{TR}} = 35.5, \quad \text{RMSE}_{\text{vI}} = 20.6, \quad \text{RMSE}_{\text{vII}} = 15.5,$$

which equals an improvement of 42 % for VARIANT I and 56 % for VARIANT II compared to the RMSE of the truncated SMs.

For further analysis, the reconstructed images are compared. In Fig. 3.9, the reconstruction results for all considered methods are shown next to the reconstruction with the original SMs as ground truth and the reconstruction with the truncated SMs. All methods are able to significantly reduce the artifacts compared to the result with the truncated SMs. VARIANT II and VARIANT II$^+$ show the best results, whereby the result from the latter is less sharp. The reconstructions using VARIANT I as well as using TRUNCATED$^+$ still show some distortions on the patch boundary. Furthermore, the reconstruction using TRUNCATED$^+$ is slightly thinner in shape than the ground truth. Compared to the original reconstruction all reconstructions using the different methods show slightly enhanced noise in areas where no

signal is. However for all methods the noise is reduced compared to the reconstruction using the truncated SMs. Method VARIANT II achieves the least noisy result.

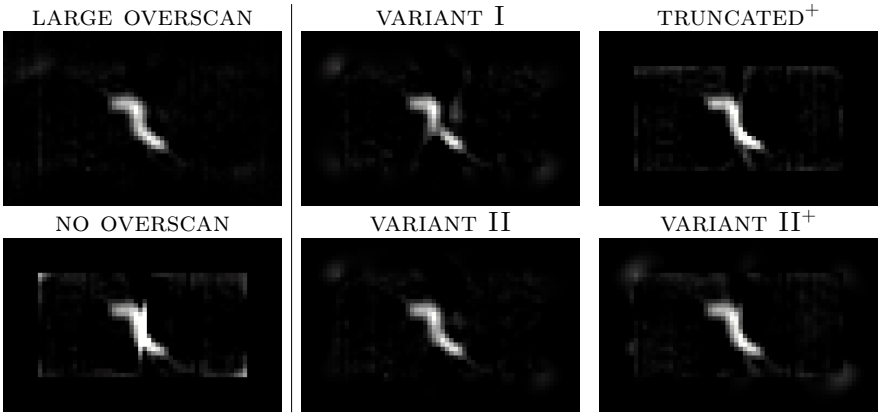

Figure 3.9: 2D reconstruction results of the different methods compared to the ground-truth reconstruction using the original SMs and the reconstruction with strong boundary artifacts using the truncated SMs (with no overscan). All reconstruction plots are normalized to the maximum value of the ground-truth reconstruction using the fully measured SMs (LARGE OVERSCAN).

The reconstruction results are quantitatively compared in Table 3.4 using the NRMSE and the NMaxAE. Note, that the improvements are calculated before the error values are rounded for better clarity.

Table 3.4: Error values for the 2D reconstruction results.

	TR	VI	VII	TR$^+$	VII$^+$
NRMSE	0.066	0.039	0.019	0.041	0.031
-impr.		41 %	71 %	39 %	54 %
NMaxAE	0.83	0.48	0.18	0.42	0.29
-impr.		42 %	78 %	49 %	66 %

Considering the error values in both measures, we can confirm that VARIANT II indeed gives the best results. VARIANT I also reduces the error significantly, but performs worse in comparison to VARIANT II. For the methods without or with less extrapolation, we find that TRUNCATED$^+$ also yields good results for the NMaxAE, which implies that strong artifacts get reduced efficiently. But the NRMSE gives a much worse result. Extrapolating the frequencies with high E_k^{os} by using VARIANT II$^+$ gives better results, especially considering the NRMSE.

Since VARIANT I could not fully resolve the artifacts, it is meaningful to gain a more detailed insight on how much overscan is needed to give artifact-free results using the plain extrapolation. We consider the results of the reconstruction using extrapolation on the sequence of step-by-step truncated SMs given in Fig. 3.10.

For the TRUNCATED reconstructions, first small artifacts on the patches boundary appear with a truncation of the SMs to an overscan of $i = 4$ lines of voxels. In comparison, the reconstructions using the simple extrapolation remain essentially artifact free up to $i = 2$. Significant artifacts start to appear for $i = 1$, which is just one remaining line of voxels as overscan.

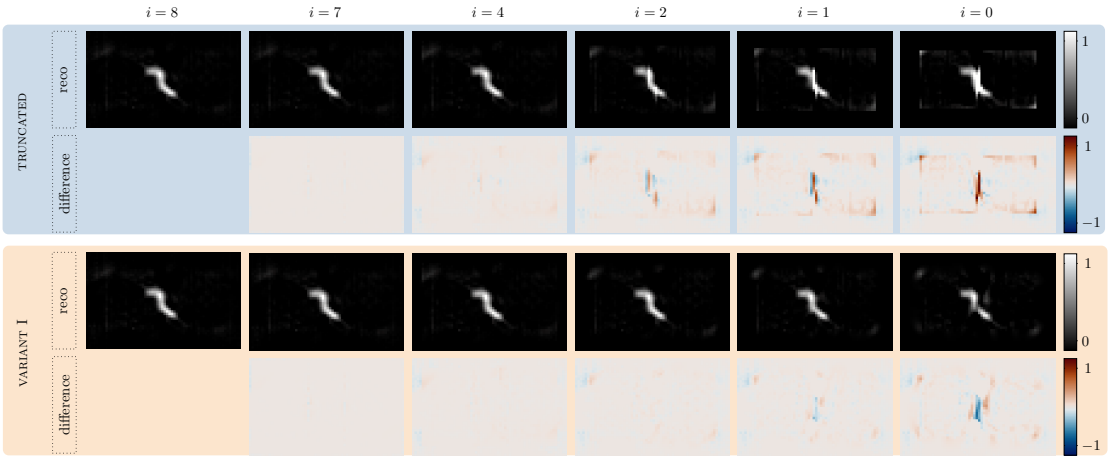

Figure 3.10: Comparison of reconstruction results for truncated system matrices with respect to truncated and extrapolated system matrices (using VARIANT I) for different truncation steps i and the difference to the full SM ($i = 8$) respectively. The reconstruction plots are normalized to the reconstruction with the full system matrix ($i = 8$), the difference plots are normalized to the maximum difference between reconstructions with full system matrices and with system matrices truncated to the FOV.

A comparison and combination of the extrapolation methods with matrix retrieval methods using DCT-based CS is shown in Fig. 3.11. Classical SM retrieval on the whole SM with optimal sparse sampling [105] on Ω and SM retrieval on the whole SM using optimal sparse sampling on the FOV and a zero padded OR are compared to a combination of CS and extrapolation. A rather moderate subsampling factor of $r = 6$, leading to $n = 264$ sampling points as well as a strong subsampling factor of $r = 12$ leading to $n = 132$ sampling points are shown. In both cases, CS on Ω is advantageous over CS with denser sampling in the FOV using a zero padded OR. The latter gives a less clear reconstruction result and artifacts at the patch boundaries. However, the combination of CS within the FOV and extrapolation within the OR gives even better results than classical CS on the whole SM. For $r = 6$ both extrapolation methods VARIANT I and VARIANT II in combination with CS give a clearer, less disturbed reconstruction result. For $r = 12$ the combined methods are able to reduce the boundary artifacts in comparison to regular CS on Ω and result in a better overal image quality.

A quantitative comparison of the CS-based reconstructions using the NRMSE is given in Table 3.5. One can see that the combined methods indeed give the best results. For subsampling factor $r = 6$ the error value of the combination of CS on the FOV and VARIANT II is very close to the NRMSE of the reconstruction using VARIANT II without subsampling with the FOV. The error value of the combination of CS on the FOV and VARIANT I is even better than the NRMSE using VARIANT I without sparse sampling. For the subsampling factor $r = 12$ the errors of all methods are higher and closer to each other.

Table 3.5: NRMSE for the cs-based reconstruction results using optimal sampling pattern.

	CS on Ω	CS on FOV	CS + vI	CS + vII
$r = 6$	0.039	0.052	0.032	0.023
$r = 12$	0.055	0.068	0.042	0.045

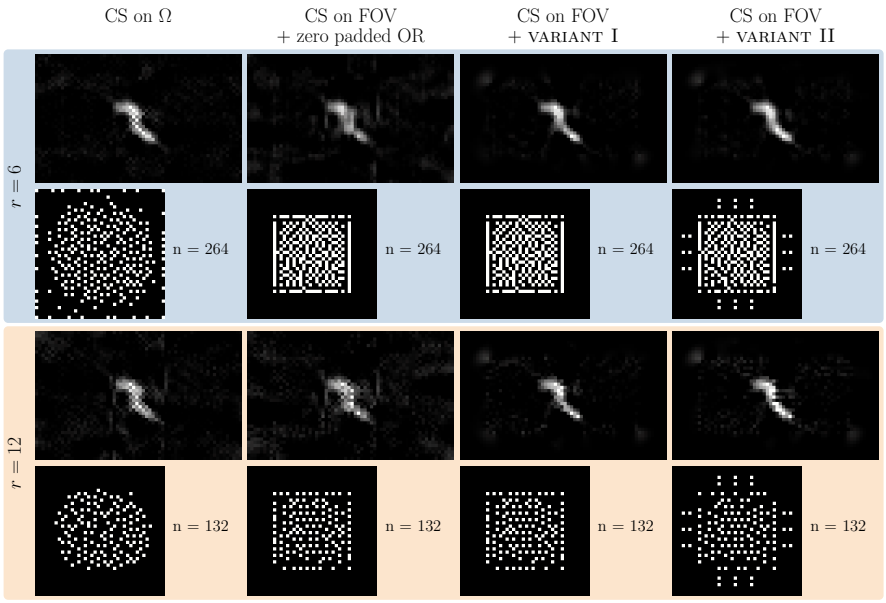

Figure 3.11: Comparison and combination of system matrix retrieval methods based on optimal sparse sampling with the proposed extrapolation methods. Given are the reconstruction results and the sampling patterns for a subsampling factor of $r = 6$ leading to $n = 264$ sampling points (first and second row) as well as for a subsampling factor of $r = 12$ leading to $n = 132$ sampling points (third and fourth row). Comparison of the methods from left to right: (1) CS on Ω using an optimal sampling pattern on Ω, (2) CS on the FOV and zero padded OR using an optimal sampling pattern on the FOV, (3) CS on the FOV, then extrapolation in OR using VARIANT I, (4) CS on the FOV, then extrapolation in OR using VARIANT II. All reconstruction results are normalized to the maximum value of the ground-truth reconstruction using the fully measured SMs.

3.4.2 3D

To present a proof of principle of the proposed methods also on 3D MPI data, we consider results on the introduced 3D-setup. In Fig. 3.12, the 2045th frequency component of the system matrix in the xy-plane on the 5th slice in z-direction is shown for both patches.

It becomes apparent, that both extrapolation variants continue the SMs phase information correctly in the overscan. In y-direction, where signal stretches up to the boundary of the large overscan, the absolute value decays much faster in the extrapolated overscan. Similar to the 2D case, VARIANT II yields a slightly better result.

To visualize the three dimensional reconstruction results, all values above a certain threshold of 0.1 are displayed in a volume plot in Fig. 3.13. Moreover, the corresponding central xy cross-sections are given as 2D heatmaps in the xy-plane.

The measured overscan of the SMs gives an artifact-free reconstruction as ground truth. Clearly visible artifacts arise along the patch boundary in the xy-planes in the reconstruction using the SMs without any overscan. In comparison, the extrapolation methods VARIANT I and VARIANT II are able to reduce the artifacts significantly. As in the 2D case, VARIANT II outperforms VARIANT I. For the methods with an altered frequency selection, a threshold of $\tau = 0.2 \approx 0.25 \max_k E_k^{\text{os}}$ was chosen. Method TRUNCATED$^+$ and method VARIANT II$^+$ also strongly reduce the boundary artifacts, but the reconstruction using TRUNCATED$^+$ has a slightly smaller volume (in width and height) with values above 0.1. The results of the

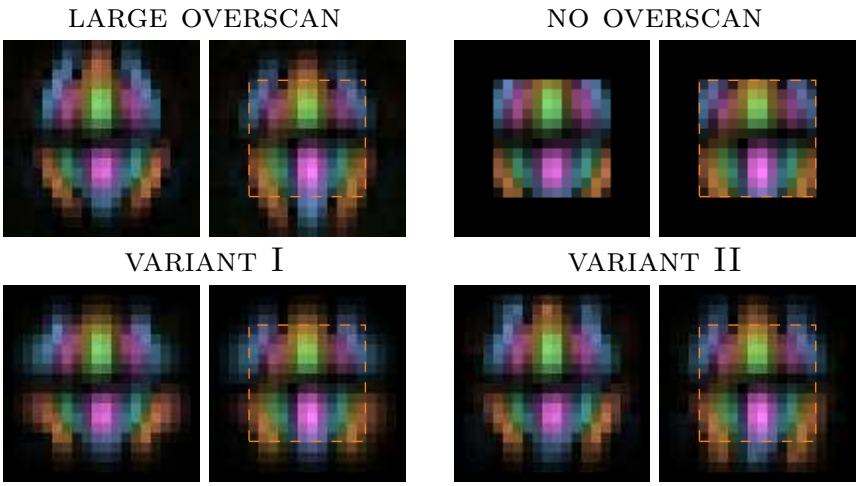

Figure 3.12: 3D system matrices for the 2045th frequency component. Displayed is the xy-plane on the 5th slice in z-direction. In the first row are the original SM (left) and the SM truncated to the FOV (right). In the second row, the extrapolated SM by VARIANT I (left) and VARIANT II (right) are shown. The complex phase is color coded, the absolute value is given by the intensity, normalized to the maximum absolute value of the original SMs. The colorbar is given in Fig. 3.8.

error analysis are summarized in Table 3.6. Again, the improvements are calculated before the error values are rounded for better clarity.

Table 3.6: Error values for the 3D reconstruction results.

	TR	VI	VII	TR^+	VII^+
NRMSE	0.043	0.020	0.015	0.030	0.018
-impr.		53 %	64 %	29 %	58 %
NMaxAE	0.61	0.35	0.32	0.38	0.32
-impr.		43 %	47 %	37 %	47 %

Considering the NRMSE, all methods show a similar error reduction as in the 2D case. The methods VARIANT I, VARIANT II and VARIANT II^+ show good results, whereas method TRUNCATED^+ performs worse. Taking into account the NMaxAE, the error of the reconstruction without overscan is not as high as on the 2D data. Thus, the relative improvements are not as high as before.

3.5 Discussion and Outlook

It was analytically reasoned and shown on measured 2D system matrices, that the signal in the OR is highly linear dependent on the signal inside the FOV. Thus, a continuation of signal into the overscan region by harmonic extrapolation is justified. The presented extrapolation methods are able to follow the wave pattern of the SMs correctly and can be used to decrease the calibration time and the consumption of persistent memory significantly, by simultaneously maintaining an artifact-free reconstruction result. If the system matrices are only acquired inside the FOV and a plain reconstruction gives strong boundary artifacts, an extrapolation using VARIANT I is not able to fully resolve the artifacts. As shown in Fig. 3.10, one or two additional lines of voxels as overscan are necessary. This would directly

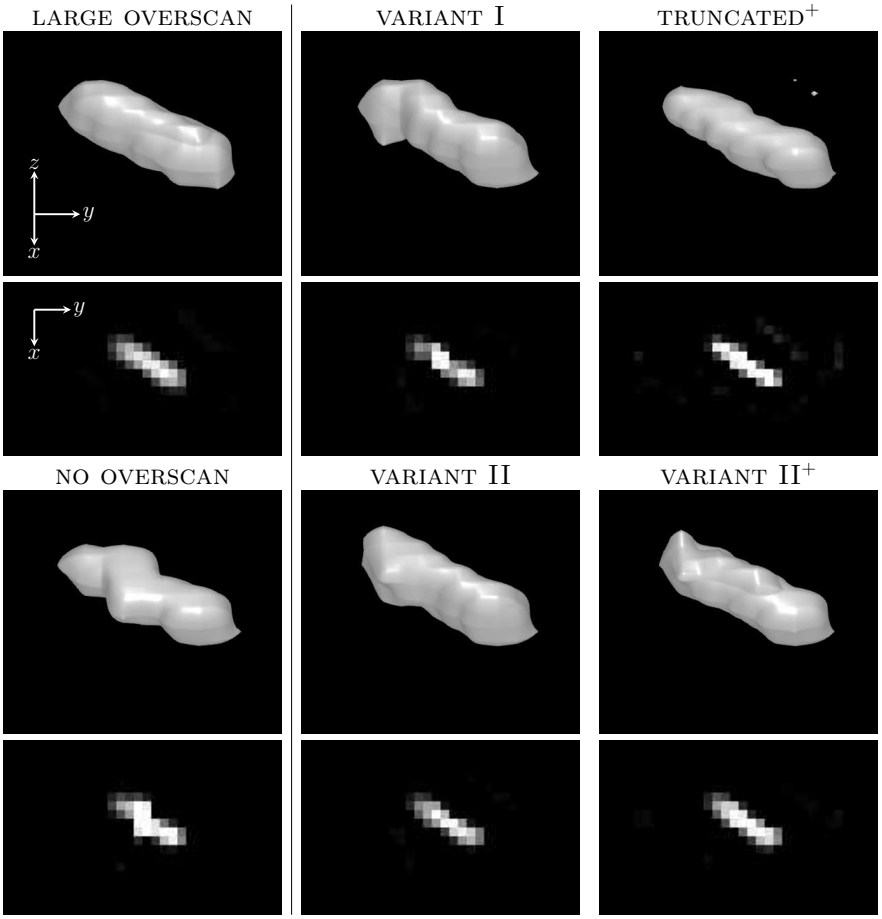

Figure 3.13: 3D reconstruction results of the different methods compared to the ground-truth reconstruction using the original SMs and the reconstruction using the truncated SMs. Displayed are all values larger than 0.1 as a 3D volume plot. Furthermore, the corresponding central xy cross-sections are shown below. All images are normalized to the maximum value of the ground-truth reconstruction using the fully measured SMs (LARGE OVERSCAN).

translate to significantly more calibration measurements. VARIANT II resolves this issue. Only the voxels in the FOV and a few equidistantly placed voxels in the OR need to be measured. On the provided 2D data, a nearly artifact-free reconstruction was achieved using 63 % less acquisition points, compared to the fully acquired SMs. The possible data reduction on 3D system matrices is even higher. On the investigated 3D configuration a reduction of 77 % of the acquisition points was achieved using VARIANT II. Since calibration time and consumption of persistent memory is linearly dependent on the amount of measured grid points, the reduction achievement directly translates to them. Concerning the placement of the additional voxels in the OR for VARIANT II we achieved good results with an equidistant distribution with at least two different distances to the FOV as shown in Fig. 3.4. However, there are probably even better sampling strategies, which need to be investigated in future work on this topic.

A simple reconstruction using only frequencies with low signal energy in the overscan region TRUNCATED+, can also reduce the boundary artifacts significantly, but gives a weaker and less clear reconstruction result. The reason is that the left-out frequencies have a high overall energy, good SNR and are therefore important for good reconstruction results. The

in-between method VARIANT II^+ is able to overcome this challenge by using all frequencies, although extrapolating only those with high signal energy in the overscan. Thus, the choice between VARIANT II and VARIANT II^+ is a trade-off between better performance (VARIANT II) and less computation time (VARIANT II^+). Since the values E_k^{os} – used to find the frequencies with low signal energy in the OR – are not known without measuring the overscan, the frequency choice for methods TRUNCATED$^+$ and VARIANT II^+ has to be made using the mixing factors. Our results show, that frequency components with one of the mixing factors equal to zero have the highest signal energy in the overscan.

In this work, a proof of concept is given for extrapolating system matrices in two and three dimensions. In practice, a major obstacle for large 3D multi-patch MPI measurements is the long calibration time and the consumption of persistent memory. Both can be lowered significantly with the proposed methods, since the extrapolation is a lot faster and can be performed right before the reconstruction. Furthermore, a patch-wise parallelization is easy to realize and speeds up the computation additionally.

The focus of the present work was mainly on regularly sampled system matrices (i.e. for VARIANT I). This implies that the method can also be applied retrospectively to already measured data. This is an important advantage over sparse sampling methods [105, 154, 124, 106], which can only be applied to future calibrations. However, we showed that extrapolation and sparse sampling can actually be combined and profit from each other. To this end, matrix retrieval was done based on an optimal sparse sampling pattern within the FOV in the first step and afterwards the extrapolation to the OR was applied. The restriction to the FOV in the first step allows to better exploit sparsity in a transform domain (e.g. the discrete cosine or the discrete Chebyshev functions domain), which has been shown in [245]. The combination of CS on the FOV with a following extrapolation gave superior results compared to classical CS on the whole SM as well as CS on the zero padded FOV using an optimal sparse sampling pattern in the FOV. Additional results using traditional random sampling patterns are given in Appendix 3.7.1.

We restricted the application of the extrapolation methods in this work to system matrices with almost no field distortions. For a possible application on large 3D configurations, this issue has to be considered, since the magnetic fields show strong imperfections in outer patches. It has to be assumed, that the provided methods will perform worse on such data, since the inhomogeneities lead to a distortion of the system matrices and a shifting of the FOVs [27, 29]. There are several possible solutions to solve this issue in future work on large multi-patch configurations. The obvious option is, to take the field distortions into account and use only the SMs acquired on the correct FOVs. However, it would be much more convenient to connect the SM extrapolation for large multi-patch configurations with SM warping. At first, the central patch could be measured in the FOV and extrapolated into a large overscan. Since the fields can be assumed to be homogeneous in the central patch, the extrapolation takes place on an undisturbed system matrix. In a second step, the SMs of the outer patches could be acquired following the methods proposed in [27]. The other direction may also be possible: warping the central FOV to all patches in a first step and using the correctly placed FOVs as the starting point for the extrapolation.

Another possible perturbation to the extrapolation is noise on the measured part of the system matrix. This could lead to errors in the extrapolation of frequencies with low SNR. On the other hand, it can be assumed that the harmonic extrapolation would smoothen noise in the OR. However, studies on the influence of SM-noise to the extrapolation remain for future work.

3.6 Conclusion

In conclusion we have investigated extrapolation methods for extending magnetic particle imaging system matrices into the overscan region. We proposed multiple variants, of which the first yields satisfying results and needs no additional measurements in the OR. The second method requires some additional measurements and can improve the accuracy further. The methods allow to substantially reduce calibration time, in particular in multi-patch MPI scenarios.

3.7 Appendix

3.7.1 Random Sampling

A comparison of the combined usage of CS and extrapolation with regular CS using a random sampling pattern is given in Fig. 3.14. As for the optimized sampling pattern, the combination of CS on the FOV using a random sampling pattern and extrapolation in the OR gives superior results at both considered sampling rates. The corresponding error values are given in Table 3.7.

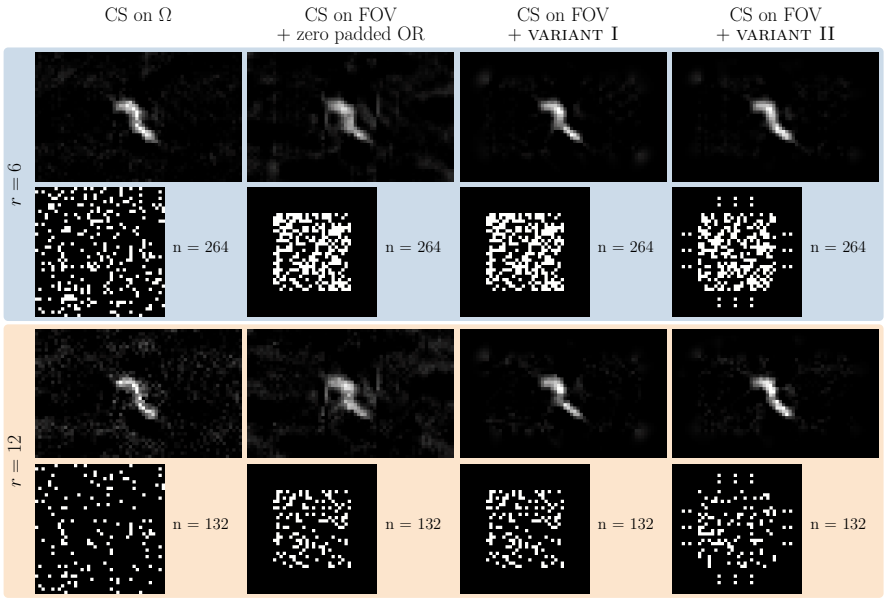

Figure 3.14: Combined use of system matrix retrieval based on random sparse sampling and extrapolation. Given are the reconstruction results and the sampling patterns for a subsampling factor of $r = 6$, leading to $n = 264$ sampling points (first and second row) as well as for a subsampling factor of $r = 12$, leading to $n = 132$ sampling points (third and fourth row). Comparison of the methods from left to right: (1) CS on Ω using a random sampling pattern on Ω, (2) CS on the FOV and zero padded OR using a random sampling pattern on the FOV, (3) CS on the FOV, then extrapolation in OR using VARIANT I, (4) CS on the FOV, then extrapolation in OR using VARIANT II. All reconstruction results are normalized to the maximum value of the ground-truth reconstruction using the fully measured SMs.

As for the optimized sampling pattern, the combination of CS in the FOV using a random sampling pattern and extrapolation in the OR gives superior results at both considered sampling rates. The corresponding error values are given in Table 3.7.

Table 3.7: NRMSE for the cs-based reconstruction results using random sampling pattern.

	CS on Ω	CS on FOV	CS + vI	CS + vII
$r = 6$	0.040	0.050	0.032	0.024
$r = 12$	0.084	0.066	0.039	0.037

3.7.2 Additional two object 2D Phantom

To show that the findings and conclusions of this work generalize to different phantoms, we show additional results in this appendix. The seahorse-shaped capillary was supplemented by a straight capillary phantom of 3 mm length to increase the complexity. The straight phantom partially juts out of the FOV. Thus, the reconstruction with the fully measured SMs is already slightly smeared out in this part, as can be seen in Fig. 3.15.

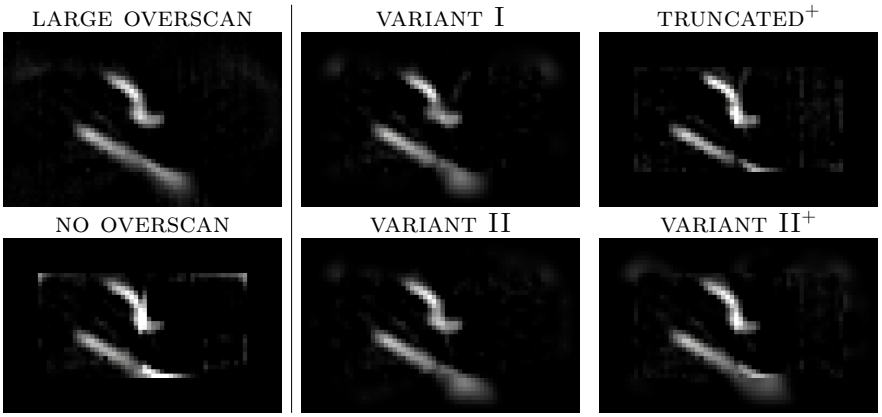

Figure 3.15: Reconstruction results of the different methods on the two object 2D data set. All reconstruction plots are normalized to the maximum value of the ground-truth reconstruction using the fully measured SMs LARGE OVERSCAN.

The reconstruction using the SMs truncated to the FOV has clearly visible boundary artifacts between the two patches on both objects. As expected from [305], the signal from the part of the straight phantom located outside of the FOV gets shifted to the border of the FOV. While the method TRUNCATED+ is able to reduce the boundary artifacts, it fails to reconstruct any data outside the FOV. The extrapolation methods show good results and reduce the boundary artifacts for both objects. Moreover, they prevent the signal shifting from the OR to the FOV and locate the signal of the straight phantom at the correct position in the OR. However, the reconstructed signal in the OR is more blurred compared to the original reconstruction using SMs with measured overscan.

Reconstruction results for this data using the combination of CS on the FOV with optimal sampling pattern and extrapolation in the OR are given in Fig. 3.16.

The results confirm that the combination of CS and extrapolation is powerful. Compared to CS using an optimal sampling pattern on Ω, the combination with extrapolation shows slightly worse results for the signal located outside the FOV for the moderate subsampling factor $r = 6$. For this case, higher sampling in the OR is beneficial. For the strong subsampling factor $r = 12$, the combination of CS on the FOV and extrapolation outperforms regular CS on Ω. This can be affirmed by looking at the NRMSE values compared to the reconstruction using the fully measured SMs in Table 3.8.

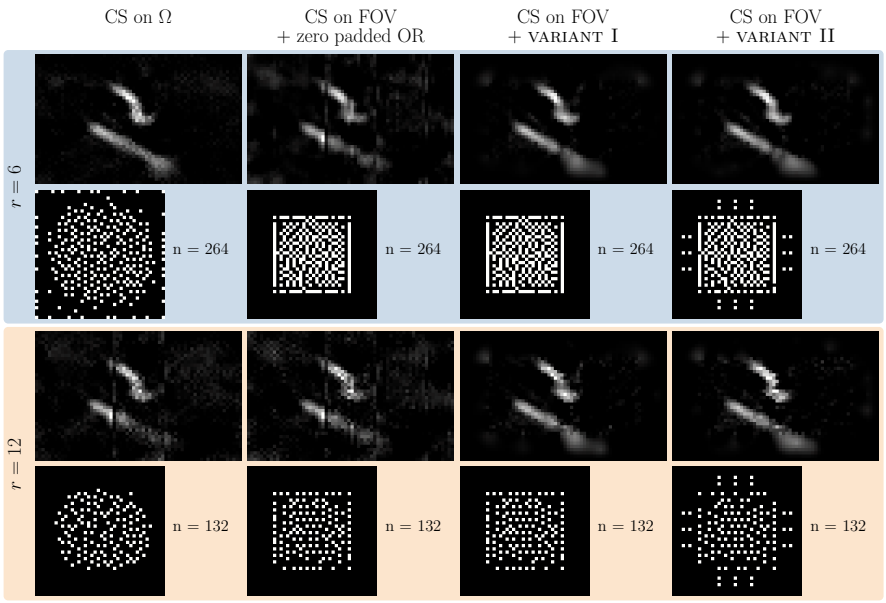

Figure 3.16: Reconstruction results and sampling patterns for the combined use of CS using optimal sampling patterns on the two object 2D data set. The figure setup is the same as for Fig 3.11.

Table 3.8: NRMSE results for the two object phantom

	TR	VI	VII	TR^+	VII^+
	0.085	0.040	0.027	0.069	0.038
		CS on Ω	CS on FOV	CS + VI	CS + VII
$r = 6$		0.035	0.069	0.041	0.034
$r = 12$		0.074	0.082	0.054	0.054

4

Handsfree MPI Reconstruction

K. Scheffler, M. Boberg, and T. Knopp, "Solving the MPI reconstruction problem with automatically tuned regularization parameters", Physics in Medicine & Biology, Vol. 69, 045024, February 2024.

Parts of this chapter have been presented at

International Workshop on Magnetic Particle Imaging 2023, Aachen, Germany.

Abstract

In the field of medical imaging, Magnetic Particle Imaging (MPI) poses a promising non-ionizing tomographic technique with high spatial and temporal resolution. In MPI, iterative solvers are used to reconstruct the particle distribution out of the measured voltage signal based on a system matrix. The amount of regularization needed to reconstruct an image of good quality differs from measurement to measurement, depending on the MPI system and the measurement settings. Finding the right choice for the three major parameters controlling the regularization is commonly done by hand and requires time and experience. In this work, we study the reduction to a single regularization parameter and propose a method that enables automatic reconstruction. The method is qualitatively and quantitatively validated on several MPI data sets showing promising results.

4.1 Introduction

Magnetic Particle Imaging (MPI) is a tomographic imaging technique with huge potential in non-invasive diagnostic imaging [87]. Using various magnetic fields, it directly measures the distribution of superparamagnetic tracer in a three-dimensional region of interest. The method is sensitive with respect to tracer concentration and enables imaging at a very high temporal and spatial resolution without ionizing radiation [87, 141]. After measuring a voltage signal in several receive coils, the particle distribution can be determined by solving an inverse problem based on a measured system matrix [141]. This system is commonly solved using a regularized least squares approach and an iterative solver [143]. Regularization is an important ingredient of this process, since it strongly influences the quality of the solution

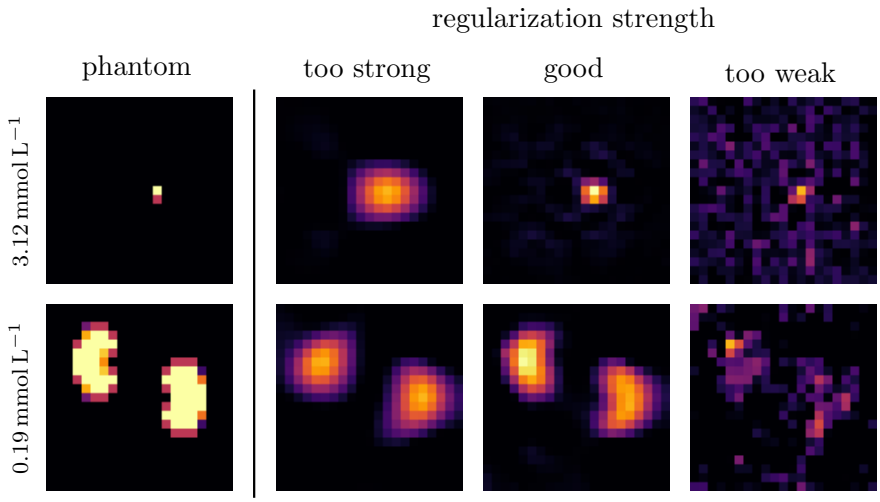

Figure 4.1: The amount of regularization strongly influences the quality of the reconstructed images in MPI.

(as it can be seen in Fig. 4.1). Using an iterative solver, the amount of regularization mainly depends on three parameters: the weighting of the regularization term itself, the frequency selection of the voltage signal and the number of total iterations [26]. For the reconstruction of a noisy measurement, the regularization needs to be strong. This is achieved by using only frequencies with good signal-to-noise ratio (SNR), a highly weighted regularization term and only few iterations. This comes at the cost of a lower resolution. For clear data, only a weak or no regularization at all is needed. Thus, the vast majority of frequency components should be used for a reconstruction with more iterations to ensure a sharp image. Generally speaking, the choice of these reconstruction parameters depends on the quality of the measurement itself, i.e., the scanner topology and the measurement settings, as well as on shape and iron concentration of the phantom. When considering time-dependent MPI data, e.g. the circulation of a tracer bolus through the cardiovascular system, the concentration may change over time. Thus, different parameters are needed for different stages of the bolus. Moreover, in the clinical context, there is a maximum iron dose for safe usage of superparamagnetic tracers in humans [258]. Thus, a high concentrated tracer circulating constantly through the body for a longer time period is not suitable. New concepts like negative contrast perfusion try to tackle this problem [191]. This underlines the importance of getting good reconstruction results on preferably low iron concentrations and thus the relevance of finding a good amount of regularization at each stage of a bolus.

Algorithms on the choice of regularization strength for general imaging inverse problems and especially magnetic resonance imaging are broadly studied in academic research. There are different strategies to emphasize: the classical methods based on the L-curve and the condition of the system [116, 166, 317], SURE-based methods [223], Bayesian approaches [232, 41] and learning-based methods [282]. However, all of these methods tackle only the regularization term and not the choice of the frequency selection. Up to now, only the L-curve approach has been adapted to MPI [145]. Considerations on an automatically chosen SNR threshold have been done for single sided MPI [298]. Furthermore, there has been proposed a more efficient frequency selection method based on the energy spectral density recently [322].

However, it remains a major challenge for each single MPI reconstruction to identify a good choice of parameters, leading to an ideal image. This is due to the complexity of the iterative solving process of the ill-posed inverse MPI reconstruction problem with different parameters not only controlling the regularization term but through the frequency selection also the system itself. The current state-of-the-art modus operandi is still trial-and-error as described in [307], requiring much experience in MPI reconstruction. In order to establish MPI in medical imaging and, in particular, taking into account medical feasibility, an easy reconstruction leading to good results would be most beneficial. The methods presented in [142] enable an online reconstruction for MPI, however all settings for the regularization must be done by hand.

Motivated from this practical point of view, we present a way to reduce the MPI reconstruction parameter set to a single parameter by adapting the SNR threshold and regularization weight in each iteration. Based on this, we propose a hands-free reconstruction method using a stopping criterion based on the quality of the data. A validation of the method is shown on various MPI data: dilution series with two different phantoms and an in vivo bolus experiment on the cardiovascular system of a mouse.

This paper is the full and extended version of our conference abstract (Scheffler et al., Hands-free reconstruction for MPI, IWMPI 2023). The method has been further developed and the focus has been broadened to include sound theoretical descriptions of the proposed methods. The evaluation of additional data, including in vivo data, and the careful discussion of the method are also substantial additions to this manuscript.

4.2 Methods

4.2.1 Basics of MPI image reconstruction

In MPI several magnetic fields are used to derive the three-dimensional density distribution of superparamagnetic iron-oxid particles (SPIOs) inside a region of interest. The particle magnetization gets excited using an excitation field, which is spatially homogeneous but sinusoidal in time. A spatial resolution is achieved by adding a time-constant spatial gradient field bringing the SPIOs in saturation everywhere but a small low-field region. The non-linear magnetization response of the SPIOs in the low-field region induces a voltage signal including higher harmonics of the excitation frequency in $L \in \{1,2,3\}$ receive coils. The connection between the frequency components (i.e. the coefficients of the Fourier series) of the voltage signal $u_k \in \mathbb{C}, k \in \mathbb{Z}$ and the particle concentration $c : \mathbb{R}^3 \to \mathbb{R}_+$ can be described by

$$u_k = \int_\Omega s_k(\boldsymbol{r}) c(\boldsymbol{r}) \, \mathrm{d}\boldsymbol{r},$$

where $s_k : \mathbb{R}^3 \to \mathbb{C}$ is the system function with support $\Omega \subset \mathbb{R}^3$. The system function is typically measured on a spatial grid with equidistantly placed grid-points $\boldsymbol{r}_n$ for $n \in I_N = \{1, ..., N\}$ by using a delta-probe. In combination with the discrete sampling of the voltage signal leading to a finite number of frequency components $k \in I_K = \{1, ..., K\}$, the discrete MPI equation can be given in matrix-vector form as

$$\boldsymbol{u}_{\text{meas}} = \boldsymbol{S}\boldsymbol{c}, \tag{4.1}$$

where $\boldsymbol{c} = (c(\boldsymbol{r}_n))_{n \in I_N}$ is the particle concentration vector, $\boldsymbol{S} = (w_n s_k(\boldsymbol{r}_n))_{k \in I_K, n \in I_N}$ is the system matrix with quadrature weights w_n and $\boldsymbol{u}_{\text{meas}} = (u_k)_{k \in I_K} + \boldsymbol{\eta}$ with $\boldsymbol{\eta} \in \mathbb{C}^K$ is the measured voltage vector with additive background noise. Solving (4.1) for the particle

concentration vector poses an ill-conditioned inverse problem, which is commonly adressed by formulating the Tikhonov regularized least squares problem

$$\boldsymbol{c}_\lambda \;=\; \underset{\boldsymbol{c}\in\mathbb{R}_+^N}{\operatorname{argmin}} \;\|\boldsymbol{S}\boldsymbol{c}-\boldsymbol{u}_{\mathsf{meas}}\|_2^2 \;+\; \lambda\,\|\boldsymbol{c}\|_2^2\,, \tag{4.2}$$

with the parameter $\lambda \in \mathbb{R}_+$ controlling the influence of the regularization term. Additional real and non-negativity constraints are beneficial [141, 306]. Using an iterative solver (e.g. the Kaczmarz method), one ends up with the reconstructed particle distribution.

In the course of the reconstruction in MPI, the regularization is controlled by three main parameters as described in [26]:

1. $\lambda \in \mathbb{R}_+$, controlling the strength of the regularization term in (4.2). Bigger values for λ lead to a stronger regularization.

2. The frequency selection, determined by a minimum frequency k_{min} and an SNR threshold $\Theta \in \mathbb{R}_+$, such that only frequency components in

$$I_{K_\Theta} = \{k \in I_K | k \geq k_{\mathsf{min}} \wedge \mathsf{SNR}_k > \Theta\}\,,$$

   where SNR_k denotes the SNR of frequency component k, are considered for reconstruction. By excluding noisy frequencies, a high threshold Θ leads to a small frequency selection and a weak noise amplification. Thus, the results get less noisy at the cost of loosing resolution. Due to the distribution of high-SNR frequencies around higher harmonics of the excitation frequency [269, 221], the connection between Θ and the number of rows in the linear system is not linear.

3. The number of iterations $\iota \in \mathbb{N}$ used by the iterative solver. Stopping the reconstruction early is equivalent to a further regularization and less noise amplification [72].

The minimum frequency is mainly for excluding frequencies close to the excitation frequency, which are hardly measured correctly due to hardware limitations [281, 277]. In the following, we will drop further considerations on the minimum frequency and consider the frequency selection only to be determined by the SNR threshold Θ. The effect of Θ to the system can be described using projections

$$\begin{aligned}\boldsymbol{P}_\Theta &: \mathbb{C}^K \to \mathbb{C}^{K_\Theta},\\ \tilde{\boldsymbol{P}}_\Theta &: \mathbb{C}^{K\times N} \to \mathbb{C}^{K_\Theta\times N}\end{aligned}$$

from K to K_Θ frequency components. Thus, we end up with the final reconstruction problem as

$$\mathsf{solve}_\iota\left(\underset{\boldsymbol{c}\in\mathbb{R}_+^N}{\operatorname{argmin}} \;\left\|\tilde{\boldsymbol{P}}_\Theta(\boldsymbol{S})\boldsymbol{c}-\boldsymbol{P}_\Theta(\boldsymbol{u}_{\mathsf{meas}})\right\|_2^2 \;+\; \lambda\;\|\boldsymbol{c}\|_2^2\right).$$

The regularization of this reconstruction process is described by the parameter set

$$\mathcal{P} \;:=\; (\lambda, \Theta, \iota)\,.$$

4.2.2 Projection to a single parameter

For the standard Kaczmarz reconstruction, the parameter set $\mathcal{P}$ is defined a priori and has to match the noise level of the used MPI scanner as well as the measurement settings. Important scanner-dependent factors are properties of the receive coils as well as the overall quality of the receive path, which includes the receive coils and all electronic components involved in voltage processing and digitization, e.g. a low-noise amplifier [301, 98]. Moreover, the amount and concentration of the tracer directly determines the SNR of the measurement and thus the amount of needed regularization. To achieve a reconstruction result of good quality without any user input, an appropriate parameter choice has to be derived automatically from the measurement data. To this end, the first goal is to condense $\mathcal{P}$ into a single parameter, i.e., mapping the regularization strength λ and the SNR threshold Θ to ι. Thus, in each iteration there are different but consistent values for λ and Θ. Starting with high values in the first iterations, these reconstruction steps only work on few high-SNR frequencies with a strong regularization. For measurements with low signal intensity, the reconstruction can already stop at this point to achieve an artifact-free image with low noise. For measurements with high signal intensity, more iterations with a higher amount of used frequencies and less regularization are needed. Thus, low values for Θ and λ are chosen for later iterations. The transition in between should be a steady and smooth decrease. These properties are satisfied by functions of the form

$$h_j(x) \;=\; \frac{\alpha_j}{1 \;+\; (\beta_j x \;-\; \beta_j)^{\gamma_j}},$$

for $1 \leq x \in \mathbb{R}$, $\alpha_j, \beta_j, \gamma_j \in \mathbb{R}_+$ and $j \in \{\Theta, \lambda\}$. Here, α_j controls the starting value in the first iteration, and β_j as well as γ_j control the behavior and slope of decrease for the transition of the parameters in later iterations. For h_Θ also a minimum SNR threshold $\Theta_{\text{min}} \in \mathbb{R}_+$ is needed, to exclude pure noise frequencies also for late iterations. It is important to note, that the values of $\alpha_\lambda, \alpha_\Theta$ and Θ_{min} are dependent on the total noise level and therefore on the receive path of the MPI scanner. Thus, it is sufficient to determine these parameters once for a certain receive path. Afterwards they can be used for all measurements using this receive path.

When altering the scanner hardware (e.g. changing the receive coil), an empty measurement $\boldsymbol{u}^f_{\text{empty}}$ over several frames $f \in \{1, \ldots, F_{\text{empty}}\}$, $F_{\text{empty}} \in \mathbb{N}$ can be used to calculate the mean noise $\bar{\eta}$ via

$$\begin{aligned}
\bar{\boldsymbol{u}}_{\text{empty}} &= \frac{1}{F_{\text{empty}}} \sum_{f=1}^{F_{\text{empty}}} \boldsymbol{u}^f_{\text{empty}}, \\
\boldsymbol{\eta} &= \frac{1}{F_{\text{empty}}} \sum_{f=1}^{F_{\text{empty}}} |\boldsymbol{u}^f_{\text{empty}} - \bar{\boldsymbol{u}}_{\text{empty}}|, \\
\bar{\eta} &= \frac{1}{K} \sum_{k \in I_K} \eta_k.
\end{aligned}$$

Then, the parameters $\alpha_\lambda, \alpha_\Theta$ and Θ_{min}, which depend on the noise level of the scanner, can be estimated by a scaling of $\bar{\eta}$. Since short empty measurements before each signal measurement are commonly done for background subtraction, auto-tuning the parameters from this empty measurement (as described in section 4.3) does not pose additional work.

4.2.3 Stopping criterion

After the described parameter projection, the number of iterations ι of the iterative solver remains to control the amount of regularization. For an automated reconstruction a suitable stopping criterion is needed. When the measurement is noisy, this stopping criterion should take effect already after few iterations. For less noisy measurements, less regularization is needed and the stopping criterion shouldn't take effect too early, allowing more iterations. Typical stopping criteria for iterative solvers are build upon the L-curve between the 2-norms of the residuum $\boldsymbol{r} = \boldsymbol{S}\boldsymbol{c} - \boldsymbol{u}_{\text{meas}}$ and $\boldsymbol{c}$. The usage of the regularized Kaczmarz method poses an advantage, since the auxiliary vector $\boldsymbol{v}_i \in \mathbb{C}^K$, calculated in each iteration step $i \in \mathbb{N}$, converges to the scaled residual $\boldsymbol{r}^\lambda = -\lambda^{-\frac{1}{2}}(\boldsymbol{S}\boldsymbol{c} - \boldsymbol{u}_{\text{meas}})$. In order to take into account the change in system size and regularization in each iteration, it is important to normalize $\boldsymbol{r}^\lambda$ with respect to the amount of considered frequencies in each iteration. Then, a stopping criterion based on a jump in the curvature $\Psi \in \mathbb{R}$ of the L-curve [145] can be used. It is meaningful that the curvature should exceed a certain level dependent on the size of the solution norm, to hinder the reconstruction from stopping too early. In conclusion, we end up with the following stopping criterion at iteration step $i \in \mathbb{N}$:

$$\frac{\Psi_i}{\|\boldsymbol{c}_1\|_2} > \delta \quad \wedge \quad \frac{\Psi_i}{\Psi_{i-1}} > \epsilon,$$

for $\delta, \epsilon \in \mathbb{R}_+$, where $\boldsymbol{c}_1$ is the particle concentration vector after the first iteration. The values for δ and ϵ describe the lower thresholds for curvature and change of curvature at which the stopping criterion takes effect.

4.2.4 Bolus reconstructions

Because of the high frame rate of typical MPI measurements, it can be assumed, that the tracer concentration does not change abruptly between two frames of time-dependent MPI data, e.g. bolus experiments. Thus, the number of iterations of the hands-free reconstruction should also not change too rapidly between two frames. To exploit this additional form of prior knowledge and enforce this behavior, we propose the following two-step flattening approach.

1. The number of iterations is not only dependent on the stopping criterion but also on the number of iterations of the previous frames. This value defines for each frame $f \in \mathbb{N}$ a number of iterations to be expected $\iota_f^{\text{exp}} \in \mathbb{N}$. The actual number of iterations must not exceed a certain margin

$$\bar{B}_\xi(\iota_f^{\text{exp}}) := \left[\xi \iota_f^{\text{exp}}, (1 + \frac{1}{\xi})\iota_f^{\text{exp}}\right], \ \xi \in (0,1),$$

   around the expected number ι_f^{exp}. When the stopping criterion is triggered before the margin around the expected number of iterations, more iterations are performed until this margin is reached. When the stopping criterion is not triggered as the highest number of iterations in the margin is reached, the reconstruction stops at this point. The margin should be big enough to allow a gradually adjustment of the number of iterations over the course of the frames, but low enough to hinder the number of iterations to jump back and forth.

2. After a first reconstruction using the stopping criterion as well as the additional constraints of step (i), a second reconstruction is performed to handle remaining peaks.

In this second round, the number of iterations over the course of the frames gets smoothed using a rolling average of the number of iterations from the first step (i).

4.2.5 Grid search reconstruction

For validation of the proposed method, a quantitative comparison to a reference solution is needed next to subjective statements on the reconstructed images. To this end, a three-dimensional parameter grid $\mathcal{P}_{l_1,l_2,l_3} := (\lambda_{l_1}, \Theta_{l_2}, \iota_{l_3})_{l_1,l_2,l_3 \in \{1,\dots,8\}}$ is introduced. Note that as mentioned before, the connection between the parameter values and the amount of regularization is non-linear. To span over a wide enough space of regularization strength, the parameter grid needs to have higher order exponential spacing in each component. A costly brute-force approach with 8^3 reconstructions is used to find the optimal parameter sets compared to a ground-truth phantom in two different measures. The normalized root mean squared error (NRMSE) was chosen because of its establishment and interpretability. Because the NRMSE does have issues when it comes to noise, we also consider the structural similarity index measure (SSIM) as a perception based measure [304]. For both measures, the reconstruction results get normalized to the interval $[0, 1]$. We ranked all reconstructions from the parameter grid in both measures, respectively. The reference reconstruction is then chosen as the reconstruction with the parameter set with the lowest additive rank over both measures.

4.3 Study Design

The proposed hands-free reconstruction was implemented by adapting the regularized Kaczmarz method from the MPIReco.jl framework in Julia [153]. The general structure of the reconstruction is given as pseudo code in Algorithm 1. Here, dcdr_i is the approximate derivative of the solution norm at the iteration $i \in \mathbb{N}_0$ as an intermediate step to calculate the approximate curvature Ψ_i. We suggest a zero-initialization for the initial values. The function getParameter() calculates λ_i and Θ_i at iteration $i \in \mathbb{N}$ by using the mapping functions h_λ and h_Θ. The full code is published under a Creative Commons Attribution 4.0 International license and can be found at `https://github.com/IBIResearch/HandsfreeReco`.

To verify the method on a broad variety of MPI data with different iron concentrations, it was tested on the dilution series described in [26]. Moreover, the bolus study describing the blood-flow of a mouse heart from [97] was used to test the hands-free reconstruction on in vivo data. All studies have been performed on the preclinical MPI system 25/20FF (Bruker Corporation, Ettlingen, Germany), however the bolus experiment used a dedicated receive coil with better SNR. Based on experience on MPI reconstruction with the Kaczmarz method, the parameters describing the slope of the mapping functions were chosen as $\beta_\lambda = 0.2, \gamma_\lambda = 5$ and $\beta_\Theta = 0.28, \gamma_\Theta = 2$. The remaining parameters dependent on the noise level of the receive path, were calculated from the mean noise of the data sets $\bar{\eta}$ (derived from empty measurements, as described in 4.2.2), such that they work for all data sets on all concentrations:

$$\alpha_\lambda = \frac{1}{5 \cdot 10^{-5}\ \bar{\eta}},\ \alpha_\Theta = 1.2 \cdot 10^{-2}\ \bar{\eta},\ \Theta_{\text{min}} = 3.1 \cdot 10^{-4}\ \bar{\eta}.$$

The resulting mapping functions are shown in Fig. 4.2. The parameters for the stopping criterion were set to $\delta = \frac{1}{4}, \epsilon = 2$.

Algorithm 1 Hands-free reconstruction

Input: $S, \boldsymbol{u}_{\text{meas}}, \alpha_{\lambda/\Theta}, \beta_{\lambda/\Theta}, \gamma_{\lambda/\Theta}, \delta, \epsilon$
  $i \leftarrow 0$
  $\boldsymbol{c}_0, r_0, \text{dcdr}_0, \Psi_0, \text{dcdr}_1, \Psi_1 \leftarrow$ getInitialValues()
  repeat
    $i \mathrel{+}= 1$
    $\lambda_i, \Theta_i \leftarrow$ getParameter$(\alpha_{\lambda/\Theta}, \beta_{\lambda/\Theta}, \gamma_{\lambda/\Theta})$
    $I_{K_{\Theta_i}} \leftarrow$ getFrequencySelection(Θ_i)
    $\boldsymbol{c}_i, \boldsymbol{v}_i \leftarrow$ performKaczmarzIter$(S, \boldsymbol{u}_{\text{meas}}, I_{K_{\Theta_i}}, \lambda_i)$
    $r_i \leftarrow \|-\lambda_i^{1/2} \boldsymbol{v}_i\|_2$
    if $i > 1$ **then**
      $\text{dcdr}_i \leftarrow (\|\boldsymbol{c}_i\|_2 - \|\boldsymbol{c}_{i-1}\|_2)/(r_i - r_{i-1})$
      $\Psi_i \leftarrow (\text{dcdr}_i - \text{dcdr}_{i-1})/\left((r_i - r_{i-1})(1+\text{dcdr}_i^2)^{3/2}\right)$
      stopIter $\leftarrow \Psi_i/\|\boldsymbol{c}_1\|_2 > \delta$ **and** $\Psi_i/\Psi_{i-1} > \epsilon$
    end if
  until stopIter
  return $\boldsymbol{c}_i$

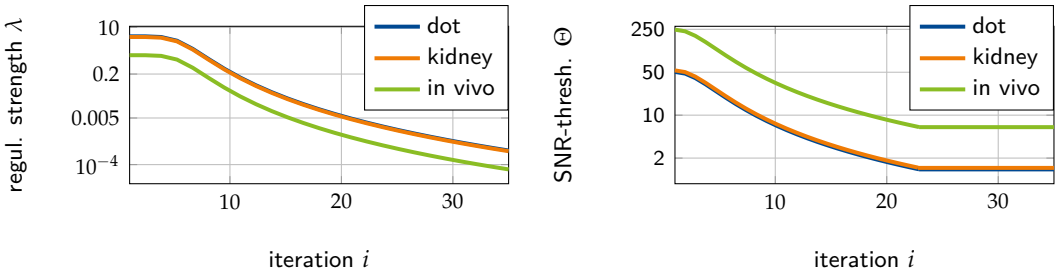

Figure 4.2: Mapping functions for the parameter condensation on the different data sets (calculated from the mean noise which is derived from empty measurements). The left image shows the course of the regularization pre-factor λ over the iterations, the right image the course of the SNR threshold Θ. Note, that the y-axes are logarithmic.

4.3.1 Dilution series

The dilution series is taken from [26] and was recorded using a three dimensional Lissajous trajectory and a gradient strength of $(-0.75, -0.75, 1.5)$ T m^{-1}. The drive-field amplitudes were set to 12 mT in each direction, resulting in a FOV of 32x32x16 mm^3. The system matrices were measured using a 2x2x1 mm^3 delta-sample filled with perimag (micromod Partikeltechnologie GmbH, Rostock, Germany) diluted to 300 mmol l^{-1} on a 21x21x24 grid.

The single dot phantom series consists of 12 measurements where the iron concentration is halved for each new measurement starting with $\kappa_1^{\text{dot}} = 400$ mmol l^{-1} in a small glass capillary with an inner diameter of 2.4 mm. The dot phantom was only filled with a small amount (20 µL) of tracer. Furthermore, we consider the dilution series on the rat kidney phantom. Two kidneys from a realistic rat phantom [66] are each filled with 781 µL tracer. The iron concentration is halved 5 times, starting with $\kappa_1^{\text{kidney}} = 3.05$ mmol l^{-1}.

For the reference reconstruction as well as the error analysis a ground truth was voxelized out of the CAD files of the dot phantom and the kidney phantom. The 8^3 sized parameter

grid for the reference reconstruction was derived proportional to higher order exponential functions giving

$$\begin{aligned}\lambda_{l_1} &\in \{1.4 \cdot 10^{-4}, 8.8 \cdot 10^{-4}, 4.5 \cdot 10^{-3}, 2 \cdot 10^{-2}, 7.6 \cdot 10^{-2}, 0.28, 1.1, 7.3\},\\ \Theta_{l_2} &\in \{1.32, 1.64, 2.24, 3.4, 5.88, 11.71, 27.33, 76\},\\ \iota_{l_3} &\in \{1, 2, 3, 5, 7, 11, 16, 25\}.\end{aligned}$$

The grid searches were performed in parallel on 8 kernels and took about 6 to 8 hours for each concentration on both phantoms resulting in a total net reconstruction time of about 5.25 days.

4.3.2 In vivo bolus experiment

In addition to phantom measurements we consider the in vivo measurements from [97], which were measured with a dedicated high-sensitivity receive chain that shows a very different frequency response and noise characteristic than the standard receive coils used in the previous phantom experiments. The measurements were performed using a finer system matrix dedicated to the fine structures in the cardiovascular system of a mouse. The cylindrical delta probe had a diameter as well as a height of 0.7 mm, filled with undiluted LS-008 ([134], 91.7 mmol l^{-1}). The system matrix was measured on a 46x36x19 grid. The measurement of the mouse itself used three separate boli of LS-008, sequentially injected into the tail vain. In this work, we only consider the second bolus with a volume of 10 µL concentrated at 9.17 mmol l^{-1}. The concentration strongly changes in the course of the bolus throughout the cardiovascular system of the mouse. Thus, different regularization strength in different stages of the bolus are needed for good image reconstruction. The measurement was performed on a 32x32x16 mm^3 sized FOV covering the mouse heart and took 21.54 ms per frame, resulting in a temporal resolution of 46 Hz. For evaluation we consider a passage of the measurement over 115 frames in total.

No averaging on the data was performed to preserve the temporal resolution. This leads to a stronger influence of noise and thus may lead to an erratic number of iterations in the course of the frames. Since we know, that the bolus does only need a gradually changing strength of regularization, we want to enforce a smooth transition in the reconstruction results between the frames. To this end, the number of iterations of the previous frames is also considered next to the plain stopping criterion. Let $\iota_f \in \mathbb{N}$ be the number of iterations of the hands-free reconstruction at frame $f \in \{4, ..., 115\}$. To get the number of expected iterations for ι_f, we weight the latest numbers of iterations via

$$\iota_f^{\text{exp}} = \frac{1}{10}\iota_{f-3} + \frac{3}{10}\iota_{f-2} + \frac{6}{10}\iota_{f-1}.$$

Then, the number of iterations ι_f for each frame is restricted to fulfill

$$\iota_f \in \bar{B}_{1/2}(\iota_f^{\text{exp}}) = \left[\frac{1}{2}\iota_f^{\text{exp}}, \frac{3}{2}\iota_f^{\text{exp}}\right]. \tag{4.3}$$

This rather large margin enables the algorithm to easily adjust the number of iterations over the course of the frames, but still allows large jumps in the number of iterations between two frames. Therefore, the course of the number of iterations over the frames is further smoothed in a second reconstruction step, by using a rolling average. In other words, we set the maximum number of iterations for each frame in the second step as the average of the

two previous and two subsequent frames from the first round. The result of this two-step flattening is exemplarily shown in Fig. 4.3.

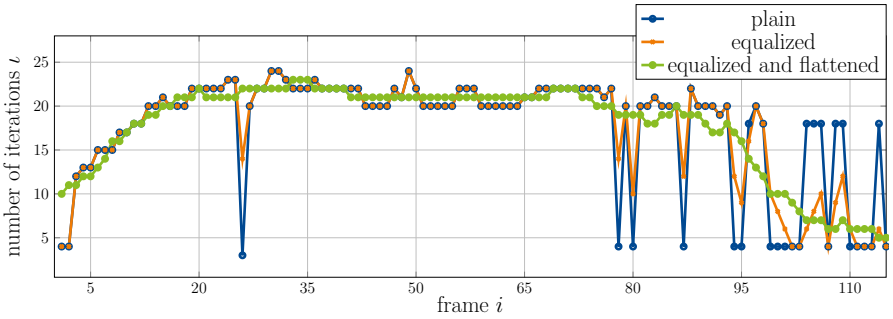

Figure 4.3: Enforcing a smooth transition between the frames of the in vivo data using the hands-free method is done by a two-step flattening. The number of iterations from the plain stopping criterion is shown in blue, the restriction by an equalization following (4.3) is shown in orange and the final flattened course is shown in green.

For anatomical reference, the reconstructed MPI data is overlayed on magnetic resonance imaging (MRI) data that was acquired with an isotropic gradient echo sequence using the preclinical 7 T device BioSpec 70/30 (Bruker Corporation, Ettlingen, Germany) as described in [97].

4.4 Results

4.4.1 Dot phantom

The reconstruction results of the dilution series with the dot phantom are shown in Fig. 4.4. On the left side (framed by the blue box), the reconstructions using the parameter projection are given, with different values for ι as the only remaining parameter. It can be seen over the course of the dilution series, that the optimal number of iterations strongly differs with the concentration. For high concentrations, the best results are achieved after many iterations ($\iota = 22$). Over the course of decreasing concentrations, the result after too many iterations (with the corresponding low regularization strength) starts to get noisy. Thus the best results are achieved after a decreasing number of iterations. Eventually, for the lowest concentrations, the best results are obtained after only one to three iterations.

The stopping criterion is triggered in a similar manner over the course of decreasing concentrations. Starting with 24 iterations for the highest concentration, the hands-free method stops after fewer iterations for each further dilution step. For the lowest concentrations, the method stops after 2 iterations. A comparison to the reference reconstruction resulting from the grid search is shown on the right side of Fig. 4.4. By using the grid search regularization parameters we are able to produce even sharper images, however, this comes with slightly enhanced noise. All grid search parameters are given in Table 4.1 next to the resulting NRMSD and SSIM values compared to the voxelized phantom.

Considering the NRMSD results of the hands-free method, the lowest error values are achieved for the highest concentrations and are very close to the NRSMD values of the grid search reconstruction. Over the course of decreasing concentrations, the NRMSD values get worse and are significantly higher than the NRMSD values of the reference images resulting from the grid search. For the lowest concentrations the NRMSD values corresponding to hands-free method and grid search are closer to each other again. The SSIM

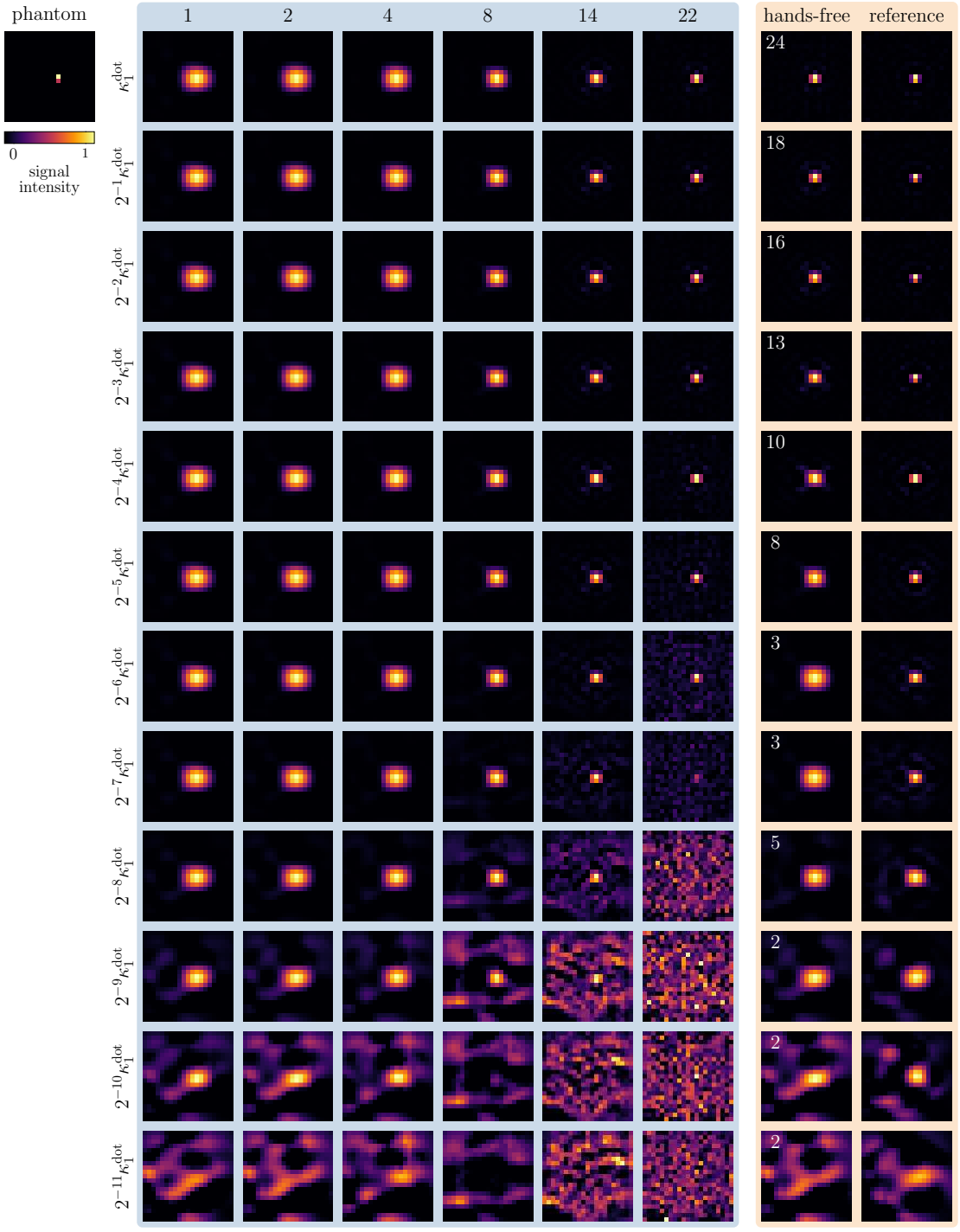

Figure 4.4: Reconstruction results for the dot phantom at each concentration ($\kappa_1^{\mathrm{dot}} = 400\,\mathrm{mmol\,l^{-1}}$) in the xy-plane with a maximum projection on the central slices in z-direction. On the left side (blue box), the reconstructions resulting from the parameter projection with various number of iterations are shown. On the right side (yellow box), the hands-free reconstruction (the number of total iterations dedicated by the stopping criterion is superposed) and the reconstructions with an optimal parameter set resulting from the grid search are shown. All results are normalized to the range $[0, 1]$, the colorbar is given next to the phantom.

Table 4.1: Error results for the dot phantom

κ_1^{dot}	hands-free			grid search		
	NRMSD	SSIM	iter.	NRMSD	SSIM	$\mathcal{P} = (\lambda, \Theta, \iota)$
400	0.014	0.874	24	0.011	0.928	(0.00014, 3.4, 25)
200	0.015	0.917	18	0.010	0.930	(0.00014, 3.4, 25)
100	0.017	0.918	16	0.011	0.918	(0.00014, 3.4, 25)
50	0.021	0.899	13	0.011	0.879	(0.00088, 3.4, 25)
25	0.029	0.872	10	0.017	0.824	(0.0045, 3.4, 3)
12.5	0.037	0.839	8	0.017	0.820	(0.0045, 3.4, 1)
6.25	0.057	0.770	3	0.021	0.797	(0.076, 3.4, 1)
3.13	0.058	0.727	3	0.024	0.657	(0.076, 5.9, 1)
1.56	0.056	0.441	5	0.042	0.556	(0.28, 27.3, 1)
0.78	0.077	0.262	2	0.068	0.335	(1.1, 76, 1)
0.39	0.150	0.098	2	0.101	0.164	(1.1, 76, 1)
0.2	0.189	0.073	2	0.164	0.109	(7.3, 76, 1)

value of both methods are similar to each other for all concentrations. On the intermediate concentrations, the SSIM values of the hands-free method are – in contrast to the NRMSD results – even higher than the SSIM values from the reconstruction resultung from the grid search.

4.4.2 Kidney phantom

The reconstruction results of the kidney phantom from the hands-free method as well as the results of the grid search are shown in Fig. 4.5. Similar to the dot-phantom, the stopping criterion is triggered at earlier iterations for lower concentrations.

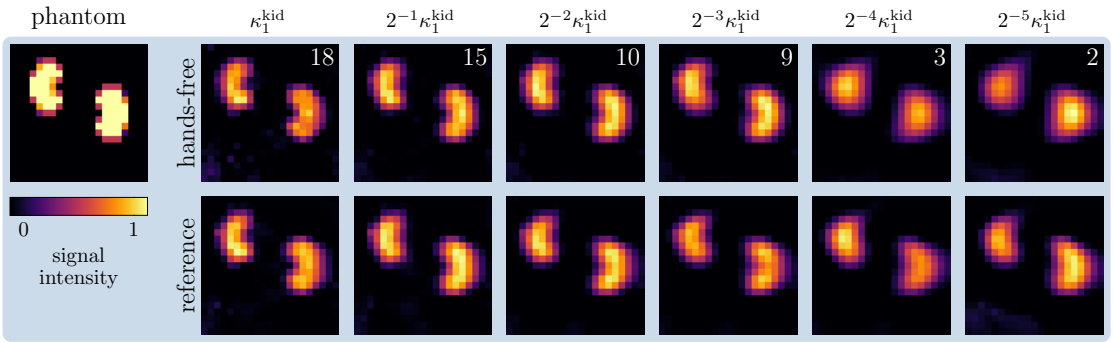

Figure 4.5: Reconstruction results for the kidney phantom. Shown are the hands-free method (top, the number of total iterations dedicated by the stopping criterion is superposed) and the optimal parameter set resulting from the grid search (bottom) for each concentration ($\kappa_1^{\text{kid}} = 3.05\,\text{mmol}\,\text{l}^{-1}$) in the xy-plane on slice 10 in z-direction. All results are normalized to the range $[0, 1]$, the colorbar is given next to the phantom.

Table 4.2: Error results for the kidney phantom

c^{kid}	hands-free			grid search		
	NRMSD	SSIM	iter.	NRMSD	SSIM	$\mathcal{P} = (\lambda, \Theta, \iota)$
3.05	0.085	0.564	18	0.080	0.619	(0.076, 2.2, 2)
1.52	0.080	0.629	15	0.079	0.601	(0.28, 2.2, 2)
0.76	0.084	0.670	10	0.086	0.666	(0.28, 5.9, 1)
0.38	0.083	0.674	9	0.088	0.688	(0.28, 11.7, 1)
0.19	0.100	0.578	3	0.097	0.613	(1.12, 11.7, 1)
0.1	0.103	0.503	2	0.097	0.530	(1.12, 11.7, 1)

In comparison to the reference image resulting from the regularization parameter set from the grid search (as given in Table 4.2), the results from the hands-free method are qualitatively similar for each iteration.

This is confirmed when considering the NRMSD as well as the SSIM of both methods in Table 4.2. The deviations to the voxelized phantom is close between both methods in both measures over all concentrations.

4.4.3 In vivo bolus

For the evaluation of the hands-free method on the in vivo bolus, we consider Fig. 4.6. Shown is the hands-free reconstruction result column-wise compared to reconstructions using a strong and a weak regularization constantly over all frames. The bolus is displayed row-wise for 8 frames with equidistant time difference of 0.32 s in a single xz-slice. The total time distance between the first and the last shown frame is 2.25 s.

By laying the reconstructed MPI signal on top of the corresponding MRI data, the flow of the bolus through the mouse can be followed. We expect to see the bolus entering the vena cava inferior in the first frames and evolve to the heart by entering the right atrium. Following the results of [97], the bolus will then fill the right ventricle and lung. However, since we show only the slice, where the vena cava and the right atrium are visible, we expect the MPI signal to vanish.

We see that the strong regularized solution lacks of accuracy in the first frames (frames 5, 20, and 35), when the bolus enters the vena cava and flows to the atrium at high concentration. When the bolus gets weaker at later frames, its position is still identifiable but the reconstructed signal is very weak.

In contrast, the solution using weak regularization has high accuracy but also shows large artifacts and noise. For later frames, the bolus is even not distinguishable from the noise anymore.

The hands-free method is able to adapt the regularization strength frame-wise (with the number of iterations after which the stopping criterion is triggered superposed in white). It generates images with high accuracy and low noise for all shown frames. After entering the vena cava inferior in frames 5 and 20, the tracer enters the right atrium of the mouse heart, as it can be seen in the frames $35, 50$ and 65. Furthermore, the vanishing of the tracer in the mouse heart in the later frames is clearly visible. For more details, a comparison to the images shown in [97] is meaningful. However, it has to be noted, that Graeser et al. use

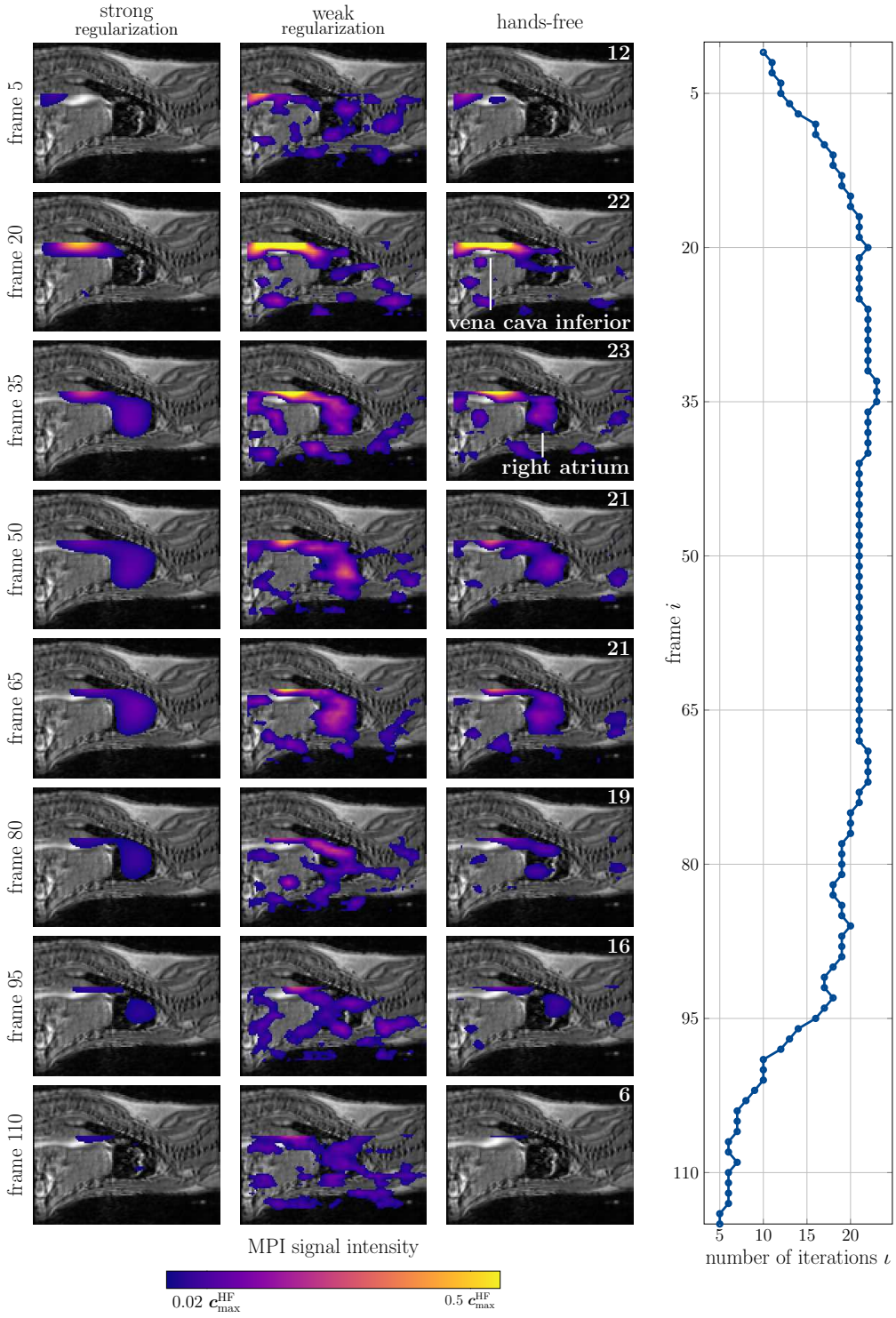

Figure 4.6: MPI results of the in vivo bolus visualized on top of corresponding MRI data. Shown is a solution using strong respectively weak regularization as well as the hands-free method on several frames with equidistant time difference. The number of iterations after which the stopping criterion was triggered is superposed in white. The results are normalized to the maximum of the hands-free solution c^{HF}_{max}, with the common colorbar given below. Furthermore, the number of iterations of the hands-free method over the course of the frames is given on the right side.

the bolus experiment with a ten-fold higher concentration. The hands-free method is able to give good results on the bolus progression at a lower concentration.

The total course of number of iterations over the frames is shown in the lower part of Fig. 4.6. It can be seen, that the number of iterations climbs (and therefore the amount of regularization shrinks), when the bolus enters the vena cava inferior at the first frames. Then, the number of iterations gradually decreases and the amount of regularization increases, as the bolus is weaker at later frames.

4.5 Discussion and Outlook

Considering the presented reconstruction results of the dilution series of the dot phantom, we see that the presented regularization parameter condensation works as intended. The number of iterations is inversely proportional to the amount of regularization and poses a trade-off between blurred images and sharp but noisy images. Thus, for high concentrations, a higher number of iterations and for low concentrations a low number of iterations gives the best results. This itself is a very promising step towards simplifying the problem of choosing the right amount of regularization for system-matrix-based MPI reconstruction.

The choice of the parameters of the mapping functions $\alpha_\lambda, \alpha_\Theta$ and Θ_{min} is dependent on the scanner hardware. The step from choosing different regularization parameter setups for each measurement to choosing different mapping function parameters only one time for an MPI system is huge. Furthermore, a first idea on auto-leveling these parameters out of the noise data was given and tested on different receive paths.

In combination with the proposed stopping criterion, the hands-free method is able to find a reasonable amount of regularization for all 12 different concentrations of the dot phantom as well as the 6 concentrations of the kidney phantom and thus over a vast range of MPI data. It selects a good compromise between resolution and noise. With enough time and computation power, it is possible to find better solutions for each measurement by a traditional reconstruction with hand-chosen regularization parameters. However, this does not weaken the huge potential of the hands-free reconstruction, since it aims to find a good reconstruction result without any user input in a short time. This goal is achieved and the hands-free reconstruction enables automatic reconstructions without experience and prior knowledge on the data. Further validation of the method requires future application to different data sets and different MPI systems. A runtime analysis of the hands-free reconstruction was not part of this work. However, since the underlying iterative solver remains, the reconstruction times are comparable to the regular Tikhonov regularized Kaczmarz method, for which online reconstruction has been shown to be possible [142].

The hands-free methods also shows its benefits on the time-dependent in vivo data with varying concentration. Whereas the reconstructions using either strong or weak (static) regularization do not give good results over all frames as they are either good for the frames with low concentration or respectively with high concentration. The hands-free method is able to adapt the regularization strength over the course of the frames and does give superior results. In comparison to [97], the hands-free method is able to give good results on a ten-fold weaker concentration. This is especially important with regard of the usability of MPI for human imaging, since too high tracer concentrations are a medical issue [258].

To hinder jumps in the course of reconstructed images, a dual approach with two rounds of reconstructions as described in 4.3.2 was used. This procedure is efficient to produce a smooth transition between the single frames. However, for an instant online reconstruction

a method using only one round of reconstruction may be beneficial. In this case, the second round can be used for post-processing the data.

Combining the results of the hands-free method on the different data sets, the hands-free method poses a very promising step for MPI application in the medical context, where fast and user friendly solutions are important, especially considering time-dependent bolus measurements. The hands-free method enables good reconstruction results on a low concentrated bolus, which is important when considering the maximum amount of human compatible iron particles. Furthermore, the method can also be used to get a fast first view on new data.

All data were derived from the same MPI scanner, but different receive coils with differing frequency responses and noise characteristics. Thus, it was shown, that the method is capable to adapt to different MPI receive chains. However, it remains to show that the method can be directly transferred to other MPI systems with different exciting frequencies and gradient strengths. In doing so, the auto-leveling of the mapping-parameters dependent on the receive path can get further investigated and improved.

Furthermore, it is meaningful to adapt different methods on hyperparameter tuning for inverse problems, like bayesian approaches or learning-based methods to the MPI setting. Adaptions on such methods would be necessary, to include the choice of the frequency selection. But especially combinations with the method presented in this paper are conceivable, for instance an advanced estimation of the parameters of the mapping functions.

4.6 Conclusion

In this work we investigated a possible simplification of the problem of finding the right amount of regularization for system matrix based MPI reconstruction. By condensing the regularization parameter triplet to a single parameter (the number of iterations of the iterative solver) and deriving a fitting stopping criterion, a method was presented, that is able to produce good reconstruction results in a fast manner. This can be achieved without additional user input, prior knowledge on the data nor additional measurements. The method was validated on several MPI measurements using different phantoms on a broad band of iron concentrations. Furthermore it was shown, that the method is very promising for in vivo bolus experiments with time-dependent concentration. This hands-free reconstruction represents a crucial step towards medical usage of MPI systems.

5

Magnetic Field Representation using Ellipsoidal Harmonics

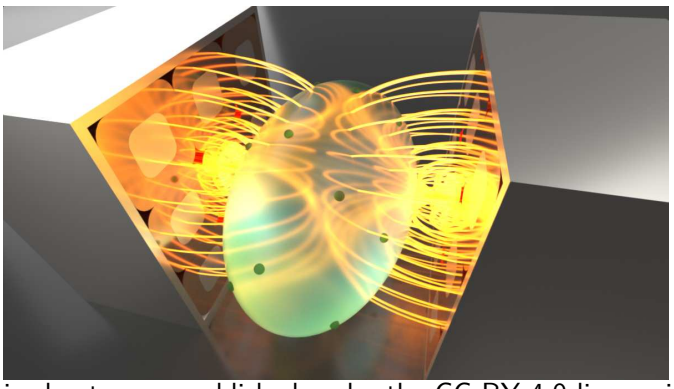

K. Scheffler, L. Meyn, F. Foerger, M. Boberg, M. Möddel, and T. Knopp, "Efficient Measurement and Representation of Magnetic Fields in Tomographic Imaging using Ellipsoidal Harmonics", Communications Physics, Vol. 8, No. 112, 2025.

In addition, the following peer-reviewed proceedings articles are presented in this chapter, as they provide additional insight on the usage of ellipsoidal harmonic expansions to measure and represent magnetic fields present in MPI.

K. Scheffler, L. Meyn, F. Foerger, M. Boberg, M. Möddel, and T. Knopp, "Ellipsoidal harmonic expansions for efficient approximation of magnetic fields in medical imaging", International Journal on Magnetic Particle Imaging, Vol. 10, 2024.
This work was presented at the International Workshop on Magnetic Particle Imaging 2024, Flüeli-Ranft, Switzerland.

K. Scheffler, L. Meyn, F. Foerger, M. Boberg, M. Möddel, and T. Knopp, "Experimental study on efficient field measurement using ellipsoidal harmonics", International Journal on Magnetic Particle Imaging, Vol. 11, 2025.
This work was presented at the International Workshop on Magnetic Particle Imaging 2025, Lübeck, Germany.

Abstract

Given the pivotal role of magnetic fields in modern medicine, there is an increasing necessity for a precise characterization of their strength and orientation at high spatial and temporal resolution. As source-free magnetic fields present in tomographic imaging can be described by harmonic polynomials, they can be efficiently represented using spherical harmonic expansions, which allows for measurement at a small set of points on a sphere surrounding the field of view. However, the majority of closed-bore systems possess a cylindrical field of view, making a sphere an inadequate choice for coverage. Ellipsoids represent a superior geometrical choice, and the theory of ellipsoidal harmonic expansions can be applied to magnetic fields in an analogous manner. Despite the mathematical principles underpinning ellipsoidal harmonics being well-established, their utilization in practical applications remains relatively limited. In this study, we present an effective and flexible approach to measuring and representing magnetic fields present in tomographic imaging, which draws upon the theory of ellipsoidal harmonic expansions.

5.1 Introduction

Magnetic fields are the basis for many applications in future medicine and play an important role in both diagnostics and therapy. For example, they can be used to drive and control magnetic micro- and nanorobots for various potential biomedical applications. Such robots have great potential in many areas of medicine as they can perform medical procedures even in remote and sensitive parts of the human body. This includes targeted delivery and release of drugs and therapeutics, cell manipulation, and minimally invasive surgery such as stenting [197, 22, 40, 167, 88, 324, 299, 57]. In addition, magnetic fields are used to visualize, navigate, and heat magnetic nanoparticles (MNP), allowing the focal treatment of tumors with hyperthermia [257, 212]. Finally, magnetic fields are at the heart of the tomographic imaging techniques magnetic resonance imaging (MRI) and magnetic particle imaging (MPI) [195] and magnetorelaxometry (MRX) [165]. Here, knowledge of the exact values of the magnetic fields in the field of view (FOV) is of great importance for signal encoding [220, 248].

In particular, the complex setup of coils or permanent magnets often leads to non-ideal magnetic fields and the benefits of accurate knowledge of the magnetic fields are manifold. Firstly, it is essential for hardware development, particularly in designing and arranging magnetic field generators to achieve ideal fields in the scanner's field of view. In the context of low-field MRI systems, which are increasingly important in the context of low-cost and point-of-care systems, high B_0-field homogeneity is a crucial factor in ensuring high-quality images [179, 80, 310]. Similarly, the non-linearity of gradient fields plays a major role in image quality [97, 179, 187, 75], so knowledge of magnetic fields is important and enables verification and quality control of imaging systems in both science and industry. Furthermore, it can be used for a precise sequence design in MRI. Moving on to image reconstruction, knowledge of the magnetic fields is very important to account for field inhomogeneity and reduce off-resonance artifacts [266, 64, 147, 159, 61, 117]. Moreover, field values can be used to enhance various reconstruction methods and mitigate the reconstruction error [4, 27].

Measurements of a magnetic field in tomographic imaging can be performed using a magnetic field sensor, such as a Hall sensor or an inductive sensor[281]. To cover a three-dimensional FOV, the sensor is moved voxel by voxel through the FOV along a dense grid. An increase in

spatial resolution directly correlates with an expansion in the number of measurement points, making this naive measurement procedure both time-consuming and labour-intensive. For illustration, a bisection of the distances results in eight times the number of measurement points. A more sophisticated alternative to the measurement on a dense grid is to employ spherical harmonics, given that source-free magnetic fields satisfy Laplace's equation and can thus be expanded into a series of spherical harmonic functions [202]. In scenarios where magnetic fields can be adequately represented by low-degree polynomials, it becomes feasible to truncate the series at an early stage. This approach enables the implementation of efficient measurement methods that require only a limited number of field evaluation points defined by a spherical t-design. A t-design is a sampling distribution that facilitates the exact integration of polynomials up to degree t [28, 33]. The magnetic field values can then be derived at any position within the sphere, i.e. sampled at any resolution. Spherical harmonic expansions also allow for a higher temporal resolution of magnetic field measurements. However, one limitation is that the size of the sphere is fixed in advance. Tomographic imaging systems with a closed bore often have a cylindrical shape. The bores are meant to fit a rodent, a human head or extremities, or even the whole human body. To cover a cylindrical FOV (shown by the green line in Figure 5.1), several spheres need to be shifted along the bore axis (indicated by the red dashed lines). Each sphere must be measured independently and the results combined. This process is tedious, reduces the temporal resolution of the measurements, and can leave parts of the field of view uncovered.

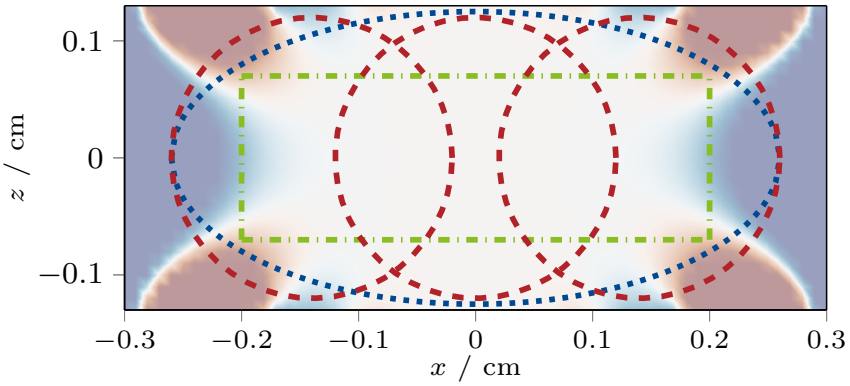

Figure 5.1: Shown is the coverage of an cylindrical field of view (displayed as a green line) when using several shifted spheres (displayed as red dashed lines) and an ellipsoid (displayed as a blue dotted line) in the central x,z-plane of the permanent magnet B_0-field presented by O'Reilly et al. [203]. The B_0-field is indicated in the background.

If we consider an ellipsoid instead, we gain two more degrees of freedom to adopt its shape. Thus, a cylindrical FOV can be covered much better (as shown by the blue dotted line in Figure 5.1). The theory of ellipsoidal harmonic functions as a basis of harmonic polynomials is well known. Although the series expansion is comparable to that of spherical harmonics, the underlying derivations for ellipsoidal coordinates are more complex. While ellipsoidal harmonic expansions have been studied in several scientific fields, such as chemical physics [226] and fluid dynamics [188], translations to practical applications are rare. In astrophysics they allow a more efficient calculation of the gravitational potential of celestial bodies [82]. Potential applications are also conceivable in other scientific fields that rely on solving equation systems of similar structure, for example plasma science [267]. For magnetic fields, and particularly in tomographic imaging, ellipsoidal harmonics have been studied to improve MRI shimming on an ellipsoidal region of interest [49, 24, 215, 214]. Moreover, ellipsoidal

coordinates can be used to improve methods in many areas of medical applications, e.g., reconstruction of ellipsoidal areas with a minimal number of radiographs in computed tomography [50], brain activity in ellipsoidal geometry [51], and electroencephalography on ellipsoidal surfaces [161]. In the context of application, effective and accurate methods for calculating the arising surface integrals are important. In this context, a variable splitting combined with Gauss quadratures has been presented [215]. Recently, a semi-analytical approach for the computation of ellipsoidal harmonics has been presented [78]. However, it is noted that for higher degree polynomials, a numerical approach is slower but more stable and accurate. It is to the best of the authors' knowledge that there is no existing literature on the use of spherical t-designs shifted to an ellipsoidal surface for the efficient computation of ellipsoidal harmonic expansions. Furthermore, there is a lack of publicly available software packages on the topic of ellipsoidal harmonics. Open-source implementations in MATLAB and Python have been presented in [18] using a simple midpoint quadrature to solve the surface integrals that arise in this context. However, this method is known to be slow to converge.

The geometric shape of prolate and oblate spheroids is an intermediate between spheres and ellipsoids. Thus, they are less flexible in covering a given FOV than ellipsoids, but still an improvement over spheres. Spheroidal harmonics could offer an advantage over ellipsoidal harmonics in some settings because their derivation is less complex [121, 9, 86, 252]. However, this work focuses on the more flexible ellipsoidal case.

The principal objective of this study is to demonstrate that ellipsoidal harmonics can be employed to effectively measure and represent magnetic fields in tomographic imaging. The following section outlines the structure of the paper. A brief introduction to ellipsoidal harmonics, along with a review of the necessary ingredients for their implementation in practice is given in the methods section 5.4. For readers interested in further details, additional information is provided in the end of the methods section 5.4.5, while the cited literature contains derivations and more detailed explanations of the mathematics. The application of ellipsoidal harmonic expansions to simulated magnetic fields present in MRI is demonstrated. A comparison with spherical harmonic expansions is provided to illustrate the potential of ellipsoidal harmonics in tomographic imaging. The software tool, written in Julia, is published as an open source package.

At the 2024 International Workshop on Magnetic Particle Imaging, the authors presented preliminary results on utilizing ellipsoidal harmonic expansions to represent magnetic fields in magnetic particle imaging [242].

5.2 Results

The main objective of this work is showcasing that magnetic fields in tomographic imaging can be represented efficiently by using ellipsoidal harmonic expansions. To illustrate this, we have performed simulation studies on magnetic fields present in MRI. The implementation of the ellipsoidal harmonic expansion was written in Julia and is published under the MIT License at `https://github.com/IBIResearch/EllipsoidalHarmonicExpansions`. The polynomial calculations and the root finding are based on the package Polynomials.jl (`https://github.com/JuliaMath/Polynomials.jl`). For spherical harmonic expansions the Julia package SphericalHarmonicExpansions.jl (`https://github.com/hofmannmartin/SphericalHarmonicExpansions.jl`) was used.

5.2.1 Experimental design: homogeneous field

Constant and ideally homogeneous B_0 fields are essential in MRI, as they polarize spins and generate magnetization. The development of B_0 fields with low energy consumption and small system size is an important topic of current research in the emerging field of low-field MRI. Arrays of permanent magnets arranged in a discretized version of a Halbach ring can be used to produce B_0 fields, where a high length-to-diameter ratio is important for high homogeneity. The higher this ratio, the more suitable ellipsoidal harmonics are for efficient field measurement compared to spherical harmonics. Such a Halbach configuration for a potential low-field and low-cost MRI with length-to-diameter ratio of 2:1 was presented by [203]. The setup consists of 23 double rings with 27 cm bore diameter. In total 2948 cuboid N48 neodynium magnets are used to generate a homogeneous 50 mT field transversal to the bore (in positive z-direction). A simulation of the setup was conducted on a three-dimensional grid comprising $61 \times 27 \times 27$ grid points and a point distance of 1 cm. This was achieved by superpositioning the magnetic fields calculated in accordance with the Biot-Savart law based on the surface currents of each individual magnet. The simulated field was interpolated to the data points of the t-designs by using cubic splines.

The reference ellipsoid was chosen with semi-axes $\boldsymbol{a} = (0.26, 0.125, 0.1249)$ m around the coordinate origin in the center of the Halbach configuration to comprise a cylindrical FOV (Ω_{FOV}) with 0.2 m height and 0.07 m radius as shown in Figure 5.1. To calculate the inner ellipsoidal harmonics, a 14-design comprising 114 data points on the reference ellipsoid was employed. Although the simulated magnetic field has a large homogeneous area, it is reasonable to assume that a t-design of this scale is necessary to accurately represent the inhomogeneities in the outer region. To validate this assumption, an ellipsoidal harmonic expansion was performed on the same reference ellipsoid using an 8-design containing only 44 data points. In addition, we also considered the conjunction of three spheres with radius 0.12 m, shifted along the x-axis to cover the FOV. Here, three separate 14-designs with 114 data points per sphere (i.e. a total of 342 data points) were used to compute the spherical harmonic expansion. Thus, in this case, the ellipsoidal representation using a single 14-design is three times more efficient than the spherical representation. Furthermore, we consider the same spheres with three separate 7-designs, each comprising 38 data points. This ensures that the total number of 114 data points is comparable to the number of data points in the ellipsoidal 14-design. The cylindrical FOV, the reference ellipsoid and the spheres are shown in Figure 5.1.

For a quantitative evaluation we set the simulated B_0 field as ground truth and consider difference maps of the locally normalized root mean squared deviation to the fields calculated by both harmonic expansions:

$$\xi_{\text{EHE}}^{B_0} := \frac{\|\boldsymbol{B}_{\text{EHE}} - \boldsymbol{B}\|_2}{\|\boldsymbol{B}\|_2}, \qquad \xi_{\text{SHE}}^{B_0} := \frac{\|\boldsymbol{B}_{\text{SHE}} - \boldsymbol{B}\|_2}{\|\boldsymbol{B}\|_2}. \tag{5.1}$$

5.2.2 Experimental design: gradient field

Gradient fields play an important role in spatial encoding in tomographic imaging. Exemplarily we consider the MRI B_0 field produced by the permanent Halbach configuration again. Appropriate coil setups for optimized linear gradients in each spatial direction have been presented by [54]. Using their gradient design tool (`https://github.com/LUMC-LowFieldMRI/GradientDesignTool/tree/master`) and the FEM software COMSOL Multiphysics (v.6.0. www.comsol.com. COMSOL AB, Stockholm, Sweden) a linear gradient was simulated along the bore, with the field oriented transversally in the direction

of B_0 on the same grid as that used for the B_0 field. As previously, the simulated field was interpolated to the data points of the t-designs by using cubic splines.

Because of the highly non-linear parts of the field in the vicinity of the coils, the reference ellipsoid was chosen with semi-axes $\boldsymbol{a} = (0.25, 0.1, 0.099)$ m around the coordinate origin in the center of the Halbach configuration to comprise a cylindrical FOV with 0.18 m height and 0.06 m radius as shown in Figure 5.2. For comparison we consider again the conjunction of three spheres with radius 0.1 m, shifted along the x-axis. The t-designs were chosen analogously to the B_0 case: a single 14-design with 114 data points on the ellipsoid and three separate 14-designs with 114 data points on each sphere. Studies with smaller t-designs on the gradient field show a similar effect as shown for the B_0 field. Therefore, we do not show it again to avoid redundancy.

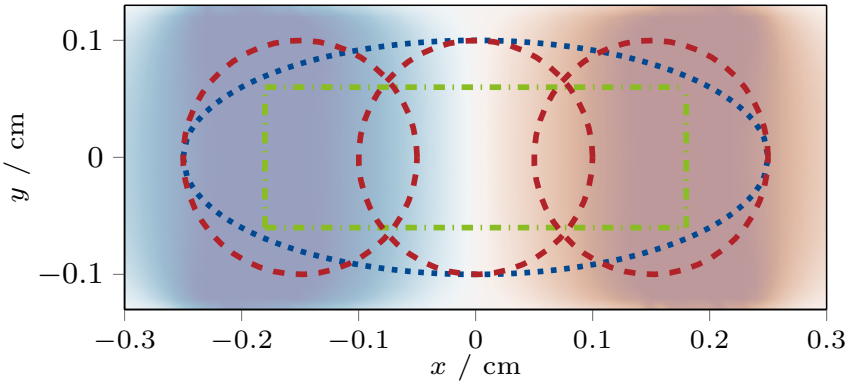

Figure 5.2: Shown is the central x,y-plane of the MRI gradient field. The reference ellipsoid (displayed as a blue dotted line) and three shifted spheres (displayed as red dashed lines) are chosen to comprise the field of view of the gradient field (displayed as a green line). The z-component of the simulated gradient field is indicated in the background.

For an error analysis, the simulated gradient field is considered as ground truth and difference maps of the globally normalized root mean squared deviation to the fields calculated by both harmonic expansions:

$$\zeta_{\mathrm{EHE}}^{\mathrm{grad}} := \frac{\|\boldsymbol{B}_{\mathrm{EHE}} - \boldsymbol{B}\|_2}{\max\limits_{\Omega_{\mathrm{FOV}}} \|\boldsymbol{B}\|_2}, \qquad \zeta_{\mathrm{SHE}}^{\mathrm{grad}} := \frac{\|\boldsymbol{B}_{\mathrm{SHE}} - \boldsymbol{B}\|_2}{\max\limits_{\Omega_{\mathrm{FOV}}} \|\boldsymbol{B}\|_2}. \tag{5.2}$$

It should be noted that a local normalization would result in a singularity due to the zero crossing of the gradient field. Therefore, a global error normalization using the maximum value inside the FOV was selected as an alternative.

5.2.3 Experimental results: homogeneous field

Exemplary results of the B_0 field in the x,z-plane are shown in Figure 5.3. In the second column, the calculated fields are given next to the ground truth. When using the 14-design, no visual differences are detectable inside the volume of the reference ellipsoid. Towards the edges and outside of these regions, slight differences can be seen. This becomes clearer when looking at the difference plots in the right column. The relative error is smaller than 1 % in most of the FOV, becomes slightly larger towards the edges of the ellipsoid (up to 5 %), and increases rapidly outside the FOV. A consideration of the difference plot of the ellipsoidal harmonic expansion with the smaller 8-design reveals that the error increases more

strongly inside the reference ellipsoid, yet remains below 10 %. A similar behavior is observed in the conjunction of the three spheres. With 14-designs, the error is smaller than 1 % inside the spheres. However, when using 7-designs, the error is visibly larger in the outer spheres, where the field tends to become less homogeneous. In this case, the result is clearly worse than for the ellipsoidal harmonic expansion with one 14-design, despite using the same total number of data points.

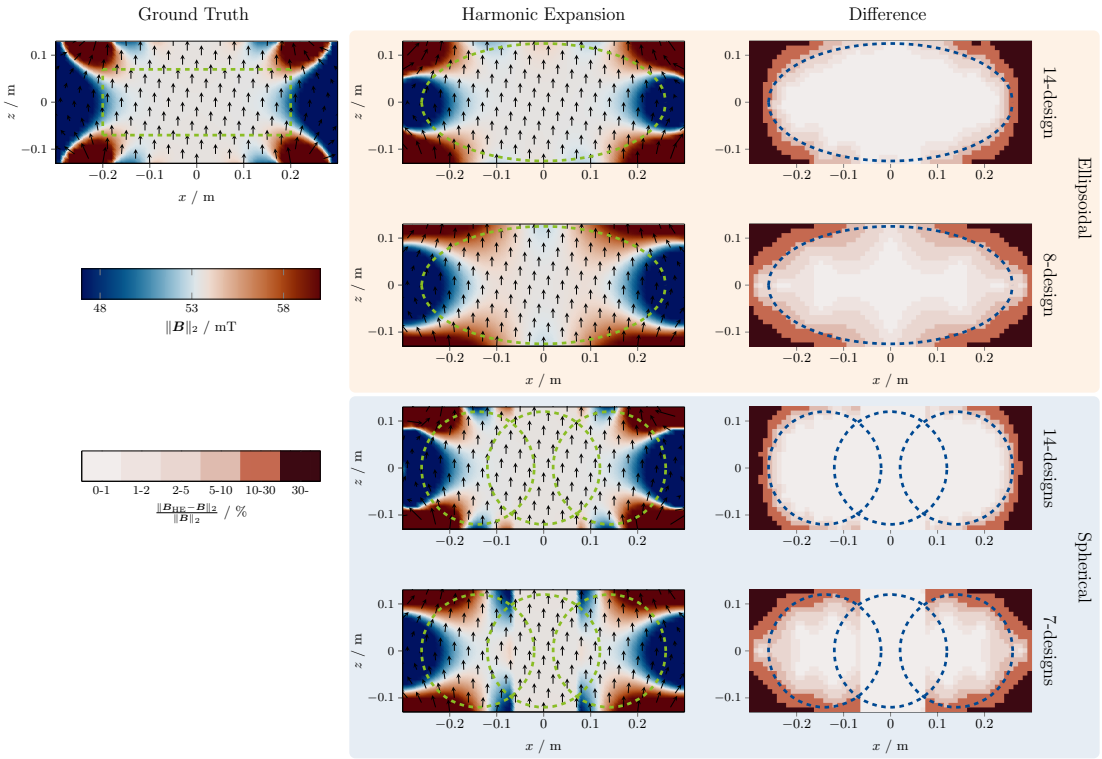

Figure 5.3: Shown are the experimental results of the B_0-field in the x,z-plane. The simulated MRI B_0-field is labeled as Ground Truth and includes the cylindrical field of view as green dashed line. The calculated B_0-fields using an ellipsoidal harmonic expansion with a 14-design and a 8-design and spherical harmonic expansions with 14-designs and 7-designs are shown and labeled accordingly. The reference ellipsoid and the spheres are indicated as green dashed lines within the field plots. A joint color bar indicating the absolute field values from 47 mT (dark blue) to 60 mT (dark red) is provided. Moreover, the relative errors (as defined in 5.1) to the ground truth are shown for all four cases, labeled as Difference plots. The reference ellipsoid and the spheres are indicated as blue dashed lines within the difference plots. A joint color bar for the difference plots indicating the relative error within six bins from 0−1 % (light pink) to >30 % (dark red) is provided.

Firstly, we consider the quantitative results for the ellipsoidal harmonic expansion on the B_0-field when using a smaller 8-design with only 44 data points. This method yielded a mean error of $\underset{\Omega_{\mathsf{FOV}}}{\text{mean}}\left(\boldsymbol{\xi}^{B_0}_{\mathsf{EHE}_8}\right) = 1.22\,\%$ and a maximum error of $\underset{\Omega_{\mathsf{FOV}}}{\max}\left(\boldsymbol{\xi}^{B_0}_{\mathsf{EHE}_8}\right) = 5.78\,\%$ inside the cylindrical FOV. The error exhibited an increase outside the FOV, approaching the edge of the reference ellipsoid, as can be observed in Figure 5.3. In the context of the ellipsoidal 14-design with 114 data points, a mean error of $\underset{\Omega_{\mathsf{FOV}}}{\text{mean}}\left(\boldsymbol{\xi}^{B_0}_{\mathsf{EHE}_{14}}\right) = 0.32\,\%$ and a maximum error of $\underset{\Omega_{\mathsf{FOV}}}{\max}\left(\boldsymbol{\xi}^{B_0}_{\mathsf{EHE}_{14}}\right) = 3.64\,\%$ were attained within the FOV. This signifies

a substantial enhancement over the 8-design. The error is negligible in the center of the reference ellipsoid, increasing towards the border.

For validation of the presented methods we also consider the error for the spherical harmonic expansions. Considering the field resulting from the concatenation of three spherical harmonic expansions with 7-designs and thus the same number of 114 total data points, a mean error of $\underset{\Omega_{\text{FOV}}}{\text{mean}}\left(\xi^{B_0}_{\text{SHE}_7}\right) = 0.55\,\%$ and a maximum error of $\underset{\Omega_{\text{FOV}}}{\max}\left(\xi^{B_0}_{\text{SHE}_7}\right) = 4.12\,\%$ was achieved inside the FOV. A mean error of $\underset{\Omega_{\text{FOV}}}{\text{mean}}\left(\xi^{B_0}_{\text{SHE}_{14}}\right) = 0.09\,\%$ and a maximum error of $\underset{\Omega_{\text{FOV}}}{\max}\left(\xi^{B_0}_{\text{SHE}_{14}}\right) = 0.54\,\%$ inside the FOV was achieved with threefold data points using the concatenation of results on three shifted spherical harmonic expansions with 14-designs.

5.2.4 Experimental results: gradient field

Qualitative results of the gradient field are plotted in the x,y-plane (transversal to the B_0-direction) in Figure 5.4. The field points in B_0-direction (positive z), thus no field arrows are displayed. Inside the regions of convergence (respectively the reference ellipsoid and the conjunction of the three spheres) and especially in the predefined FOV no visual differences to the ground truth are detectable. This is underlined by difference plots in the second row of Figure 5.4. The relative error is smaller than 1 % everywhere in the FOV and increasing outside the edges regions of convergence. The linearity of the gradient in the center line of the Halbach configuration is showcased on the lower left side. Between -0.15 m and 0.15 m the gradient shows nearly perfect linearity. In this section, all three lines are visually on top of each other. The difference from the harmonic expansion gradients to the ground truth increases on the outer ends (outside the reference ellipsoid and the outer spheres, respectively).

Using the 14-design on the reference ellipsoid for the simulated gradient field, a mean error of $\underset{\Omega_{\text{FOV}}}{\text{mean}}\left(\xi^{\text{grad}}_{\text{EHE}}\right) = 0.34\,\%$ and a maximum error of $\underset{\Omega_{\text{FOV}}}{\max}\left(\xi^{\text{grad}}_{\text{EHE}}\right) = 2.19\,\%$ have been attained inside the FOV. Again the error increases towards the border of the ellipsoid but remains below 1 % for the majority of the FOV. Considering the three shifted spheres with threefold data points for a spherical harmonic expansion, a mean error of $\underset{\Omega_{\text{FOV}}}{\text{mean}}\left(\xi^{\text{grad}}_{\text{SHE}}\right) = 0.16\,\%$ and a maximum error of $\underset{\Omega_{\text{FOV}}}{\max}\left(\xi^{\text{grad}}_{\text{SHE}}\right) = 2.23\,\%$ was achieved inside the FOV.

5.3 Discussion

Although the geometric form of an ellipsoid can be continuously simplified to a sphere, such a reduction from ellipsoidal to spherical harmonics is not straightforward and unique [52]. However, as shown in the methods section 5.4, spherical and ellipsoidal harmonic expansions have great similarities in structure. In both cases, we consider a linear combination of basis functions of harmonic polynomials up to a certain degree on the spherical or ellipsoidal FOV. In both cases we have to solve a surface integral (on the sphere or reference ellipsoid) to obtain the coefficients. These surface integrals can be solved efficiently using t-designs. To do this, we use the transformation formula 5.12 between the two integrals to define ellipsoidal t-designs on the reference ellipsoid from their counterparts on the unit sphere. This transformation step is crucial for an efficient calculation of ellipsoidal harmonic expansions and thus enables their use for efficient representation of magnetic fields.

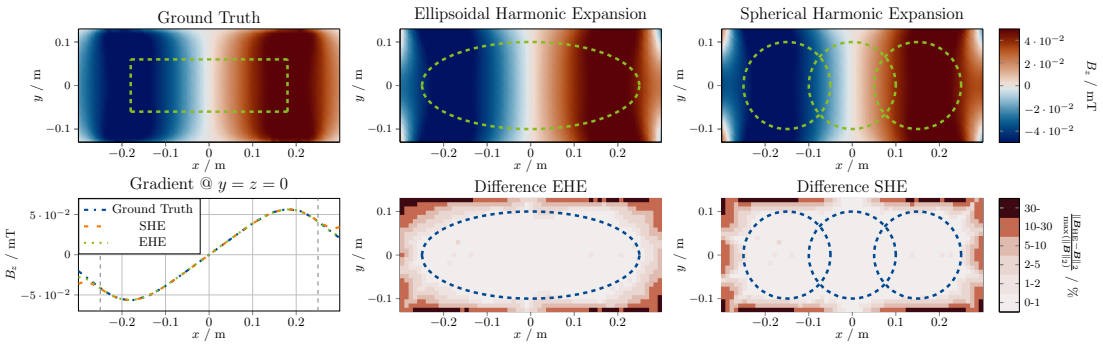

Figure 5.4: Shown are the experimental results of the MRI gradient field in the x, y-plane. The simulated gradient field is labeled as Ground Truth and includes the cylindrical field of view as green dashed line. Heatmaps of the calculated gradient fields using ellipsoidal and spherical harmonics are shown and labeled accordingly. The reference ellipsoid and the spheres are indicated as green dashed lines within the field plots. A joint color bar indicating the z-component of the field values from $-0.05\,\mathrm{mT}$ (dark blue) to $0.05\,\mathrm{mT}$ (dark red) is provided. The relative errors (as defined in 5.2) to the ground truth are shown for both cases, labeled as Difference EHE for the ellipsoidal harmonic expansion and Difference SHE for the spherical harmonic expansion. The reference ellipsoid and the spheres are indicated as blue dashed lines within the difference plots. A joint color bar for the difference plots indicating the relative error within six bins from $0-1\,\%$ (light pink) to $>30\,\%$ (dark red) is provided. Moreover, the B_z values of the ground truth, the spherical harmonic expansion (SHE) and the ellipsoidal harmonic expansion (EHE) at $y = z = 0$ are compared in a separate line-plot labeled as Gradient @ $y = z = 0$. The border of the ellipsoid and the spheres in $x - direction$ are displayed as gray dashed lines.

In order to validate the accuracy of the numerical integration using ellipsoidal t-designs and – by doing so – to demonstrate the representation of magnetic fields present in tomographic imaging using ellipsoidal harmonic expansions, a permanent magnet Halbach ring array for low field MRI was considered. In this context, a high length-to-diameter ratio directly correlates with enhanced field homogeneity. This allows the FOV to be efficiently covered by an ellipsoid, thereby underscoring the practical utility of ellipsoidal harmonics. Two ellipsoidal t-designs of different sizes were used to emphasize the gain in accuracy with increasing t. Three shifted spheres were used for comparison. We considered two spherical t-designs, one of them with the same total number of data points compared to the larger ellipsoidal t-design. This allows for a direct comparison and highlights the gain in accuracy that can be achieved with ellipsoidal harmonic expansions.

The results presented in section 5.2.3 show that the ellipsoidal harmonic expansion – efficiently computed using an ellipsoidal t-design – is fully capable of recovering the B_0 field. Although a small 8-design with only 44 data points can be interesting to get a first impression of the fields, it produces some inaccuracies. In contrast, the larger 14-design with 114 data points gives a very good result. With a mean error of less than $1\,\%$ within the FOV, the accuracy is comparable to the field recovered using a spherical harmonic expansion, but requires only a third of the data points. Compared to a spherical harmonic expansion with the same number of data points, the ellipsoidal harmonic expansion achieves a gain in accuracy. For both methods, the error increases in the outer regions of the FOV. This is expected because both expansions converge only within the reference ellipsoid or spheres.

The results on the gradient field presented in section 5.2.4 corroborate these assertions. The mean error within the reference ellipsoid is notably minimal, falling well below $1\,\%$. This is comparable to the mean error obtained using spherical harmonics on the conjunction of

three shifted spheres, but again using only a third of the data points. The overall smaller error can be explained by the good linearity of the gradient field within the selected reference ellipsoid and spheres.

It should be noted that for both methods there is also an error in the interpolation of the field values to the points of the corresponding t-design. The results in this paper are based on simulated fields. In actual measurements, there will be discrepancies due to factors such as the accuracy of the robot resulting in small displacements and the accuracy of the magnetometer due to time drifts or measurement noise. The analysis of the total error for real magnetic field measurements remains a subject for future research. However, t-designs represent a very robust quadrature in the context of node displacements and function evaluation.

In general, we can conclude that ellipsoidal harmonic expansions provide a valuable gain for efficient measurement and representation of magnetic fields in tomographic imaging. Two additional degrees of freedom compared to spherical regions provide significant advantages in covering a variety of scanner bores. Therefore, ellipsoidal harmonic expansions should be considered over spherical harmonic expansions whenever the physical dimensions require this geometric flexibility. An effective and accurate calculation of the ellipsoidal coefficients was presented by solving the surface integrals using ellipsoidal t-designs. To this end, the implementation of precise transformations between Cartesian coordinates and ellipsoidal coordinates must be handled carefully, taking into account the sign conventions. To reduce the computational cost, it is mandatory to construct the $(\frac{T}{2}+1)^2$ Lamé functions depending on the selected reference ellipsoid and t-design only once before the field evaluations. The Lamé functions can be computed efficiently by setting up the determinants of matrices up to size $\frac{T}{2}^2$ as defined in subsection 5.4.6 and finding their roots in a fast way. The Lamé functions can be stored for later evaluation of the fields. A fast implementation in Julia is published alongside the paper. It should be noted that the presented methods and the provided code could also be of great use in other research fields where ellipsoidal harmonics are applied (e.g., chemical physics, fluid dynamics, astrophysics and plasma science).

A comprehensive examination of the measurement and representation of magnetic fields in tomographic imaging employing prolate or oblate spheroidal harmonics is of significant interest. These harmonics provide an intermediate level of flexibility and complexity, situated between spherical and ellipsoidal harmonics. Consequently, this research question serves as a logical starting point for future studies.

The flexibility gained in covering a cylindrical FOV using ellipsoidal harmonic expansions pose a great advantage for high temporal resolution magnetic field measurements. Such measurements provide valuable insight into signal generation, for example in MRI or MPI. A spherical single-shot magnetic field measurement device capable of a measurement rate of 10 Hz has recently been presented [74]. A similar ellipsoidal device could be designed to provide such a measurement rate over a larger non-spherical FOV.

5.4 Methods

5.4.1 Spherical harmonics series expansion

Solid real spherical harmonics can be used for an efficient representation of source-free magnetic fields inside an arbitrary spherical volume as follows [28]. Let us consider a ball

$\mathcal{B}_R(\boldsymbol{p})$ with arbitrary radius $R \in \mathbb{R}_+$ and center $\boldsymbol{p} \in \mathbb{R}^3$. Further, let the function $f : \mathcal{B}_R(\boldsymbol{p}) \to \mathbb{R}$ fulfill Laplace's equation with Dirichlet boundary conditions, i.e.

$$\begin{cases} \Delta f(\boldsymbol{a}) = 0, & \forall \boldsymbol{a} \in \overset{\circ}{\mathcal{B}}_R(\boldsymbol{p}), \\ f(\boldsymbol{a}) = F(\boldsymbol{a}), & \forall \boldsymbol{a} \in \partial\mathcal{B}_R(\boldsymbol{p}), \end{cases}$$

where $F \in C^\infty(\partial\mathcal{B}_R(\boldsymbol{p}))$. Then f can be represented through

$$f(\boldsymbol{a}) = \sum_{n=0}^{\infty} \sum_{m=-n}^{n} A_S^{n,m}(\boldsymbol{p}, R) \left(\frac{1}{R}\right)^n Z_n^m(\boldsymbol{a} - \boldsymbol{p}) \ \forall \boldsymbol{a} \in \mathcal{B}_R(\boldsymbol{p}), \tag{5.3}$$

where the spherical coefficients are calculated on the unit sphere via

$$A_S^{n,m}(\boldsymbol{p}, R) = \oint_{S^2} F(R\boldsymbol{a} + \boldsymbol{p}) Z_n^m(\boldsymbol{a}) \, \mathrm{d}\boldsymbol{a}, \tag{5.4}$$

and the normalized real solid spherical harmonics are given as

$$Z_n^m : \mathbb{R}^3 \to \mathbb{R}, \ (r, \vartheta, \phi) \mapsto \gamma_S^{n,|m|} r^n P_n^{|m|}(\cos\vartheta) \begin{cases} \sqrt{2}\cos m\phi, & m > 0, \\ \sqrt{2}\sin|m|\phi, & m < 0, \\ 1, & m = 0. \end{cases} \tag{5.5}$$

Here, P_n^m are the associated Legendre polynomials and $\gamma_S^{n,|m|} = \sqrt{\frac{2n+1}{4\pi}\frac{(n-m)!}{(n+m)!}}$ is the spherical normalization factor.

If f is a polynomial of maximum degree $N \in \mathbb{N}$, the outer sum in equation (5.3) can be truncated to $n \in \{0, 1, ..., N\}$. Since we assume that the magnetic field $\boldsymbol{B} : \mathcal{B}_R(\boldsymbol{p}) \to \mathbb{R}^3$ inside the chosen ball, its components can be described by a harmonic polynomial of maximum degree $N \in \mathbb{N}$ and thus $N+1$ summands in the outer sum are sufficient for an exact spherical harmonic expansion. Furthermore, following [28], the spherical coefficients $A_S^{n,m}$ can be calculated exactly by using a spherical t-design $\{\boldsymbol{y}_i\}$ with $L \in \mathbb{N}$ nodes $\boldsymbol{y}_i \in S^2$ and $i \in \{0, ..., L-1\}$ for t $\geq 2N$.

5.4.2 Ellipsoidal harmonics series expansion

The objective of the following sections is to extend the considerations of the last section to ellipsoids. For a detailed reference work on ellipsoidal harmonics we refer to [52]. Let us now consider a region of ellipsoidal shape $\Omega \subset \mathbb{R}^3$, called reference ellipsoid. The reference ellipsoid is defined by its three semi-axes $0 < a_3 < a_2 < a_1$ via

$$\frac{x^2}{a_1^2} + \frac{y^2}{a_2^2} + \frac{z^2}{a_3^2} = 1. \tag{5.6}$$

A reference ellipsoid with its semi-axes is visualized in Figure 5.5.

The linear eccentricities of the reference ellipsoid are given as

$$h_1 = \sqrt{(a_2^2 - a_3^2)}, \quad h_2 = \sqrt{(a_1^2 - a_3^2)}, \quad h_3 = \sqrt{(a_1^2 - a_2^2)}. \tag{5.7}$$

In order to describe the Laplace's partial differential equation inside the reference ellipsoid, we introduce an orthogonal ellipsoidal coordinate system ρ, μ, ν. A proper definition of ρ, μ, ν and the connection to Cartesian coordinates can be found in subsection 5.4.5.

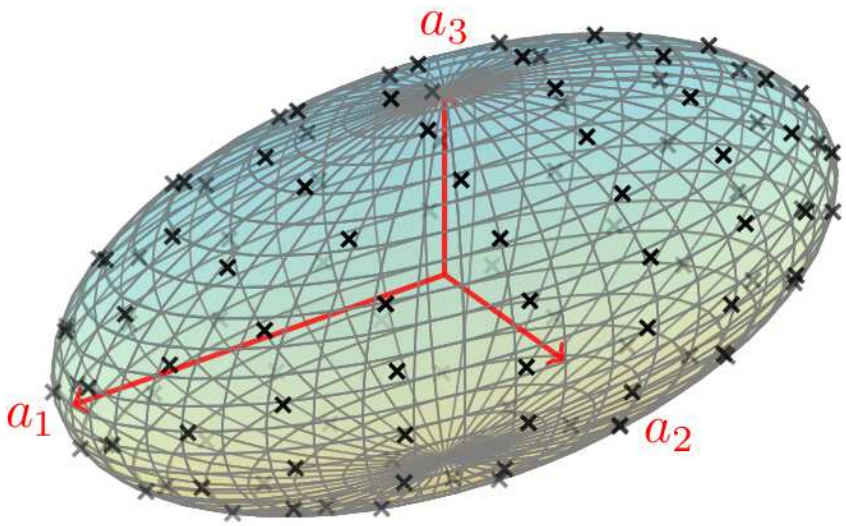

Figure 5.5: Shown is a reference ellipsoid defined by its semi-axes $0 < a_3 < a_2 < a_1$ displayed as red arrows. Furthermore, the measurement points of an ellipsoidal t-design (with t $= 14$) are indicated as crosses on the ellipsoidal surface.

Let the function $f : \Omega \to \mathbb{R}$ fulfill Laplace's equation inside the reference ellipsoid, i.e.

$$\begin{cases} \Delta f(\rho,\mu,\nu) = 0, & h_2 \leq \rho < a_1, \\ f(\rho,\mu,\nu) = F(\mu,\nu), & \rho = a_1, \end{cases}$$

where $F \in C^\infty(S_{a_1})$ and S_{a_1} describes the surface of the reference ellipsoid.

Expressing Laplace's equation inside the reference ellipsoid in ellipsoidal coordinates and using a separation of variables leads to the Lamé equation. Solutions of this equation are the so called Lamé functions $E_n^m : \mathbb{R} \to \mathbb{R}$ with degree $n \in \mathbb{N}$ and order $m \in \{1, ..., 2n+1\}$. The exact definitions are given in more detail in subsection 5.4.6.

With the Lamé functions at hand, we consider the inner ellipsoidal harmonics

$$\mathbb{E}_n^m(\rho,\mu,\nu) = E_n^m(\rho)E_n^m(\mu)E_n^m(\nu), \tag{5.8}$$

which form a basis of the harmonic polynomials of degree $n \leq N,\ N \in \mathbb{N}$ (more details are given in subsection 5.4.7).

It follows, that

$$f(\rho,\mu,\nu) = \sum_{n=0}^{\infty} \sum_{m=1}^{2n+1} A_{a_1}^{n,m} \mathbb{E}_n^m(\rho,\mu,\nu), \tag{5.9}$$

and on the boundary

$$F(\mu,\nu) = \sum_{n=0}^{\infty} \sum_{m=1}^{2n+1} A_{a_1}^{n,m} E_n^m(a_1) S_n^m(\mu,\nu). \tag{5.10}$$

$S_n^m(\mu,\nu) = E_n^m(\mu)E_n^m(\nu)$ are the so-called surface ellipsoidal harmonics and the coefficients $A_{a_1}^{n,m} \in \mathbb{R}$ are obtained from their orthogonality via

$$A_{a_1}^{n,m} = \frac{1}{\gamma_{a_1}^{n,m} E_n^m(a_1)} \oint_{S_{a_1}} F(\mu,\nu) S_n^m(\mu,\nu)\ \mathrm{d}\Omega(\mu,\nu), \tag{5.11}$$

with the ellipsoidal normalization factor $\gamma_{a_1}^{n,m}$ as defined in subsection 5.4.7..

Furthermore, if f is a polynomial of maximum degree $N \in \mathbb{N}$, the outer sums in equation (5.9) and equation (5.10) can be truncated to $n \in \{0,1,...,N\}$.

5.4.3 Quadrature on ellipsoidal surface

In order to solve the surface integrals in equations (5.11) and (5.30) numerically, we consider the following transformation-formula between integrals on ellipsoidal surfaces and spheres

$$\oint_{S_{a_1}} F(\mu,\nu)\ \mathrm{d}\Omega(\mu,\nu) = \int_0^{2\pi}\int_0^{\pi} F(\mu(\vartheta_e,\varphi_e),\nu(\vartheta_e,\varphi_e)) \sin\vartheta_e\ \mathrm{d}\vartheta_e\ \mathrm{d}\varphi_e, \tag{5.12}$$

where F is defined on the surface of the reference ellipsoid and $\vartheta_e \in [0,\pi], \varphi_e \in [0,2\pi)$ are so-called elliptospherical coordinates (see chapter 6 in [52]). We consider a spherical t-design $\{\boldsymbol{y}_i\}$ [21] with $L \in \mathbb{N}$ nodes $\boldsymbol{y}_i \in \mathbb{S}^2$ and $i \in \{0,...,L-1\}$, i.e. for a polynomial g on the unit sphere with maximum degree t $\in \mathbb{N}$ it holds, that

$$\oint_{\mathbb{S}^2} g(\boldsymbol{y})\ \mathrm{d}\Omega = \frac{4\pi}{L}\sum_{i=0}^{L-1} g(\boldsymbol{y}_i).$$

In particular, if we consider g such that $F(\mu(\vartheta_e,\varphi_e),\nu(\vartheta_e,\varphi_e)) = g(\vartheta_e,\varphi_e)$ it follows, that

$$\begin{aligned}\oint_{S_{a_1}} F(\mu,\nu)\ \mathrm{d}\Omega(\mu,\nu) &= \int_0^{2\pi}\int_0^{\pi} F(\mu(\vartheta_e,\varphi_e),\nu(\vartheta_e,\varphi_e)) \sin\vartheta_e\ \mathrm{d}\vartheta_e\ \mathrm{d}\varphi_e \\ &= \int_0^{2\pi}\int_0^{\pi} g(\vartheta_e,\varphi_e) \sin\vartheta_e\ \mathrm{d}\vartheta_e\ \mathrm{d}\varphi_e \\ &= \frac{4\pi}{L}\sum_{i=0}^{L-1} g(\boldsymbol{y}_i),\end{aligned}$$

and F is a polynomial with maximum degree $t \in \mathbb{N}$ on the ellipsoidal surface, if and only if g is a polynomial with maximum degree $t \in \mathbb{N}$ on the unit sphere. Here, the angular coordinates ϑ_e, φ_e can be transformed into Cartesian coordinates on the unit sphere using

$$(y_1,y_2,y_3) = (\sin(\vartheta_e)\cos(\varphi_e), \sin(\vartheta_e)\sin(\varphi_e), \cos(\vartheta_e))$$

and further into Cartesian coordinates on the ellipsoidal surface using

$$(x_1,x_2,x_3) = \left(y_3\rho, y_1\sqrt{\rho^2-h_3^2}, y_2\sqrt{\rho^2-h_2^2}\right).$$

Using this coordinate transformation on the spherical t-design $\{\boldsymbol{y}_i\} \subset \mathbb{S}^2$, we get points $\{\boldsymbol{x}_i\} \subset S_{a_1}$ on the ellipsoidal surface. Since $F(\boldsymbol{x}_i) = g(\boldsymbol{y}_i)$ follows directly from $F(\mu(\vartheta_e,\varphi_e),\nu(\vartheta_e,\varphi_e)) = g(\vartheta_e,\varphi_e)$, $\{\boldsymbol{x}_i\}$ poses an ellipsoidal t-design, i.e.

$$\oint_{S_{a_1}} F(\mu,\nu)\ \mathrm{d}\Omega(\mu,\nu) = \frac{4\pi}{L}\sum_{i=0}^{L-1} F(\boldsymbol{x}_i).$$

As a result of these considerations, $\gamma_{a_1}^{n,m}$ and A_n^m can be calculated exactly using an ellipsoidal t-design with t $\geq 2n$.

Despite the fact that quadratures using a t-design are exact for integrals over polynomials with maximal degree t, the robustness of such quadratures is primarily contingent on disturbances in the node positions and errors in the function evaluation at these positions. The first point is often addressed by introducing small neighborhoods around the node positions in which the design remains a positive quadrature rule. The determination of upper limits for the radius of these neighborhoods remains an active area of research [326, 325]. An important property of a t-design is the uniformity of its quadrature weights, which makes it particularly robust to perturbations in node positions compared to other quadratures. The evaluation of the function is subject to uncertainty due to measurement and interpolation errors. Furthermore, the consideration of functions as polynomials is often subject to specific assumptions. However, upper limits for the quadrature error do exist for continuously differentiable functions. The error diminishes with increasing smoothness of the functions under consideration and larger values of t [312].

5.4.4 Efficient calculation of source-free magnetic fields

As mentioned above, the magnetic fields inside the bore of MRI scanners can be assumed to be harmonic. We consider an ellipsoidal region $\Omega \subset \mathbb{R}^3$ inside the bore and define the semi-axes of the reference ellipsoid accordingly. Further, we assume that the magnetic field $\boldsymbol{B} : \Omega \to \mathbb{R}^3$ can be described by a harmonic polynomial of maximum degree $N \in \mathbb{N}$

$$\boldsymbol{B}(\rho, \mu, \nu) = \sum_{n=0}^{N} \sum_{m=1}^{2n+1} \boldsymbol{A}_{a_1}^{n,m} \mathbb{E}_n^m(\rho, \mu, \nu). \tag{5.13}$$

Considering an ellipsoidal t-design $\{\boldsymbol{x}_i\}$ with t $\geq 2N$ we transform the $L \in \mathbb{N}$ nodes into ellipsoidal coordinates (ρ, μ, ν) using the transformation given in subsection 5.4.5. After obtaining an ellipsoidal t-design in ellipsoidal coordinates $\{(\rho_i, \mu_i, \nu_i)\}$, the coefficients $\boldsymbol{A}_{a_1}^{n,m}$ can be calculated exactly via

$$\boldsymbol{A}_{a_1}^{n,m} = \frac{4\pi}{L \gamma_{a_1}^{n,m} E_n^m(a_1)} \sum_{i=0}^{L-1} \boldsymbol{B}(\rho_i, \mu_i, \nu_i) S_n^m(\mu_i, \nu_i), \tag{5.14}$$

$$\gamma_{a_1}^{n,m} = \frac{4\pi}{L} \sum_{i=0}^{L-1} \left(S_n^m(\mu_i, \nu_i)\right)^2. \tag{5.15}$$

5.4.5 Ellipsoidal coordinates

In this section we give a proper definition of the ellipsoidal coordinates ρ, μ, ν, in which the Laplace partial differential equation can be decomposed into separable functions. This definition is based on the work presented in [52]. Moreover, using ellipsoidal coordinates ρ, μ, ν, the surface of a triaxial ellipsoid can be expressed easily in comparison to Cartesian coordinates. However, integration schemes are commonly given in Cartesian coordinates. Thus, analytical conversion between the coordinate systems is crucial and thus also given below.

For a parameter $s \in \mathbb{R}$, a family of confocal quadrics based on the reference ellipsoid (5.6) is given by

$$\frac{x^2}{a_1^2 + s} + \frac{y^2}{a_2^2 + s} + \frac{z^2}{a_3^2 + s} = 1, \tag{5.16}$$

and especially, when $-a_3^2 < s < \infty$, (5.16) represents a triaxial ellipsoid. For every point (x, y, z) with $xyz \neq 0$, (5.16) is a cubic equation in s with three real roots (see chapter 1 in [52])

$$-a_1^2 < s_3 < -a_2^2 < s_2 < -a_3^2 < s_1 < \infty,$$

defining an ellipsoidal coordinate system. Now, we can introduce ellipsoidal coordinates with dimension of length (ρ, μ, ν) by

$$s_1 = \rho^2 - a_1^2, \quad s_2 = \mu^2 - a_1^2, \quad s_3 = \nu^2 - a_1^2. \tag{5.17}$$

Given a point in these ellipsoidal coordinates, the corresponding Cartesian coordinates can be calculated with the following connection formula [121, 37, 209]

$$\begin{aligned} x &= \frac{1}{h_2 h_3}\rho\mu\nu, \\ y &= \frac{1}{h_1 h_3}\sqrt{\rho^2 - h_3^2}\sqrt{\mu^2 - h_3^2}\sqrt{h_3^2 - \nu^2}, \\ z &= \frac{1}{h_2 h_1}\sqrt{\rho^2 - h_2^2}\sqrt{h_2^2 - \mu^2}\sqrt{h_2^2 - \nu^2}, \end{aligned} \tag{5.18}$$

where $0 \leq \nu \leq h_3 \leq \mu \leq h_2 \leq \rho < \infty$ and $\text{sign}(x) = \text{sign}(\nu)$, $\text{sign}(y) = \text{sign}(\sqrt{h_3^2 - \nu^2})$, $\text{sign}(z) = \text{sign}(\sqrt{h_2^2 - \mu^2})$ and h_1, h_2, h_3 as in (5.7). Thus, to fully fix a Cartesian coordinate in space, we need to store the signs next to the values of ρ, μ and ν.

To obtain the ellipsoidal coordinates given Cartesian coordinates, we start by substituting the system (5.18) into (5.16) and get the cubic equation

$$s^3 + c_2 s^2 + c_1 s + c_0 = 0$$

where

$$\begin{aligned} c_2 &= a_1^2 + a_2^2 + a_3^2 - x^2 - y^2 - z^2, \\ c_1 &= a_1^2 a_2^2 + a_1^2 a_3^2 + a_2^2 a_3^2 \\ &\quad - (a_2^2 + a_3^2)x^2 - (a_1^2 + a_3^2)y^2 - (a_1^2 + a_2^2)z^2, \\ c_0 &= a_1^2 a_2^2 a_3^2 - a_2^2 a_3^2 x^2 - a_1^2 a_3^2 y^2 - a_1^2 a_2^2 z^2. \end{aligned}$$

This equation has the three real roots

$$\begin{aligned} s_1 &= 2\sqrt{p}\cos\left(\frac{\omega}{3}\right) - \frac{c_2}{3}, \\ s_2 &= 2\sqrt{p}\cos\left(\frac{\omega}{3} - \frac{2\pi}{3}\right) - \frac{c_2}{3}, \\ s_3 &= 2\sqrt{p}\cos\left(\frac{\omega}{3} - \frac{4\pi}{3}\right) - \frac{c_2}{3}, \end{aligned}$$

where

$$\begin{aligned} \omega &= \begin{cases} \arccos\left(\frac{q}{p^{3/2}}\right), & \text{for } q < p^{3/2}, \\ 0, & \text{for } q \geq p^{3/2}, \end{cases} \\ p &= \frac{c_2^2 - 3c_1}{9}, \\ q &= \frac{9c_1c_2 - 27c_0 - 2c_2^3}{54}. \end{aligned}$$

Using equation (5.17) we can calculate ρ, μ, ν while taking into account the above sign conventions.

A family of ellipsoids in ellipsoidal coordinates is given by

$$\frac{x^2}{\rho^2} + \frac{y^2}{\rho^2 - h_3^2} + \frac{z^2}{\rho^2 - h_2^2} = 1.$$

For a given reference ellipsoid (a_1, a_2, a_3), a constant $\rho \in (h_2, \infty)$ describes the surface of an ellipsoid from that family and especially by setting $\rho = a_1$ the surface of the reference ellipsoid.

5.4.6 Lamé functions

This section is based on the work [52].

Lamé functions can be divided in four classes

$$\begin{aligned}
\mathcal{K} &= \{P(\chi)\}, \\
\mathcal{L} &= \{\sqrt{|\chi^2 - h_3^2|}P(\chi)\}, \\
\mathcal{M} &= \{\sqrt{|\chi^2 - h_2^2|}P(\chi)\}, \\
\mathcal{N} &= \{\sqrt{|\chi^2 - h_3^2|}\sqrt{|\chi^2 - h_2^2|}P(\chi)\},
\end{aligned}$$

where $P(\chi) = a_0\chi^n + a_1\chi^{n-2} + ... + a_k\chi^{n-2k} + ...$ is a polynomial of maximum degree n, $a_k \in \mathbb{R}$ and $\chi \in \{\rho, \mu, \nu\}$. There are always $2n+1$ linearly independent Lamé functions of degree n, distributed over the four classes and sorted using the index $m = 1, ..., 2n+1$. Developing the Lamé functions of degree n for a given reference ellipsoid is an $\mathcal{O}(n^3)$ problem for all four classes, presented in [52]. The prefactors of the classes $\mathcal{L}, \mathcal{M}$ and $\mathcal{N}$ involve square roots where the sign conventions need to be respected for $x = \mu$ and $x = \nu$, but the polynomial parts remain the same.

We follow the derivations in chapter 3 of [52] for the calculations of the Lamé functions. Let $\alpha = h_3^2 + h_2^2$ and $\beta = h_3^2 h_2^2$.

Lamé functions in class $\mathcal{K}$

Lamé functions of class $\mathcal{K}$ and degree $n \in \mathbb{N}$ have the form

$$K_n(\chi) = \sum_{k=0}^{\infty} a_k \chi^{n-2k} \tag{5.19}$$

with coefficients $a_k \in \mathbb{R}$ and $\chi \in \{\rho, \mu, \nu\}$. We define

$$r = \begin{cases} \frac{n}{2}, & \text{for } n \text{ even}, \\ \frac{n-1}{2}, & \text{for } n \text{ odd}. \end{cases}$$

When substituting equation (5.19) into the Lamé equation, the following algebraic system can be found

$$\begin{aligned}
2(k+2)(2n-2k-1)a_{k+1} = & \\
\alpha\left[p - (n-2k)^2\right]a_k & \\
+ \beta(n-2k+2)(n-2k+1)a_{k-1}, &
\end{aligned} \tag{5.20}$$

for $k \in \{0,...,r\}$ and initial coefficients $a_0 = 1,\ a_{-1} = 0$. Moreover, it holds, that $\forall k \geq r+1 : a_k = 0$. For equation (5.20) non-trivial solutions exist for $r+1$ different constants p. These constants can be determined by solving

$$\begin{vmatrix} K_{1,1} & K_{1,2} & 0 & \dots & & & 0 \\ K_{2,1} & K_{2,2} & K_{2,3} & \ddots & & & \vdots \\ 0 & K_{3,2} & K_{3,3} & \ddots & & & \\ \vdots & \ddots & \ddots & \ddots & & & \\ & & & & K_{r-1,r-1} & K_{r-1,r} & 0 \\ & & & & K_{r,r-1} & K_{r,r} & K_{r,r+1} \\ 0 & \dots & & & 0 & K_{r+1,r} & K_{r+1,r+1} \end{vmatrix} = 0,$$

where

$$\begin{aligned} K_{j,j} &= -\alpha\left[p-(n-2j+2)^2\right] \text{ for } j \in \{1,...,r+1\} \\ K_{j,j+1} &= 2j(2n-2j+1), \text{ for } j \in \{1,...,r\} \\ K_{j+1,j} &= -\beta(n-2j+1)(n-2j+2), \text{ for } j \in \{1,...,r\}. \end{aligned} \tag{5.21}$$

For each of the $r+1$ solutions p, $r+1$ coefficients a_k can be calculated recursively and we thus obtain $r+1$ Lamé functions of class $\mathcal{K}$ and degree n.

Lamé functions in classes $\mathcal{L}$ and $\mathcal{M}$

Lamé functions of class $\mathcal{L}$ and degree $n \in \mathbb{N}$ have the form $L_n(\chi) = \sqrt{|\chi^2 - h_3^2|}P_{n-1}(\chi)$, where

$$P_{n-1}(\chi) = \sum_{k=0}^{\infty} b_k \chi^{n-1-2k} \tag{5.22}$$

with coefficients $b_k \in \mathbb{R}$ and $\chi \in \{\rho, \mu, \nu\}$. Note, that the sign convention needs to be respected for the non-polynomial part when evaluating for $\chi = \nu$. We define

$$r = \begin{cases} \frac{n}{2}, \text{ for } n \text{ even}, \\ \frac{n+1}{2}, \text{ for } n \text{ odd}. \end{cases}$$

When substituting equation (5.22) into the Lamé equation, the following algebraic system can be found

$$\begin{aligned} 2(k+1)(2n-2k-1)b_{k+1} = & \\ & \left(\alpha\left[p-(n-2k-1)^2\right] - (2n-4k-1)h_2^2\right) b_k \\ & + \beta(n-2k+1)(n-2k)b_{k-1}, \end{aligned} \tag{5.23}$$

for $k \in \{0, ..., r-1\}$ and initial coefficients $b_0 = 1,\ b_{-1} = 0$. Moreover, it holds, that $\forall k \geq r : b_k = 0$. For equation (5.23) non-trivial solutions exist for r different constants p. These constants can be determined by solving

$$\begin{vmatrix} L_{1,1} & L_{1,2} & 0 & \dots & & & & 0 \\ L_{2,1} & L_{2,2} & L_{2,3} & \ddots & & & & \vdots \\ 0 & L_{3,2} & L_{3,3} & \ddots & & & & \\ \vdots & \ddots & \ddots & \ddots & & & & \\ & & & & L_{r-2,r-2} & L_{r-2,r-1} & 0 & \\ & & & & L_{r-1,r-2} & L_{r-1,r-1} & L_{r-1,r} & \\ 0 & \dots & & & 0 & L_{r,r-1} & L_{r,r} & \end{vmatrix} = 0,$$

where

$$\begin{aligned} L_{j,j} &= -\alpha \left[p - (n-2j+1)^2\right] + (2n-4j+4)h_2^2, \\ &\quad \text{for } j \in \{1, ..., r\} \\ L_{j,j+1} &= 2j(2n-2j+1), \text{ for } j \in \{1, ..., r-1\} \\ L_{j+1,j} &= -\beta(n-2j+1)(n-2j), \text{ for } j \in \{1, ..., r-1\}. \end{aligned} \tag{5.24}$$

With r solutions p the coefficients b_k can be calculated and we obtain r Lamé functions of class $\mathcal{L}$ and degree n.

Lamé functions of class $\mathcal{M}$ and degree $n \in \mathbb{N}$ have the form $M_n(\chi) = \sqrt{|\chi^2 - h_2^2|}P_{n-1}(\chi)$. Here, the sign convention needs to be respected for the non-polynomial part when evaluating for $\chi = \mu$. The calculation of the coefficients b_k is similar to class $\mathcal{L}$, but h_2^2 needs to be replaced with h_3^2 in equations (5.23) and (5.24).

Lamé functions in class $\mathcal{N}$

Lamé functions of class $\mathcal{N}$ and degree $n \in \mathbb{N}$ have the form $N_n(\chi) = \sqrt{|\chi^2 - h_3^2|}\sqrt{|\chi^2 - h_2^2|}P_{n-2}(\chi)$, where

$$P_{n-2}(\chi) = \sum_{k=0}^{\infty} c_k \chi^{n-2-2k} \tag{5.25}$$

with coefficients $c_k \in \mathbb{R}$ and $\chi \in \{\rho, \mu, \nu\}$. Note, that the sign convention needs to be respected for the non-polynomial part when evaluating for $\chi = \nu$ and $\chi = \mu$. We define

$$r = \begin{cases} \frac{n}{2}, \text{ for } n \text{ even}, \\ \frac{n-1}{2}, \text{ for } n \text{ odd}. \end{cases}$$

When substituting equation (5.25) into the Lamé equation, the following algebraic system can be found

$$\begin{aligned} 2(k+1)(2n-2k-1)c_{k+1} = & \\ \alpha \left[p - (n-2k-1)^2\right] c_k & \\ + \beta(n-2k-1)(n-2k)c_{k-1}, & \end{aligned} \tag{5.26}$$

for $k \in \{0, ..., r-1\}$ and initial coefficients $c_0 = 1,\ c_{-1} = 0$. Moreover, it holds, that $\forall k \geq r : c_k = 0$. For equation (5.26) non-trivial solutions exist for r different constants p. These constants can be determined by solving

$$\begin{vmatrix} N_{1,1} & N_{1,2} & 0 & \dots & & & & 0 \\ N_{2,1} & N_{2,2} & N_{2,3} & \ddots & & & & \vdots \\ 0 & N_{3,2} & N_{3,3} & \ddots & & & & \\ \vdots & \ddots & \ddots & \ddots & & & & \\ & & & & N_{r-2,r-2} & N_{r-2,r-1} & 0 & \\ & & & & N_{r-1,r-2} & N_{r-1,r-1} & N_{r-1,r} & \\ 0 & \dots & & & 0 & N_{r,r-1} & N_{r,r} & \end{vmatrix} = 0,$$

where

$$\begin{aligned} N_{j,j} &= -\alpha \left[p - (n-2j+1)^2\right], \text{ for } j \in \{1, ..., r\} \\ N_{j,j+1} &= 2j(2n-2j+1), \text{ for } j \in \{1, ..., r-1\} \\ N_{j+1,j} &= -\beta(n-2j-1)(n-2j), \text{ for } j \in \{1, ..., r-1\}. \end{aligned} \tag{5.27}$$

With these r solutions p the coefficients c_k can be calculated and we obtain r Lamé functions of class $\mathcal{N}$ and degree n.

5.4.7 Ellipsoidal Harmonics

This section is based on the work [52].

After calculation of the Lamé functions, the inner ellipsoidal harmonics $\mathbb{E}_n^m$ can be derived as the product of the Lamé functions evaluated at the ellipsoidal coordinates

$$\mathbb{E}_n^m(\rho, \mu, \nu) = E_n^m(\rho) E_n^m(\mu) E_n^m(\nu). \tag{5.28}$$

It is shown in [52], that $\mathbb{E}_n^m$ are harmonic polynomials. It follows directly, that $\{\mathbb{E}_n^m : n \leq N\}$ for $N \in \mathbb{N}$ is a set with $[2N+1] + [2(N-1)+1] + ... + [2(1)+1] + [1] = (N+1)^2$ linearly independent elements and a subset of the set of harmonic polynomials. Since the space of harmonic polynomials with degree $n \leq N$ has the dimension $(N+1)^2$, it follows that $\{\mathbb{E}_n^m : n \leq N\}$ is a maximal linear independent subset and thus a basis of the harmonic polynomials of degree $n \leq N$.

Furthermore, we define surface ellipsoidal harmonics S_n^m as

$$S_n^m(\mu, \nu) = E_n^m(\mu) E_n^m(\nu), \tag{5.29}$$

recalling, that $\rho = a_1$ holds on the surface of the reference ellipsoid S_{a_1}. It follows, that also $E_n^m(\rho) = E_n^m(a_1)$ is a constant on the ellipsoid surface and thus $S_n^m(\mu, \nu) = {}^{\mathbb{E}_n^m(a_1,\mu,\nu)}/_{E_n^m(a_1)}$ is a polynomial with maximum degree n. In [52] it is shown, that the surface ellipsoidal harmonics are orthogonal to each other with normalization constants $\gamma_{a_1}^{n,m} \in \mathbb{R}$ given via

$$\gamma_{a_1}^{n,m} = \oint_{S_{a_1}} \left(S_n^m(\mu, \nu)\right)^2 \, \mathrm{d}\Omega(\mu, \nu). \tag{5.30}$$

5.5 Inproceedings 1: Simulation Study

Abstract

Exact knowledge on the magnetic fields used in tomographic imaging systems is important for accurate sequence planning and model-based image reconstruction in existing devices. It is common to measure the magnetic fields on a small subset of points and use spherical harmonics to approximate the fields inside a spherical region. However, most scanner bores could be better filled using a cylindrical or ellipsoidal region. In this work, we present the application of ellipsoidal harmonics for efficient approximation of a typical magnetic field in magnetic particle imaging.

5.5.1 Introduction

In tomographic imaging methods based on magnetic fields, e.g. magnetic resonance imaging and magnetic particle imaging (MPI), the exact values of the magnetic fields in the field of view (FOV) are of great interest and play a major role in signal encoding [220, 248]. Depending on the scanners underlying coil setup, the magnetic fields are by no means ideal in the FOV. For instance in MPI, knowledge on the non-linearity of the magnetic fields can be used for accurate sequence design, to speed up the calibration process when using multiple patches [27], or for higher accuracy of model-based system matrices [4]. Furthermore, knowing the exact values of the magnetic fields is important for the development and verification of new receive coils or field generators [97, 75].

The magnetic fields can be measured using a magnetic field sensor attached to a robot. The naive ansatz, covering every position on a highly resolved three-dimensional grid would be a long and tedious process. For this reason, more efficient measurement methods were introduced in which the field can be expanded very efficiently into a series of spherical harmonic functions with only a few measurement points on a spherical surface in the form of t-designs [28, 33]. However, typical scanner bores have a cylindrical shape, such that several spheres, shifted along the bore axis, have to be measured to cover the entire FOV. But even when the spheres are shifted with big overlap, this procedure leaves areas uncovered by any of the spheres. In this work we instead consider an ellipsoidal volume, which much better covers typical scanner bores. To this end, we consider ellipsoidal harmonic functions and the associated series expansion, which has not yet been applied to describe magnetic fields in tomographic imaging so far. However, in astrophysics calculations of the gravitational potential of (non ideally round) celestial bodies get more efficient using ellipsoidal harmonics [82]. In this study we show, how ellipsoidal harmonics can be used to efficiently measure and represent magnetic fields in MPI.

5.5.2 Methods and Materials

Theory

Magnetic fields in a source-free region $\Omega_{\mathrm{FOV}} \subset \mathbb{R}^3$ can be assumed to be harmonic, i.e. they fulfill Laplace's equation. This applies to all magnetic fields $\boldsymbol{B} : \mathbb{R}^3 \to \mathbb{R}^3$ that are located within the bore of an MPI scanner, as no currents flow there. The transformation of the Laplace equation $\Delta B_i(\boldsymbol{x}) = 0$, for $i \in \{1,2,3\}$ and $\boldsymbol{x} \in \Omega_{\mathrm{FOV}}$ into an ellipsoidal coordinates, starts with the definition of a reference ellipsoid

$$\frac{x_1^2}{a_1^2} + \frac{x_2^2}{a_2^2} + \frac{x_3^2}{a_3^2} = 1, \tag{5.31}$$

where $0 < a_3 < a_2 < a_1$ are the three semi-axes and $x_1, x_2, x_3 \in \mathbb{R}$ Cartesian coordinates. The linear eccentricities of the reference ellipsoid are given as

$$h_1 = \sqrt{(a_2^2 - a_3^2)}, h_2 = \sqrt{(a_1^2 - a_3^2)}, h_3 = \sqrt{(a_1^2 - a_2^2)}. \tag{5.32}$$

By introducing an orthogonal ellipsoidal coordinate system ρ, μ, ν with $0 \leq \nu^2 \leq h_3^2 \leq \mu^2 \leq h_2^2 \leq \rho^2 < \infty$ and performing a separation of variables on the Laplace equation, one ends up with the so-called Lamé equation [52], whose solutions $E_n^m : \mathbb{R} \to \mathbb{R}$ for $m \in \mathbb{N}, n \in \mathbb{N}_0$ are called Lamé functions. Lamé functions can be divided in four classes

$$\begin{aligned}
\mathcal{K} &= \{P(x)\}, \\
\mathcal{L} &= \{\sqrt{|x^2 - h_3^2|}P(x)\}, \\
\mathcal{M} &= \{\sqrt{|x^2 - h_2^2|}P(x)\}, \\
\mathcal{N} &= \{\sqrt{|x^2 - h_3^2|}\sqrt{|x^2 - h_2^2|}P(x)\},
\end{aligned}$$

where $P(x) = \alpha_0 x^n + \alpha_1 x^{n-2} + ... + \alpha_k x^{n-2k} + ...$ is a polynomial of maximum degree n and $x \in \{\rho, \mu, \nu\}$. There are always $2n + 1$ Lamé functions of degree n, distributed over the four classes and sorted using the index $m = 1, ..., 2n + 1$. The conversion between Cartesian coordinates (x_1, x_2, x_3) and ellipsoidal coordinates (ρ, μ, ν) is not straightforward and additional sign conventions have to be respected to achieve uniqueness. We refer the interested reader to [209]. Lamé functions of each class can be determined for a given reference ellipsoid, by solving an $\mathcal{O}(n^3)$ eigenvalue problem for each class and each $n \in \mathbb{N}$ [52], leading to the inner ellipsoidal harmonics $\mathbb{E}_n^m(\rho, \mu, \nu) = E_n^m(\rho)E_n^m(\mu)E_n^m(\nu)$ and the surface ellipsoidal harmonics $S_n^m(\mu, \nu) = E_n^m(\mu)E_n^m(\nu)$. On the ellipsoidal surface holds $\rho = a_1$. With help of the inner ellipsoidal harmonics $\mathbb{E}_n^m$ with $n \leq L$, which pose a basis of the harmonic polynomials with maximum degree $L \in \mathbb{N}$, the magnetic field components can be calculated inside the reference ellipsoid (by placing Dirichlet boundary conditions on the surface) using the following expansion:

$$B_i(\rho, \mu, \nu) \approx \sum_{n=0}^{L} \sum_{m=1}^{2n+1} A_n^m \mathbb{E}_n^m(\rho, \mu, \nu), \tag{5.33}$$

where

$$A_n^m = \frac{1}{\gamma_n^m E_n^m(a_1)} \oint_{S_{a_1}} B_i(a_1, \mu, \nu) S_n^m(\mu, \nu) \, \mathrm{d}\Omega(\mu, \nu), \tag{5.34}$$

$$\gamma_n^m = \oint_{S_{a_1}} S_n^m(\mu, \nu)^2 \, \mathrm{d}\Omega(\mu, \nu), \tag{5.35}$$

where S_{a_1} is the surface of the reference ellipsoid. Equation (5.33) is exact, if the magnetic field can be described by a polynomial of maximum degree L. Under this assumption, the surface integrals in (5.34) can be calculated exactly using a finite sum over an ellipsoidal t-design with $t \geq 2L$ (this follows from the existence of a transformation between ellipsoidal surface integrals and spherical surface integrals given in [52]). To this end, the Cartesian coordinates (y_1, y_2, y_3) of a spherical t-design need to be shifted to the ellipsoid surface using

$$x_1 = y_3 a_1, \; x_2 = y_1 \sqrt{a_1^2 - h_3^2}, \; x_3 = y_2 \sqrt{a_1^2 - h_2^2},$$

and converted to ellipsoidal coordinates afterwards.

Simulations

To demonstrate the accuracy and applicability of the presented expansion, we consider the x-drive field of the preclinical MPI system (25/20 FF) from Bruker Corporation, Ettlingen, Germany. Field amplitude values calculated by the FEM software COMSOL Multiphysics[1] are used on the ellipsoidal surface points given by the t-design. To highlight the benefits of ellipsoidal harmonics, we want the magnetic field to be calculated inside a cylinder of 21.2 cm length and 9 cm diameter, which are the dimensions of the dedicated receive coil presented in [97]. To this end, the reference ellipsoid is set using the semi-axis $\boldsymbol{a} = (17.5, 5.61, 5.6)$ cm and an ellipsoidal 12-design with 86 points is chosen, as displayed in Figure 5.6. The implementation of the ellipsoidal harmonic expansion was written in Julia.

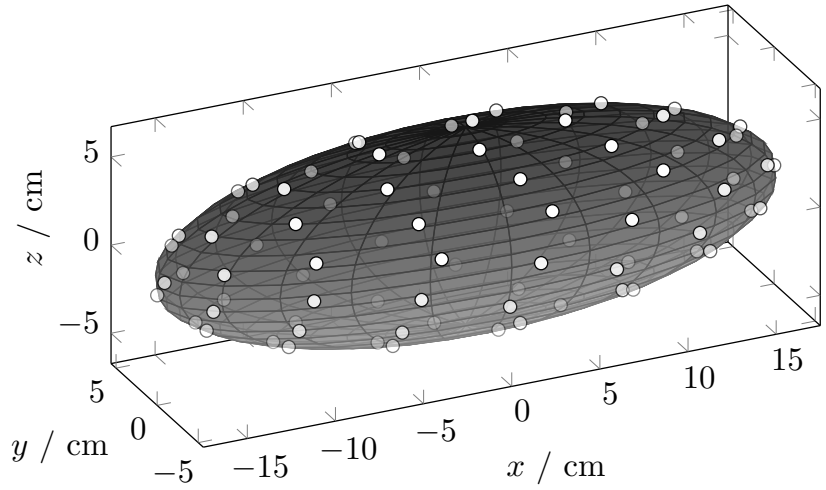

Figure 5.6: Surface-plot of the reference ellipsoid with semi-axis $\boldsymbol{a} = (17.5, 5.61, 5.6)$ cm. The 86 points of an ellipsoidal 12-design are displayed on top.

5.5.3 Results

The calculated field for $z = 0$ on an 71×23 rectangular grid using the ellipsoidal harmonic expansion is shown in the upper plot in Figure 5.7. The magnetic field aligns in negative x-direction, as it would be expected for the x-drive field. For comparison, the simulated magnetic field using COMSOL is shown on the same grid as well as a difference plot. The absolute error inside the ellipsoid has a mean value of 0.1 mT equaling 1.5 % of the mean absolute value of the simulated field and gets slightly larger towards the edges of the ellipsoid (with a maximum absolute error of 0.8 mT). Outside the ellipsoid, the absolute error gets very large, which can be even observed in the plotted fields and not only in the difference plot.

5.5.4 Discussion and Conclusion

With the presented ellipsoidal harmonic expansion, a typical MPI drive-field could be represented effectively using only 86 data points for the above given reference ellipsoid enveloping a cylinder of 21.2 cm length and 9 cm diameter. Using spherical harmonics to represent the magnetic field in the full cylinder, at least three separate spheres along the x-axis would be necessary.

[1] COMSOL Multiphysics v.6.0. www.comsol.com. COMSOL AB, Stockholm, Sweden

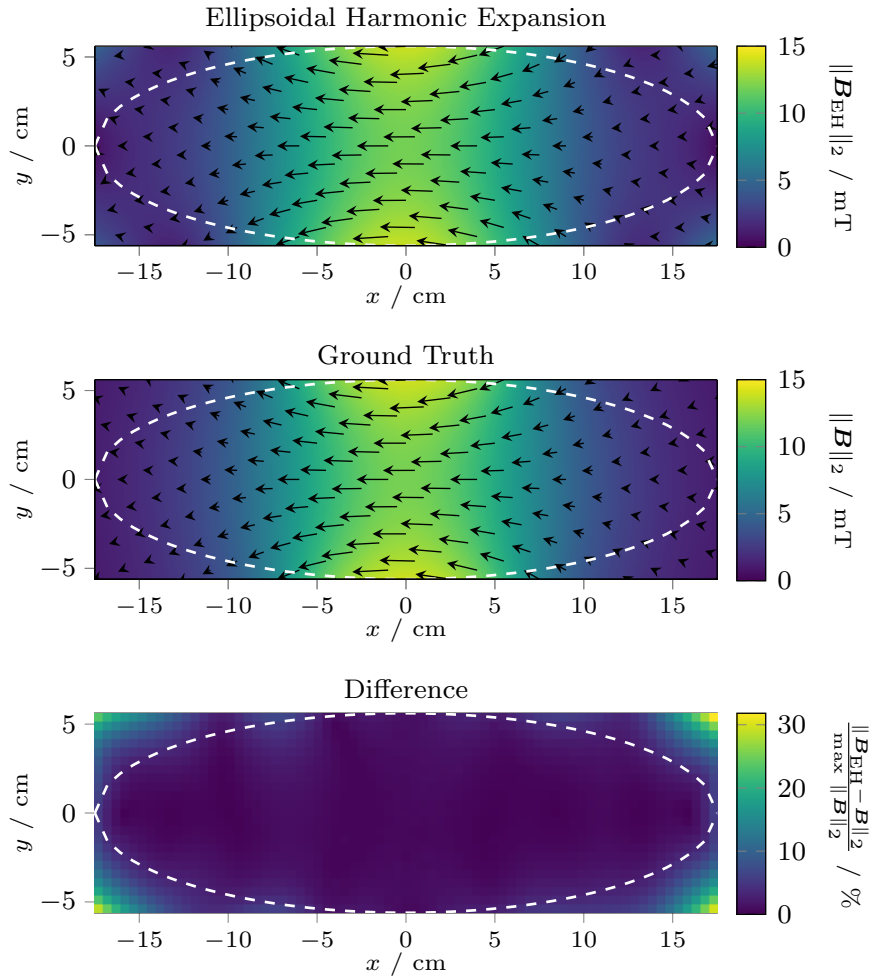

Figure 5.7: Shown are the calculated magnetic fields in the xy-plane for $z = 0$ using ellipsoidal harmonics (top) and the simulation software COMSOL (middle). The norm is color-coded, the field direction is displayed using field arrows. Furthermore, a difference plot is given (bottom).

The small absolute error of the field inside the ellipsoid underlines the accuracy of the ellipsoidal expansion. It was to be expected, that the error raises outside the ellipsoid, since equation (5.33) is not valid there. The slightly increasing error close to the edge of the ellipsoid could be circumvented by using a reference ellipsoid, which is slightly bigger than the FOV. Moreover, a lower truncation error could be expected, when using a larger ellipsoidal t-design, with $t > 12$. When using the method on measured data, the rather small approximation error has to be contextualized to the displacement error of the robot and the accuracy of the magnetic field sensor.

Concluding, ellipsoidal harmonic expansion proves to be a very powerful tool for the effective measurement and representation of magnetic fields in tomographic imaging devices. The effectiveness of this method was demonstrated through the simulation of a drive-field on a preclinical MPI-scanner. In comparison to the currently used spherical harmonics, two more degrees of freedom allow to much better match the region of interest. This is especially useful for an oval scanner bore [99]. An in-dept error analysis as well as a profound variety of test cases remain necessary for future work.

5.6 Inproceedings 2: Experimental Study

Abstract

This work demonstrates the application of ellipsoidal harmonic expansions for magnetic field representation in Magnetic Particle Imaging (MPI) using measured data. While previous studies focused on simulated fields, we validate the method with field data acquired from a selection field generator of an MPI head imaging system using an ellipsoidal t-design. The approach is validated by comparing the harmonic expansion results to dense principal axis measurements, confirming accurate field characterization. This study highlights the potential of ellipsoidal harmonics to improve the speed and accuracy of magnetic field measurements and representation in MPI.

5.6.1 Introduction

Understanding magnetic fields in Magnetic Particle Imaging (MPI) is essential for optimizing system performance and accuracy. Field inhomogeneities or distortions can cause inaccurate spatial representation of nanoparticles, affecting diagnostic outcomes or industrial processes. Accurate field knowledge allows for improved system design, leading to higher image quality and more precise nanoparticle localization.

Measuring magnetic fields on a dense three-dimensional grid is time-consuming and inefficient. To overcome this, more efficient measurement techniques have been developed enabling the magnetic field to be effectively represented as a series expansion of harmonic functions [28, 33]. To determine the coefficients of this expansion, only a limited number of measurement points, arranged according to t-designs, are required. These points are typically distributed on a spherical surface. Recently, the use of Ellipsoidal Harmonic Expansions (EHE) was introduced. They offer two more degrees of freedom enabling a much more flexible and efficient description of magnetic fields in MPI as scanner bores usually have cylindrical shape [242].

While ellipsoidal harmonics have previously been applied to simulated data, this study extends their application to experimentally acquired data. We demonstrate the effectiveness of this approach by collecting field data from the gradient field of our institute's head imaging system [280] using an ellipsoidal t-design. To assess the accuracy and reliability of the method we compare the ellipsoidal harmonic representation with dense measurements taken along the principal axes.

5.6.2 Methods and Materials

Source-free magnetic fields $\boldsymbol{B} : \mathbb{R}^3 \supset \Omega \to \mathbb{R}^3$ can be represented by a polynomial of maximum degree $N \in \mathbb{N}$. Thus, using an EHE within a reference ellipsoid defined by it's semi-axes $(a_1, a_2, a_3) \in \mathbb{R}^3$, the field can be expressed as:

$$\boldsymbol{B}(\rho, \mu, \nu) = \sum_{n=0}^{N} \sum_{m=1}^{2n+1} \boldsymbol{A}_{a_1}^{n,m} \mathbb{E}_n^m(\rho, \mu, \nu). \tag{5.36}$$

Here (ρ, μ, ν) are ellipsoidal coordinates, $\mathbb{E}_n^m : \mathbb{R} \to \mathbb{R}$ are inner ellipsoidal harmonics of degree $n \in \mathbb{N}$ and order $m \in \{1, ..., 2n+1\}$ and $A_{a_1}^{n,m} \in \mathbb{R}$ denote the according coefficients. To compute these coefficients, surface integrals over the reference ellipsoid need to be solved, for which we employ an ellipsoidal t-design as a quadrature. For further details on the theory of ellipsoidal harmonics, ellipsoidal t-designs and how to use them to describe magnetic fields, we refer to [242, 52].

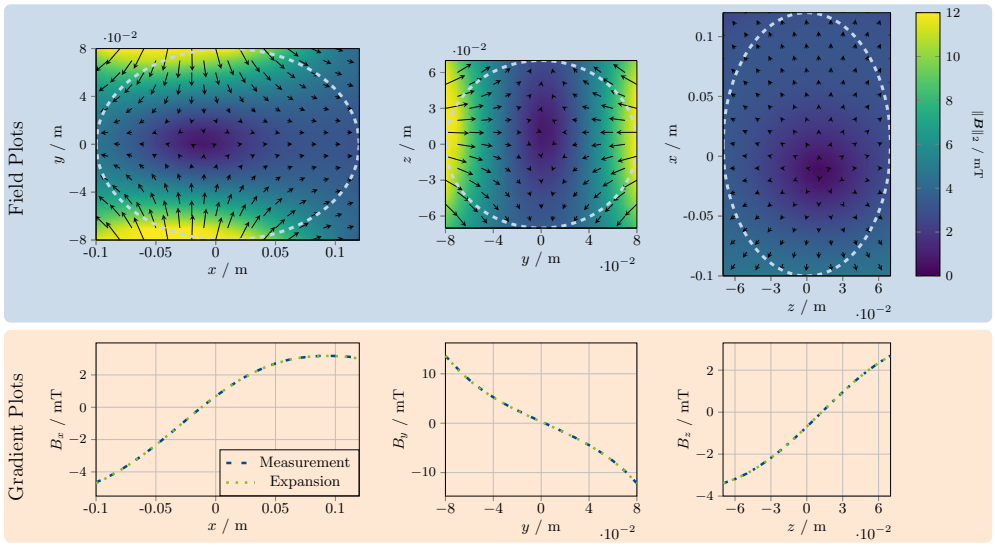

Figure 5.8: Top row: sectional views of the magnetic field resulting from the ellipsoidal harmonic expansion. Bottom row: comparison of the field values with the test measurements along the principle axis.

A reference ellipsoid with $\boldsymbol{a} = (0.11, 0.08, 0.07)$ m centered at $(0.01, 0, 0)$ m was chosen to cover the scanner bore of the imaging system described in [280]. An ellipsoidal t-design with $t = 14$ was used, defining 114 measurement points on the surface of the reference ellipsoid. Measurements used a three-axis Hall-effect sensor on a robot connected to a 3-channel Gaussmeter (M460, Lake Shore Cryotronics). For verification, measurements were taken at 55 control points (Ω_{ctrl}) with equidistant intervals of 0.01 m on the three main axes: 23 in x-direction ($y = z = 0$ m), 17 in y-direction ($x = 0.01$ m, $z = 0$ m) and 15 in z-direction ($x = 0.01$ m, $y = 0$ m). A quantitative evaluation is done by calculating the mean relative error normalized by the mean field.

5.6.3 Results

In Figure 5.8 sectional views of the magnetic field obtained from the EHE are shown for each central plane. The characteristics of the MPI selection field are well represented and the dominant y-gradient is clearly visible. White dashed lines show the reference ellipsoid on which the points of the t-design are located. A comparison of the gradients on the control points is shown along the principal axes in the second row. No visual differences are apparent. Quantitative analysis confirms a high accuracy with a mean error of $\xi = 0.78\,\%$.

5.6.4 Discussion and Conclusion

The results clearly demonstrate that EHE are a powerful tool for measuring and representing magnetic fields in MPI. While previous work has only used simulated field data, we have shown in this study that the method can also be applied to measured data. The greater flexibility of the geometric shape of an ellipsoid permits superior coverage of typical MPI scanner bores in comparison to the well-established spherical harmonic expansions. Potential measurement inaccuracies did not affect the stability of the method in our case as the mean error below 1 % confirms. However, a sophisticated error analysis remains for future work.

6

Discussion

Chapter 2 provided a structured overview of the challenges and necessary advancements for the clinical translation of MPI. It examined the current state of research and highlighted critical issues such as hardware requirements, tracer availability, regulatory approval, image reconstruction, and algorithmic developments. Despite MPI's promise as a highly sensitive and quantitative imaging modality, its clinical adoption is currently hindered by the lack of tailored and medically approved tracers, accredited hardware solutions, and sufficient robustness in patient environments. Additionally, state-of-the-art image reconstruction remains reliant on manual input from imaging experts and does not yet meet the diverse requirements of different clinical applications.

A key takeaway from this discussion is the intricate interplay between different research domains in MPI. Hardware developments influence reconstruction strategies, while algorithmic advancements can compensate for limitations in signal detection and tracer performance. The challenge of achieving clinically viable MPI solutions is thus not confined to any single research track but instead depends on a holistic approach that integrates hardware, tracer development, and computational methodologies. For instance, the development of fast image acquisition, in combination with robust and efficient reconstruction algorithms, directly impacts MPI's feasibility for real-world medical applications.

A major strategic milestone for the field would be the ability to generate super-resolved, high-contrast images with minimal calibration effort and without the need for manual parameter fine-tuning. This could be achieved through a combination of sophisticated reconstruction methodologies and deep-learning-based approaches that leverage accurate modeling of the MPI system equation. Furthermore, a breakthrough such as the publication of the first human MPI image would not only validate MPI's clinical potential but also serve as a catalyst for accelerated research efforts and industrial investment. Such progress would further drive the development of tailored, medically approved tracers optimized for MPI's unique signal generation mechanism.

Within this broader landscape, the cumulative part of this dissertation has contributed to advancing MPI toward clinical usability by focusing on improvements in calibration, regularization, and efficient field representation. These contributions directly address key challenges in image reconstruction.

Chapter 3 introduced an extrapolation method to reduce the extensive measurement effort required for system matrix calibration. This addresses a fundamental limitation in MPI, where system matrix acquisition can be highly time-consuming and impractical for clinical

deployment. By enabling accurate extrapolation of calibration data to a larger FOV, this method paves the way for significantly streamlined workflows in clinical applications. More importantly, its full potential lies in its integration with complementary techniques such as compressed sensing and learning-based approaches, which could further minimize calibration requirements while maintaining reconstruction accuracy.

Chapter 4 tackled another major challenge in MPI image reconstruction – regularization tuning – by proposing an automated parameter selection approach. This method reformulates the complex interplay of multiple regularization parameters into a single hyperparameter: the number of iterations in the iterative solver. By simplifying parameter selection, this approach reduces the manual fine-tuning required for high-quality image reconstruction, making MPI more accessible for clinical use. Furthermore, learning-based strategies trained on diverse MPI datasets could enhance this approach by optimizing termination criteria across different imaging scenarios, measurement settings, and noise statistics. The ability to automatically adapt regularization to varying clinical conditions represents a crucial step toward robust and user-independent MPI reconstruction.

Finally, Chapter 5 explored a novel approach to efficiently measure and represent magnetic fields using ellipsoidal harmonic expansions. This method has broad applicability to all tomographic imaging modalities relying on magnetic fields with different geometric configurations. The demonstrated effectiveness of ellipsoidal harmonic expansions for field modeling in cylindrical bores of both MRI and MPI suggests their potential for multimodal imaging systems. Notably, this method could contribute to the development of integrated MPI/MRI platforms, which combine the high anatomical resolution of MRI with MPI's high-sensitivity functional imaging capabilities. Such hybrid systems could offer unparalleled advantages by merging background tissue data from MRI with functional or contrast-enhanced imaging from MPI within a single scanner, thereby expanding MPI's clinical utility.

The findings and methodologies presented in this dissertation contribute to the overarching goal of making MPI clinically viable. By addressing fundamental challenges in image reconstruction and calibration, these contributions help pave the way for MPI's transition from a promising preclinical technology to a deployable clinical imaging modality. Future research must continue to bridge the gap between theoretical advancements and practical implementation, ensuring that innovations in tracers, hardware, and computational techniques collectively result in reliable and scalable imaging solutions. Furthermore, the clinical adoption of MPI critically depends on rigorous validation of its quantitative capabilities. Establishing MPI as a robust quantitative imaging tool requires reproducibility across different MPI systems, tracer formulations, and imaging protocols. Standardized calibration procedures, inter-scanner variability assessments, and harmonized data acquisition strategies are necessary to meet regulatory requirements and ensure consistency in clinical applications. Addressing these challenges will be instrumental in unlocking MPI's full potential for quantification in medical diagnostics and therapeutic monitoring. Moreover, achieving clinical translation requires not only improvements in image reconstruction, hardware and tracer, but also seamless integration into clinical workflows. To maximize MPI's impact, future research must continue to explore its role in clinical decision-making, ensuring that it provides actionable diagnostic or therapeutic insights beyond what is currently achievable with established imaging techniques.

Acknowledgments

I want to thank all my colleagues at the Institute of Biomedical Imaging and everyone who has collaborated with me during the past four years. It's been a great time of learning, teamwork, and shared curiosity. I'm especially grateful to Tobias Knopp for his guidance, his open door, and the way he supports and encourages people to grow. Finally, I want to thank my family and friends for their endless support and for bringing so much joy and balance into my life.

During the preparation of this dissertation, I also used language tools such as DeepL Write (DeepL SE, Cologne, Germany) and ChatGPT (OpenAI, San Francisco, USA) to help refine the wording and improve readability. These tools were used only for language editing and had no influence on the scientific content or original research presented here.

Bibliography

1. Aderhold, E., Mirzojan, L., Scheel, J.-P., Ahlborg, M., Sevecke, F., Stagge, P., Kretov, E., Buzug, T. & Graeser, M. Thermal Considerations Towards a Highly Flexible Multi-Core Selection and Focus Field Generator. en. doi:10.18416/IJMPI.2025.2503019 (2025).
2. Ahlborg, M., Kaethner, C., Knopp, T., Szwargulski, P. & Buzug, T. M. Using data redundancy gained by patch overlaps to reduce truncation artifacts in magnetic particle imaging. *Physics in Medicine and Biology* **61,** 4583–4598. doi:10.1088/0031-9155/61/12/4583 (2016).
3. Akiko Ohki, Tomomi Kuboyabu, Marina Aoki, Mikiko Yamawaki & Kenya Murase. Quantitative Evaluation of Tumor Response to Combination of Magnetic Hyperthermia Treatment and Radiation Therapy Using Magnetic Particle Imaging. *International Journal of Nanomedicine and Nanosurgery* **2.** doi:10.16966/2470-3206.117 (2016).
4. Albers, H., Knopp, T., Möddel, M., Boberg, M. & Kluth, T. Modeling the magnetization dynamics for large ensembles of immobilized magnetic nanoparticles in multi-dimensional magnetic particle imaging. *Journal of Magnetism and Magnetic Materials* **543** (2022).
5. Albers, H., Thieben, F., Boberg, M., Scheffler, K., Knopp, T. & Kluth, T. Model-based Calibration and Image Reconstruction with Immobilized Nanoparticles. en. *International Journal on Magnetic Particle Imaging IJMPI.* doi:10.18416/IJMPI.2023.2303002 (2023).
6. Antonelli, A., Sfara, C., Rahmer, J., Gleich, B., Borgert, J. & Magnani, M. Red Blood Cells as Carriers in Magnetic Particle Imaging. *Biomedizinische Technik/Biomedical Engineering* **58.** doi:10.1515/bmt-2012-0065 (Jan. 2013).
7. Antonelli, A., Szwargulski, P., Scarpa, E. S., Thieben, F., Cordula, G., Ambrosi, G., Guidi, L., Ludewig, P., Knopp, T. & Magnani, M. Development of Long Circulating Magnetic Particle Imaging Tracers: Use of Novel Magnetic Nanoparticles and Entrapment into Human Erythrocytes. *Nanomedicine* **15,** 739–753. doi:10.2217/nnm-2019-0449 (Apr. 2020).
8. Arami, H., Teeman, E., Troksa, A., Bradshaw, H., Saatchi, K., Tomitaka, A., Gambhir, S. S., Häfeli, U. O., Liggitt, D. & Krishnan, K. M. Tomographic magnetic particle imaging of cancer targeted nanoparticles. *Nanoscale* **9,** 18723–18730. doi:10.1039/C7NR05502A (47 2017).
9. Arnaoudov, I. & Venkov, G. Relations between spheroidal and spherical harmonics. *Doklady Bolgarskoi Akademiya Nauk* **63** (Jan. 2010).
10. Askin, B., Güngör, A., Alptekin Soydan, D., Saritas, E. U., Top, C. B. & Cukur, T. PP-MPI: A deep plug-and-play prior for magnetic particle imaging reconstruction, 105–114. doi:10.1007/978-3-031-17247-2_11 (2022).
11. Aşkın, B., Güngör, A., Soydan, D. A., Top, C. B. & Cukur, T. *A CNN Based Super-Resolution Technique for Magnetic Particle Imaging System Matrix* in *2021 29th Signal Processing and Communications Applications Conference (SIU)* (2021), 1–4. doi:10.1109/SIU53274.2021.9477772.
12. Bai, S., Gai, L., Zhang, Q., Kang, Y., Liu, Z., He, Y., Liu, W., Jiang, T., Du, Z., Du, S., Gao, S., Zhang, M. & Li, T. Development of a human-size magnetic particle imaging device for sentinel lymph node biopsy of breast cancer. *Frontiers in Bioengineering and Biotechnology* **12.** doi:10.3389/fbioe.2024.1327521 (Feb. 2024).
13. Bai, S., Li, T., Li, K., Huang, P., Du, Z., Yoshida, T. & Zhang, M. *High Resolution Enlarged Open-Bore Narrow-band Magnetic Particle Imaging Based on Double-layer Linear Scanning Structure* in *2023 IEEE International Magnetic Conference - Short Papers* (2023), 1–2. doi:10.1109/INTERMAGShortPapers58606.2023.10228607.
14. Bakenecker, A. C., von Gladiss, A., Schwenke, H., Behrends, A., Friedrich, T., Lüdtke-Buzug, K., Neumann, A., Barkhausen, J., Wegner, F. & Buzug, T. M. Navigation of a magnetic micro-robot through a cerebral aneurysm phantom with magnetic particle imaging. *Sci. Rep.* **11,** 14082. doi:10.1038/s41598-021-93323-4 (July 2021).
15. Bakenecker, A. C., Ahlborg, M., Debbeler, C., Kaethner, C., Buzug, T. M. & Lüdtke-Buzug, K. Magnetic particle imaging in vascular medicine. *Innovative Surgical Sciences* **3,** 179–192. doi:doi:10.1515/iss-2018-2026 (2018).
16. Bakenecker, A. C., von Gladiss, A., Friedrich, T., Heinen, U., Lehr, H., Lüdtke-Buzug, K. & Buzug, T. M. Actuation and visualization of a magnetically coated swimmer with magnetic particle imaging. *Journal of Magnetism and Magnetic Materials* **473,** 495–500. doi:https://doi.org/10.1016/j.jmmm.2018.10.056 (2019).

17. Baltruschat, I. M., Szwargulski, P., Griese, F., Grosser, M., Werner, R. & Knopp, T. *3d-SMRnet: Achieving a new quality of MPI system matrix recovery by deep learning* in *International Conference on Medical Image Computing and Computer-Assisted Intervention* (2020), 74–82.
18. Bardhan, J. P. & Knepley, M. G. Computational science and re-discovery: open-source implementation of ellipsoidal harmonics for problems in potential theory. *Computational Science & Discovery* **5,** 014006. doi:10.1088/1749-4699/5/1/014006 (July 2012).
19. Basu, T., Engel-Wolf, S. & Menzer, O. The Ethics of Machine Learning in Medical Sciences: Where Do We Stand Today? *Indian Journal of Dermatology* **65.** doi:10.4103/ijd.IJD_419_20 (2020).
20. Baum, R. A. & Baum, S. Interventional Radiology: A Half Century of Innovation. *Radiology* **273.** PMID: 25340439, S75–S91. doi:10.1148/radiol.14140534 (2014).
21. Beentjes, C. H. L. *Quadrature on a spherical surface* tech. rep. https://cbeentjes.github.io/files/Ramblings/QuadratureSphere.pdf (2015).
22. Bente, K., Codutti, A., Bachmann, F. & Faivre, D. Biohybrid and Bioinspired Magnetic Microswimmers. *Small* **14,** 1–25. doi:10.1002/smll.201704374 (2018).
23. Bercovich, E. & Javitt, M. C. Medical Imaging: From Roentgen to the Digital Revolution, and Beyond. *Rambam Maimonides medical journal* **9.** doi:10.5041/RMMJ.10355 (2018).
24. Besio, S., Pittaluga, S., Punzo, V. & Trequattrini, A. Elliptical Coils for Dedicated MRI Magnets. *IEEE Transactions on Applied Superconductivity* **18,** 908–911. doi:10.1109/TASC.2008.922275 (2008).
25. Billings, C., Langley, M., Warrington, G., Mashali, F. & Johnson, J. A. Magnetic Particle Imaging: Current and Future Applications, Magnetic Nanoparticle Synthesis Methods and Safety Measures. *International Journal of Molecular Sciences* **22,** 7651. doi:10.3390/ijms22147651 (July 2021).
26. Boberg, M., Gdaniec, N., Szwargulski, P., Werner, F., Möddel, M. & Knopp, T. Simultaneous imaging of widely differing particle concentrations in MPI: Problem statement and algorithmic proposal for improvement. *Physics in Medicine and Biology* **66.** doi:10.1088/1361-6560/abf202 (2021).
27. Boberg, M., Knopp, T. & Möddel, M. Reducing displacement artifacts by warping system matrices in efficient joint multi-patch magnetic particle imaging. *International Journal on Magnetic Particle Imaging* **6.** doi:10.18416/IJMPI.2020.2009030 (2020).
28. Boberg, M., Knopp, T. & Möddel, M. Unique Compact Representation of Magnetic Fields using Truncated Solid Harmonic Expansions. *European Journal of Applied Mathematics*. doi:10.1017/S0956792524000883 (2025).
29. Boberg, M., Knopp, T., Szwargulski, P. & Möddel, M. Generalized MPI multi-patch reconstruction using clusters of similar system matrices. *IEEE Transactions on Medical Imaging* **39,** 1347–1358. doi:10.1109/TMI.2019.2949171 (2020).
30. Borgert, J., Schmidt, J. D., Schmale, I., Bontus, C., Gleich, B., David, B., Weizenecker, J., Jockram, J., Lauruschkat, C., Mende, O., Heinrich, M., Halkola, A., Bergmann, J., Woywode, O. & Rahmer, J. *Biomedizinische Technik/Biomedical Engineering* **58,** 551–556. doi:doi:10.1515/bmt-2012-0064 (2013).
31. Brandt, C., Kluth, T., Knopp, T. & Westen, L. *Dynamic image reconstruction with motion priors in application to 3D magnetic particle imaging* 2023. doi:10.48550/ARXIV.2306.11625.
32. Bredies, K., Lorenz, D., *et al. Mathematical image processing* (Springer, 2018).
33. Bringout, G. & Buzug, T. A robust and compact representation for magnetic fields in magnetic particle imaging. *Biomed Tech* **59,** 978–1 (2014).
34. Buchholz, O., Bär, S., Franke, J., Wei, H., Münkel, C., Saj, K. & Hofmann, U. *Theranostics based on MPI for brain interventions: an in vivo pilot study* 2024.
35. Bui, M. P., Le, T.-A. & Yoon, J. A Magnetic Particle Imaging-Based Navigation Platform for Magnetic Nanoparticles Using Interactive Manipulation of a Virtual Field Free Point to Ensure Targeted Drug Delivery. *IEEE Transactions on Industrial Electronics* **68,** 12493–12503. doi:10.1109/TIE.2020.3039219 (Dec. 2021).
36. Bui, M. P., Park, M., Le, T.-A. & Yoon, J. A Development of 3D Navigation System for Micro-Nano Robot Based on a Magnetic Particle Imaging System. *International Journal on Magnetic Particle Imaging IJMPI,* Vol 9 No 1 Suppl 1 (2023). doi:10.18416/IJMPI.2023.2303046 (Mar. 2023).
37. Byerly, W. E. *An Elementary Treatise on Fourier's Series and Spherical, Cylindrical, and Ellipsoidal Harmonics, With Applications to Problems in Mathematical Physics* (Ginn & Company, 1893).
38. Camfferman, F. A., de Goederen, R., Govaert, P., Dudink, J., van Bel, F., Pellicer, A. & Cools, F. Diagnostic and predictive value of Doppler ultrasound for evaluation of the brain circulation in preterm infants: a systematic review. *Pediatric Research* **87,** 50–58. doi:10.1038/s41390-020-0777-x (Mar. 2020).
39. Campbell, B. C. *et al.* Acute Stroke Imaging Research Roadmap IV: Imaging Selection and Outcomes in Acute Stroke Clinical Trials and Practice. *Stroke* **52,** 2723–2733. doi:10.1161/STROKEAHA.121.035132. eprint: https://www.ahajournals.org/doi/pdf/10.1161/STROKEAHA.121.035132 (2021).
40. Ceylan, H., Yasa, I. C., Kilic, U., Hu, W. & Sitti, M. Translational prospects of untethered medical microrobots. *Progress in Biomedical Engineering* **1.** doi:10.1088/2516-1091/ab22d5 (2019).
41. Chaabene, S., Chaari, L. & Kallel, A. Bayesian sparse regularization for parallel MRI reconstruction using complex Bernoulli–Laplace mixture priors. *Signal, Image and Video Processing* **14,** 445–453. doi:10.1007/s11760-019-01567-5 (2020).
42. Chan, C. T. & Gambhir, S. S. in *Encyclopedia of Diagnostic Imaging* (ed Baert, A. L.) 950–954 (Springer Berlin Heidelberg, Berlin, Heidelberg, 2008). doi:10.1007/978-3-540-35280-8_1246.
43. Chandrasekharan, P., Tay, Z. W., Hensley, D., Zhou, X. Y., Fung, B. K., Colson, C., Lu, Y., Fellows, B. D., Huynh, Q., Saayujya, C., Yu, E., Orendorff, R., Zheng, B., Goodwill, P., Rinaldi, C. & Conolly, S. Using magnetic

particle imaging systems to localize and guide magnetic hyperthermia treatment: tracers, hardware, and future medical applications. *Theranostics* **10,** 2965–2981. doi:10.7150/thno.40858 (Feb. 2020).

44. Chandrasekharan, P., Tay, Z. W., Zhou, X. Y., Yu, E., Orendorff, R., Hensley, D., Huynh, Q., Fung, K. L. B., VanHook, C. C., Goodwill, P., Zheng, B. & Conolly, S. A perspective on a rapid and radiation-free tracer imaging modality, magnetic particle imaging, with promise for clinical translation. *British Journal of Radiology* **91,** 20180326. doi:10.1259/bjr.20180326. eprint: https://academic.oup.com/bjr/article-pdf/91/1091/20180326/57382482/bjr.20180326.pdf (June 2018).
45. Chen, X., Huang, P., Ren, S., Meng, Y., Zhang, Z., Chen, D. & Zhu, S. An effective reconstruction method for magnetic particle imaging based on deep neural networks constrained by a physical model. doi:10.18416/IJMPI.2023.2303038 (2023).
46. Coffey, W. T. & Kalmykov, Y. P. Thermal Fluctuations of Magnetic Nanoparticles: Fifty Years after Brown. *Journal of Applied Physics* **112,** 121301. doi:10.1063/1.4754272 (Dec. 2012).
47. Cooley, C. Z., Mandeville, J. B., Mason, E. E., Mandeville, E. T. & Wald, L. L. Rodent Cerebral Blood Volume (CBV) changes during hypercapnia observed using Magnetic Particle Imaging (MPI) detection. *NeuroImage* **178,** 713–720. doi:https://doi.org/10.1016/j.neuroimage.2018.05.004 (2018).
48. Croft, L. R., Goodwill, P., Ferguson, M., Krishnan, K. & Conolly, S. Relaxation in X-Space Magnetic Particle Imaging. *Springer Proceedings in Physics* **140,** 149–153. doi:10.1007/978-3-642-24133-8_24 (2012).
49. Crozier, S., Forbes, L. K. & Brideson, M. Ellipsoidal harmonic (Lamé) MRI shims. *IEEE Transactions on Applied Superconductivity* **12,** 1880–1885. doi:10.1109/TASC.2002.805958 (2002).
50. Dassios, G. & Sleeman, B. D. A Note on the Reconstruction of Ellipsoids from the X-Ray Transform. *Mathematical Medicine and Biology: A Journal of the IMA* **8,** 141–147. doi:10.1093/imammb/8.2.141 (June 1991).
51. Dassios, G. in *Mathematical Modeling in Biomedical Imaging I: Electrical and Ultrasound Tomographies, Anomaly Detection, and Brain Imaging* (ed Ammari, H.) 133–202 (Springer Berlin Heidelberg, Berlin, Heidelberg, 2009). doi:10.1007/978-3-642-03444-2_4.
52. Dassios, G. *Ellipsoidal Harmonics - Theorie and Applications* doi:10.1017/CBO9781139017749 (Cambridge University Press, 2012).
53. Davida, A. & Basari, B. The hardware, tracer, and signal processing methods of magnetic particle imaging: A review. *Journal of Applied Physics* **136,** 220701. doi:10.1063/5.0220219. eprint: https://pubs.aip.org/aip/jap/article-pdf/doi/10.1063/5.0220219/20297640/220701_1_5.0220219.pdf (Dec. 2024).
54. De Vos, B., Fuchs, P., O'Reilly, T., Webb, A. & Remis, R. Gradient Coil Design and Realization for a Halbach-Based MRI System. *IEEE Transactions on Magnetics* **56.** doi:10.1109/TMAG.2019.2958561. eprint: 1912.08500 (2020).
55. Deissler, R. J., Wu, Y. & Martens, M. A. Dependence of Brownian and Néel Relaxation Times on Magnetic Field Strength. *Medical Physics* **41,** 012301. doi:10.1118/1.4837216 (Jan. 2014).
56. Draack, S., Schilling, M. & Viereck, T. Magnetic particle imaging of particle dynamics in complex matrix systems. *Physical Sciences Reviews* **8,** 213–237. doi:doi:10.1515/psr-2019-0123 (2023).
57. Dreyfus, R., Boehler, Q., Lyttle, S., Gruber, P., Lussi, J., Chautems, C., Gervasoni, S., Berberat, J., Seibold, D., Ochsenbein-Kölble, N., Reinehr, M., Weisskopf, M., Remonda, L. & Nelson, B. J. Dexterous helical magnetic robot for improved endovascular access. *Science Robotics* **9.** doi:10.1126/scirobotics.adh0298 (2024).
58. Droigk, C., Durán, D. H., Maass, M., Knopp, T. & Scheffler, K. *Efficient Chebyshev Reconstruction for the Anisotropic Equilibrium Model in Magnetic Particle Imaging* 2025. arXiv: 2504.12981 [physics.med-ph].
59. Droigk, C., Maass, M., Eulers, M. & Mertins, A. Adaption of direct Chebyshev reconstruction to an anisotropic particle model. *Int. J. Magn. Part. Imag.* **9,** 2303027. doi:10.18416/IJMPI.2023.2303027 (2023).
60. Droigk, C., Maass, M. & Mertins, A. Direct multi-dimensional Chebyshev polynomial based reconstruction for magnetic particle imaging. *Physics in Medicine and Biology* **67.** doi:10.1088/1361-6560/ac4c2e (2022).
61. Dubovan, P. I., Gilbert, K. M. & Baron, C. A. A correction algorithm for improved magnetic field monitoring with distal field probes. *Magnetic Resonance in Medicine* **90,** 2242–2260. doi:10.1002/mrm.29781 (2023).
62. Eberbeck, D., Wiekhorst, F., Wagner, S. & Trahms, L. How the size distribution of magnetic nanoparticles determines their magnetic particle imaging performance. *Appl. Phys. Lett.* **98,** 182502. doi:10.1063/1.3586776 (May 2011).
63. Eberbeck, D., Dennis, C. L., Huls, N. F., Krycka, K. L., Gruttner, C. & Westphal, F. Multicore Magnetic Nanoparticles for Magnetic Particle Imaging. *IEEE Transactions on Magnetics* **49,** 269–274. doi:10.1109/TMAG.2012.2226438 (2013).
64. Eggers, H., Knopp, T. & Potts, D. Field inhomogeneity correction based on gridding reconstruction for magnetic resonance imaging. *IEEE Transactions on Medical Imaging* **26,** 374–384 (2007).
65. Erb, W., Weinmann, A., Ahlborg, M., Brandt, C., Bringout, G., Buzug, T. M., Frikel, J., Kaethner, C., Knopp, T., März, T., Möddel, M., Storath, M. & Weber, A. Mathematical analysis of the 1D model and reconstruction schemes for magnetic particle imaging. *Inverse Probl.* **34,** 055012. doi:10.1088/1361-6420/aab8d1 (May 2018).
66. Exner, M., Szwargulski, P., Knopp, T., Gräser, M. & Ludewig, P. 3D printed anatomical model of a rat for medical imaging. *Current directions in biomedical engineering* **5,** 187–190. doi:10.15480/882.2419 (2019).
67. Ferguson, R. M., Khandhar, A. P., Kemp, S. J., Arami, H., Saritas, E. U., Croft, L. R., Konkle, J., Goodwill, P. W., Halkola, A., Rahmer, J., Borgert, J., Conolly, S. M. & Krishnan, K. M. Magnetic particle imaging with tailored iron oxide nanoparticle tracers. *IEEE Trans. Med. Imaging* **34,** 1077–1084. doi:10.1109/TMI.2014.2375065 (May 2015).

68. Ferguson, R. M., Minard, K. R. & Krishnan, K. M. Optimization of nanoparticle core size for magnetic particle imaging. *Journal of Magnetism and Magnetic Materials* **321.** Proceedings of the Seventh International Conference on the Scientific and Clinical Applications of Magnetic Carriers, 1548–1551. doi:https://doi.org/10.1016/j.jmmm.2009.02.083 (2009).
69. Finas, D., Baumann, K., Sydow, L., Heinrich, K., Gräfe, K., Buzug, T. & Lüdtke-Buzug, K. in *Biomedizinische Technik* 81–83 (Springer, 2012). doi:10.1515/bmt-2012-4158.
70. Finas, D., Baumann, K., Sydow, L., Heinrich, K., Rody, A., Gräfe, K., Buzug, T. M. & Ludtke-Buzug, K. SPIO Detection and Distribution in Biological Tissue - A Murine MPI-SLNB Breast Cancer Model. *IEEE Transactions on Magnetics* **51,** 1–4. doi:10.1109/TMAG.2014.2358272 (2015).
71. Firbank, M. J., Harrison, R. M., Williams, E. D. & Coulthard, A. Quality assurance for MRI: practical experience. *The British Journal of Radiology* **73,** 376–383. doi:10.1259/bjr.73.868.10844863 (Apr. 2000).
72. Fleming, H. E. Equivalence of regularization and truncated iteration in the solution of ill-posed image reconstruction problems. *Linear Algebra and its Applications* **130,** 133–150. doi:https://doi.org/10.1016/0024-3795(90)90210-4 (1990).
73. Foerger, F., Boberg, M., Faltinath, J., Knopp, T. & Möddel, M. Design and Optimization of a Magnetic Field Generator for Magnetic Particle Imaging with Soft Magnetic Materials. *Advanced Intelligent Systems* **6,** 2400017. doi:https://doi.org/10.1002/aisy.202400017. eprint: https://advanced.onlinelibrary.wiley.com/doi/pdf/10.1002/aisy.202400017 (2024).
74. Foerger, F., Hackelberg, N., Boberg, M., Möddel, M., Thieben, F., Mohn, F. & Knopp, T. *Single-Shot Magnetic Field Measurements for MPI* in *13th International Workshop on Magnetic Particle Imaging* (2024), 1.
75. Foerger, F., Hackelberg, N., Boberg, M., Scheel, J.-P., Thieben, F., Mirzojan, L., Mohn, F., Möddel, M., Graeser, M. & Knopp, T. Flexible Selection Field Generation using Iron Core Coil Arrays. *International Journal on Magnetic Particle Imaging IJMPI,* Vol 9 No 1 Suppl 1 (2023). doi:10.18416/IJMPI.2023.2303023 (Mar. 2023).
76. Foerger, F., Jürß, P., Boberg, M., Hau, T., Knopp, T. & Möddel, M. Current-to-Field Prediction for Non-Linear Magnetic Systems via Neural Networks. en. doi:10.18416/IJMPI.2025.2503009 (2025).
77. Fong, D. C. L. & Saunders, M. LSMR: An iterative algorithm for sparse least-squares problems. *SIAM Journal on Scientific Computing* **33,** 2950–2971. doi:10.1137/10079687X. arXiv: 1006.0758 (2011).
78. Fragoyiannis, G. & Vafeas, P. A semi-analytical approach for the computation of ellipsoidal harmonics. *Journal of Computational and Applied Mathematics* **437,** 115418. doi:https://doi.org/10.1016/j.cam.2023.115418 (2024).
79. Franke, J., Heinen, U., Lehr, H., Weber, A., Jaspard, F., Ruhm, W., Heidenreich, M. & Schulz, V. System characterization of a highly integrated preclinical hybrid MPI-MRI scanner. *IEEE Transactions on Medical Imaging* **35,** 1993–2004. doi:10.1109/TMI.2016.2542041 (2016).
80. Gach, H. M. B0 field homogeneity recommendations, specifications, and measurement units for MRI in radiation therapy. *Med Phys.* **47,** 4101–4114. doi:10.1002/mp.14306 (2020).
81. Gapyak, V., Rentschler, C. E., März, T. & Weinmann, A. An l1-plug-and-play approach for MPI using a zero shot denoiser with evaluation on the 3D open MPI dataset. *Physics in Medicine & Biology* **70,** 025028. doi:10.1088/1361-6560/ada5a1 (Jan. 2025).
82. Garmier, R. & Barriot, J.-P. Ellipsoidal Harmonic expansions of the gravitational potential: Theory and application. *Celestial Mechanics and Dynamical Astronomy* **79,** 235–275. doi:10.1023/A:1017555515763 (Apr. 2001).
83. Gdaniec, N., Boberg, M., Möddel, M., Szwargulski, P. & Knopp, T. Suppression of Motion Artifacts Caused by Temporally Recurring Tracer Distributions in Multi-Patch Magnetic Particle Imaging. *IEEE Transactions on Medical Imaging* **39,** 3548–3558. doi:10.1109/TMI.2020.2998910 (2020).
84. Geethanath, S., Reddy, R., Konar, A. S., Imam, S., Sundaresan, R., D. R., R. B. & Venkatesan, R. Compressed Sensing MRI: A Review. *Critical Reviews in Biomedical Engineering* **41,** 183–204. doi:10.1615/critrevbiomedeng.2014008058 (2013).
85. Gevaert, J., Van Beek, K., Sehl, O. C. & Foster, P. J. VivoTrax+ Improves the Detection of Cancer Cells with Magnetic Particle Imaging. *International Journal on Magnetic Particle Imaging,* Vol 8 No 2 (2022). doi:10.18416/IJMPI.2022.2210001 (Oct. 2022).
86. Gil, A. & Segura, J. A code to evaluate prolate and oblate spheroidal harmonics. *Computer Physics Communications* **108,** 267–278. doi:https://doi.org/10.1016/S0010-4655(97)00126-4 (1998).
87. Gleich, B. & Weizenecker, J. Tomographic imaging using the nonlinear response of magnetic particles. *Nature* **435,** 1214–1217. doi:10.1038/nature03808 (2005).
88. Gleich, B., Schmale, I., Nielsen, T. & Rahmer, J. Miniature magneto-mechanical resonators for wireless tracking and sensing. *Science* **380,** 966–971. doi:10.1126/science.adf5451 (2023).
89. Gleich, B., Weizenecker, J., Timminger, H., Bontus, C., Schmale, I., Rahmer, J., Schmidt, J., Katzenbach, J. & Borgert, J. *Fast MPI Demonstrator with Enlarged Field of View* in *ISMRM* **18** (Stockholm, 2010), 218.
90. GmbH, B. B. *Bruker Announces the World's First Preclinical Magnetic Particle Imaging (MPI) System.* Sept. 2013.
91. Goodwill, P., Yu, E. & Conolly, S. *Design and construction of a second generation high-resolution MPI field free line scanner* in *2015 5th International Workshop on Magnetic Particle Imaging (IWMPI)* (2015), 1–1. doi:10.1109/IWMPI.2015.7107031.

92. Goodwill, P. W. & Conolly, S. M. The X-space Formulation of the Magnetic Particle Imaging Process: 1-D Signal, Resolution, Bandwidth, SNR, SAR, and Magnetostimulation. *IEEE Transactions on Medical Imaging* **29,** 1851–1859. doi:10.1109/TMI.2010.2052284 (2010).
93. Goodwill, P. W. & Conolly, S. M. Multidimensional X-space Magnetic Particle Imaging. *IEEE Transactions on Medical Imaging* **30,** 1581–1590. doi:10.1109/TMI.2011.2125982 (2011).
94. Goodwill, P. W., Konkle, J. J., Zheng, B., Saritas, E. U. & Conolly, S. M. Projection X-space Magnetic Particle Imaging. *IEEE Transactions on Medical Imaging* **31,** 1076–1085. doi:10.1109/TMI.2012.2185247 (2012).
95. Graas, A., Coban, S. B., Batenburg, K. J. & Lucka, F. Just-in-time deep learning for real-time X-ray computed tomography. *Sci. Rep.* **13.** doi:10.1038/s41598-023-46028-9 (Nov. 2023).
96. Graeser, M., Bente, K., Neumann, A. & Buzug, T. M. Trajectory dependent particle response for anisotropic mono domain particles in magnetic particle imaging. *J. Phys. D: Appl. Phys.* **49,** 045007. doi:10.1088/0022-3727/49/4/045007 (2016).
97. Graeser, M., Knopp, T., Szwargulski, P., Friedrich, T., Von Gladiss, A., Kaul, M., Krishnan, K. M., Ittrich, H., Adam, G. & Buzug, T. M. Towards picogram detection of superparamagnetic iron-oxide particles using a gradiometric receive coil. *Scientific Reports* **7.** doi:10.1038/s41598-017-06992-5. eprint: 1704.01789 (2017).
98. Graeser, M., Ludewig, P., Szwargulski, P., Foerger, F., Liebing, T., Forkert, N. D., Thieben, F., Magnus, T. & Knopp, T. Design of a head coil for high resolution mouse brain perfusion imaging using magnetic particle imaging. *Physics in Medicine and Biology* **65,** 235007. doi:10.1088/1361-6560/abc09e (Nov. 2020).
99. Gräser, M., Thieben, F., Szwargulski, P., Werner, F., Gdaniec, N., Boberg, M., Griese, F., Möddel, M., Ludewig, P., van de Ven, D., *et al.* Human-sized magnetic particle imaging for brain applications. *Nature communications* **10,** 1–9 (2019).
100. Gräser, M., Wegner, F., Schumacher, J., Ahlborg, M., Gräfe, K., Aderhold, E., Blancke Soares, Y., Lüdtke-Buzug, K., Neumann, A., Stagge, P., Wei, H., Ackers, J. & Buzug, T. M. „Magnetic particle imaging“: Von der Forschung zur klinischen Perspektive. *Die Radiologie* **62,** 496–503. doi:10.1007/s00117-022-01011-9 (May 2022).
101. Grau-Ruiz, D., Rigla, J. P., Pallás, E., Algarín, J. M., Borreguero, J., Bosch, R., López-Comazzi, G., Galve, F., Díaz-Caballero, E., Gramage, C., González, J. M., Pellicer, R., Ríos, A., Benlloch, J. M. & Alonso, J. Magneto-Stimulation Limits in Medical Imaging Applications with Rapid Field Dynamics. *Physics in Medicine & Biology* **67,** 045016. doi:10.1088/1361-6560/ac515c (Feb. 2022).
102. Griese, F., Knopp, T., Gruettner, C., Thieben, F., Müller, K., Loges, S., Ludewig, P. & Gdaniec, N. Simultaneous Magnetic Particle Imaging and Navigation of large superparamagnetic nanoparticles in bifurcation flow experiments. *Journal of Magnetism and Magnetic Materials* **498,** 166206. doi:https://doi.org/10.1016/j.jmmm.2019.166206 (2020).
103. Griese, F., Latus, S., Schlüter, M., Graeser, M., Lutz, M., Schlaefer, A. & Knopp, T. In-Vitro MPI-guided IVOCT Catheter Tracking in Real Time for Motion Artifact Compensation. *arXiv* **20,** e0230821. doi:10.1371/journal.pone.0230821 (2019).
104. Grosser, M., Boberg, M., Bahe, M. & Knopp, T. Enhanced compressed sensing recovery of multi-patch system matrices in MPI. en. *International Journal on Magnetic Particle Imaging,* Vol 6 No 2 Suppl. 1 (2020). doi:10.18416/IJMPI.2020.2009035 (2020).
105. Grosser, M. & Knopp, T. Optimized sampling patterns for the sparse recovery of system matrices in Magnetic Particle Imaging. *International Journal on Magnetic Particle Imaging* **7** (2021).
106. Grosser, M., Möddel, M. & Knopp, T. Using low-rank tensors for the recovery of MPI system matrices. *IEEE Transactions on Computational Imaging* **6,** 1389–1402 (2020).
107. Grosser, M., Möddel, M. & Knopp, T. Exploiting the Fourier Neural Operator for Parameter Identification in MPI. en. doi:10.18416/IJMPI.2024.2403004 (2024).
108. Güngör, A., Askin, B., Soydan, D. A., Saritas, E. U., Top, C. B. & Çukur, T. TranSMS: Transformers for super-resolution calibration in magnetic particle imaging. *IEEE Transactions on Medical Imaging* (2022).
109. Güngör, A., Askin, B., Soydan, D. A., Top, C. B., Saritas, E. U. & Çukur, T. DEQ-MPI: A Deep Equilibrium Reconstruction With Learned Consistency for Magnetic Particle Imaging. *IEEE Transactions on Medical Imaging* **43,** 321–334. doi:10.1109/TMI.2023.3300704 (2024).
110. Hackelberg, N., Grosser, M., Tsanda, A., Mohn, F., Scheffler, K., Möddel, M. & Knopp, T. RegularizedLeastSquares.Jl: Modality Agnostic Julia Package for Solving Regularized Least Squares Problems. *International Jounal on Magnetic Particle Imaging* **10.** doi:10.18416/IJMPI.2024.2403028 (Mar. 2024).
111. Hackelberg, N., Schumacher, J., Ackers, J., Möddel, M., Förger, F., Graeser, M. & Knopp, T. MPIMeasurements.jl: An Extensible Julia Framework for Composable Magnetic Particle Imaging Devices. en. *International Journal on Magnetic Particle Imaging IJMPI,* Vol 9 No 1 Suppl 1 (2023). doi:10.18416/IJMPI.2023.2303069 (2023).
112. Hackelberg, N., Schumacher, J., Graeser, M. & Knopp, T. A Flexible High-Performance Signal Generation and Digitization Plattform based on Low-Cost Hardware. en. *International Journal on Magnetic Particle Imaging,* Vol 8 No 1 Suppl 1 (2022). doi:10.18416/IJMPI.2022.2203063 (2022).
113. Haegele, J., Biederer, S., Wojtczyk, H., Gräser, M., Knopp, T., Buzug, T. M., Barkhausen, J. & Vogt, F. M. Toward cardiovascular interventions guided by magnetic particle imaging: first instrument characterization. *Magn. Reson. Med.* **69,** 1761–1767. doi:10.1002/mrm.24421 (June 2013).

114. Haegele, J., Duschka, R. L., Graeser, M., Schaecke, C., Panagiotopoulos, N., Lüdtke-Buzug, K., Buzug, T. M., Barkhausen, J. & Vogt, F. M. Magnetic Particle Imaging: Kinetics of the Intravascular Signal in Vivo. *International journal of nanomedicine* **9,** 4203–4209. doi:10.2147/IJN.S49976 (2014).
115. Haegele, J., Vaalma, S., Panagiotopoulos, N., Barkhausen, J., Vogt, F. M., Borgert, J. & Rahmer, J. Multi-color magnetic particle imaging for cardiovascular interventions. *Phys. Med. Biol.* **61,** N415–N426. doi:10.1088/0031-9155/61/16/N415 (Aug. 2016).
116. Hansen, C. & O'Leary, D. P. The use of the L-curve in the regularization of discrete ill-posed problems. *SIAM Journal on Scientific Computing* **14,** 1487–1503 (1993).
117. Haskell, M. W., Nielsen, J. F. & Noll, D. C. Off-resonance artifact correction for MRI: A review. *NMR in Biomedicine* **36,** 1–24. doi:10.1002/nbm.4867 (2023).
118. Henn, M.-A., Quelhas, K. N., Bui, T. & Woods, S. Improving model-based MPI image reconstructions: baseline recovery, receive coil sensitivity, relaxation and uncertainty estimation. *International Journal on Magnetic Particle Imaging* **8** (2022).
119. Hernández Durán, D., Scheffler, K., Möddel, M. & Knopp, T. Efficient Iterative Reconstruction for an MPI Equilibrium Model with Anisotropy. en. doi:10.18416/IJMPI.2025.2503015 (2025).
120. Hetherington, H. P., Moon, C. H., Schwerter, M., Shah, N. J. & Pan, J. W. Dynamic B0 shimming for multiband imaging using high order spherical harmonic shims. *Magnetic Resonance in Medicine* **85,** 531–543. doi:https://doi.org/10.1002/mrm.28438. eprint: https://onlinelibrary.wiley.com/doi/pdf/10.1002/mrm.28438 (2021).
121. Hobson, E. W. *The Theory of and Ellipsoidal Harmonics* (Cambridge University Press, 1931).
122. Huang, Q. & Zeng, Z. A review on real-time 3D ultrasound imaging technology. *Biomed Res. Int.* **2017,** 1–20. doi:10.1155/2017/6027029 (2017).
123. Hui, H., Liu, J., Zhang, H., Zhong, J., He, J., Zhang, B., Zhang, H., Li, Q., Li, H. & Tian, J. In Vivo Measurement of Cerebral SPIO Concentration in Nonhuman Primate Using Magnetic Particle Imaging Detector. *IEEE Magnetics Letters* **14,** 1–5. doi:10.1109/LMAG.2023.3281933 (2023).
124. Ilbey, S., Top, C. B., Güngör, A., Çukur, T., Saritas, E. U. & Güven, H. E. Fast system calibration with coded calibration scenes for magnetic particle imaging. *IEEE Transactions on Medical Imaging* **38,** 2070–2080 (2019).
125. Inaba, Y. & Lindner, J. R. Molecular imaging of disease with targeted contrast ultrasound imaging. *Translational Research* **159.** IN-DEPTH COVERAGE: CARDIOVASCULAR IMAGING, 140–148. doi:https://doi.org/10.1016/j.trsl.2011.12.001 (2012).
126. Johnson, K. A., Fox, N. C., Sperling, R. A. & Klunk, W. E. Brain imaging in Alzheimer disease. *Cold Spring Harbor perspectives in medicine* **2.** doi:10.1101/cshperspect.a006213 (2012).
127. Kabasawa, H. MR Imaging in the 21st Century: Technical Innovation over the First Two Decades. *Magnetic Resonance in Medical Sciences* **21,** 71–82. doi:10.2463/mrms.rev.2021-0011 (2022).
128. Kaczmarz, S. Angenäherte Auflösung von Systemen Linearer Gleichungen. *Bulletin of the International Academy Polonica Sciences Letters A* **35,** 355–357 (1937).
129. Kaethner, C., Erb, W., Ahlborg, M., Szwargulski, P., Knopp, T. & Buzug, T. M. Non-Equispaced System Matrix Acquisition for Magnetic Particle Imaging Based on Lissajous Node Points. *IEEE Transactions on Medical Imaging* **35,** 2476–2485. doi:10.1109/TMI.2016.2580458 (2016).
130. Kaissis, G. A., Makowski, M. R., Rückert, D. & Braren, R. F. Secure, privacy-preserving and federated machine learning in medical imaging. *Nature Machine Intelligence* **2,** 305–311. doi:10.1038/s42256-020-0186-1 (June 2020).
131. Kampf, T., Rückert, M. A., Behr, V. C. & Vogel, P. Modular Simulation Framework for Magnetic Particle Imaging. en. *International Journal on Magnetic Particle Imaging IJMPI,* Vol 9 No 1 Suppl 1 (2023). doi:10.18416/IJMPI.2023.2303081 (2023).
132. Katti, G., Ara, S. A. & Shireen, A. Magnetic Resonance Imaging (MRI) – A Review. *International Journal of Dental Clinics* **3** (2011).
133. Kayapinar, M. H., Alpman, A. & Saritas, E. U. Fourier Neural Operator for Coupled Brown-Neel Rotation Model. en. doi:10.18416/IJMPI.2024.2403008 (2024).
134. Khandhar, A. P., Keselman, P., Kemp, S. J., Ferguson, R. M., Goodwill, P. W., Conolly, S. M. & Krishnan, K. M. Evaluation of PEG-coated iron oxide nanoparticles as blood pool tracers for preclinical magnetic particle imaging. *Nanoscale* **9,** 1299–1306. doi:10.1039/c6nr08468k (2017).
135. Kluth, T. Mathematical models for magnetic particle imaging. *Inverse Problems* **34,** 1–20. doi:10.1088/1361-6420/aac535. arXiv: 1803.07408 (2018).
136. Kluth, T., Albers, H., Maass, M., Droigk, C., Boberg, M., Thieben, F., Scheffler, K. & Knopp, T. *Recent Progress in Model-Based Reconstruction using Approximate Particle Models and low Calibration Effort* in *13th International Workshop on Magnetic Particle Imaging* (2024), 1.
137. Kluth, T., Jin, B. & Li, G. On the degree of ill-posedness of multi-dimensional magnetic particle imaging. *Inverse Problems* **34,** 095006. doi:10.1088/1361-6420/aad015 (July 2018).
138. Kluth, T., Szwargulski, P. & Knopp, T. Towards accurate modeling of the multidimensional magnetic particle imaging physics. *New Journal of Physics* **21** (2019).
139. Knipe, H. *Fracture-dislocation of the ankle* https://radiopaedia.org/cases/30190. Radiopaedia, 2014. doi:10.53347/rID-30190.

140. Knopp, T., Biederer, S., Sattel, T., Weizenecker, J., Gleich, B., Borgert, J. & Buzug, T. M. Trajectory analysis for magnetic particle imaging. *Physics in Medicine & Biology* **54,** 385. doi:10.1088/0031-9155/54/2/014 (Dec. 2008).
141. Knopp, T., Gdaniec, N. & Möddel, M. Magnetic particle imaging: from proof of principle to preclinical applications. *Physics in Medicine and Biology* **62,** R124. doi:10.1088/1361-6560/aa6c99 (2017).
142. Knopp, T. & Hofmann, M. Online reconstruction of 3D magnetic particle imaging data. *Physics in Medicine and Biology* **61,** N257. doi:10.1088/0031-9155/61/11/N257 (May 2016).
143. Knopp, T., Rahmer, J., Sattel, T. F., Biederer, S., Weizenecker, J., Gleich, B., Borgert, J. & Buzug, T. M. Weighted iterative reconstruction for magnetic particle imaging. *Physics in Medicine and Biology* **55,** 1577–1589. doi:10.1088/0031-9155/55/6/003 (Feb. 2010).
144. Knopp, T., Them, K., Kaul, M. & Gdaniec, N. Joint reconstruction of non-overlapping magnetic particle imaging focus-field data. *Physics in Medicine and Biology* **60,** L15. doi:10.1088/0031-9155/60/8/L15 (2015).
145. Knopp, T., Biederer, S., Sattel, T. & Buzug, T. M. Singular value analysis for magnetic particle imaging, 4525–4529. doi:10.1109/NSSMIC.2008.4774296 (2008).
146. Knopp, T., Biederer, S., Sattel, T. F., Rahmer, J., Weizenecker, J., Gleich, B., Borgert, J. & Buzug, T. M. 2D model-based reconstruction for magnetic particle imaging. *Medical Physics* **37,** 485–491 (2010).
147. Knopp, T., Eggers, H., Dahnke, H., Prestin, J. & Sénégas, J. Iterative off-resonance and signal decay correction for improved multi-echo imaging in MRI. *IEEE Trans Med Imaging* **28,** 394–404 (2009).
148. Knopp, T., Jürß, P. & Grosser, M. A deep learning approach for automatic image reconstruction in MPI. doi:10.18416/IJMPI.2023.2303008 (2023).
149. Knopp, T., Möddel, M., Griese, F., Werner, F., Szwargulski, P., Gdaniec, N. & Boberg, M. MPIFiles.jl: A Julia Package for Magnetic Particle Imaging Files. *Journal of Open Source Software* **4,** 1331. doi:10.21105/joss.01331 (2019).
150. Knopp, T., Sattel, T. F., Biederer, S., Rahmer, J., Weizenecker, J., Gleich, B., Borgert, J. & Buzug, T. M. Model-based reconstruction for magnetic particle imaging. *IEEE Transactions on Medical Imaging* **29,** 12–18 (2009).
151. Knopp, T., Szwargulski, P., Griese, F. & Gräser, M. OpenMPIData: An initiative for freely accessible magnetic particle imaging data. *Data in Brief,* 104971 (2019).
152. Knopp, T., Szwargulski, P., Griese, F., Grosser, M., Boberg, M. & Möddel, M. MPIReco.jl: Julia package for image reconstruction in MPI. *International Journal on Magnetic Particle Imaging* **5.** doi:10.18416/ijmpi.2019.1907001 (2019).
153. Knopp, T., Szwargulski, P., Griese, F., Grosser, M., Boberg, M. & Möddel, M. MPIReco.jl: Julia package for image reconstruction in MPI. *International Journal on Magnetic Particle Imaging* **5.** doi:10.18416/IJMPI.2019.1907001 (2019).
154. Knopp, T. & Weber, A. Sparse reconstruction of the magnetic particle imaging system matrix. *IEEE Transactions on Medical Imaging* **32,** 1473–1480 (2013).
155. Konkle, J. J., Goodwill, P. W., Carrasco-Zevallos, O. M. & Conolly, S. M. Projection Reconstruction Magnetic Particle Imaging. *IEEE Transactions on Medical Imaging* **32,** 338–347. doi:10.1109/TMI.2012.2227121 (2013).
156. Konkle, J. J., Goodwill, P. W., Hensley, D. W., Orendorff, R. D., Lsustig, M. & Conolly, S. M. A Convex Formulation for Magnetic Particle Imaging X-Space Reconstruction. *PLOS ONE* **10** (ed Najbauer, J.) e0140137. doi:10.1371/journal.pone.0140137 (Oct. 2015).
157. Konovalov, A. B. Compressed-sensing-inspired reconstruction algorithms in low-dose computed tomography: A review. *Physica Medica* **124,** 104491. doi:https://doi.org/10.1016/j.ejmp.2024.104491 (2024).
158. Kuboyabu, T., Ohki, A., Banura, N. & Murase, K. Usefulness of Magnetic Particle Imaging for Monitoring the Effect of Magnetic Targeting. *Open Journal of Medical Imaging* **06,** 33–41. doi:10.4236/ojmi.2016.62004 (2016).
159. Lacroix, M., Frouin, F., Dirand, A. S., Nioche, C., Orlhac, F., Bernaudin, J. F., Brillet, P. Y. & Buvat, I. Correction for Magnetic Field Inhomogeneities and Normalization of Voxel Values Are Needed to Better Reveal the Potential of MR Radiomic Features in Lung Cancer. *Frontiers in Oncology* **10.** doi:10.3389/fonc.2020.00043 (2020).
160. Lampe, J., Bassoy, C., Rahmer, J., Weizenecker, J., Voss, H., Gleich, B. & Borgert, J. Fast reconstruction in magnetic particle imaging. *Physics in Medicine and Biology* **57,** 1113–1134. doi:10.1088/0031-9155/57/4/1113 (Feb. 2012).
161. Law, S., Nunez, P. & Wijesinghe, R. High-resolution EEG using spline generated surface Laplacians on spherical and ellipsoidal surfaces. *IEEE Transactions on Biomedical Engineering* **40,** 145–153. doi:10.1109/10.212068 (1993).
162. Lewin, J. S. Future directions in minimally invasive intervention. *Trans. Am. Clin. Climatol. Assoc.* **128,** 346–352 (2017).
163. Li, H., Li, L., Liu, Y., Deng, Y., Zhu, Y., Huang, L., Long, T., Zeng, L., Shu, Y. & Peng, D. Predictive value of CT and 18F-FDG PET/CT features on spread through air space in lung adenocarcinoma. *BMC Cancer* **24.** doi:10.1186/s12885-024-12220-x (2024).
164. Lieb, F. & Knopp, T. A wavelet-based sparse row-action method for image reconstruction in magnetic particle imaging. *Medical Physics* **48,** 3893–3903. doi:https://doi.org/10.1002/mp.14938. eprint: https://aapm.onlinelibrary.wiley.com/doi/pdf/10.1002/mp.14938 (2021).

165. Liebl, M., Wiekhorst, F., Eberbeck, D., Radon, P., Gutkelch, D., Baumgarten, D., Steinhoff, U. & Trahms, L. Magnetorelaxometry procedures for quantitative imaging and characterization of magnetic nanoparticles in biomedical applications. *Biomedical Engineering/Biomedizinische Technik* **60,** 427–443 (2015).
166. Lin, F. H., Kwong, K. K., Belliveau, J. W. & Wald, L. L. Parallel imaging reconstruction using automatic regularization. *Magnetic Resonance in Medicine* **51,** 559–567. doi:10.1002/mrm.10718 (2004).
167. Liu, D., Guo, R., Wang, B., Hu, J. & Lu, Y. Magnetic Micro/Nanorobots: A New Age in Biomedicines. *Advanced Intelligent Systems* **4.** doi:10.1002/aisy.202200208 (2022).
168. Liu, S., Chiu-Lam, A., Rivera-Rodriguez, A., DeGroff, R., Savliwala, S., Sarna, N. & Rinaldi-Ramos, C. M. Long Circulating Tracer Tailored for Magnetic Particle Imaging. *Nanotheranostics* **5,** 348–361. doi:10.7150/ntno.58548 (2021).
169. Ludewig, P., Gdaniec, N., Sedlacik, J., Forkert, N. D., Szwargulski, P., Graeser, M., Adam, G., Kaul, M. G., Krishnan, K. M., Ferguson, R. M., Khandhar, A. P., Walczak, P., Fiehler, J., Thomalla, G., Gerloff, C., Knopp, T. & Magnus, T. Magnetic Particle Imaging for Real-Time Perfusion Imaging in Acute Stroke. *ACS Nano* **11.** PMID: 28976180, 10480–10488. doi:10.1021/acsnano.7b05784 (2017).
170. Ludewig, P., Graeser, M., Forkert, N. D., Thieben, F., Rández-Garbayo, J., Rieckhoff, J., Lessmann, K., Förger, F., Szwargulski, P., Magnus, T. & Knopp, T. Magnetic particle imaging for assessment of cerebral perfusion and ischemia. *Wiley Interdiscip. Rev. Nanomed. Nanobiotechnol.* **14,** e1757. doi:10.1002/wnan.1757 (Jan. 2022).
171. Lüdtke-Buzug, K., Haegele, J., Biederer, S., Sattel, T. F., Erbe, M., Duschka, R. L., Barkhausen, J. & Vogt, F. M. Comparison of commercial iron oxide-based MRI contrast agents with synthesized high-performance MPI tracers. *Biomedizinische Technik/Biomedical Engineering* **58,** 527–533. doi:doi:10.1515/bmt-2012-0059 (2013).
172. Ludwig, F., Eberbeck, D., Löwa, N., Steinhoff, U., Wawrzik, T., Schilling, M. & Trahms, L. Characterization of Magnetic Nanoparticle Systems with Respect to Their Magnetic Particle Imaging Performance. *Biomedizinische Technik/Biomedical Engineering* **58.** doi:10.1515/bmt-2013-0013 (Jan. 2013).
173. Maass, M., Bente, K., Ahlborg, M., Medimagh, H., Phan, H., Buzug, T. M. & Mertins, A. Optimized compression of MPI system matrices using a symmetry-preserving secondary orthogonal transform. *International Journal on Magnetic Particle Imaging* **2,** 1–5 (2016).
174. Maass, M., Droigk, C., Albers, H., Scheffler, K., Mertins, A., Kluth, T. & Knopp, T. Magnetic particle imaging with non-oriented immobilized particles. en. doi:10.18416/IJMPI.2024.2403007 (2024).
175. Maass, M., Kluth, T., Droigk, C., Albers, H., Scheffler, K., Mertins, A. & Knopp, T. Equilibrium Model With Anisotropy for Model-Based Reconstruction in Magnetic Particle Imaging. *IEEE Transactions on Computational Imaging* **10,** 1588–1601. doi:10.1109/TCI.2024.3490381 (2024).
176. Maass, M. & Mertins, A. On the representation of magnetic particle imaging in Fourier space. *International Journal on Magnetic Particle Imaging* **5.** doi:10.18416/ijmpi.2019.1912001 (2019).
177. Magnetic Insight, Inc. *Magnetic Insight Momentum MPI Scanner* 2017.
178. *Medical Imaging Systems: An Introductory Guide* en (eds Maier, A., Steidl, S., Christlein, V. & Hornegger, J.) (Springer, 2018).
179. Marques, J. P., Simonis, F. F. & Webb, A. G. Low-field MRI: An MR physics perspective. *Journal of Magnetic Resonance Imaging* **49,** 1528–1542. doi:10.1002/jmri.26637 (2019).
180. Mason, E. E., Cooley, C. Z., Cauley, S. F., Griswold, M. A., Conolly, S. M. & Wald, L. L. Design Analysis of an MPI Human Functional Brain Scanner. *International Journal on Magnetic Particle Imaging* **3.** doi:10.18416/ijmpi.2017.1703008 (2017).
181. Mason, E. E., Mattingly, E., Herb, K., Śliwiak, M., Franconi, S., Cooley, C. Z., Slanetz, P. J. & Wald, L. L. Concept for Using Magnetic Particle Imaging for Intraoperative Margin Analysis in Breast-Conserving Surgery. *Scientific Reports* **11,** 13456. doi:10.1038/s41598-021-92644-8 (June 2021).
182. Mattingly, E., Mason, E., Herb, K., Śliwiak, M., Brandt, K., Cooley, C. & Wald, L. OS-MPI: an open-source magnetic particle imaging project. en. *International Journal on Magnetic Particle Imaging,* Vol 6 No 2 Suppl. 1 (2020). doi:10.18416/IJMPI.2020.2009059 (2020).
183. Mattingly, E., Sliwiak, M., Mason, E. E., Chacon-Caldera, J., Barksdale, A. C., Niebel, F. H., Herb, K., Graeser, M. & Wald, L. L. Design, construction and validation of a magnetic particle imaging (MPI) system for human brain imaging. *Physics in Medicine & Biology*. doi:10.1088/1361-6560/ad9db0 (2024).
184. McCollough, C. H. & Rajiah, P. S. Milestones in CT: Past, Present, and Future. *Radiology* **309.** PMID: 37847140, e230803. doi:10.1148/radiol.230803 (2023).
185. McDonough, C., Pagan, J. & Tonyushkin, A. Implementation of the surface gradiometer receive coils for the improved detection limit and sensitivity in the single-sided MPI scanner. *Physics in Medicine & Biology* **67,** 245009. doi:10.1088/1361-6560/aca5ec (Dec. 2022).
186. McDonough, C., Chrisekos, J. & Tonyushkin, A. *Dual mode imaging of phantoms in two orthogonal planes with a single-sided FFL MPI scanner* 2024.
187. Mesri, H. Y., David, S., Viergever, M. A. & Leemans, A. The adverse effect of gradient nonlinearities on diffusion MRI: From voxels to group studies. *NeuroImage* **205,** 116127. doi:https://doi.org/10.1016/j.neuroimage.2019.116127 (2020).
188. Miloh, T. Maneuvering Hydrodynamics of Ellipsoidal Forms. *Journal of Ship Research* **23,** 66–75. doi:10.5957/jsr.1979.23.1.66 (1979).
189. Möddel, M., Knopp, T., Werner, R., Weller, D. & Salamon, J. M. *Toward Employing the Full Potential of Magnetic Particle Imaging: Exploring Visualization Techniques and Clinical Use Cases for Real-Time 3D Vascular*

Imaging in *Medical Imaging 2019: Biomedical Applications in Molecular, Structural, and Functional Imaging* **10953** (International Society for Optics and Photonics, 2019), 65. doi:10.1117/12.2512442.

190. Möddel, M., Meins, C., Dieckhoff, J. & Knopp, T. Viscosity quantification using multi-contrast magnetic particle imaging. *New Journal of Physics* **20,** 083001. doi:10.1088/1367-2630/aad44b (Aug. 2018).
191. Mohn, F., Exner, M., Szwargulski, P., Möddel, M., Knopp, T. & Graeser, M. *Saline bolus for negative contrast perfusion imaging in magnetic particle imaging* 2023. arXiv: 2303.05439 [physics.med-ph].
192. Mohn, F., Scheffler, K., Ackers, J., Weimer, A., Wegner, F., Thieben, F., Ahlborg, M., Vogel, P., Graeser, M. & Knopp, T. Characterization of the Clinically Approved MRI Tracer Resotran for Magnetic Particle Imaging in a Comparison Study. *Physics in Medicine & Biology* **69,** 135014. doi:10.1088/1361-6560/ad5828 (July 2024).
193. Moor, L., Scheibler, S., Gerken, L., Scheffler, K., Thieben, F., Knopp, T., Herrmann, I. & Starsich, F. MPI tracer interactions and their effect on signal stability. en. *International Journal on Magnetic Particle Imaging* **8.** doi:10.18416/IJMPI.2022.2203056 (2022).
194. Moor, L., Scheibler, S., Gerken, L., Scheffler, K., Thieben, F., Knopp, T., Herrmann, I. K. & Starsich, F. H. L. Particle interactions and their effect on magnetic particle spectroscopy and imaging. *Nanoscale* **14,** 7163–7173. doi:10.1039/D1NR08402J (19 2022).
195. Mukhatov, A., Le, T.-A., Pham, T. T. & Do, T. D. A comprehensive review on magnetic imaging techniques for biomedical applications. *Nano Select* **4,** 213–230. doi:10.1002/nano.202200219 (2023).
196. Murase, K., Aoki, M., Banura, N., Nishimoto, K., Mimura, A., Kuboyabu, T. & Yabata, I. Usefulness of Magnetic Particle Imaging for Predicting the Therapeutic Effect of Magnetic Hyperthermia. *Open Journal of Medical Imaging* **05,** 85–99. doi:10.4236/ojmi.2015.52013 (2015).
197. Nelson, B. J., Kaliakatsos, I. K. & Abbott, J. J. Microrobots for minimally invasive medicine. *Annual Review of Biomedical Engineering* **12,** 55–85. doi:10.1146/annurev-bioeng-010510-103409 (2010).
198. Neumann, A. & Buzug, T. M. Simulations of magnetic particles with arbitrary anisotropies. *Int. J. Magn. Part. Imag.* **6,** 2009032. doi:10.18416/IJMPI.2020.2009032 (2020).
199. Nigam, S., Gjelaj, E., Wang, R., Wei, G.-W. & Wang, P. Machine Learning and Deep Learning Applications in Magnetic Particle Imaging. *Journal of Magnetic Resonance Imaging* **61,** 42–51. doi:https://doi.org/10.1002/jmri.29294. eprint: https://onlinelibrary.wiley.com/doi/pdf/10.1002/jmri.29294 (2025).
200. Nigam, S., Gjelaj, E., Wang, R., Wei, G.-W. & Wang, P. Machine Learning and Deep Learning Applications in Magnetic Particle Imaging. *Journal of Magnetic Resonance Imaging* **61,** 42–51. doi:10.1002/jmri.29294 (Feb. 2024).
201. Nothnagel, N., Rahmer, J., Gleich, B., Halkola, A., Buzug, T. M. & Borgert, J. Steering of Magnetic Devices With a Magnetic Particle Imaging System. *IEEE Transactions on Biomedical Engineering* **63,** 2286–2293. doi:10.1109/TBME.2016.2524070 (2016).
202. O'donnell, M., Karr, S. G., Barber, W. D., Wang, J. M. & Edelstein, W. A. *Method for homogenizing a static magnetic field over an arbitrary volume* US Patent US4680551A. 1987.
203. O'Reilly, T., Teeuwisse, W. M. & Webb, A. G. Three-dimensional MRI in a homogenous 27 cm diameter bore Halbach array magnet. *Journal of Magnetic Resonance* **307,** 106578. doi:10.1016/j.jmr.2019.106578 (2019).
204. Ospel, J., Jaffray, A., Schulze-Zachau, V., Kozerke, S. & Federau, C. Spatial Resolution and the Magnitude of Infarct Volume Measurement Error in DWI in Acute Ischemic Stroke. *American Journal of Neuroradiology* **41,** 792–797. doi:10.3174/ajnr.A6520. eprint: https://www.ajnr.org/content/41/5/792.full.pdf (2020).
205. Ou, X., Chen, X., Xu, X., Xie, L., Chen, X., Hong, Z., Bai, H., Liu, X., Chen, Q., Li, L. & Yang, H. Recent Development in X-Ray Imaging Technology: Future and Challenges. *Research* **2021.** doi:10.34133/2021/9892152 (2021).
206. Ozaslan, A. A., Utkur, M., Canpolat, U., Tuncer, M. A., Karli Oguz, K. & Saritas, E. U. PNS Limits for Human Head-Size MPI Systems: Preliminary Results. *International Journal on Magnetic Particle Imaging,* Vol 8 No 1 Suppl 1 (2022). doi:10.18416/IJMPI.2022.2203028 (Mar. 2022).
207. Pacheco, M. O., Gerzenshtein, I. K., Stoppel, W. L. & Rinaldi-Ramos, C. M. Advances in Vascular Diagnostics using Magnetic Particle Imaging (MPI) for Blood Circulation Assessment. *Advanced Healthcare Materials* **13,** 2400612. doi:https://doi.org/10.1002/adhm.202400612. eprint: https://advanced.onlinelibrary.wiley.com/doi/pdf/10.1002/adhm.202400612 (2024).
208. Pagan, J., McDonough, C., Vo, T. & Tonyushkin, A. Single-Sided Magnetic Particle Imaging Device With Field-Free-Line Geometry for In Vivo Imaging Applications. *IEEE Transactions on Magnetics* **57,** 1–5. doi:10.1109/TMAG.2020.3008596 (2021).
209. Panou, G. *A Study on Geodetic Boundary Value Problems in Ellipsoidal Geometry* PhD thesis (July 2014). doi:10.12681/eadd/38080.
210. Patrick Vogel, Stefan Herz, Mriz Herzberg, Teresa Reichl, Johanna Günther, Martin Rückert, Thomas Kampf, Andreas Wörle, Volker Behr. *Stroke Cap - a Mobile Stroke Unit Prototype* 2024.
211. Paysen, H., Kosch, O., Wells, J., Loewa, N. & Wiekhorst, F. Characterization of noise and background signals in a magnetic particle imaging system. *Physics in Medicine & Biology* **65,** 235031. doi:10.1088/1361-6560/abc364 (Nov. 2020).
212. Peiravi, M., Eslami, H., Ansari, M. & Zare-Zardini, H. Magnetic hyperthermia: Potentials and limitations. *Journal of the Indian Chemical Society* **99,** 100269. doi:10.1016/j.jics.2021.100269 (2022).
213. Peng, Y., Shi, C., Kistenev, Y. V., Vrazhnov, D. A. & Cherkasova, O. P. in *Advances in Brain Imaging Techniques* (eds Mazumder, N., Gangadharan, G. & Kistenev, Y. V.) 163–182 (Springer Nature Singapore, Singapore, 2022). doi:10.1007/978-981-19-1352-5_10.

214. Pittaluga, S., Besio, S., Punzo, V. & Trequattrini, A. Racetrack coils for dedicated MRI magnets. *IEEE Transactions on Applied Superconductivity* **20,** 786–789. doi:10.1109/TASC.2010.2040724 (2010).
215. Punzo, V., Besio, S., Pittaluga, S. & Trequattrini, A. Solution of Laplace equation on non axially symmetrical volumes. *IEEE Transactions on Applied Superconductivity* **16,** 1815–1818. doi:10.1109/TASC.2005.864858 (2006).
216. Quelhas, K. N., Henn, M.-A., Farias, R., Tew, W. L. & Woods, S. I. GPU-accelerated parallel image reconstruction strategies for magnetic particle imaging. *Physics in Medicine & Biology* **69,** 135005. doi:10.1088/1361-6560/ad5510 (June 2024).
217. Rahmer, J., Halkola, A., Gleich, B., Schmale, I. & Borgert, J. First experimental evidence of the feasibility of multi-color magnetic particle imaging. *Phys. Med. Biol.* **60,** 1775–1791. doi:10.1088/0031-9155/60/5/1775 (Mar. 2015).
218. Rahmer, J., Gleich, B., Bontus, C., Schmale, I., Schmidt, J., Kanzenbach, J., Woywode, O., Weizenecker, J. & Borgert, J. Results on rapid 3D magnetic particle imaging with a large field of view. *Proceedings of the International Society for Magnetic Resonance in Medicine* **19,** 629 (2011).
219. Rahmer, J., Stehning, C. & Gleich, B. Remote Magnetic Actuation Using a Clinical Scale System. *PLoS ONE* **13,** e0193546. doi:10.1371/journal.pone.0193546 (2018).
220. Rahmer, J., Weizenecker, J., Gleich, B. & Borgert, J. Signal encoding in magnetic particle imaging: properties of the system function. *BMC medical imaging* **9,** 1–21. doi:10.1186/1471-2342-9-4 (2009).
221. Rahmer, J., Weizenecker, J., Gleich, B. & Borgert, J. Analysis of a 3-D system function measured for magnetic particle imaging. *IEEE Transactions on Medical Imaging* **31,** 1289–1299. doi:10.1109/TMI.2012.2188639 (2012).
222. Rahmer, J., Wirtz, D., Bontus, C., Borgert, J. & Gleich, B. Interactive Magnetic Catheter Steering With 3-D Real-Time Feedback Using Multi-Color Magnetic Particle Imaging. *IEEE Transactions on Medical Imaging* **36,** 1449–1456. doi:10.1109/TMI.2017.2679099 (2017).
223. Ramani, S., Liu, Z., Rosen, J., Nielsen, J. F. & Fessler, J. A. Regularization parameter selection for nonlinear iterative image restoration and mri reconstruction using GCV and SURE-based methods. *IEEE Transactions on Image Processing* **21,** 3659–3672. doi:10.1109/TIP.2012.2195015 (2012).
224. Ramlawi, B. The Era of Catheter-Based and Minimally Invasive Cardiac Surgery. *Methodist DeBakey Cardiovascular Journal* **12,** 3. doi:10.14797/mdcj-12-1-3 (Jan. 2016).
225. Reimer, P. & Balzer, T. Ferucarbotran (Resovist): A New Clinically Approved RES-specific Contrast Agent for Contrast-Enhanced MRI of the Liver: Properties, Clinical Development, and Applications. *European Radiology* **13,** 1266–1276. doi:10.1007/s00330-002-1721-7 (2003).
226. Rinaldi, D. Lamé's functions and ellipsoidal harmonics for use in chemical physics. *Computers and Chemistry* **6,** 155–160. doi:10.1016/0097-8485(82)85008-0 (1982).
227. Rösch, E. L., Zhong, J., Lak, A., Liu, Z., Etzkorn, M., Schilling, M., Ludwig, F., Viereck, T. & Lalkens, B. Point-of-need detection of pathogen-specific nucleic acid targets using magnetic particle spectroscopy. *Biosensors and Bioelectronics* **192,** 113536. doi:https://doi.org/10.1016/j.bios.2021.113536 (2021).
228. Rösch, J., Keller, F. S. & Kaufman, J. A. The Birth, Early Years, and Future of Interventional Radiology. *Journal of Vascular and Interventional Radiology* **14,** 841–853. doi:https://doi.org/10.1097/01.RVI.0000083840.97061.5b (2003).
229. Roy, O. & Vetterli, M. The effective rank: A measure of effective dimensionality. *European Signal Processing Conference,* 606–610. doi:10.5281/ZENODO.40328 (2007).
230. Salamon, J., Hofmann, M., Jung, C., Kaul, M. G., Werner, F., Them, K., Reimer, R., Nielsen, P., Vom Scheidt, A., Adam, G., Knopp, T. & Ittrich, H. Magnetic Particle / Magnetic Resonance Imaging: In-Vitro MPI-Guided Real Time Catheter Tracking and 4D Angioplasty Using a Road Map and Blood Pool Tracer Approach. *PLOS ONE* **11** (ed Yamamoto, M.) e0156899. doi:10.1371/journal.pone.0156899 (June 2016).
231. Sanela, A. & Dawood, T. *Sonography Fetal Assessment, Protocols, and Interpretation* https://www.ncbi.nlm.nih.gov/books/NBK576427/. StatPearls, 2023. doi:10.53347/rID-30190.
232. Saquib, S. S., Bouman, C. A. & Sauer, K. ML parameter estimation for Markov random fields with applications to Bayesian tomography. *IEEE Transactions on Image Processing* **7,** 1029–1044. doi:10.1109/83.701163 (1998).
233. Saritas, E. U., Goodwill, P. W., Zhang, G. Z. & Conolly, S. M. Magnetostimulation Limits in Magnetic Particle Imaging. *IEEE Transactions on Medical Imaging* **32,** 1600–1610. doi:10.1109/TMI.2013.2260764 (2013).
234. Sattel, T. F., Knopp, T., Biederer, S., Gleich, B., Weizenecker, J., Borgert, J. & Buzug, T. M. Single-sided device for magnetic particle imaging. *Journal of Physics D: Applied Physics* **42,** 022001. doi:10.1088/0022-3727/42/2/022001 (Feb. 2009).
235. Scheffler, K., Boberg, M., Grosser, M. & Knopp, T. *Sparsifying system matrices by combined usage of compressed sensing and extrapolation* in *12th International Workshop on Magnetic Particle Imaging* (2023), 1.
236. Scheffler, K., Boberg, M. & Knopp, T. Boundary artifact reduction by extrapolating system matrices outside the field-of-view in joint multi-patch MPI. *International Journal on Magnetic Particle Imaging* **8.** doi:10.18416/IJMPI.2022.2203019 (2022).
237. Scheffler, K., Boberg, M. & Knopp, T. Extrapolation of System Matrices in Magnetic Particle Imaging. *IEEE Transactions on Medical Imaging* **42,** 1121–1132. doi:10.1109/TMI.2022.3224310 (2023).
238. Scheffler, K., Boberg, M. & Knopp, T. Hands-free reconstruction for MPI. *International Journal on Magnetic Particle Imaging* **9.** doi:10.18416/IJMPI.2023.2303025 (2023).

239. Scheffler, K., Boberg, M. & Knopp, T. Solving the MPI Reconstruction Problem with Automatically Tuned Regularization Parameters. *Physics in Medicine & Biology* **69,** 045024. doi:10.1088/1361-6560/ad2231 (Feb. 2024).
240. Scheffler, K., Foerger, F. & Knopp, T. Experimental study on efficient field measurement using ellipsoidal harmonics. *International Journal on Magnetic Particle Imaging IJMPI* **11** (Mar. 2025).
241. Scheffler, K., Meyn, L., Foerger, F., Boberg, M., Martin, M. & Knopp, T. Ellipsoidal Harmonic Expansions for Efficient Approximation of Magnetic Fields in Medical Imaging. *International Journal on Magnetic Particle Imaging IJMPI* **10.** doi:10.18416/IJMPI.2024.2403006 (Mar. 2024).
242. Scheffler, K., Meyn, L., Foerger, F., Boberg, M., Möddel, M. & Knopp, T. *Ellipsoidal harmonic expansions for efficient approximation of magnetic fields in medical imaging* in *Conference Proceedings published as Supplement in the International Journal on Magnetic Particle Imaging* **10** (2024), 1–4. doi:10.18416/IJMPI.2024.2403006.
243. Scheffler, K., Meyn, L., Foerger, F., Boberg, M., Möddel, M. & Knopp, T. Efficient Measurement and Representation of Magnetic Fields in Tomographic Imaging using Ellipsoidal Harmonics. *Communications Physics* **8.** doi:10.1038/s42005-025-02012-5 (2025).
244. Scheffler, K., Thieben, F., Mohn, F., Graeser, M. & Knopp, T. *MPI Signal Performance of Resotran* in *12th International Workshop on Magnetic Particle Imaging* (2023), 1.
245. Schmiester, L., Möddel, M., Erb, W. & Knopp, T. Direct image reconstruction of Lissajous-type magnetic particle imaging data using Chebyshev-based matrix compression. *IEEE Transactions on Computational Imaging* **3,** 671–681 (2017).
246. Schrank, F., Pantke, D. & Schulz, V. Deep learning MPI super-resolution by implicit representation of the system matrix. en. *International Journal on Magnetic Particle Imaging,* Vol 8 No 1 Suppl 1 (2022). doi:10.18416/IJMPI.2022.2203020 (2022).
247. Schrank, F. & Schulz, V. Multi-purpose deep learning framework for MPI based on contrastive learning. en. *International Journal on Magnetic Particle Imaging IJMPI,* Vol 9 No 1 Suppl 1 (2023). doi:10.18416/IJMPI.2023.2303001 (2023).
248. Schultz, G. *Magnetic resonance imaging with nonlinear gradient fields: signal encoding and image reconstruction* (Springer Science & Business Media, 2013).
249. Schwenck, J., Sonanini, D., Cotton, J. M., Rammensee, H.-G., la Fougère, C., Zender, L. & Pichler, B. J. Advances in PET imaging of cancer. *Nature Reviews Cancer* **23,** 474–490. doi:10.1038/s41568-023-00576-4 (May 2023).
250. Seldinger, S. I. Catheter Replacement of the Needle in Percutaneous Arteriography: A new technique. *Acta Radiologica* **39.** PMID: 13057644, 368–376. doi:10.3109/00016925309136722 (1953).
251. Shah, S. A., Reeves, D. B., Ferguson, R. M., Weaver, J. B. & Krishnan, K. M. Mixed Brownian alignment and Néel rotations in superparamagnetic iron oxide nanoparticle suspensions driven by an ac field. *Phys. Rev. B* **92,** 094438. doi:10.1103/PhysRevB.92.094438 (9 Sept. 2015).
252. Shaqfa, M. & van Rees, W. M. Spheroidal harmonics for generalizing the morphological decomposition of closed parametric surfaces. *Construction and Building Materials* **454,** 138967. doi:https://doi.org/10.1016/j.conbuildmat.2024.138967 (2024).
253. Shasha, C. & Krishnan, K. M. Nonequilibrium Dynamics of Magnetic Nanoparticles with Applications in Biomedicine. *Advanced Materials* **33,** 1904131. doi:https://doi.org/10.1002/adma.201904131 (2021).
254. Shen, Y., Hu, C., Zhang, P., Tian, J. & Hui, H. A novel software framework for magnetic particle imaging reconstruction. *International Journal of Imaging Systems and Technology* **32,** 1119–1132. doi:https://doi.org/10.1002/ima.22707. eprint: https://onlinelibrary.wiley.com/doi/pdf/10.1002/ima.22707 (2022).
255. Shim, C. Y. & Lindner, J. R. Cardiovascular Molecular Imaging with Contrast Ultrasound: Principles and Applications. *Korean Circulation Journal* **44,** 1. doi:10.4070/kcj.2014.44.1.1 (2014).
256. Slavu, L. M., Antonelli, A., Scarpa, E. S., Abdalla, P., Wilhelm, C., Silvestri, N., Pellegrino, T., Scheffler, K., Magnani, M., Rinaldi, R. & Di Corato, R. Optimization of magnetic nanoparticles for engineering erythrocytes as theranostic agents. *Biomater. Sci.* **11,** 3252–3268. doi:10.1039/D3BM00264K (9 2023).
257. Sohail, A., Ahmad, Z., Bég, O. A., Arshad, S. & Sherin, L. A review on hyperthermia via nanoparticle- mediated therapy. *Bulletin du Cancer* **104,** 452–461. doi:10.1016/j.bulcan.2017.02.003 (2017).
258. Southern, P. & Pankhurst, Q. A. Commentary on the clinical and preclinical dosage limits of interstitially administered magnetic fluids for therapeutic hyperthermia based on current practice and efficacy models. *International Journal of Hyperthermia* **34,** 671–686. doi:10.1080/02656736.2017.1365953 (2018).
259. Starmans, L. W. E., Burdinski, D., Haex, N. P. M., Moonen, R. P. M., Strijkers, G. J., Nicolay, K. & Grüll, H. Iron oxide nanoparticle-micelles (ION-micelles) for sensitive (molecular) magnetic particle imaging and magnetic resonance imaging. *PLoS One* **8,** e57335. doi:10.1371/journal.pone.0057335 (Feb. 2013).
260. Starsich, F., Feye, J., Nissler, R., Da Silva Andre, G., Totter, E., Scheffler, K., Thieben, F., Mayr, E., Franke, J., Knopp, T. & Herrmann, I. Responsive Mn-Ferrite Nanoparticles for Multicolor Magnetic Particle Imaging, Sensing, and Reactive Oxygen Species Degradation. *Advanced Sensor Research*. doi:10.26434/chemrxiv-2025-b676k (Apr. 2025).
261. Storath, M., Brandt, C., Hofmann, M., Knopp, T., Salamon, J., Weber, A. & Weinmann, A. Edge Preserving and Noise Reducing Reconstruction for Magnetic Particle Imaging. *IEEE Transactions on Medical Imaging* **36,** 74–85. doi:10.1109/TMI.2016.2593954 (2017).
262. Sun, C., Lee, J. S. & Zhang, M. Magnetic Nanoparticles in MR Imaging and Drug Delivery. *Advanced Drug Delivery Reviews* **60,** 1252–1265. doi:10.1016/j.addr.2008.03.018 (Aug. 2008).

263. Sun, S., Chen, Y., Janssen, K.-J., Viereck, T., Schilling, M., Ludwig, F., Xu, L. & Zhong, J. Sparse-Representation-Based Image Reconstruction for Magnetic Particle Imaging. *IEEE Transactions on Instrumentation and Measurement* **73,** 1–9. doi:10.1109/TIM.2023.3332394 (2024).
264. Sun, S., Chen, Y., Zhao, M., Xu, L. & Zhong, J. Image Reconstruction for Magnetic Particle Imaging Based on Sparse Representation and Deep Learning. *IEEE Transactions on Instrumentation and Measurement* **73,** 1–9. doi:10.1109/TIM.2024.3381661 (2024).
265. Suskin, P., Foerger, F., Jürß, P., Boberg, M., Knopp, T. & Möddel, M. Power-Efficient Control of Non-Linear Magnetic Field Generators for MPI. en. doi:10.18416/IJMPI.2025.2503023 (2025).
266. Sutton, B. P., Noll, D. C. & Fessler, J. A. Fast, iterative image reconstruction for MRI in the presence of field inhomogeneities. *IEEE transactions on medical imaging* **22,** 178–188 (2003).
267. Svarnas, P., Papadopoulos, P. K., Vafeas, P., Gkelios, A., Clément, F. & Mavon, A. Influence of Atmospheric Pressure Guided Streamers (Plasma Bullets) on the Working Gas Pattern in Air. *IEEE Transactions on Plasma Science* **42,** 2430–2431. doi:10.1109/TPS.2014.2322098 (2014).
268. Szwargulski, P., Möddel, M., Gdaniec, N. & Knopp, T. Efficient joint image reconstruction of multi-patch data reusing a single system matrix in magnetic particle imaging. *IEEE Transactions on Medical Imaging* **38,** 932–944. doi:10.1109/TMI.2018.2875829 (2019).
269. Szwargulski, P. & Knopp, T. Influence of the receive channel number on the spatial resolution in magnetic particle imaging. *International Journal on Magnetic Particle Imaging* **3** (2017).
270. Szwargulski, P., Knopp, T., Boberg, M., Salamon, J., Scheitenberger, V., Göttsche, T., Linemann, R., Wegner, F., Friedrich, T., Barkhausen, J., Buzug, T. M. & Ahlborg, M. First Complex Trials Using a Dedicated Balloon Catheter for Magnetic Particle Imaging. *International Journal on Magnetic Particle Imaging* **8.** doi:10.18416/ijmpi.2022.2203004 (2021).
271. Szwargulski, P., Wilmes, M., Javidi, E., Thieben, F., Graeser, M., Koch, M., Gruettner, C., Adam, G., Gerloff, C., Magnus, T., Knopp, T. & Ludewig, P. Monitoring Intracranial Cerebral Hemorrhage Using Multicontrast Real-Time Magnetic Particle Imaging. *ACS Nano* **14,** 13913–13923. doi:10.1021/acsnano.0c06326 (Oct. 2020).
272. Tay, Z. W., Chandrasekharan, P., Chiu-Lam, A., Hensley, D. W., Dhavalikar, R., Zhou, X. Y., Yu, E. Y., Goodwill, P. W., Zheng, B., Rinaldi, C. & Conolly, S. M. Magnetic Particle Imaging-Guided Heating in Vivo Using Gradient Fields for Arbitrary Localization of Magnetic Hyperthermia Therapy. *ACS Nano* **12,** 3699–3713. doi:10.1021/acsnano.8b00893 (Apr. 2018).
273. Tay, Z. W., Chandrasekharan, P., Fellows, B. D., Arrizabalaga, I. R., Yu, E., Olivo, M. & Conolly, S. M. Magnetic Particle Imaging: An Emerging Modality with Prospects in Diagnosis, Targeting and Therapy of Cancer. *Cancers* **13.** doi:10.3390/cancers13215285 (2021).
274. Tay, Z. W., Hensley, D. W., Vreeland, E. C., Zheng, B. & Conolly, S. M. The Relaxation Wall: Experimental Limits to Improving MPI Spatial Resolution by Increasing Nanoparticle Core Size. *Biomedical Physics & Engineering Express* **3,** 035003. doi:10.1088/2057-1976/aa6ab6 (May 2017).
275. Tay, Z. W., Savliwala, S., Hensley, D. W., Fung, K. B., Colson, C., Fellows, B. D., Zhou, X., Huynh, Q., Lu, Y., Zheng, B., Chandrasekharan, P., Rivera-Jimenez, S. M., Rinaldi-Ramos, C. M. & Conolly, S. M. Superferromagnetic Nanoparticles Enable Order-of-Magnitude Resolution & Sensitivity Gain in Magnetic Particle Imaging. *Small Methods* **5,** 2100796. doi:10.1002/smtd.202100796 (Nov. 2021).
276. Tay, Z., Kim, H.-J., Ho, J. S. & Olivo, M. A Magnetic Particle Imaging Approach for Minimally Invasive Imaging and Sensing With Implantable Bioelectronic Circuits. *IEEE Transactions on Medical Imaging* **43,** 1740–1752. doi:10.1109/TMI.2023.3348149 (2024).
277. Them, K., Kaul, M. G., Jung, C., Hofmann, M., Mummert, T., Werner, F. & Knopp, T. Sensitivity enhancement in magnetic particle imaging by background subtraction. *IEEE Transactions on Medical Imaging* **35,** 893–900. doi:10.1109/TMI.2015.2501462 (2016).
278. Thieben, F., Mickoleit, F., Tessaro, S., Ludewig, P., Schüler, D., Garbayo, J., Uebe, R. & Knopp, T. Development of Optimized Magnetic Particle Imaging Tracers Utilizing Genetically Engineered Magnetosomes. *International Journal on Magnetic Particle Imaging*. **9.** inproceedings, 1–4. doi:10.18416/IJMPI.2023.2303066 (2023).
279. Thieben, F., Albers, H., Mohn, F., Foerger, F., Boberg, M., Scheffler, K., Möddel, M., Kluth, T. & Knopp, T. Experimental Parameter Calibration of the Scanner Model for Model-Based MPI. en. doi:10.18416/IJMPI.2024.2403025 (2024).
280. Thieben, F., Foerger, F., Mohn, F., Hackelberg, N., Boberg, M., Scheel, J.-P., Möddel, M., Graeser, M. & Knopp, T. System characterization of a human-sized 3D real-time magnetic particle imaging scanner for cerebral applications. *Commun Eng* **3.** doi:10.1038/s44172-024-00192-6 (Mar. 2024).
281. Thieben, F., Knopp, T., Boberg, M., Foerger, F., Graeser, M. & Möddel, M. On the receive path calibration of magnetic particle imaging systems. *IEEE Transactions on Instrumentation and Measurement* **72,** 1–15. doi:10.1109/TIM.2022.3219461 (2023).
282. Toma, T. T. & Weller, D. S. Fast automatic parameter selection for MRI reconstruction. *Proceedings - International Symposium on Biomedical Imaging,* 1078–1081. doi:10.1109/ISBI45749.2020.9098569 (Apr. 2020).
283. Top, C. B. & Güngör, A. Tomographic Field Free Line Magnetic Particle Imaging With an Open-Sided Scanner Configuration. *IEEE Transactions on Medical Imaging* **39,** 4164–4173. doi:10.1109/TMI.2020.3014197 (2020).
284. Trotter, J., Pantel, A. R., Teo, B.-K. K., Escorcia, F. E., Li, T., Pryma, D. A. & Taunk, N. K. Positron Emission Tomography (PET)/Computed Tomography (CT) Imaging in Radiation Therapy Treatment Planning: A Review

of PET Imaging Tracers and Methods to Incorporate PET/CT. *Advances in Radiation Oncology* **8,** 101212. doi:https://doi.org/10.1016/j.adro.2023.101212 (2023).

285. Tsanda, A., Jürß, P., Hackelberg, N., Grosser, M., Möddel, M. & Knopp, T. Extension of the Kaczmarz algorithm with a deep plug-and-play regularizer. en. doi:10.18416/IJMPI.2024.2403010 (2024).
286. Tsanda, A., Scheffler, K., Reiss, S. & Knopp, T. Denoising the system matrix with deep neural networks for better MPI reconstruction. *International Jounal on Magnetic Particle Imaging* **11** (Mar. 2025).
287. Uecker, M., Zhang, S., Voit, D., Karaus, A., Merboldt, K.-D. & Frahm, J. Real-time MRI at a resolution of 20 ms. *NMR Biomedicine* **23,** 986–994. doi:10.1002/nbm.1585 (Oct. 2010).
288. Vaalma, S., Rahmer, J., Panagiotopoulos, N., Duschka, R. L., Borgert, J., Barkhausen, J., Vogt, F. M. & Haegele, J. Magnetic Particle Imaging (MPI): Experimental Quantification of Vascular Stenosis Using Stationary Stenosis Phantoms. *PLoS ONE* **12,** e0168902. doi:10.1371/journal.pone.0168902 (2017).
289. Vaquero, J. J. & Kinahan, P. Positron Emission Tomography: Current Challenges and Opportunities for Technological Advances in Clinical and Preclinical Imaging Systems. *Annual Review of Biomedical Engineering* **17,** 385–414. doi:10.1146/annurev-bioeng-071114-040723 (2015).
290. Varoquaux, G. & Cheplygina, V. Machine learning for medical imaging: methodological failures and recommendations for the future. *npj Digital Medicine* **5,** 48. doi:10.1038/s41746-022-00592-y (Apr. 2022).
291. Veiseh, O., Gunn, J. W. & Zhang, M. Design and Fabrication of Magnetic Nanoparticles for Targeted Drug Delivery and Imaging. *Advanced Drug Delivery Reviews* **62,** 284–304. doi:10.1016/j.addr.2009.11.002 (2010).
292. Viard, A., Eustache, F. & Segobin, S. History of Magnetic Resonance Imaging: A Trip Down Memory Lane. *Neuroscience* **474.** Brain imaging, 3–13. doi:https://doi.org/10.1016/j.neuroscience.2021.06.038 (2021).
293. Viereck, T., Draack, S., Schilling, M. & Ludwig, F. Multi-spectral Magnetic Particle Spectroscopy for the investigation of particle mixtures. *Journal of Magnetism and Magnetic Materials* **475,** 647–651. doi:https://doi.org/10.1016/j.jmmm.2018.11.021 (2019).
294. Vogel, P., Rückert, M. A., Greiner, C., Günther, J., Reichl, T., Kampf, T., Bley, T. A., Behr, V. C. & Herz, S. iMPI: portable human-sized magnetic particle imaging scanner for real-time endovascular interventions. *Sci. Rep.* **13,** 10472. doi:10.1038/s41598-023-37351-2 (June 2023).
295. Vogel, P., Lother, S., Rückert, M. A., Kullmann, W. H., Jakob, P. M., Fidler, F. & Behr, V. C. MRI Meets MPI: A Bimodal MPI-MRI Tomograph. *IEEE Transactions on Medical Imaging* **33,** 1954–1959. doi:10.1109/TMI.2014.2327515 (2014).
296. Vogel, P., Markert, J., Rückert, M. A., Herz, S., Keßler, B., Dremel, K., Althoff, D., Weber, M., Buzug, T. M., Bley, T. A., Kullmann, W. H., Hanke, R., Zabler, S. & Behr, V. C. Magnetic Particle Imaging meets Computed Tomography: first simultaneous imaging. *Scientific Reports* **9.** doi:10.1038/s41598-019-48960-1 (Sept. 2019).
297. Vogel, P., Rückert, M., Günther, J., Reichl, T., Kampf, T., Gruschwitz, P., Augustin, A. M., Grunz, J.-P., Kleefeldt, F., Peter, D., Ergün, S., Bley, T., Behr, V., Herz, S. & Hartung, V. iMPI-guided angiography in a human cadaveric perfusion model. en. doi:10.18416/IJMPI.2025.2503030 (2025).
298. Volkens, H., Blancke Soares, Y., Buzug, T. & Gräfe, K. Algorithm for computing optimal SNR thresholds of a single-sided FFP MPI device. *International Journal on Magnetic Particle Imaging* **8.** doi:10.18416/IJMPI.2022.2203043 (2022).
299. Von Arx, D., Fischer, C., Torlakcik, H., Pane, S., Nelson, B. J. & Boehler, Q. Simultaneous Localization and Actuation Using Electromagnetic Navigation Systems. *IEEE Transactions on Robotics* **40,** 1292–1308. doi:10.1109/TRO.2023.3340324 (2024).
300. Von Gladiss, A., Graeser, M., Szwargulski, P., Knopp, T. & Buzug, T. M. Hybrid system calibration for multidimensional magnetic particle imaging. *Physics in Medicine and Biology* **62,** 3392–3406. doi:10.1088/1361-6560/aa5340 (Apr. 2017).
301. Von Gladiss, A., Graeser, M., Behrends, A., Chen, X. & Buzug, T. M. Efficient hybrid 3D system calibration for magnetic particle imaging systems using a dedicated device. *Scientific Reports* **10,** 1–12. doi:10.1038/s41598-020-75122-5 (2020).
302. Wang, S., Hossack, J. A. & Klibanov, A. L. From Anatomy to Functional and Molecular Biomarker Imaging and Therapy: Ultrasound Is Safe, Ultrafast, Portable, and Inexpensive. *Investigative Radiology* **55,** 559–572. doi:10.1097/rli.0000000000000675 (June 2020).
303. Wang, Y.-X. J. Superparamagnetic Iron Oxide Based MRI Contrast Agents: Current Status of Clinical Application. *Quantitative Imaging in Medicine and Surgery* **1,** 35–40. doi:10.3978/j.issn.2223-4292.2011.08.03 (Dec. 2011).
304. Wang, Z., Bovik, A. C., Sheikh, H. R. & Simoncelli, E. P. Image quality assessment: From error visibility to structural similarity. *IEEE Transactions on Image Processing* **13,** 600–612. doi:10.1109/TIP.2003.819861 (2004).
305. Weber, A., Werner, F., Weizenecker, J., Buzug, T. M. & Knopp, T. Artifact free reconstruction with the system matrix approach by overscanning the field-free-point trajectory in magnetic particle imaging. *Physics in Medicine and Biology* **61,** 475–487. doi:10.1088/0031-9155/61/2/475 (2015).
306. Weizenecker, J., Gleich, B., Rahmer, J., Dahnke, H. & Borgert, J. Three-dimensional real-time in vivo magnetic particle imaging. *Physics in Medicine and Biology* **54,** L1. doi:10.1088/0031-9155/54/5/L01 (Feb. 2009).
307. Weizenecker, J., Borgert, J. & Gleich, B. A simulation study on the resolution and sensitivity of magnetic particle imaging. *Physics in Medicine and Biology* **52,** 6363–6374. doi:10.1088/0031-9155/52/21/001 (2007).

308. Weizenecker, J. The Fokker–Planck equation for coupled Brown–Néel-rotation. *Physics in Medicine & Biology* **63,** 035004. doi:10.1088/1361-6560/aaa186 (Jan. 2018).
309. Weizenecker, J., Gleich, B., Rahmer, J. & Borgert, J. Micro-magnetic simulation study on the magnetic particle imaging performance of anisotropic mono-domain particles. *Phys. Med. Biol.* **57,** 7317. doi:10.1088/0031-9155/57/22/7317 (2012).
310. Wenzel, K., Alhamwey, H., O'Reilly, T., Riemann, L. T., Silemek, B. & Winter, L. B0-Shimming Methodology for Affordable and Compact Low-Field Magnetic Resonance Imaging Magnets. *Frontiers in Physics* **9,** 1–12. doi:10.3389/fphy.2021.704566 (2021).
311. Withers, P. J., Bouman, C., Carmignato, S., Cnudde, V., Grimaldi, D., Hagen, C. K., Maire, E., Manley, M., Du Plessis, A. & Stock, S. R. X-ray computed tomography. *Nature Reviews Methods Primers* **1.** doi:10.1038/s43586-021-00015-4 (Feb. 2021).
312. Womersley, R. S. in *Contemporary Computational Mathematics - A Celebration of the 80th Birthday of Ian Sloan* (eds Dick, J., Kuo, F. Y. & Woźniakowski, H.) 1243–1285 (Springer International Publishing, Cham, 2018). doi:10.1007/978-3-319-72456-0_57.
313. Wu, L., Zhang, Y., Steinberg, G., Qu, H., Huang, S., Cheng, M., Bliss, T., Du, F., Rao, J., Song, G., Pisani, L., Doyle, T., Conolly, S., Krishnan, K., Grant, G. & Wintermark, M. A Review of Magnetic Particle Imaging and Perspectives on Neuroimaging. *American Journal of Neuroradiology* **40,** 206–212. doi:10.3174/ajnr.A5896. eprint: https://www.ajnr.org/content/40/2/206.full.pdf (2019).
314. Yang, X., Shao, G., Zhang, Y., Wang, W., Qi, Y., Han, S. & Li, H. Applications of Magnetic Particle Imaging in Biomedicine: Advancements and Prospects. *Frontiers in Physiology* **13.** doi:10.3389/fphys.2022.898426 (July 2022).
315. Yeo, K. H., Rodrigo, I., Kuo, R., Chandrasekharan, P., Fellows, B. & Conolly, S. Characterizing the Performance of Commercial Magnetic Particles for Magnetic Particle Imaging. *International Journal on Magnetic Particle Imaging,* Vol 8 No 1 Suppl 1 (2022). doi:10.18416/IJMPI.2022.2203080 (Mar. 2022).
316. Yin, L., Li, W., Du, Y., Wang, K., Liu, Z., Hui, H. & Tian, J. Recent developments of the reconstruction in magnetic particle imaging. *Visual Computing for Industry, Biomedicine, and Art* **5.** doi:10.1186/s42492-022-00120-5 (Oct. 2022).
317. Ying, L., Xu, D. & Liang, Z.-P. On Tikhonov regularization for image reconstruction in parallel MRI. *IEEE Engineering in Medicine and Biology Society* **2,** 1056–9. doi:10.1109/IEMBS.2004.1403345 (Feb. 2004).
318. Yoshida, T., Othman, N. B. & Enpuku, K. Characterization of Magnetically Fractionated Magnetic Nanoparticles for Magnetic Particle Imaging. *Journal of Applied Physics* **114,** 173908. doi:10.1063/1.4829484 (Nov. 2013).
319. Zdun, L., Boberg, M. & Brandt, C. Joint multi-patch reconstruction: fast and improved results by stochastic optimization. en. *International Journal on Magnetic Particle Imaging,* Vol 8 No 2 (2022). doi:10.18416/IJMPI.2022.2212002 (2022).
320. Zhang, H., Zhang, B., Li, J., Zhou, G., Lei, S., An, Y. & Tian, J. A Novel Hand-Held Multi-Color Magnetic Particle Imaging Device Based on Rapid Frequency Conversion. *IEEE Transactions on Biomedical Engineering* **71,** 3602–3611. doi:10.1109/TBME.2024.3434961 (2024).
321. Zhang, H. & Qie, Y. Applying Deep Learning to Medical Imaging: A Review. *Applied Sciences* **13.** doi:10.3390/app131810521 (2023).
322. Zhang, P., Liu, J., Li, Y., Yin, L., An, Y., Zhong, J., Hui, H. & Tian, J. Dual-feature frequency component compression method for accelerating reconstruction in magnetic particle imaging. *IEEE Transactions on Computational Imaging* **9,** 289–297. doi:10.1109/TCI.2023.3255787 (2023).
323. Zhao, J., Shen, Y., Liu, X., Hou, X., Ding, X., An, Y., Hui, H., Tian, J. & Zhang, H. MPIGAN: An end-to-end deep based generative framework for high-resolution magnetic particle imaging reconstruction. *Med. Phys.* **51,** 5492–5509. doi:10.1002/mp.17104 (Aug. 2024).
324. Zhou, J., Li, M., Li, N., Zhou, Y., Wang, J. & Jiao, N. System integration of magnetic medical microrobots: from design to control. *Frontiers in Robotics and AI* **10,** 1–10. doi:10.3389/frobt.2023.1330960 (2023).
325. Zhou, Y. Quadrature rules with neighborhood of spherical designs on the two-sphere. *Applied Mathematics and Computation* **367,** 124769. doi:https://doi.org/10.1016/j.amc.2019.124769 (2020).
326. Zhou, Y. & Chen, X. Spherical t_e-designs for approximations on the sphere. *Mathematics of Computation* **87,** 2831–2855. doi:10.1090/mcom/3306 (2018).
327. Ziller, A., Mueller, T. T., Stieger, S., Feiner, L. F., Brandt, J., Braren, R., Rueckert, D. & Kaissis, G. Reconciling privacy and accuracy in AI for medical imaging. *Nature Machine Intelligence* **6,** 764–774. doi:10.1038/s42256-024-00858-y (July 2024).